Numerical Study of the Mechanical Properties of Lunar Soil by the Discrete Element Method

Chiara Modenese

St Anne's College, Oxford

Thesis submitted in fulfilment of the requirements for the degree of Doctor of Philosophy at the University of Oxford

Trinity Term, 2013

Abstract

Lunar soil, defined as the finest part of the lunar regolith which covers the entire surface of the Moon, has shown to have remarkable shear strength properties, highlighted by the clearly visible effects of soil cohesion. The main objective of this thesis is to unveil the physical explanations causing this unusual soil behaviour in a waterless, airless, lunar environment.

Ultra-High Vacuum (UHV), in particular, is considered responsible for increasing the strength of surface energy forces due to lunar soil outgassing. In turn, the presence of surface energy forces, arising from van der Waals intermolecular forces, is thought to alter the mechanical properties of lunar soil.

A particle-based microscopic approach by means of the Discrete Element Method (DEM) was utilised to investigate the effects of surface energy forces on the macroscopic soil behaviour. A micro-mechanical contact model, based on the JKR theory, was selected to describe the inter-granular behaviour between lunar soil particles. Physical and geometrical parameters typical of lunar soil were employed. Several triaxial tests were run to identify a link, if any, between the microscopic surface energy parameter and the macroscopic soil cohesion, which was interpreted as a true soil cohesion. In addition, very low stress levels and high soil densities were simulated in order to take into account the low gravitational field and the high state of soil compaction caused by continuous meteorite impacts on the Moon.

Results from triaxial tests were analysed at both the peak and critical state. It was found that in the ideal case of perfectly spherical grains, the presence of adhesion is a source of noticeable macroscopic soil cohesion. However, no influence was observed in terms of macroscopic friction angle. Furthermore, a brittle macroscopic soil behaviour was revealed, owing to the simulated inter-granular chemical bonds and the very low stress conditions applied. Finally, similar to the behaviour of cemented sands, very little cohesion was recorded at the critical state.

Subsequently, particle shape effects were investigated by complementing the numerical model with a simple form of inter-particle rolling resistance. Simulations were also run with non-convex grains of increasing geometrical complexity in order to simulate more realistically the irregular shapes of lunar soil grains. In both cases, the interplay of surface energy forces with particle shape effects resulted in even higher shear strength, with predictions similar to the estimates of shear strength for real lunar soil. Once again, the peak strength was dominated by macroscopic cohesion which, on the other hand, was hardly observable at the critical state, confirming the tendency observed from spherical grains.

Finally, the practical implications of the above findings were discussed in terms of bearing capacity, trafficability and slope stability on the lunar surface. In particular an analytical approach, based on the bearing capacity problem, was devised to study the performance of a rigid wheel rotating on a lunar terrain and operating under different dynamic conditions.

To my parents

Acknowledgements

First, and above all, I would like to thank my family for their total support throughout my doctoral studies. Without their effortless yet dedicated love and encouragement, this thesis would have never been possible.

I am also extremely grateful to my supervisors, Dr. Stefano Utili and Prof. Guy Houlsby, for their invaluable professional guidance. Driven by their knowledge and passion for research, they have helped me find a solution to the most intricate problems. Their support has also greatly contributed to further develop my critical thinking and analytical skills.

This research experience was made even more enjoyable thanks to the friendships of my office colleagues, with whom I shared both difficult and cheerful moments. Thanks to their contribution, I now better appreciate the advantage of sharing knowledge in an interdisciplinary and collaborative environment.

I would also like to thank all the users and developers of YADE software, whose invaluable guidance and advice have largely contributed to the success of this research project. In particular, I would like to acknowledge Dr. Bruno Chareyre and Dr. Vaclav Smilauer not only for their relentless technical support, but also for countless stimulating discussions in the interesting field of computational granular materials.

In addition, I wish to express my sincere gratitude to Dr. Colin Thornton and Dr. Otis Walton for though-provoking scientific discussions and constructive advice. Colin's frankness and openness to research have encouraged me to develop a critical eye in an evergrowing competitive research environment. I am most grateful to Otis for sharing his physics knowledge with me and for the clarity of his explanations on topics I was not always truly familiar with.

I must also thank Dr. Giles Kimminau for his assistance with improving my academic writing and the proofreading of this work.

Finally, I wish to acknowledge the fact that this work was in part financially supported by the Engineering and Physical Sciences Research Council (EPSRC) and by a St. Anne's College graduate scholarship.

Contents

Chapter 1

Introduction

The Moon, the Earth's natural satellite, has always been an attractive object for human beings, and lot of effort has been spent over the years in planning and conducting space explorations, some of which were successfully brought to completion. During the Apollo period (1963–1972), a large amount of lunar data was returned back to the Earth, and important studies were performed to answer intriguing questions and build invaluable knowledge on the physics and chemistry of the Moon (e.g. Vey and Nelson, 1966; Blum et al., 1967; Nelson and Vey, 1968; Grossman et al., 1970). This knowledge now represents a very powerful source of information, available for consultation to lunar scientists and engineers wishing to carry out further research.

Successful achievements from earlier explorations have increased the competition between Europe, China, USA, and Russia, and therefore their involvement towards new lunar missions (both robotic and manned). International organisations are helping to achieve the goal of a future return to the Moon, among them is the European Space Agency (ESA), to which the UK belongs. Collaboration between industry and academic research is deemed to play a key role in taking advantage of both recent advanced industrial technologies, such as new rover wheels (e.g. Ding et al., 2010; Chhaniyara et al., 2012), along with scientific tools to run numerical analysis (e.g. Li et al., 2010; Nakashima et al., 2010; Knuth et al., 2012).

The research presented in this thesis aims to address some of the currently unanswered

questions concerning the mechanics of soils in the lunar environment. The characteristics of which are a wide temperature variation, a very thin atmosphere and a low gravitational field. The aim is to increase our understanding of the geotechnical behaviour of lunar soil, which is referred to as the finest fraction of the lunar regolith – a soil layer covering the entire surface of the Moon to a maximum depth of 15 meters where it meets the underlying bedrock (Carrier et al., 1991). Lunar soil is a very fine dusty sand, resulting from intensive space weathering which is caused by the continuous meteorite impacts (Carrier et al., 1991). Lunar soil has also shown to have remarkable shear strength and cohesive properties, as witnessed by the Apollo astronauts and seen in the many pictures taken of the Moon's regolith showing the smooth vertical walls of deep trenches (see Fig. 1.1).

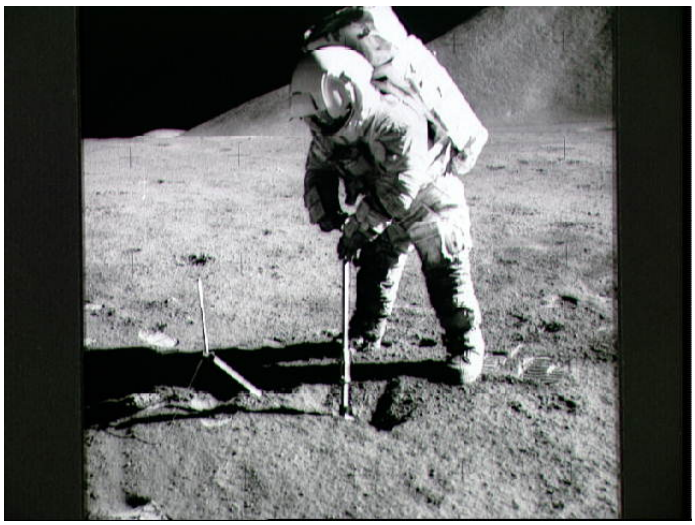

Figure 1.1: An astronaut digging a trench into the lunar soil during Apollo 15 (NASA Image AS15-92-12424).

The mechanical behaviour of lunar soil is still largely unknown due to the lack of experimental data. Of particular concern are the mysterious cohesiveness and high shearing resistance mentioned above. However, such a knowledge is crucial to guarantee the success of future operations on the Moon, such as digging into the soil, bulk sampling, vehicular activities and the construction of a proper lunar base.

Due to its granular structure, lunar soil represents an ideal candidate for numerical studies that are based on micro–mechanical multi–scale physical methods. Amid these approaches is the Discrete Element Method (DEM), which allows soil to be modelled as a collection of

grains interacting through contact laws defined at the microscopic scale (Cundall and Strack, 1979). The DEM was selected in this thesis as the most suitable tool to conceive and analyse experiments of lunar soil. This is deemed to offer a more valuable means of identifying the physical parameters governing lunar soil mechanics than continuum models which can fail to capture the microscopic phenomena occurring at the grain scale which in turn rule the macroscopic behaviour.

1.1 Research questions and thesis objectives

The main goal of the numerical work carried out in this thesis is to develop a thorough understanding of the fundamental mechanical behaviour of lunar soil by means of numerical element tests. The challenge is to provide a credible explanation for the high shear strength and visible cohesion of lunar soil based on physical parameters. Based on the findings of past experimental investigations (Perko and Nelson, 2000; Perko et al., 2001; Walton, 2008; Chang and Hicher, 2009), it is hypothesised that intermolecular surface energy forces, *i.e.* van der Waals forces, are thought to play a dominant role in the soil mechanics of a lunar-like environment. The fundamental questions arising from this hypothesis, and addressed by the present research, are: (i) how, and to what extent, do intermolecular surface energy forces determine lunar soil shearing strength resistance? (ii) what is the interplay between surface energy and elastic forces? (iii) how does this interplay affect the mechanical behaviour of the soil? Providing an answer to these questions is not only of scientific interest but will also be invaluable to assist in-situ extraterrestrial activities. Knowing and understanding the lunar soil mechanics is a prerequisite for solving many problems related to mining and geotechnical engineering which will be faced by future planetary missions. A deep knowledge of lunar soil physical properties will also enhance the mobility of lunar vehicles through a more informed approach to the wheel-soil interaction design.

The objectives and scopes of this work are not only limited to the above research questions. Despite the unusual nature of the principal material examined in this thesis, the

potential range of applicability of this study is far broader than directly related to lunar soil. Contributions will be made to at least three other fields of study, unrelated to lunar research, as introduced below.

(i) ***The DEM and the mechanics of fine cohesive powders***

First of all, the capabilities of the DEM technique to capture the behaviour of soils under both terrestrial and extraterrestrial conditions will be explored. The challenge is to show that a multi–scale approach can provide a reliable answer to the effects produced by intermolecular attractive forces upon the macroscopic behaviour. The interest, in particular, is on the bridge between surface energy microscopic properties and the macroscopic soil cohesion. The use of interparticle relationships, built from the association of continuum contact mechanics models and analytic theories of adhesion phenomena, will help identify such a link.

Given the physical properties and the very fine size of lunar soil grains, it is foreseen that the outcomes of this research will lead to new perspectives in the study of the rheological behaviour of cohesive powders, the handling of which has often caused great challenges such as flowability problems (Walton et al., 2007; Ramé et al., 2010).

(ii) ***Critical state soil mechanics***

This research will also provide insight into the ability of the DEM to reproduce experimental data when modelling the critical state of soils. Although this has already been attempted by other scientists with some success (Peña et al., 2009; Sitharam and Vinod, 2009; Zhao and Evans, 2011), a rigorous treatment is still missing in the literature, especially one that includes a realistically wide particle size distribution. The challenge posed by this problem is largely computational. This is because geotechnical element tests are generally run in the laboratory under quasi-static conditions. The quasi-static requirement, combined with the modelling of micrometer sized particles, contribute to greatly increase the computational load, because the small minimum size of the lunar soil grains dictates the critical time step necessary to assure the stability of the numerical scheme. Some alternative solutions are available to complete the simulations within a reasonable amount of time but their effectiveness has to be rigorously

verified to avoid a misleading interpretation of the results, as will be demonstrated in this thesis.

(iii) ***Sand behaviour at low confining pressures***

This thesis will also numerically investigate the soil behaviour at very low pressures in order to take account of the low gravity field of the lunar environment. The difficulties arising from the application of low confining pressure in a traditional triaxial test apparatus, can be easily overcome by the DEM. Thus the results will not only help the understanding of lunar soil mechanics, but they will also increase our knowledge of soil behaviour at low stresses, with possible future application to the study of liquefaction phenomena.

1.2 Thesis outline

Chapter 2 presents a review of lunar soil geotechnical properties. In particular, a characteristic particle size distribution is determined as an average curve of the data acquired from samples brought back to Earth with the Luna and Apollo missions.

A critical review of the physical phenomena involving contact adhesion is provided in Chapter 3. The goal is to identify a suitable constitutive model of micro-mechanical contact behaviour to be adopted in the DEM numerical experiments of lunar soil. A contact model is selected that takes into account the potential effects of the lunar environment on the mechanical properties of the surface soil.

Chapter 4 presents a numerical investigation into the ability of DEM to model soils under quasi-static conditions. The objective of which is to highlight the numerical difficulties and limits of the corresponding solutions which arise when the low confining pressures and inter-particle properties, typical of the lunar environment, are simulated.

Chapter 5 presents a series of triaxial DEM experiments studying the effect of interface energy, which is thought to be the origin of lunar soil cohesion. In an attempt to reproduce the high friction angle of real lunar material, some rolling resistance is added to the contact

model. The results obtained with rolling resistance and surface energy are further compared with a more realistic DEM model where the effects of particle shape are accounted for. Final judgements are advanced concerning the nature of the shearing strength in lunar soil.

Chapter 6 discusses the practical implications, in geotechnical terms, of the high shear strength obtained for lunar soil in Chapter 5. Three main geotechnical problems, of practical interest in lunar soil exploration activities, are considered: (i) the problem of static ultimate bearing capacity, (ii) the study of trafficability, such as the ability of a soil to support a vehicle and provide sufficient thrust for movement, and finally (iii) the problem of soil slope stability.

Finally, Chapter 7 provides a summary of the results and the main points of conclusion obtained from the analyses presented in the previous chapters. Recommendations for future research are also reported.

1.3 Author's contribution

The simulations presented in this thesis have been carried out by the author and the work was performed under the supervision of Prof. Guy Houlsby and Dr. Stefano Utili. The DEM platform called YADE (Smilauer et al., 2010), employed to run the numerical tests, is being developed by a large community of international researchers as part of an open source DEM project. The author has implemented and thoroughly verified all the contact models used in this study, in addition to providing a large contribution to the overall software development process, which includes co-authoring the software user manual (Smilauer et al., 2010)

Part of the content presented in this thesis has been presented at two international conferences and three papers have been published in the form of conference proceedings (Modenese et al., 2012a,b,c), one of which has been awarded with a second place in the best student paper competition (Modenese et al., 2012c). Two papers discussing the work of chapters 4 and 5, respectively, are under preparation and will be soon submitted to an international journal.

Chapter 2

Background

In this chapter, a complete description of the geotechnical properties of the lunar soil will be given. Particular emphasis will be placed on the possible definition of a suitable particle size distribution to be adopted in the later numerical analysis. A critical review of the parameters affecting the shear strength of the soil, such as particle shape, soil density, cohesion and friction angle, will be provided. Finally, a survey of the geotechnical properties of the lunar soil simulants will be carried out.

2.1 What is lunar soil?

The lunar soil is generally defined as the finest fraction of the lunar regolith, namely the layer of heterogeneous material which covers nearly the entire surface of the Moon, overlying a region of fractured bedrock (Carrier et al., 1991). The thickness of the lunar regolith can vary from a depth of 4-5 metres in the maria regions[1] up to 10-15 metres in the highland regions. The difference between mare and highland areas is mainly in their mineralogical composition, as will be seen later.

The lunar regolith is composed of five basic particle types: crystalline rock fragments, mineral fragments, breccias, agglutinates, and glasses. The composition of the soil reflects the main processes involved in its formation. These include comminution from the continuous impacts and cratering on the lunar surface, and agglutination (the welding of mineral and rock fragments) caused by micrometeorite impacts and solar wind which then lead to the

[1]Maria regions are lighter areas on the lunar surface having lower altitude than highland regions.

formation of very irregular particle shapes (Carrier et al., 1991). Space weathering is the collective term by which all these processes are known.

An adequate knowledge of lunar soil mechanical properties is crucial in order to assist future operations on the Moon such as construction and mining. It is hoped that it will also promote in-situ resource utilisation (ISRU), which is to maximise the use of resources available in space, thereby reducing the payload that needs to be carried into space. The lunar environmental factors which are the high temperature fluctuations, ultra-high vacuum and a weak gravitational field are likely to affect the soil properties. A brief comparison of the physical properties of the Moon and Earth is presented in Tab. 2.1.

Property	Moon	Earth
Mass	7.35×10^{22}kg	5.98×10^{24}kg
Radius	1,738km	6,371km
Surface area	37.9×10^{6}km^2	510.1×10^{6}km^2
Gravity	1.62m/s^2	9.81m/s^2
Diurnal temperature range	-233℃– 122℃	10℃– 20℃
Atmosphere	3×10^{-15}bar (night)	1014mbar

Table 2.1: Comparison between the physical properties of the Moon and Earth.

2.2 Engineering properties of lunar soil

2.2.1 Particle Size Distribution

The particle size distribution is one of the parameters determining the strength and compressibility of the soil. Sieve analyses are usually performed for particles bigger than 10μm. On the other hand, finer particles can be analysed using the scanning electron microscope (SEM) technique. In terms of lunar soil, particles smaller than 10μm are considered to be a part of the lunar dust and will therefore be excluded from the current investigation.

According to the ASTM[2] geotechnical classification system, the lunar soil can be described as a silty sand material. The average particle size is about 72μm and the material is

[2]American Section of the International Association for Testing Materials

well graded. A summary of the most representative geotechnical size parameters is reported in Tab. 2.2.

Parameter	Average	Range
D_{50} [μm]	72	46 – 110
$C_u = D_{60}/D_{10}$	16	8.7 – 30
$C_c = D_{30}^2/(D_{10}D_{60})$	1.2	0.7 – 2.0

Table 2.2: Parameters of the PSD of lunar soil (after Carrier, 2003).

The Lunar Grain Size Catalogue (LGSC) (Graf, 1993) provides a considerable amount of information concerning the samples which have been collected during both manned and robotic missions. To date a total amount of roughly 382kg of lunar soil has been brought back to Earth. The LGSC is a valuable source of information because it brings together the data gathered for each returned sample, detailing location, depth from the surface, and results obtained from sieve analyses. Samples were returned by a total of nine planetary missions: three Soviet Union Luna missions (1959-1976) and six US Apollo missions (1969-1972).

The variability of the lunar geology is vast. The lunar surface can be divided into two main geological environments: the (dark) maria and the (light) highlands regions, with the regolith thickness ranging from 4m up to 10m, respectively (Carrier et al., 1991). They differ both in the physical and mineralogical sense. Highland regions are more cratered and are mainly composed of feldsphatic minerals, whereas maria regions are flat areas whose mineralogical composition is formed by large quantities of pyroxene.

The scope of the following investigation is to identify whether it is possible to determine a representative Particle Size Distribution (PSD) of the lunar soil, notwithstanding the mineralogical and morphological surface features separating the maria and highland regions. A polynomial was fitted to the sieve analysis data from each separate landing described in the LGSC, and these curves were compared as seen in Fig. 2.1. There is little difference between the various PSDs from different locations and therefore it was considered valid to obtain a composite curve by fitting to an aggregate data set including all the samples, as illustrated in Fig. 2.2. Note that all the curves were obtained by a sixth degree polynomial

interpolation using linear regression analysis. Tab. 2.3 reports the values for the coefficient of determination R^2 and the standard deviation σ obtained for the fitted PSD of each mission and for the total regression distribution, demonstrating the good quality of the fitting.

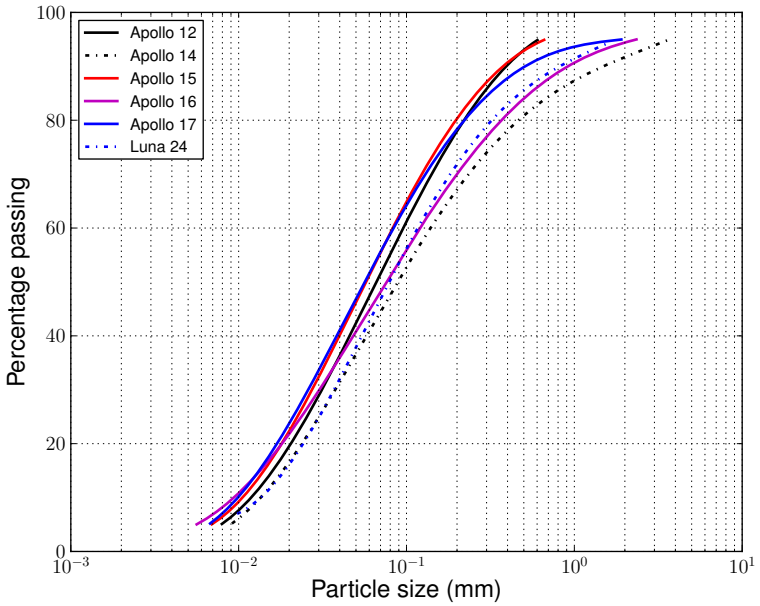

Figure 2.1: Comparison between the PSDs each representative of a different landing site.

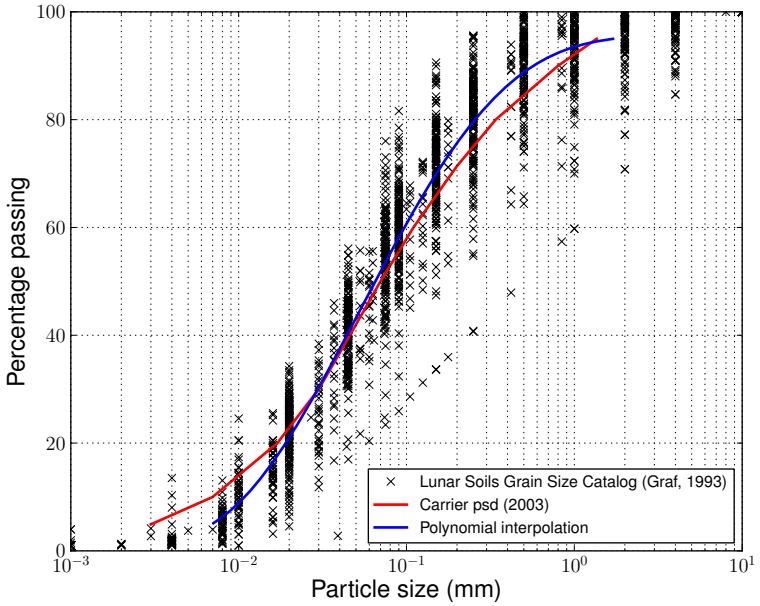

Figure 2.2: Comparison between the interpolation of the LGSC and the Carrier's findings (Carrier, 2003).

It was also found that the composite PSD curve compares well with the earlier findings reported by Carrier (2003), whose analysis included additional data from outside the

Mission	Number of samples	Coefficient R^2 [-]	Standard deviation σ [pp]
Apollo 12	15	0.89	5.02
Apollo 14	19	0.93	9.61
Apollo 15	52	0.90	4.50
Luna 24	6	0.90	3.30
Apollo 16	34	0.89	6.07
Apollo 17	35	0.86	7.01
All missions	162	0.92	7.28

Table 2.3: Statistical parameters of lunar soil samples analyses.

LGSC (Carrier, 2003) (see Fig. 2.2).

In conclusion, it can be stated that since there is no significant difference between PSDs corresponding to different lunar regions, it is possible to determined a representative PSD for lunar soil, in agreement with previous observations (Carrier, 2003).

In the DEM simulations, the representative PSD obtained in Fig. 2.2 will be considered. However, due to the computational limits, only a constrained discrete PSD, characterised by a ratio of maximum to minimum particle size equal to $R_D = D_{100}/D_0 = 8$, will actually be simulated, as indicated in Fig. 2.3. The largest particles will not be included because their contribution to the strength of the material was found to be negligible whenever the presence of fine particles becomes significant (Ueda et al., 2011). On the other hand, it is important to capture the effect of grading since this may influence the critical state of the soil, as numerically shown by Wood and Maeda (2008). However, the inclusion of the smallest particles is precluded by the need to limit the computational time.

2.2.2 Particle shape, macroscopic cohesion and friction angle

Particle shapes are also amongst the factors which are expected to significantly affect the mechanical behaviour of the soil. In particular, lunar soil grains are characterised by very elongated and subangular to angular shapes (Carrier et al., 1991). Such irregular shapes may be responsible for high particle interlocking, which in turn contributes towards the high shear strength shown by the lunar soil.

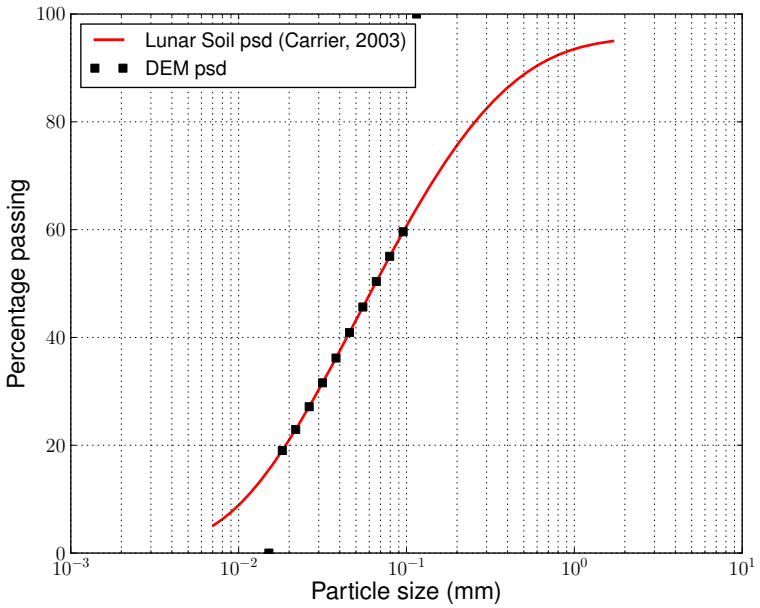

Figure 2.3: Constrained particle size distribution to be adopted in the numerical simulations of lunar soil.

The highly irregular shape of lunar grains is predominantly due to the presence of agglutinates, which are aggregates of mineral and rock fragments melted together and caused by the millions of micrometeorites impacting the lunar surface every day. Fig. 2.4 shows an SEM of an example of agglutinate particle. Agglutinates have been observed to increase the porosity of the lunar soil due to the presence of both inter–granular and intra–granular voids inside them (Carrier et al., 1991). A summary of the main particles shape parameters of the lunar soil is provided in Tab. 2.4.

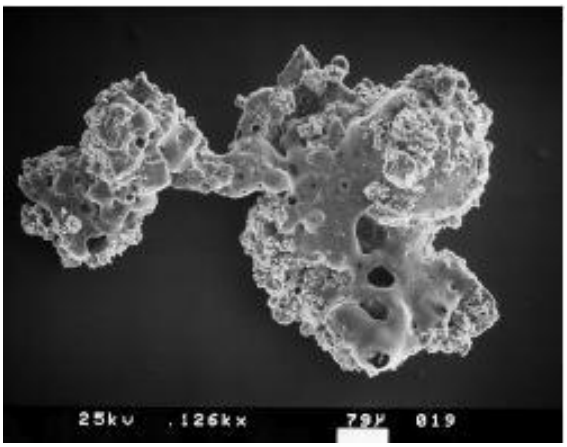

Figure 2.4: Irregular agglutinate particle part of the soil sample 10084 (NASA Image S87-38811).

Parameter	Average value	Description
Median particle size	40 μm – 130 μm	
Avg. particle size	70 μm	
Avg. elongation	1.35	Somewhat elongated
Avg. roundness	0.22	Subgranular to angular
Avg. specific surface area	0.5 m^2/g	Irregular, reentrant

Table 2.4: Shape parameters for lunar soil particles (Carrier et al., 1991).

As already mentioned, it is intuitive to think that irregular particle shapes more easily generate particle interlocking than rounded grains can do, as they fit tightly together, thereby influencing the shear strength of the soil. Understanding the causes of the high lunar soil shear strength is of fundamental importance in order to characterise its mechanical behaviour. Unfortunately, laboratory experiments on real lunar materials are very rare, for a variety of reasons (Carrier et al., 1991) such as:

(i) the lack of lunar material available for soil testing (only about 380 kg of soil have been brought back to Earth);

(ii) the complication of running laboratory tests under ultra-high vacuum, typical of the lunar environment, which poses several technical challenges in terms of testing equipments;

(iii) the difficulty to perform tests at very low confining pressures in order to match lunar surface conditions (only Scott (1987) was apparently able to perform miniature triaxial tests on real lunar samples. However, complete results have never been published).

Notwithstanding the above difficulties, a series of terrestrial laboratory-based miniature geotechnical tests has been carried out on the returned lunar soil, to complement the several direct observations recorded from the human and robotic interactions on the lunar surface. These include direct miniature shear tests, cone penetrometer and vane shear in–situ tests (Vey and Nelson, 1966; Houston and Namiq, 1971; Jaffe, 1971; Hovland and Mitchell, 1973; Carrier et al., 1991).

All the estimates of the cohesion and friction angle, as derived from the aforementioned experimental data, are reported in Fig. 2.5, where the high shear strength results from the

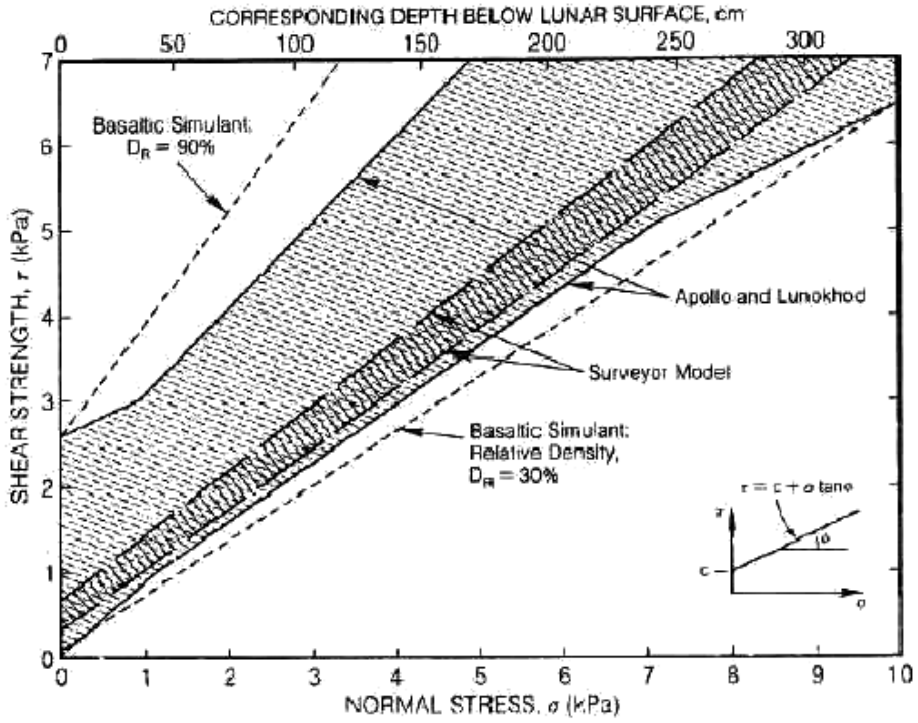

Figure 2.5: Estimates of shear strength properties and comparison with results from lunar soil basaltic simulants (after Carrier et al., 1991).

very high soil density (see Carrier et al., 1991, and references therein). The data are also compared with the shear strength of a basaltic lunar soil simulant of low and high relative density (Carrier et al., 1991). A summary of the recommended values of lunar soil cohesion and friction angle varying with depth is provided in Table 2.5 (Mitchell et al., 1972; Carrier et al., 1991).

Depth (cm)	Cohesion, c (kPa)		Friction angle, ϕ (deg)	
	Average	Range	Average	Range
0 – 15	0.52	0.44 – 0.62	42	41 – 43
0 – 30	0.90	0.74 – 1.1	46	44 – 47
30 – 60	3.0	2.4 – 3.8	54	52 – 55
0 – 60	1.6	1.3 – 1.9	49	48 – 51

Table 2.5: Best estimates of lunar soil shear strength parameters at increasing depth, *i.e.* soil density (after Carrier et al., 1991).

Although the evaluated range of lunar soil shear strength parameters is large (see Table 2.5), due to the uncertainties behind some of the methods used to generate such parameters (*e.g.* penetrometer test results were used to back–calculate soil friction and cohe-

sion (Carrier et al., 1991)), it is apparent that soil resistance increases with soil density and soil depth. Therefore, in order to account for this variability, the DEM tests will consider the simulation of samples prepared at both high and low relative density, as Chapter 5 will show.

2.2.3 Relative density, bulk density and porosity

The relative density strongly affects the exhibited mechanical behaviour and therefore is a fundamental parameter for the study of soil behaviour. In particular, the soil density influences the soil dilatancy, which in turn, is related to the shear strength of the soil (Schofield and Wroth, 1968). The relative density parameter is defined as:

$$D_R = \frac{e_{max} - e}{e_{max} - e_{min}} \quad , \tag{2.1}$$

where e_{max} and e_{min} are the maximum and minimum void ratio respectively. The relative density is a more convenient parameter for the comparison of different soils than absolute density because it is computed relative to the loosest and densest possible conditions of the type of soil under examination. To give an idea of the lunar soil density as a function of depth, the average of the available data on lunar soil relative density is summarised by increasing depth in Table 2.6 (Carrier et al., 1991).

Depth (cm)	Relative Density, D_R (%)	Description
0 – 15	65 ± 3	Medium to dense
0 – 30	74 ± 3	Dense
30 – 60	92 ± 3	Very dense
0 – 60	83 ± 3	Dense

Table 2.6: Variation of relative density with soil depth (Carrier et al., 1991).

In terms of bulk density versus depth, an empirical hyperbolic relation fitting the observed experimental data has been established by lunar scientists (Carrier et al., 1991) defined as:

$$\rho = 1.92\,\frac{z + 12.2}{z + 18} \quad , \tag{2.2}$$

where z indicates the depth from the lunar surface. This relation, $\rho(z)$, is plotted in Fig. 2.6.

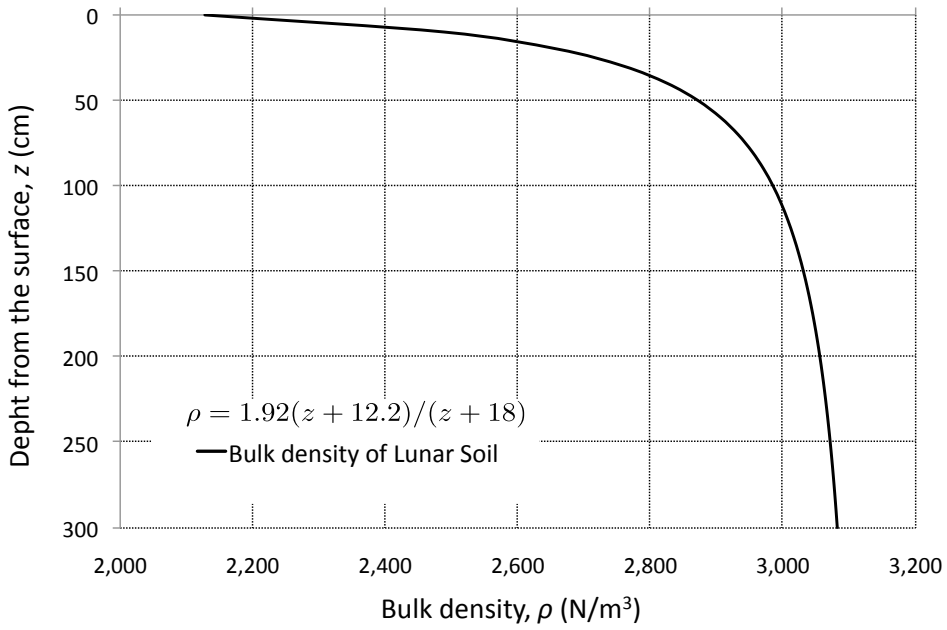

Figure 2.6: In-situ bulk density of lunar soil (Carrier et al., 1991; Carrier, 2005).

One striking feature of Fig. 2.6 is the high rate at which the bulk density increases with depth. In other words, the lunar soil is only under loose conditions at the surface quickly becoming highly compacted. It has also been argued that at larger depths there is no significant variations in the lunar soil relative density, which stays close to 90% (Carrier, 2005).

The relatively high density just below the surface is due to the continuous micrometeorites impacts on the lunar surface. Nevertheless, the surface porosity still maintains relatively high values, in the range between 40% and 50%. This is thought of as a by–product of both the presence of agglutinates and the high interlocking between lunar grains. A summary of the average porosity at different depths from the lunar surface is reported in Table 2.7.

Depth (cm)	Average Porosity, n (%)	Average Void Ratio, e
0 – 15	52 ± 2	1.07 ± 0.07
0 – 30	49 ± 2	0.96 ± 0.07
30 – 60	44 ± 2	0.78 ± 0.07
0 – 60	46 ± 2	0.87 ± 0.07

Table 2.7: Estimates of lunar soil average porosity and corresponding void ratio at increasing depth (Carrier et al., 1991).

2.2.4 Shear strength of lunar regolith simulants

The lack of available real lunar material on Earth has led researchers to design and produce large quantities of lunar soil simulants. The aim is to use these lunar-like materials for geotechnical testing as well as for the assessment of the mobility performance of rovers to potentially operate on the lunar surface.

Lunar regolith simulants are terrestrial materials produced from terrestrial rocks and minerals, especially designed to match the mechanical and chemico-physical properties of the lunar soil. The fidelity of lunar simulants to the real lunar material, however, is variable and often depends on the type of application the simulant was originally conceived for (e.g. fundamental geotechnical tests, trafficability studies, material processing, mineralogical studies).

There is an increasing number of lunar simulants from a variety of different producers having various compositions. A list of successful and recommended lunar simulants (Schrader et al., 2010b) includes: MLS-1 (Perkins and Madson, 1996), JSC-1 (Willman et al., 1995; Perkins and Madson, 1996; Klosky et al., 2000), JSC-1A (Alshibli and Hasan, 2009; Arslan et al., 2010; Hasan and Alshibli, 2010; Lee et al., 2010; Ramé et al., 2010; LaMarche et al., 2011), FJS-1 (Matsushima et al., 2009), GRC-1 (Oravec et al., 2010) and NU-LHT (He, 2010). Most of the simulants produced so far are mare basaltic simulants, *i.e.* they resemble the lunar soil of the maria region. However, recently the geotechnical properties of regolith highland simulants have also been investigated in detail (He, 2010). Although the fundamental properties of highland simulants in terms of mineral composition differ substantially from those of mare simulants, the geotechnical soil properties are found to be very similar.

There are several factors to consider when investigating how closely a regolith simulant is able to replicate the behaviour of lunar soil (Schrader et al., 2010a). The main simulant properties that should match the regolith include: grain size, particle size distribution, particle density, bulk density, mineralogy, grain shape, bulk chemistry, magnetic properties, compressive strength and shear strength (Sibille et al., 2005). Although mineral and chemical compositions may be relevant in determining the mechanical behaviour of the material when subjected to temperature changes or other environmental effects, greater attention will be placed on the physical properties of interest in this study, such as the geotechnical properties. Geometric attributes like the size and shape of the particles, the particle size distribution, the contact relationship between grains, and the way particles aggregate together, are amongst the factors expected to have a strong influence on the mechanical behaviour of the regolith simulant. Therefore, based on these factors, the geotechnical properties of the aforementioned lunar simulants will be compared in the following section.

2.2.4.1 Particle Size Distribution of lunar soil simulants

The PSDs of the various lunar simulants mentioned above are plotted together in Fig. 2.7. The JSC-1 simulant (Willman et al., 1995; Perkins and Madson, 1996; Klosky et al., 2000) is a basalt mare regolith which contains a mixture of lithic fragments, mineral fragments and irregular vesicular glassy particles (Klosky et al., 2000). MLS-1 has an analogous physical composition to JSC-1 but was designed to be a crushed high-titanium basalt (Perkins and Madson, 1996). It can be seen that MLS-1 has a slightly coarser PSD than JSC-1.

The JSC-1A simulant was introduced later to replace the discontinued JSC-1 as another standard low-titanium mare basalt simulant (Zeng et al., 2010) with the particle size distribution closely resembling the original.

FJS-1 simulant is a Japanese low-titanium mare basalt simulant (Matsushima et al., 2009) which was produced with highly irregular particles but having a coarser particle size distribution with respect to the other simulants. Finally, GRC-1 was recently manufactured in large quantities for evaluating lunar vehicle tractive performances (Oravec et al., 2010).

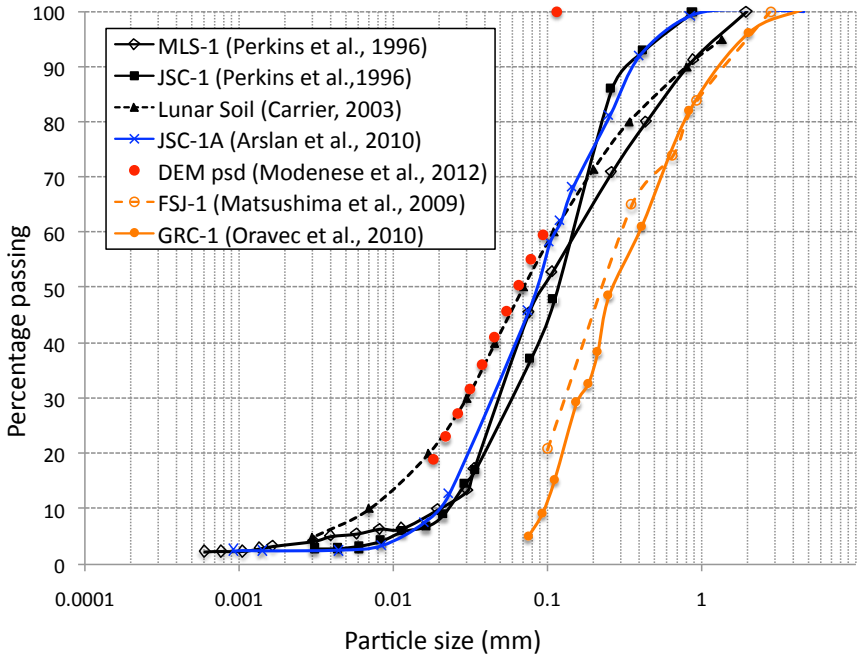

Figure 2.7: Comparison of different regolith simulants PSDs.

It should be noted that the PSDs of FJS-1 and GRC-1 are similar, both lacking very fine particles.

Fig. 2.7 also shows the PSD of real lunar soil as determined in Sec. 2.2.1. The distributions of JSC-1, JSC-1A and MLS-1 match fairly well with real lunar soil, however, MLS-1 does not contain the glassy material typical of the regolith. On the other hand, the PSDs of GRC-1 and FJS-1 simulants do not include the very fine fraction characterising lunar soil, and they can therefore be classified as poorly graded sands.

In conclusion, the simulants JSC-1 and JSC-1A seem to offer the best approximation of the lunar regolith, both in terms of particle size distribution and mineralogy and hence only these two will be considered in the following discussion.

2.2.4.2 Shear strength properties of JSC-1 and JSC-1A lunar simulants

Several triaxial tests were carried out on JSC-1 and JSC-1A samples at different confining pressures and relative densities (McKay et al., 1994; Willman et al., 1995; Perkins and Madson, 1996; Klosky et al., 2000; Arslan et al., 2010; Zeng et al., 2010). Details of the

results in terms of shear strength and cohesion are reported in Table 2.8 for different relative densities.

The following considerations regarding the geotechnical properties of JSC-1 and JSC-1A regolith simulants can be made from an examination of the experimental data:

(i) friction angles were found to be correlated with relative density. Experiments were carried out at high relative densities, although values near 90 or 100%, *i.e.* similar to the soil density on the lunar surface, were impracticable to achieve;

(ii) the analysis of the experimental data revealed friction angles ranging between 40° and 56°, thus in line with the high shear strength estimated for lunar soil (see Sec. 2.2.2);

(iii) the shear strength resistance was analysed in detail at the peak state but very little information was provided at the critical state, probably due to the technical difficulties arising when performing tests that reach very large strains, *i.e.* greater than 20%;

(iv) considering that tests were conducted under terrestrial conditions and in the absence of water, true soil cohesion was never observed. Some apparent cohesion, however, resulted from the adoption of a linear Mohr-Coulomb shear failure criterion to fit the experimental data (Klosky et al., 2000).

	JSC-1				JSC-1A			
	ρ (g/cm^3)	D_R (%)	ϕ (°)	c (kPa)	ρ (g/cm^3)	D_R (%)	ϕ (°)	c (kPa)
McKay et al., 1994	-	-	45	$\leq$1				
Willman et al., 1995	1.50	-	45	$\leq$1				
	1.60	-	45	$\leq$1				
	1.65	-	45	$\leq$1				
Perkins and Madons, 1996	1.78	-	48 – 64	0.0				
Klosky et al., 1996	1.62	40	44.4	3.9				
	1.72	60	52.7	13.4				
Klosky et al., 2000	1.62	53	44.4	3.9				
	1.72	75	49.5	6.2				
	1.81	95	53.6	14.4				
Alshibli et al., 2009					1.63	18.6	40	2
					1.88	73.7	49	5
Arslan et al., 2010					1.71	35.69	43.9	1.4
					1.79	53.56	44.5	1.4
					1.88	73.76	48	1.4
Zeng et al., 2010					1.65	24.6	41.87	0.0
					1.78	54.7	46.48	0.0
					1.94	84.6	56.70	0.0

Table 2.8: Peak shear strength of JSC-1 and JSC-1A simulants tested under terrestrial conditions.

Some measurements of residual or critical friction angles were also reported for samples of JSC-1A in the range of 34° to 40° (Arslan et al., 2010). However, particles with diameter smaller than 0.075mm were disregarded from the analysis, which could prevent a direct comparison with the best estimates of lunar soil shear strength. Other results of residual shear strength were reported for JSC-1A samples (Alshibli and Hasan, 2009) to increase with density in the range of 37° to 41° (tangent values). The reason for the critical friction angle's dependency upon the relative density were not given in the paper but it is likely that the tests were not performed up to a sufficiently high level of strain (Alshibli and Hasan, 2009, Fig. 3 and 4).

The available information on the geotechnical properties of lunar soil simulants represents an important contribution towards a better understanding of lunar soil mechanics. However, there are some important limitations to take into account. The first one is represented by the difficulty in applying very low stress levels, similar to those experienced on the lunar surface, in the laboratory. This is expected to have major consequences on geotechnical properties such as shear strength. An attempt to overcome this problem was made by developing a modified triaxial test apparatus, capable of applying very low confining pressures, to conduct tests on JSC-1 samples (Klosky et al., 2000). Peak friction angles, up to 53°, were obtained for very dense samples. These results were derived by fitting a line to all the experimental data obtained at both very low (1 to 20 kPa) and relatively high pressures (up to 80kPa) (Klosky et al., 2000). Moreover, the soil friction angles were computed using a linear Mohr-Coulomb failure criterion, therefore disregarding potential non-linearities of the failure envelope at very small stresses. The limitations of this data analysis can be better seen by restricting the fit to the dense samples that were tested at confining pressures between 1 and 20 kPa, ruling out the data that correspond to higher stress levels. The results in terms of (secant) friction angle versus confining pressure are reported in Fig. 2.8. The friction angles now have values up to 67° for the samples prepared at $D_R = 75\%$ and up to 60° for the samples at $D_R = 53\%$, thus much higher than the results reported in the original paper (Klosky et al., 2000). This shows that both pressure and relative density have a non-negligible effect on the friction angle. It also shows that extremely high shear resistance, perhaps more

representative of lunar soil, can be obtained if the data is examined at low confining levels.

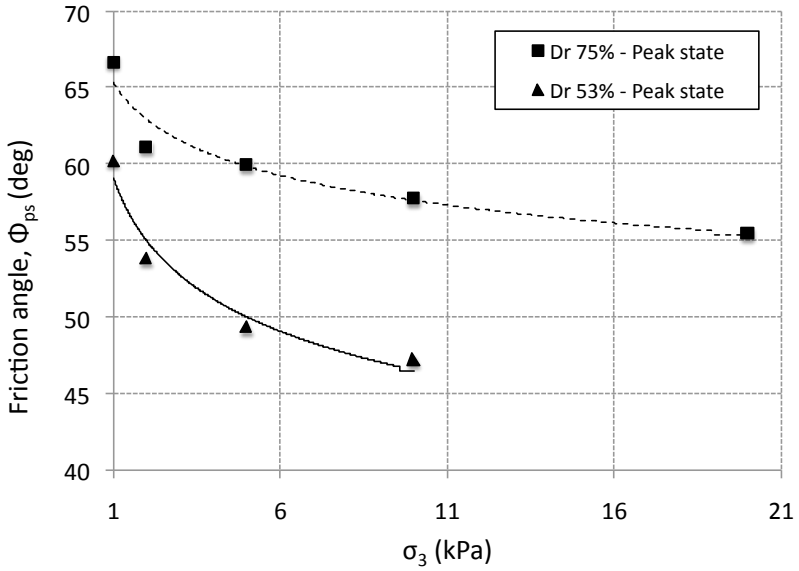

Figure 2.8: Peak friction angles of JSC-1 samples analysed versus cell confining pressures under triaxial loading (after Klosky et al., 2000).

The importance of confining pressure was also pointed out by Alshibli and Hasan (2009) who carried out tests of JSC-1A samples at low stresses. Friction angles as high as 60° for a confining pressure of 10 kPa and a relative density of 75% were observed. Note that this is also in line with the results obtained for JSC-1 samples as discussed above (see Fig. 2.8).

Other lunar environmental conditions, which are likely to affect the geotechnical properties of lunar soil and lunar soil simulants, include the ultra-high vacuum conditions of the Moon. The available experimental data that highlights the effects of vacuum on soil shear strength is reviewed in the next section.

2.2.5 Empirical soil behaviour under ultra-high vacuum

An extensive experimental program was run at the time of the Apollo missions, aiming to unveil the effects of lunar environmental conditions on the soil mechanical behaviour (Vey and Nelson, 1963, 1965, 1966). Direct shear tests were run on materials of different mineralogy (quartz, olivine, enstatite and obsidian) with a PSD typical of lunar soil. The direct shear

test apparatus was contained in a vacuum chamber in order to simulate the ultra-high vacuum conditions of the Moon (10^{-9} Torr). Under vacuum a net increase of shear strength was observed (see Fig. 2.9). The cause of this rise in shear strength was attributed to the absence of gas and high surface cleanliness produced by the ultra-high vacuum (Nelson and Vey, 1968).

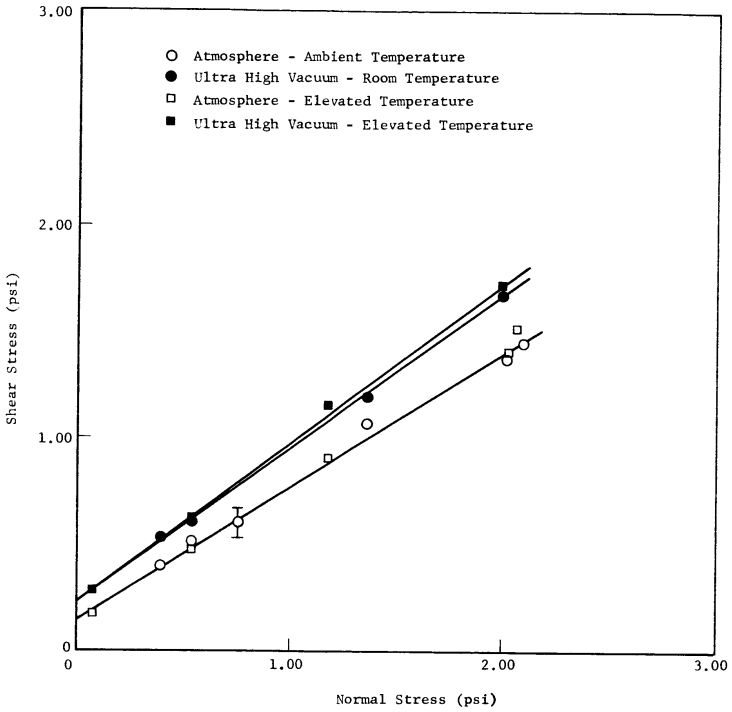

Figure 2.9: Direct shear test results of quartz powder shown on a Mohr-Coulomb plane. Tests were carried out at both terrestrial and ultra-high vacuum conditions. The picture was taken from NASA-CR-75323 (Vey and Nelson, 1966) and used with permission of NASA.

The main outcomes of the study can be summarised as follows (Vey and Nelson, 1966; Nelson and Vey, 1968):

(i) the ultra-high vacuum increased both the soil stiffness as well as the soil shear strength;

(ii) the development of bonds at the particle surface asperities due to inter-particle forces (van der Waals) was considered responsible for the increase in shear strength;

(iii) the increase in shear strength was characterised by an increase in both friction and cohesion;

(iv) the increase of shear strength was only observed at low normal stresses;

(v) the peak shear strength occurred at very low strains;

(vi) bonds created under ultra-high vacuum seemed to be effective only at the peak strength of the material;

(vii) the mineralogy affected the level of outgassing and therefore was found to play a crucial role in determining the soil shear strength.

A similar investigation was carried out on a lunar soil simulant by employing a torsional vane shear test in an ultra-high vacuum chamber (10^{-9}–10^{-11} Torr) (Johnson et al., 1973). The results confirmed that ultra-high vacuum significantly increased the soil shear strength.

Although the direct shear and torsional vane tests conducted under ultra-high vacuum (Vey and Nelson, 1966; Johnson et al., 1973) may provide only an approximate explanation for the unusual behaviour of lunar soil, they prove that ultra-high vacuum conditions are likely to have non-negligible effects on the geotechnical properties of lunar soil.

2.3 Summary

In this chapter, the main geotechnical properties of lunar soil have been described. Details have been provided concerning the soil density, soil porosity and particle shapes. A representative particle size distribution has been established by averaging the available experimental data obtained from sieve analysis of returned lunar samples from different locations, and therefore different mineralogies.

A review of the geotechnical properties of lunar soil simulants, in terms of soil density and shear strength parameters, has been presented. The differences between the existing lunar soil simulants in terms of particle size distribution and shear strength parameters have been highlighted. Due to the lack of experimental data available on real lunar soil, the goal was to identify the lunar soil simulant that more closely resembles the properties of the lunar regolith. This lunar soil simulant will be used as a reference soil during the calibration process of the DEM numerical model in Chapter 5.

Finally, the experimental evidence for the effects of ultra-high vacuum on the mechanical

soil behaviour has been discussed. Past investigations illustrated that a visible increase in soil shear strength was recorded under ultra-high vacuum conditions. Although no conclusive explanation was provided with regards the physical reasons for the rise in shear strength, this phenomenon was associated with a possible increase of the soil surface cleanliness and the consequent development of strong inter-particle chemical bonds. Probing the accuracy of these assumptions is one of the main goals of this thesis.

Chapter 3

A micro-mechanical contact model for lunar soil

This chapter provides a review of the relevant literature on the modelling of particle contact adhesion. Physical contact parameters, such as interface energy and surface cleanliness, are discussed in detail. Finally, a micro-mechanical contact model that is suitable for lunar soil is proposed.

3.1 Introduction

The objective of this chapter is to identify a micro–mechanical relationship that is able to account for the effects of van der Waals intermolecular forces among lunar soil grains. The final goal is to shed light on the reasons behind the high shear strength, particularly in the form of cohesion, exhibited by lunar soil. Direct estimations (*e.g* astronaut's footprints and trench excavations (Hovland and Mitchell, 1973; Carrier et al., 1991)) as well as laboratory tests (*e.g.* direct and miniature shear tests (Vey and Nelson, 1966; Nelson and Vey, 1968; Mitchell et al., 1972; Carrier et al., 1991)) suggest that lunar soil is unusually cohesive with respect to terrestrial materials of comparable gradation and mineral composition (Nelson and Vey, 1968). Based on previous studies (Perko and Nelson, 2000; Walton et al., 2007; Walton, 2010; Lee et al., 2010), there seem to be at least three plausible explanations for the high cohesion of lunar soil:

(i) high particle interlocking caused by the very irregular shapes of lunar soil grains;

(ii) the very low gravitational field (approximately only one sixth of the Earth's) could cause surface energy forces to prevail over body forces (Perko et al., 2001);

(iii) the lunar environmental characteristics, such as high temperature fluctuations, an absence of water and ultra-high vacuum (UHV), are thought to alter (increase) the strength of surface energy forces, in turn influencing lunar soil mechanics.

Of the above possible explanations for lunar soil cohesion, points (ii) and (iii) concern surface energy forces. In Chapter 5 we shall investigate the influence of adhesion on the macroscopic soil behaviour by the DEM. However, before doing so we first need to select a contact model that is suitable for describing the lunar soil. This chapter consists of a literature review and discussion of microscopic adhesion phenomena in order to inform this selection.

The established physical theories which reproduce the contact behaviour of elastically non-linear frictional adhesive particles shall be described. The non–linear elastic behaviour models the contact deformation in response to the applied load, while adhesion is caused by surface energy forces. In addition, intergranular friction accounts for the surface roughness of the individual particles. These three main aspects of the intergranular behaviour (such as non-linear elasticity, adhesion and friction) will at first be introduced independently to allow a better understanding of the phenomena involved. Their mutual interaction will then be tackled by means of a comprehensive contact model. Particular emphasis will be placed on the assumptions required to derive the various analytical treatments.

3.2 Hertzian elastic contact theory for macroscopic bodies

The non-linear contact behaviour between two elastic macroscopic bodies can be accurately described by the Hertzian contact theory (Hertz, 1882; Johnson, 1985). This deals with the purely elastic contact between two non-conforming bodies, *i.e.* two bodies which touch at

a single point or along a line (Johnson, 1985). The theory was derived under the following hypotheses (Johnson, 1985):

(i) each contacting body can be treated as an elastic half space;

(ii) the contact area is much smaller than the surfaces of the two bodies (small strain conditions apply);

(iii) the contacting surfaces are frictionless, which means that only normal compressive forces are considered;

(iv) no tension is allowed to be sustained at the contact;

(v) very importantly, it is assumed that at the contact point each surface can be approximated as parabolic.

Hertz predicted the following distribution of normal contact pressure:

$$p = p_o \left[1 - \left(\frac{r}{a}\right)^2\right]^{0.5} \tag{3.1}$$

where p_o is the maximum pressure at the centre of the contact, r is the distance from the centre and a is the contact radius, as illustrated in Fig. 3.1.

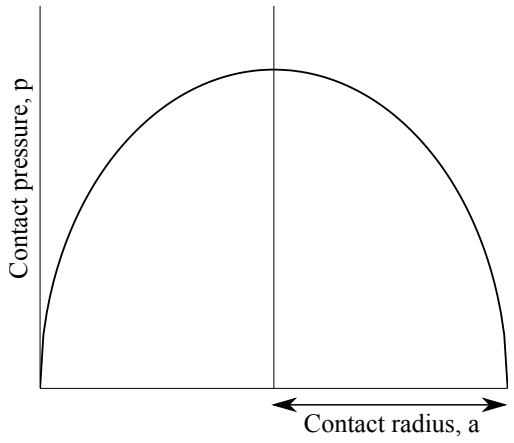

Figure 3.1: Contact pressure distribution as predicted by the Hertzian theory (Johnson, 1985), according to Eq. 3.1.

The normal contact force, P, was derived by integrating the contact pressure distribution (Johnson, 1985):

$$P = \int_0^a p(r) 2\pi r \, dr = \frac{2}{3} p_o \pi a^2 \quad . \tag{3.2}$$

Moreover, the relationship between the contact load and the overlap the particles u_n is given by

$$P = \frac{4}{3} E^* \sqrt{R^*} u_n^{\frac{3}{2}} \tag{3.3}$$

where u_n is calculated by the difference between the sum of the radii and the distance between the centroids of the two spheres, while the equivalent elastic modulus, E^*, and equivalent radius, R^*, are expressed as the following:

$$\frac{1}{E^*} = \frac{1-\nu_1^2}{E_1} + \frac{1-\nu_2^2}{E_2} \quad , \qquad \frac{1}{R^*} = \frac{1}{R_1} + \frac{1}{R_2} \tag{3.4}$$

where ν_1 and ν_2 are the Poisson's ratios of the two contacting bodies. It was also noted that u_n is geometrically related to the contact radius by the following expression (Johnson, 1985):

$$a^2 = R^* u_n \quad , \tag{3.5}$$

which, substituting Eq. 3.5 into Eq. 3.3, provides the following relationship between the contact radius and the contact load:

$$a = \sqrt[3]{\frac{3PR^*}{4E^*}} \quad . \tag{3.6}$$

3.3 Modelling adhesion between soil grains

There are several mechanisms in nature which are responsible for intermolecular adhesion: chemical (ionic, covalent and hydrogen bonds), dispersive (van der Waals forces) and electrostatic mechanisms. Depending on the mechanism, the resultant intermolecular forces can either be permanent or exist only under certain conditions, they can be a function of

particle size or surface roughness, result in different strengths and be effective at different interparticle ranges (Israelachvili, 1991).

Given the lack of moisture on the lunar surface, adhesion produced by hydrogen bonds will be disregarded. On the other hand, van der Waals surface energy forces are expected to prevail over electrostatic interactions, due to their very short-range nature (Perko et al., 2001). This is because electrostatic interactions act at a relatively long range, and are more likely to affect the motion of particles. Although this could be relevant in some circumstances such as the study of lunar dust levitation–related problems, it is beyond the scope of this thesis.

3.3.1 Van der Waals intermolecular forces

Van der Waals (vdW) intermolecular forces arise from the formation of instantaneous electromagnetic dipoles, *i.e.* a separation of positive and negative charges, due to the fluctuation of electron clouds in a nearby molecule or atom (Israelachvili, 1991). Molecules can experience both dipole-dipole and induced-dipole to dipole electrostatic interactions, which are very short-range forces whose potential energy varies with d^6, where d is the distance between the centroids of the dipoles.

We discuss below the potential energies experienced by the interaction of two atoms or molecules, an atom and a flat surface, two flat surfaces and finally two macroscopic spherical bodies. The motivation for exploring these first-principle relationships is to gain a basic understanding of the physical phenomena that cause adhesion. It is essential to understand these physical phenomena in order to adequately model the microscopic behaviour, especially when using these microscopic models to understand the macroscopic material behaviour, as we seek to do in this thesis.

3.3.1.1 Atom–atom interaction

In the literature, the definition of vdW forces often comprises both attractive and repulsive interactions of electromagnetic origin between atoms or molecules. However, in a vacuum the repulsive interaction is negligible (Israelachvili, 1991). There are a few contributions to the vdW forces but the largest of all is the so-called London contribution which predicts that, given two identical atoms interacting in a vacuum, they are characterised by the interaction energy, w, according to (Israelachvili, 1991):

$$w(r) = -\frac{C}{r^6} \tag{3.7}$$

where r is the interatomic distance, C is the London dispersion coefficient. Note that a negative sign is used to imply an attractive force.

3.3.1.2 Atom–surface and surface–surface interaction

In order to extend the calculation of an atom–atom interaction to that of an atom with a planar surface, the assumption of additivity is required (Johnson, 1985). This assumption neglects the interactions between pairs of atoms, thus allowing calculation of the interaction energy as the sum of the interaction of that atom with the interactions of all the atoms contained in the surface. This assumption has been found to be valid when the interaction occurs in a gaseous phase, such as in the lunar environment (Johnson, 1985). The interaction energy between an atom and a flat surface is given by (Johnson, 1985):

$$w(D) = -\frac{\pi \rho_a C}{6D^3} \tag{3.8}$$

where ρ_a is the density of atoms in the surface and D the distance between the atom and the body.

Under the assumption of additivity, it can also be demonstrated that for two flat surfaces

the vdW interaction potential energy is given by:

$$w(D) = -\frac{\pi \rho_a^2 C}{12 D^2} \qquad \text{(per unit area)}, \tag{3.9}$$

which, substituting the Hamaker coefficient $A = \pi^2 C \rho_a^2$, becomes:

$$w(D) = -\frac{A}{12\pi D^2} \qquad \text{(per unit area)}. \tag{3.10}$$

A summary of the vdW interaction energies corresponding to the three elementary cases introduced so far is provided in Table 3.1.

Configuration	Scheme	Intermolecular vdW potential
atom–atom	• •	$w(r) = -\frac{C}{r^6}$
atom–surface	• |	$w(D) = -\frac{\pi C \rho}{6 D^3}$
surface–surface	| |	$w(D) = -\frac{\pi C \rho^2}{12 D^2} = -\frac{A}{12\pi D^2}$ (per unit area)

Table 3.1: Potential energies under different configurations.

3.3.1.3 Sphere–sphere interaction and the Derjaguin approximation

The interparticle attractive force experienced by two spheres at distance D can be obtained as a function of the surface–surface potential energy expressed by Eq. 3.10 (Derjaguin, 1934; Israelachvili, 1991). The formula is known as the Derjaguin approximation (Derjaguin et al., 1975) and is valid provided that:

(i) the radii of the two contacting spheres, R_1 and R_2 respectively, are much higher than the interparticle distance D;

(ii) the area of interaction is assumed locally flat, meaning that the curvatures of the two interacting bodies can be reasonably neglected.

Under the above assumptions, the intermolecular forces can be integrated over small circular regions of flat area $2\pi x \mathrm{d}x$ (see Fig. 3.2). These areas are characterised by a vdW interaction

force computed as:

$$f(Z) = \frac{\partial w(Z)}{\partial D} \tag{3.11}$$

where $w(Z)$ is the surface–surface interaction potential expressed by Eq. 3.10 and $Z = D + z_1 + z_2$, the distance between the two flat surfaces considered (see Fig. 3.2).

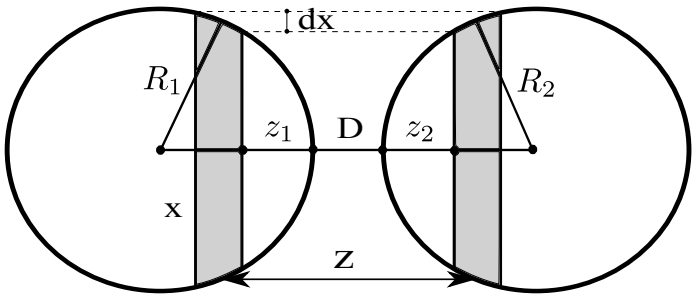

Figure 3.2: Sphere–sphere interaction. The Derjaguin approximation allows the potential to be computed as a function of the interaction between two flat surfaces.

Under the usual assumption of additivity, the total interaction force can be obtained by integrating the unitary force $2\pi x \mathrm{d}x f(Z)$ over the volumes of the two bodies, that is:

$$P(D) = \int_{Z=D}^{\infty} 2\pi\, x \mathrm{d}x\, f(Z) \quad . \tag{3.12}$$

Using the chord theorem and symbols as indicated in Fig. 3.2, the distance Z can be reformulated as:

$$Z = D + z_1 + z_2 = D + \frac{x^2}{2}\left(\frac{1}{R_1} + \frac{1}{R_2}\right) \quad . \tag{3.13}$$

Differentiating Eq. 3.13 with respect to x, we obtain:

$$\mathrm{d}Z = \left(\frac{1}{R_1} + \frac{1}{R_2}\right) x \mathrm{d}x \quad . \tag{3.14}$$

Equation (3.12) then becomes:

$$P(D) = \int_{Z=D}^{\infty} 2\pi \left(\frac{R_1 R_2}{R_1 + R_2}\right) f(Z)\mathrm{d}Z = 2\pi \left(\frac{R_1 R_2}{R_1 + R_2}\right) w(D) = 2\pi R_{eq} w(D) \tag{3.15}$$

where $w(D)$ is the potential energy between two flat surfaces separated by distance D and is expressed by Eq. 3.10 and R_{eq} is the so-called equivalent radius.

Furthermore, when the two spherical bodies come into contact, *i.e.* when the interparticle distance reaches the interfacial equilibrium distance D_0[1], the interaction energy w can be expressed as 2γ where γ is the surface energy per unit area (Johnson, 1985). In this case, the adhesion force between two rigid spherical bodies is computed as:

$$P(D_0) = F_{ad} = 2\pi R_{eq} w(D_0) = -4\pi\gamma R_{eq} \quad . \tag{3.16}$$

The main consequence of the Derjaguin approximation is that the attractive or adhesion force between two spheres, expressed by Eq. 3.16, is directly proportional to the interface energy γ. Note that the latter is defined as half of the energy needed to separate two flat surfaces from their equilibrium position to infinity (Johnson, 1985) (see Sec. 3.3.2).

It is worth pointing out that the adhesion force predicted by the Derjaguin approximation (Eq. 3.16) holds true only for contacts between non-deformable solids. It will be seen later how the effect of deformability can be approximated in the presence of adhesion (see Sec. 3.3.3).

3.3.2 Surface energy and surface cleanliness parameters for lunar soil

The surface energy γ is a material parameter, defined per unit area, which in a vacuum is equal to half of the work required to separate two identical surfaces when only considering the adhesive component, and it is expressed by Eq. 3.10. Thus, at contact, the surface energy per unit area is expressed by:

$$\gamma = \frac{A}{24\pi D_0^2} \quad . \tag{3.17}$$

[1]The equilibrium distance D_0 is defined as the distance of two spheres in contact.

The relationship between γ and D_0 is illustrated in Fig. 3.3.

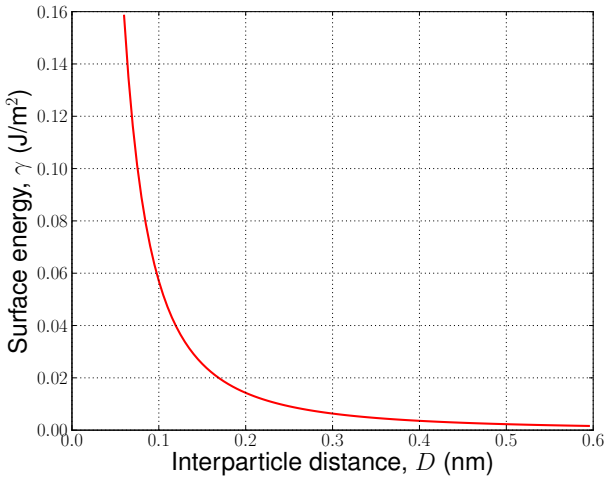

Figure 3.3: Relationship between surface energy and interparticle equilibrium distance according to Eq. 3.17, assuming a Hamaker coefficient for lunar soil equal to 4.3×10^{-20} J (Perko et al., 2001).

It is non-trivial to determine γ experimentally. The difficulty lies in the ability to isolate the contribution due to surface energy from other failure mechanisms taking place during the separation of two adhered surfaces. It is more common, instead, to measure the force of adhesion and then infer the corresponding surface energy using Eq. 3.16. This measurement can be achieved using an AFM (atomic force microscope) under controlled environmental conditions (*e.g.* UHV), and can also provide details about the surface topography.

Surface cleanliness is a physical parameter introduced by Perko et al. (2001) in order to quantify the amount of soil outgassing that occurs on the lunar surface. For short range interactions, the interpartilce equilibrium separation distance D_0 is taken to be twice the thickness of the gas layer adhering to the particles. The thickness of this layer is dependent on the surrounding environment, and on the Moon the environmental conditions cause this to be very thin as seen in the high levels of outgassing. The surface cleanliness parameter is defined as:

$$S = \frac{\Omega}{t} \quad , \tag{3.18}$$

where Ω is the diameter of an atomic oxygen ion (O^{-2}) equal to $1.32\mathring{A}$ and where t is half of the equilibrium distance D_0. Surface cleanliness can thus range from 0 (when the

thickness approaches infinity) to 1 (if very high gas desorption occurs), as shown in Fig. 3.4. The effects of the gas desorption on the soil behaviour were investigated earlier by Nelson and Vey (1968) who found that the soil shear strength is highly dependent on the surface cleanliness of the soil grains.

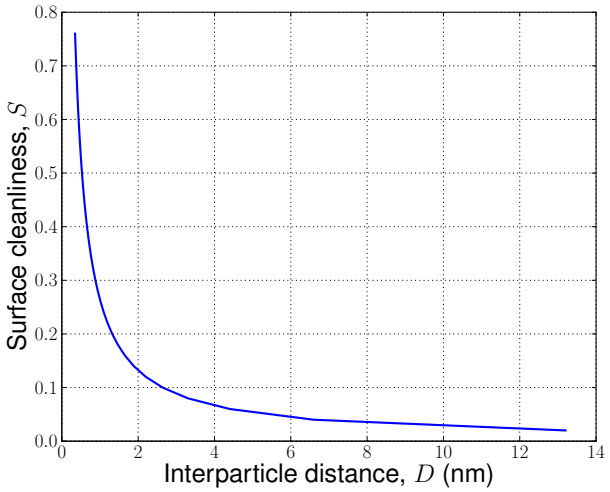

Figure 3.4: Surface cleanliness versus the equilibrium interparticle distance D_0.

Furthermore, Perko et al. (2001) developed a micro-mechanical model capable of estimating the soil shear strength which takes into consideration the vdW interparticle forces. The effect of the vdW forces is considered through their influence on the thickness t of the adsorbed gas layer. This in turn determines the surface cleanliness parameter (see Eq. 3.18) which is used as the model input. Simulations were run for soils of various mineral and chemical compositions and under various environmental conditions (Perko et al., 2001). When simulating lunar soil with a very high surface cleanliness parameter, the soil friction angle and cohesion at the critical state were increased by 24° and 0.5 kPa, respectively (Perko et al., 2001). The additional contributions to soil shear strength were in line with the discrepancies obtained from laboratory and in-situ tests conducted under terrestrial and lunar conditions (Perko et al., 2001).

More recently, Chang and Hicher (2009) proposed a new constitutive model for lunar soil on the basis of the method developed by Perko et al. (2001). By means of triaxial tests run under different environmental conditions, they observed an increase in the net soil shear strength of approximately 10% when including surface energy forces. Their re-

sults corresponded to an interparticle equilibrium distance D_0 in the range of 0.6 to 0.3nm. According to Eq. 3.17 and Eq. 3.18, and assuming an approximate Hamaker coefficient of 4.3×10^{-20}J [2] (Perko et al., 2001), these values would correspond to a range of surface cleanliness parameter between 0.44 and 0.88 and interface surface energy between 1.58 and 6.33 mJ/m^2, respectively. However, the results obtained by Chang and Hicher (2009) cannot be considered representative of lunar soil since tests were run employing the physical parameters of a uniform Hostun sand. Moreover, the constitutive model adopted by Chang and Hicher (2009) is inappropriate, as will be discussed later in Sec. 3.3.3.

Despite the fact that the surface cleanliness parameter may provide a simple means to evaluate the soil shear strength in different environments (Perko et al., 2001), a representative value of lunar soil surface energy has not yet been established. However, Wilkinson (2009) made surface energy measurements for lunar soil simulants employing a novel technology called Inverse Gas Chromatography (IGC). For the simulant JSC-1A (Klosky et al., 2000), Wilkinson (2009) found a value of γ around 80mJ/m^2, which increased to about 100mJ/m^2 when temperature effects were also taken into account. However, in this thesis, a value of γ equal to 0.07J/m^2 will be employed in the numerical simulations of lunar soil (see Chapter 5). This value is only slightly more conservative than implied by the IGC experiments on JSC-1A simulant (Wilkinson, 2009), but it is in line with DEM simulations by Baran et al. (2009) who were influenced by undisclosed NASA data. Note that once a value of γ is established, the corresponding value of surface cleanliness can also be obtained using Eq. 3.17 and 3.18.

3.3.3 Adhesion theories for deformable contact bodies

A model aimed to describe accurately the integranular behaviour of soil particles must also take account of the soil's elastic deformability. This is because soil grains are never perfectly rigid but react to normal applied loads with contact deformations. The same logic is applied

[2] A precise determination of the Hamaker coefficient is difficult to obtain since it depends on the complex mineral composition of lunar soil (Perko et al., 2001).

in the DEM, where contact deformations are considered by allowing particles to physically overlap according to a predefined contact load-displacement relationship. Therefore it is important to identify a theory which integrates the effects of interparticle adhesive forces (as discussed in the previous section) with the influence of contact elastic deformations from applied loads.

In the following sections, a critical review is given of two well-established formulations modelling the effect of adhesion between elastic contact bodies. These formulations are known as the DMT (Derjaguin et al., 1975) and the JKR (Johnson et al., 1971) contact theories. Particular emphasis will be placed on the assumptions behind each model.

3.3.3.1 The DMT model

The DMT model dates back to 1975 (Derjaguin et al., 1975) and was developed with the intent to account for the presence of vdW attractive forces at the contact between elastic macroscopic bodies. The theory assumes that the action of vdW forces is confined to an external area surrounding the contact zone. As a consequence, the reciprocal influence between vdW interactions and elastic contact forces is neglected. At the same time, the presence of vdW forces gives rise to a constant attractive force. This is in addition to the elastic contact load predicted by the classical Hertzian solution (see Sec. 3.2). Note that the Hertzian contact pressure distribution is unaltered since vdW forces are supposed to act only outside the contact region.

Derjaguin et al. (1975) found that the adhesion force tends asymptotically to a constant value as soon as the contact is loaded and, consequently, depends only marginally on the contact deformation. The DMT adhesion force was derived using a thermodynamic approach (Derjaguin et al., 1975) and it was found equal to:

$$P_{ad} = -4\pi R^* \gamma \tag{3.19}$$

where R^* is the equivalent contact radius given by Eq. 3.4. Note that this result coincides with the Derjaguin approximation (Eq. 3.16) which predicts the vdW attractive force between two non-deformable bodies in mutual contact.

According to Derjaguin et al. (1975) the adhesion force given by Eq. 3.19 is then added to the repulsive Hertzian contact force, Eq. 3.3. Therefore the total contact load–displacement relationship can be written as:

$$P = -4\pi R^* \gamma + \frac{4}{3} E^* \sqrt{R^*} u_n^{\frac{3}{2}} \tag{3.20}$$

The above relationship is illustrated in Fig. 3.5, where the Hertzian elastic solution is also shown.

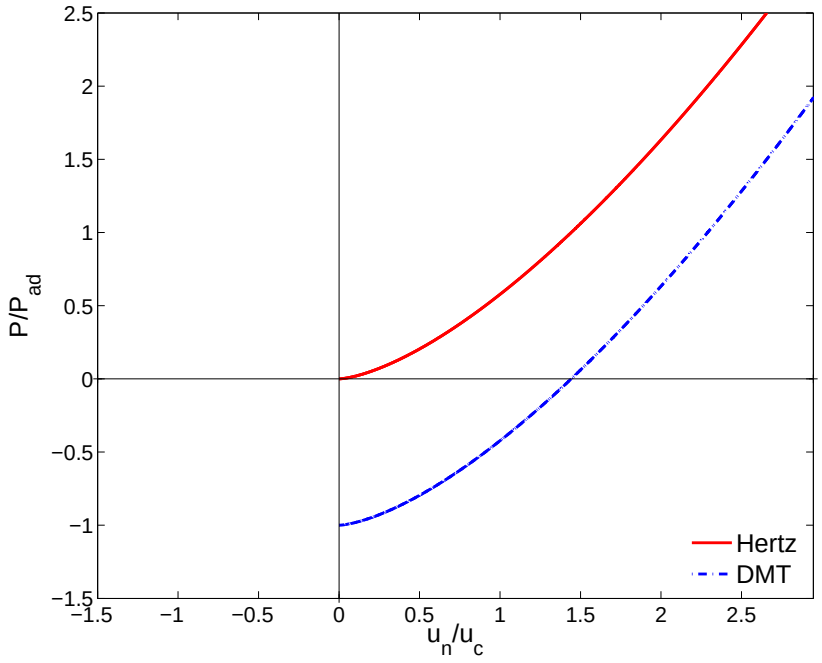

Figure 3.5: Comparison between Hertz and DMT contact models. The normal force is normalised by the DTM adhesion force, Eq. 3.19, while the contact overlapping is normalised by the displacement $u_c = 3/2(\pi^2 \gamma^2 R^*/2E^{*2})$.

Although the DMT adhesion force is assumed to be independent of the elastic deformations, the contact area is predicted to increase as a result of adhesion, in agreement with the experimental findings (Derjaguin et al., 1975). The relationship between the contact radius and the external applied load was given by Hertz in Eq. 3.6. In the presence of adhesion,

however, the external load no longer coincides with the contact load (Pashley, 1984). The contact load is now computed as the difference between the applied force, *i.e.* the elastic Hertzian reaction force, and the DMT attractive force P_{ad} (Eq. 3.19). The DMT contact radius will then follow the relationship:

$$a = \sqrt[3]{\frac{3R^*}{4E^*}\left(4\pi R^*\gamma + \frac{4}{3}E^*\sqrt{R^*}u_n^{\frac{3}{2}}\right)} \quad . \tag{3.21}$$

Consequently, when no external load is applied the contact radius is finite owing to the presence of adhesion and it is expressed by:

$$a_0 = \sqrt[3]{\frac{3\pi R^{*2}\gamma}{E}} \quad . \tag{3.22}$$

3.3.3.2 The JKR formulation

The JKR theory (Johnson, 1985; Johnson et al., 1971) provides an analytical description of the contact behaviour between elastic adhesive bodies. Although the JKR model was initially proposed as an alternative to the DMT formulation (see Sec. 3.3.3.1), it was subsequently discovered that the two theories are at either end of a spectrum of possible solutions that depend on the deformability of the contact bodies (Tabor, 1977), as will be discussed later in Sec. 3.3.3.3.

The JKR theory is essentially a modified version of the Hertzian contact theory. It combines the presence of elastic deformations with the influence of vdW forces acting inside the contact region. The equations governing the JKR formulation were derived by means of energy arguments (Johnson et al., 1971). On a similar way to the DMT solution, the contact area is enlarged by the presence of adhesion and this results in an effective contact radius, a, equal to (Johnson et al., 1971):

$$a^3 = \frac{R^*P_1}{K} = \frac{R^*}{K}\left(P + 2P_{ad} \pm \sqrt{4P_{ad}^2 + 4PP_{ad}}\right) \quad , \tag{3.23}$$

where P is the contact load, and K is an equivalent stiffness defined as:

$$K = \frac{4}{3}\pi(k_1 + k_2) \quad , \tag{3.24}$$

$$k_1 = \frac{1-\nu_1^2}{\pi E_1}, \quad k_2 = \frac{1-\nu_2^2}{\pi E_2} \quad , \tag{3.25}$$

and where the adhesion force, P_{ad} is predicted as:

$$P_{ad} = -3\gamma\pi R^* \quad . \tag{3.26}$$

Note that the JKR theory can be related back to the Hertzian model by relating the effective contact radius a to an effective Hertzian load, P_1 as indicated in Eq. 3.23. Once again the force of adhesion is simply defined as a function of the surface energy γ and of the equivalent particle radius (see Eq. 3.26).

The normal stress distribution predicted by the JKR formulation is characterised by compression in the centre, and infinite tension at the edge (see Fig. 3.6) (Johnson et al., 1971). The infinite tension at the edge results from the JKR assumption of neglecting adhesion forces outside the contact zone. An alternative theory of adhesion proposed by Maugis (1992) would avoid this problem, as will be mentioned later.

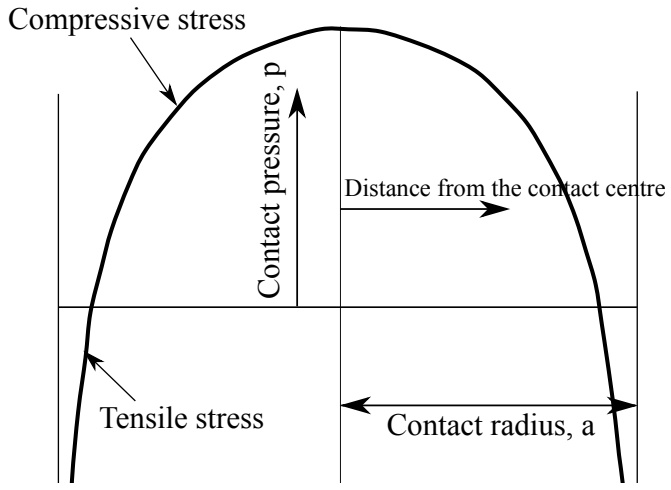

Figure 3.6: JKR normal stress distribution at the contact (Thornton and Ning, 1998).

The JKR solution (Johnson et al., 1971) also provides the relationship between the normal

contact force and the overlapping distance (see Fig. 3.9), which reads (Johnson et al., 1971):

$$\frac{u_n}{u_c} = \frac{3(P/P_{ad}) + 2 \pm 2(1 + P/P_{ad})^{\frac{1}{2}}}{3^{\frac{2}{3}} \left[P/P_{ad} + 2 \pm 2(1 + P/P_{ad})^{\frac{1}{2}}\right]^{\frac{1}{3}}} \quad , \tag{3.27}$$

where

$$u_c = \left(\frac{3P_{ad}^2}{16E^{*2}R^*}\right)^{\frac{1}{3}} = \frac{3}{2}\left(\frac{\pi^2\gamma^2R^*}{2E^{*2}}\right) \tag{3.28}$$

is the separation distance at which the contact breaks. Note that this equation is valid only if the loading–unloading case is displacement–controlled (see Fig. 3.7); if force–control is applied, the point of separation is C rather than S (see Fig. 3.9).

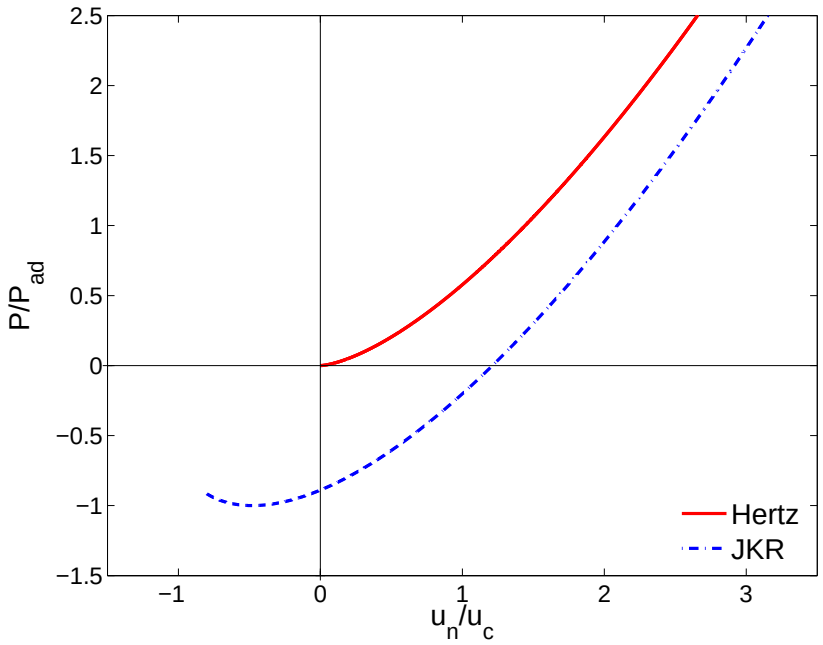

Figure 3.7: Comparison between the normal contact force to the overlapping distance between the JKR and Hertz contact models.

A relationship was also derived between the contact radius and distance of approach (Johnson et al., 1971):

$$\frac{u_n}{u_c} = 3^{\frac{1}{3}}\left(\frac{a}{a_c}\right)^2\left[1 - \frac{4}{3}\left(\frac{a}{a_c}\right)^{-\frac{3}{2}}\right], \qquad a_c = \left(\frac{9\pi\gamma R^{*2}}{4E^*}\right)^{\frac{1}{3}} \quad , \tag{3.29}$$

as shown in Fig. 3.8.

It is important to notice that work is required in order to break the contact. This can be

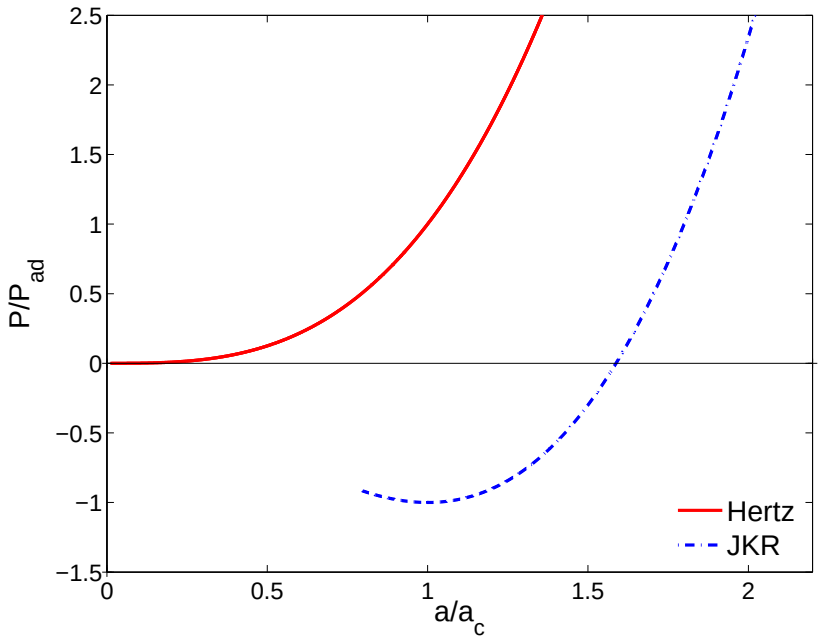

Figure 3.8: Comparison between the normal contact radius to the overlapping distance between the JKR and Hertz contact models.

seen in the single loading–unloading cycle illustrating in Fig. 3.9. The contact forms at point A and follows the JKR force–distance relationship passing through the equilibrium position (point B) and then reaching the maximum point D where the unloading phase begins. At this point, the normal displacement returns back through the zero position at A continuing with negative overlap up to the point of separation S (see Fig. 3.9). Although from point A to S no physical contact occurs, the vdW interactions still attract the particles together until the point of breakage is reached, when the surface energy is finally released (point S). Since the loading and unloading paths do not coincide, the work indicated by the shadowed area in Fig. 3.9 is lost. This can be quantified by calculating the area above the curve ACS (see Fig. 3.9); the integral cannot be evaluated analytically, though a reasonable estimate can be found in Thornton and Ning (1998):

$$W = 7.09 \left(\frac{(2\gamma)^5 R^{*4}}{E^{*2}} \right)^{\frac{1}{3}}. \tag{3.30}$$

As already pointed out, the JKR model accounts for the interplay between elastic and vdW forces in the contact region, but fails to consider the occurrence of plastic contact

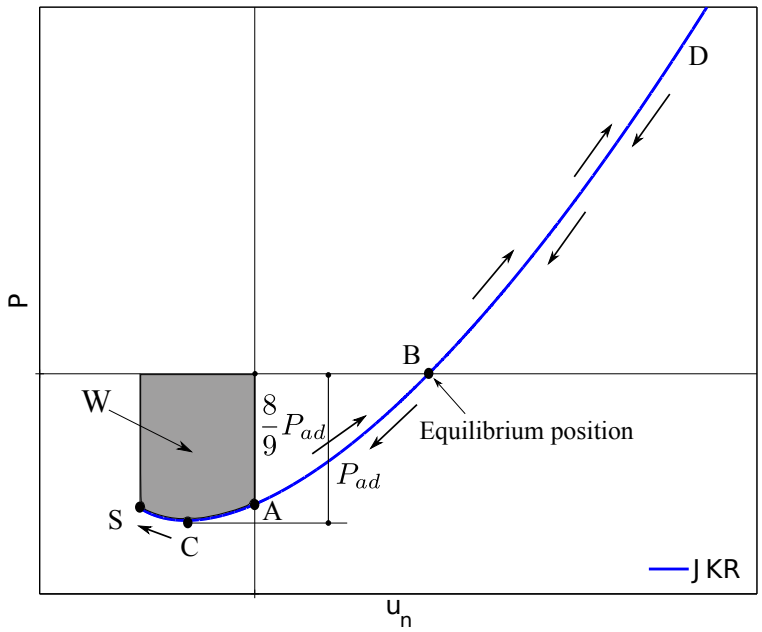

Figure 3.9: The JKR force–displacement relationship. The contact forms at point A and follows the JKR force–distance relationship passing through the equilibrium position (point B) and then reaching the maximum point D where the unloading phase begins. At this point, the normal displacement returns back through the zero position at A continuing with negative overlap up to the point of separation S.

deformations. Given the very low confining pressures in the lunar soil surface, neglecting plastic contact behaviour seems to be a reasonable assumption. However, when the JKR adhesion force (Eq. 3.26) is higher than the maximum elastic load supported at the contact, adhesion alone can be the cause of plastic contact deformations (Walton, 2008). This could be the case for micron-scale particles (Walton, 2008) because the maximum elastic load is dependent on the square of the particle size.

Plastic deformations due to adhesion alone are estimated to take place for particle sizes smaller than (Walton, 2008):

$$R_Y \approx 1 \times 10^7 \frac{\gamma}{E} \quad . \tag{3.31}$$

Taking a Young's modulus of 70GPa, which is typical of quartz, and the value of the surface energy in line with the estimates for lunar soil of 0.07J/m^2, the particle radius at which yielding would occur is calculated to be 10μm. This is smaller than the average lunar soil particle size and therefore it is acceptable to neglect the effect of plastic deformations on the contact behaviour.

Finally, it is worth recalling that the JKR theory is limited to smooth contact bodies under quasi-static normal loading. Nevertheless, adhesion is generally reduced by the surface roughness of real materials, as determined by the height and distribution of asperities (Johnson, 1985). On the other hand, an analytical contact model that accounts for these phenomena would be extremely difficult to formulate and the implementation in a DEM code impracticable. Moreover, since there is no experimental data for the surface roughness of lunar soil, and given fact that the presence of UHV produces extremely clean and dry surfaces (Douglas Aircraft Company, 1968; Perko et al., 2001), the influence of surface roughness on adhesion phenomena will be disregarded in this study.

3.3.3.3 Choice of a normal contact model for lunar soil

The DMT and JKR contact models predict different values for the adhesion force[3]. In particular, the maximum value of the JKR adhesion force (Eq. 3.26) is found to be 4/3 of the value given by the DMT model (Eq. 3.19). Due to this difference, the scientific community has considered these two theories as contradictory. The solution to the problem was first identified by Tabor (1977), as outlined below. Based on the work of Tabor, it is possible to make an appropriate selection for the modelling of lunar soil grains.

Tabor (1977) was the first to reconcile the DMT and JKR contact theories. He introduced a new dimensionless parameter, known as the Tabor parameter, expressed as:

$$\mu = \left(\frac{R^* 4\gamma^2}{E^{*2} D_0^3} \right)^{\frac{1}{3}} \quad , \tag{3.32}$$

When two adhesive bodies come into contact they deform, forming a neck around the contact surface. The Tabor parameter represents the ratio between the interparticle separation at the shoulder surrounding the neck and the particle equilibrium distance D_0 (Tabor, 1977). It was later found (Greenwood, 1997) that for $\mu < 3$ (*i.e.* for very hard bodies), the DMT model

[3]The DMT model specifies an adhesion force which is constant with particle overlap as given in Eq. 3.19, whereas the JKR model has an adhesion force which varies with particle distance. For the purpose of comparison we consider the maximum value of the adhesive force which corresponds to point C on Fig. 3.9 and given by Eq. 3.26.

should be adopted, whereas for $\mu > 3$ (*i.e.* for more compliant bodies) the JKR solution provides a more realistic description of interfacial adhesion phenomena. Therefore, it was concluded that there is no contradiction between the models, but that the two solutions are limiting cases from a range of solutions where the distinguishing element is the Tabor parameter.

Subsequently, two theories (Muller et al., 1980; Maugis, 1992), known as the Muller and Maugis-Dugdale models, were developed using the Tabor parameter to account for the transition between the DTM and JKR solution. Without entering into a detailed discussion, it can be said that they confirm the suitability of the Tabor parameter as a means to judge the applicability of the DMT and JKR models.

Given that a precise value of surface energy has not yet been determined for the lunar soil, only a rough estimate of the Tabor parameter can be made. As mentioned in Sec. 3.3.2, an approximate value of γ for lunar soil is $0.07 \mathrm{J/m^2}$. Using this value, the Tabor parameter is computed in Tab. 3.2 taking into account the contact parameters typical of lunar soil grains (Perko et al., 2001) and the grain radii at 5, 50 and 95% of the typical lunar soil's PSD. The values of the Tabor parameter computed in Tab. 3.2 are all greater than 3, suggesting that the JKR contact model is suitable for the modelling of lunar soil grains with regards to adhesion.

	Radius at 5%	Radius at 50%	Radius at 95%
Surface energy ($\mathrm{mJ/m^2}$)	70	70	70
Shear Modulus (GPa)	28	28	28
Poisson's ratio	0.25	0.25	0.25
Young Modulus (GPa)	70	70	70
Hamaker coefficient (J)	4.3×10^{-20}	4.3×10^{-20}	4.3×10^{-20}
Interparticle distance (nm)	0.09	0.09	0.09
Radius (mm)	0.005	0.035	0.5
Tabor parameter	3.01	5.75	13.96

Table 3.2: Tabor parameter computed for the lunar soil physical parameters and the grain radii at 5, 50 and 95% of the typical lunar soil's PSD.

Another way to assess the suitability of the two models is to consider their main discrep-

ancies and assumptions. The DMT model assumes that vdW forces only act outside of the contact region, with the contact force given by the sum of a constant adhesion force and the Hertzian elastic load. With regards to adhesion, no energy is needed in order to detach the two particles. The JKR model on the other hand, assumes that vdW forces cause adhesion inside the contact zone with two important consequences:

(i) the contact pressure distribution changes such that tension force, induced by adhesion, are sustained (see Fig. 3.6);

(ii) energy is required to detach the two particles (see Fig. 3.9), consistent with the concept that the contact is due to interfacial surface energy.

These two phenomena resulting from the JKR model suggest that it could provide a physically more realistic description of adhesion than the DMT model.

3.3.4 Frictional behaviour in the presence of adhesion

The frictional behaviour in the presence of adhesion is rather complex and not yet fully understood from a physical point of view. There is currently no consensus in the literature on the interplay between adhesion and friction. In the absence of adhesion, Amonton's law (1996) states that the limiting frictional force exerted between two contacting bodies is directly proportional to the normal contact force and is not dependent on the contact area. In this case, the frictional force can be expressed as:

$$F_{s,max} = \mu P \quad , \tag{3.33}$$

where μ is the coefficient of friction. The law, known as Coulomb's friction law, is often modified to account for shear resistance at zero normal load by introducing a constant, so that:

$$F_{s,max} = \mu P + c \quad , \tag{3.34}$$

where c is the term which accounts for the true cohesion of the material. However, as pointed out by Kendall (1986), Eq. 3.34 defines a linear relationship between the shear resistance and normal load which does not comply with the experimental observations carried out with adhesion. Based on a series of experimental measurements of the friction coefficient between fine wet sand particles, Kendall (1986) elaborated a revised formulation for adhesive bodies, with adhesion modelled by the JKR solution (see Sec. 3.3.3.2). In particular, he found that the friction force computed by multiplying the effective Hertzian load P_1 of the JKR model (used in Eq. 3.23) with the friction coefficient μ, provided a better description of the experimental data than obtained using the linear Coulomb's criterion (Eq. 3.33). The modified limiting friction force was expressed as (Kendall, 1986):

$$F_{s,max} = \mu P_1 = \mu \left(P + 2P_{ad} \pm \sqrt{4P_{ad}^2 + 4PP_{ad}} \right) \tag{3.35}$$

where P_{ad} is the JKR adhesion force (Eq. 3.26). This relationship between the shear and the normal contact force is non-linear, in contrast with the linear Coulomb's law, as shown in Fig. 3.10.

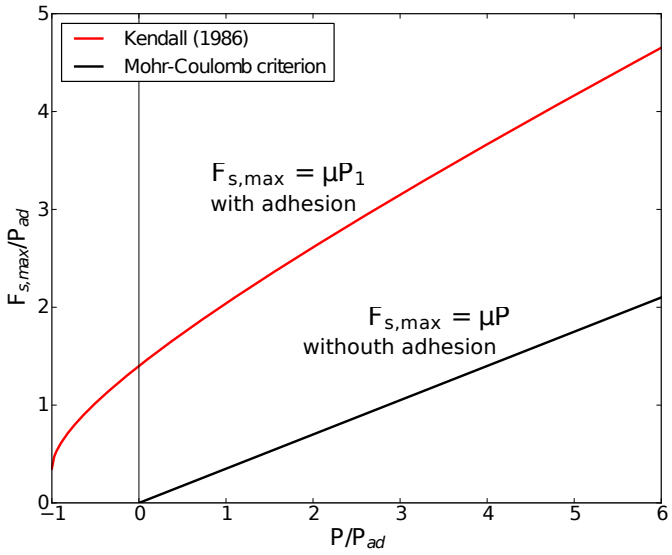

Figure 3.10: Maximum shear force versus normal contact force with and without adhesion (Kendall, 1986). The relationship for the adhesive case is expressed by Eq. 3.35, while the classical Coulomb's law follows Eq. 3.33. Both curves are normalised with respect to the JKR adhesion force (Eq. 3.26).

For contacts experiencing tangential forces less than the limit predicted by the Coulomb's

law (Eq. 3.33), or by the Kendall solution when accounting for adhesion (Eq. 3.35), the analytical model proposed by Mindlin and Deresiewicz (1953) provides a faithful description of the shear force–displacement contact behaviour. Mindlin and Deresiewicz (1953) found that partial slip must always take place in order to avoid the occurrence of infinite tangential stresses at the edge of the contact region. In other words, micro-slip must occurs at the edges of the contact zone, where the tangential stresses reach the maximum shear value as stated by the Coulomb's law (see Fig. 3.11).

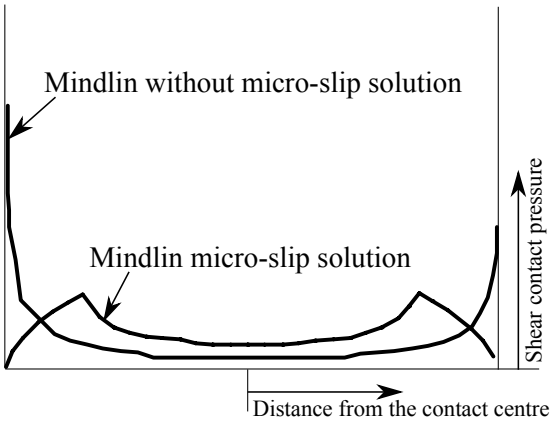

Figure 3.11: Comparison between the tangential stress distributions obtained with and without micro-slip (Mindlin and Deresiewicz, 1953; Thornton and Ning, 1998). Neglecting the occurrence of micro-slip at the edges of the contact region results in infinite tangential stress.

However, due to the complexity of the problem, they concluded that an analytic solution for the general case of an oblique impact between two particles, where both normal and shear contact stresses take place, could not be derived. Instead, non-linear solutions in terms of shear force–displacement law were proposed for various specific cases (combinations of the normal and shear contact forces where either variable increases, is held constant or decreases) (Mindlin and Deresiewicz, 1953). In all cases the solutions were dependent upon the loading history, confirming the complexity of the problem (Mindlin and Deresiewicz, 1953).

A simpler version of the Mindlin and Deresiewicz contact model was proposed earlier by Mindlin (1949) in which he disregarded the manifestation of a micro-slip at the edges of the contact area (Mindlin and Deresiewicz, 1953). In this case, the shear force–displacement

relationship is linear,

$$F_s = 8aG^* u_s \quad , \tag{3.36}$$

where u_s is the shear displacement, a the contact radius and G^* the equivalent contact shear modulus expressed as a function of the shear moduli and Poisson's ratios of the contacting particles, *i.e.*:

$$\frac{1}{G^*} = \frac{2-\nu_1}{G_1} + \frac{2-\nu_2}{G_2} \quad . \tag{3.37}$$

It can be noted that the relationship given by Eq. 3.36 is actually non-linear in the general case of changing u_n, as shown in Fig. 3.12. This is because the contact radius varies non-linearly with the contact load P, as predicted by the Hertzian model (Eq. 3.6). A linear shear force–displacement relationship is obtained only for the special case of constant particle overlap (see Fig. 3.12).

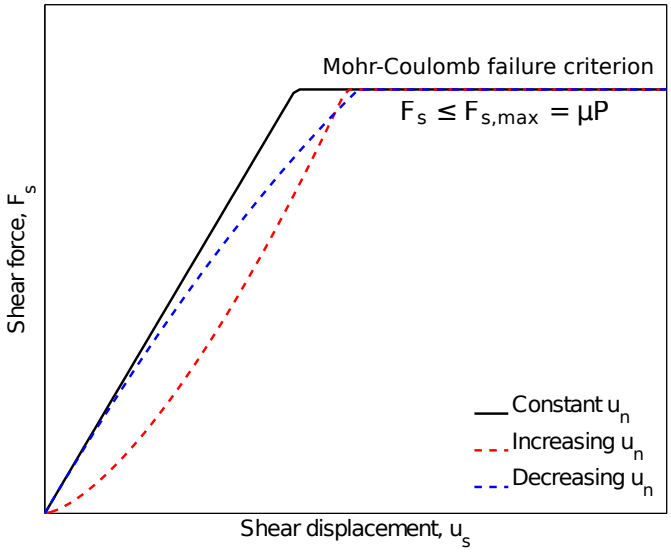

Figure 3.12: Shear force versus shear displacement for constant, increasing and decreasing particles overlap according to Mindlin solution without micro-slip (Mindlin, 1949).

Due to its simplicity, the Mindlin solution without micro-slip is more suitable to be implemented in a DEM code than the full Mindlin and Deresiewicz contact model and will therefore be selected for the study of lunar soil. The only drawback of the simplified theory lies in the unphysical prediction of infinite tangential stresses at the edge of the contact zone. On the other hand, as previously illustrated in Fig. 3.6, the JKR normal pressure distribution also leads to infinite tensile forces at the edge of the contact region. Therefore,

it seems reasonable to conclude that the Mindlin no micro-slip solution is at least consistent with the JKR model, if we consider that the normal pressure limits the shear stress, according to Coulomb's law.

3.4 Verification of contact models in Yade

The Hertzian and JKR contact models presented in this chapter were thoroughly implemented by the author into the Discrete Element Method (DEM) open-source code Yade (see Chapter 4 for a description of the numerical scheme). The code was written in C++ language following the sign conventions adopted in Yade (Smilauer et al., 2010). The adequacy of the implementation was verified by comparing the numerical and analytical solutions by means of element tests. In particular, normal impact tests of two spheres (with and without adhesion) were used to calculate the numerical solution in terms of contact load versus particle overlap. Results were in perfect agreement with the analytical solutions corresponding to the HM and JKR models respectively (comparison not shown in this thesis). The verification was complemented by the calculation of the various energy components (elastic potential energy, kinetic energy and energy dissipation) during the impact. As expected, energy was conserved for the tests run with the HM model whereas the contacts with adhesion were characterised by an energy loss equal to the work computed in Eq. 3.30.

The contact behaviour in the shear direction following the Mindlin without micro-slip solution (Sec. 3.3.4) was verified separately using a simple shear test between two spherical particles. Two non-dynamic overlapping particles were generated and one of them was subject to a constant incremental rotation so as to reproduce a certain amount of shear displacement (pure sliding). Although for non-dynamic bodies the software does not integrate the equation of motion (*i.e.* no contact reaction forces are applied to the particles), the shear and normal contact forces and displacements can still be computed and thus verified. The test resulted in a shear force-displacement diagram obtained under a constant value of normal applied force. The numerical solution was consistent with the relationship obtained

in Fig. 3.12 for constant overlap.

3.5 Summary

In this chapter a comprehensive description of the contact behaviour between macroscopic bodies, with and without the presence of surface energy forces, was provided. The influence of adhesion, induced by vdW intermolecular forces, was considered at various scales, from the atomic to the macroscopic. The adhesion force between two rigid macroscopic bodies was stated under the assumption of additivity.

The role of the surface energy and surface cleanliness parameters was discussed in relation to the lunar environmental conditions of UHV and low confining pressures. A representative value of the surface energy of 70mJ/m^2 was identified in agreement with previous studies on the lunar soil mechanics.

Subsequently, the role of elastic deformations was taken into account when modelling contact adhesion phenomena. To this end, two well-established continuum models, the DMT and JKR theories, were discussed in detail. Based on a critical assessment of the assumptions and the range of applicability of each theory, the JKR model was chosen as the most appropriate to describe the normal contact behaviour of lunar soil grains. This choice was complemented by the simplified Mindlin no micro-slip solution which is used to model the shear contact behaviour. Finally, Coulomb's law was modified in order to account for the interplay between adhesion and friction, as according to Kendall (1986).

Chapter 4

Numerical method and simulations of quasi-static deformations

This chapter discusses the ability of the Discrete Element Method (DEM) to model laboratory experiments under quasi-static (QS) conditions. Results obtained from simulations of drained triaxial tests under terrestrial conditions, and conducted for particles with Hertzian contacts, are shown at various stress levels and at a wide range of strain rates. By means of dimensional analysis, a new method is identified as the most appropriate to achieve results in accordance with the critical state soil mechanics theory under QS conditions.

4.1 Introduction

For tests run under quasi-static (QS) conditions, particle density or strain rate are often scaled up in Discrete Element Method (DEM) simulations by orders of magnitude (typically from 6 to 12), in comparison with the values employed in laboratory experiments. The reason is to make the simulation runtime affordable (see e.g. Thornton and Antony, 1998). By definition, QS equilibrium is considered to be achieved when the response of the material is rate independent. Thus, although QS conditions can be taken for granted in laboratory experimental tests, this is not the case for DEM experiments. Unfortunately, in most of the literature concerning DEM (Radjai and Dubois, 2011), the effect of density scaling is often either ignored or only assessed at the peak strength of the material.

It is of particular importance to show that the numerical experiments are effectively run under QS conditions, in order to ensure a meaningful comparison between numerical and experimental results. This chapter presents a numerical investigation by DEM of the effect of strain rate on the macroscopic behaviour of a silty sand material under extremely dense conditions, with PSD typical of lunar soil. This will inform the later QS simulations run under lunar conditions, as will be further discussed in Chapter 5.

The main objective is to establish when QS conditions are attained for a wide range of pressure, strain rate and particle density. A numerical campaign of triaxial compression tests is run under 3D periodic boundary conditions to assess the influence of density scaling and shear strain rate at both small and large strains. The wide PSD obtained for lunar soil in Chapter 2 is used in the simulations. Particle-particle interactions obey the non-linear Hertz-Mindlin no micro-slip solution introduced in Chapter 3. The results are interpreted in terms of dimensionless numbers employed to assess the inertia of the system (da Cruz et al., 2005). Particular emphasis is given to macroscopic observations at the critical state, *i.e.* the state at which the soil can be sheared continuously without further change in stresses and volume (Schofield and Wroth, 1968).

There is significant interest in the literature to assess the ability of DEM to reproduce the critical state of soils (Wood and Maeda, 2008; Sitharam and Vinod, 2009; Zhao and Evans, 2011). This is due to the numerous advantages presented by a numerical experiment, such as the sample reproducibility, the possibility of running parametric studies, and the ease of controlling complex loading programmes. With regard to the critical state, the influence of pressure is analysed in detail. This study is combined with the previous investigation of the effects of strain rate on the soil behaviour. It is shown that increasing the confining pressure at a constant inertial value leads to contradictory results, *i.e* higher critical state porosities for higher pressures. Finally, a new definition of a dimensionless inertial parameter is advanced, which appears to produce results in agreement with the principles of critical state soil mechanics theory.

4.2 The Discrete Element Method

DEM is a numerical technique which allows modelling of a granular material as a collection of particles which interact at the contact points following a given force-displacement relationship (see Section 4.2.1). The method was first advanced by Cundall and Strack (1979) and was originally applied for the analysis of rock mechanics (Cundall, 1971). Due to its simplicity and wide range of applicability, it is now employed by numerous researchers to study the mechanics of granular materials as well as other applications (Lu and McDowell, 2006; Ng, 2009; Plassiard et al., 2009; Lane et al., 2010). An explicit numerical scheme is used to integrate the translational and rotational equations of motion for the particles respectively:

$$\begin{aligned} m_i \frac{d^2}{dt^2}\vec{x}_i &= \vec{F}_i + m_i\vec{g} \quad , \\ I_i \frac{d}{dt}\vec{\omega}_i &= \vec{T}_i \quad , \end{aligned} \tag{4.1}$$

where m_i is the mass of the particle i, $\vec{x}_i$ the position of its centroid, $\vec{F}_i$ the total force, I_i the particle moment of inertia about the centroid, $\vec{\omega}_i$ the angular velocity and finally $\vec{T}_i$ the total torque. The resultant forces in Eq. 4.1 are updated each time step and are obtained from the corresponding network of contact forces. For more details on the method's implementation, see the user manual of the DEM open-source code adopted in this study, YADE (Smilauer et al., 2010).

The time step of the explicit numerical scheme was selected in order to avoid numerical instability. In the present simulations, the time step was determined using the method already implemented in YADE (Smilauer et al., 2010) with an additional safety factor of 0.3. The method implemented in Yade considers the amount of time that an elastic wave takes to propagate within a given particle. Assuming the Young's modulus and density of the particles as continuum quantities, the formula for the critical time step reads:

$$\Delta t_{cr} = \min_i R_i \sqrt{\frac{\rho_i}{E_i}} \quad , \tag{4.2}$$

where ρ_i is the particle density, R_i the particle radius and E_i the particle Young's modulus.

The safety factor of 0.3 is applied as a coefficient to the above equation based on the work of Smilauer (2010). He compared the result from Eq. 4.2 with the critical time step calculated from the minimum eigenvalue of a system of interacting particles. Assuming uncoupled degrees of freedom, each translational degree of freedom of each particle has a critical time step of (Itasca, 1999):

$$\Delta t_{cr} = \sqrt{\frac{m}{k}} \quad , \tag{4.3}$$

where k is an estimated equivalent contact stiffness (Itasca, 1999). He found that the method based on Eq. 4.2 satisfied the condition of Eq. 4.3 if a coefficient of 0.3 was used. The resulting time step was found to produce both stable and accurate numerical solutions (see Sec. 4.8).

4.2.1 The contact model

In this section, an overview of the micro-mechanical model used in this study is provided. The contact force model adopted in this work resembles the Hertz-Mindlin (HM) no micro-slip solution (Mindlin, 1949) which is valid for elastic contact bodies as discussed in Chapter 3. As mentioned there, the model was implemented by the author into the DEM open–source YADE code (Smilauer et al., 2010). The normal force is computed at each time step from the current overlapping between two grains in contact. The shear force, on the other hand, is updated in an incremental fashion, which is the only correct way of doing it, as recently demonstrated by Thornton et al. (2011). In particular, we recall that the elastic normal force is expressed by the Hertzian solution (Johnson, 1985) as:

$$F_{n,el} = \frac{4}{3} E^* \sqrt{R^*} u_n^{3/2} \quad , \tag{4.4}$$

where the equivalent effective Young's modulus E^* and the equivalent particle radius R^* are respectively equal to:

$$E^* = \left(\frac{1-\nu_1^2}{E_1} + \frac{1-\nu_2^2}{E_2} \right)^{-1} \quad , \quad R^* = \left(\frac{1}{R_1} + \frac{1}{R_2} \right)^{-1} \quad , \tag{4.5}$$

and where ν_1 and ν_2 are the Poisson's ratios of each interacting particle. The shear force is linearly related to the relative shear displacement at the contact, according to the Mindlin no micro-slip solution (Mindlin, 1949). This is expressed as:

$$F_s = 8G^* \sqrt{R^* u_n} u_s \quad , \tag{4.6}$$

with the equivalent effective shear modulus G^* being equal to:

$$G^* = \left(\frac{2-\nu_1}{G_1} + \frac{2-\nu_2}{G_2} \right)^{-1} \quad . \tag{4.7}$$

Finally, the normal and tangential contact stiffnesses are equal to:

$$k_n = 2E^* \sqrt{R^* u_n} \quad , \tag{4.8}$$

$$k_s = 8G^* \sqrt{R^* u_n} \quad . \tag{4.9}$$

As a detail of the implementation, it is worth mentioning that a scaling rule is applied to the shear force F_s every time the normal force at the contact decreases, *i.e.* $\Delta F_n \leq 0$, to account for the fact that less shear stress is now experienced at the contact due to the reduced normal force. This is necessary whenever the simplified HM no micro-slip solution is applied. This is described as a heuristic method whereby the introduction of non-physical energy into the system is prevented (Agnolin and Roux, 2007).

To account for dissipation mechanisms at the contact, sliding is included in the model. The shear force is limited according to the Mohr-Coulomb (MC) failure criterion such that $F_s \leq F_{s,max} = \mu F_{n,el}$, where μ is the coefficient of interparticle friction. Some viscous damping can also be added, both in normal and tangential directions, to simulate further inelastic behaviour, as schematically illustrated in Fig. 4.1.

A non-linear viscous model was implemented by the author, similar to the model proposed by Kuwabara and Kono (1987). The main feature of this model is that the coefficient of restitution and the total collision time are not constant but decrease as the impact velocity

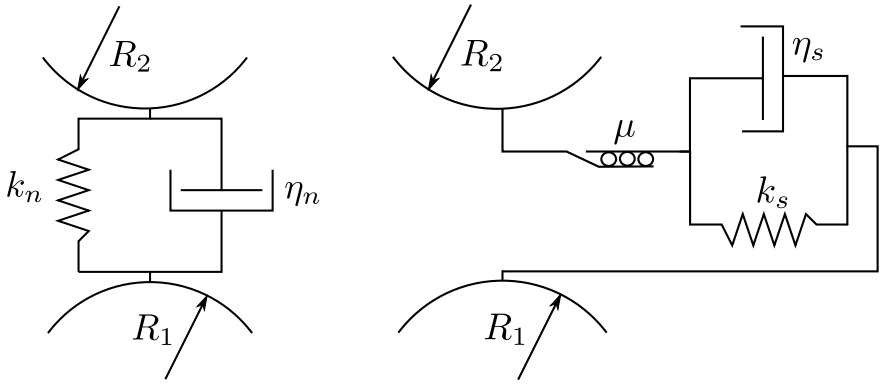

(a) Contact model in the normal direction.

(b) Contact model in the shear direction. The dashpot is deactivated whenever sliding occurs.

Figure 4.1: Schematic of normal and shear contact behaviour.

increases. This seems to be a realistic solution since it was found to fit well to experimental data (Walton and Braun, 1986). The following set of damping coefficients were employed:

$$\eta_n = c_{n,crit}\zeta_n = 2\sqrt{m^* k_n}\zeta_n \tag{4.10}$$

$$\eta_s = c_{s,crit}\zeta_s = 2\sqrt{m^* k_s}\zeta_s \tag{4.11}$$

in which m^* is an effective mass equal to $\frac{m_1 m_2}{m_1+m_2}$ and k_n, k_s are the current tangential normal and shear stiffnesses as expressed by Eq. 4.8, and 4.9 and ζ_n, ζ_s fractions of the critical damping coefficients of a linear spring–dashpot system of stiffness k_n and k_s respectively. Substituting Eq. 4.8 and 4.9 into Eq. 4.10 and 4.11, the coefficients of damping can be rewritten as:

$$\eta_n = 2\sqrt{m^* 2E^* \sqrt{R^*} u_n^{1/2}}\zeta_n \quad , \tag{4.12}$$

$$\eta_s = 4\sqrt{m^* 2G^* \sqrt{R^*} u_n^{1/2}}\zeta_s \quad . \tag{4.13}$$

The normal and shear contact viscous forces are finally computed as:

$$F_{n,v} = \eta_n v_{n,rel} \quad , \tag{4.14}$$

$$F_{s,v} = \eta_s v_{s,rel} \quad . \tag{4.15}$$

The total normal force, $F_n = F_{n,el} + F_{n,v}$, is then employed to compute the maximum tangential force allowed by the MC criterion. The normal viscous component could exceed the value of the elastic repulsive force $F_{n,el}$ producing a negative normal force. This would represent a non-physical meaningless situation, hence in this case F_n is set to zero (as was suggested in Thomas and Thorsten (2007) but for a linear spring-dashpot model).

Finally, it is appropriate to emphasise that the introduction of viscous damping in this work was not to mimic some real physical behaviour, but as a numerical tool to facilitate the attainment of QS equilibrium states within a reasonable computational time. On the other hand, under truly QS conditions, viscous damping should not affect the response. If some influence on the macroscopic behaviour is introduced due to contact viscous damping, it introduces creep into the model. Whether viscous damping is a suitable tool to model creep or other forms of energy dissipation occurring during particle interactions (*e.g.* particles undergoing permanent deformations), is an open question which needs further research. At present, the insufficient experimental data available do not allow researchers to draw firm conclusions. Hence, there is also significant uncertainty on what a realistic range of values for viscous damping may be.

4.3 The quasi-static condition

As previously stated, QS conditions are attained whenever the response of the physical system is shown to be independent of the rate of loading. In such a case, the inertial forces are negligible in comparison with the mechanical contact forces arising from the applied loads. Hence, the total kinetic energy of the system is not required to be nil, but simply small enough so as not to influence the overall observed mechanical behaviour (see e.g. di Prisco and Imposimato, 1997).

QS conditions have been an active subject of previous research. For instance, Roux and Combe (2003) showed by means of 2D simulations that different responses occur at small and large strains. They found that at very small strains the behaviour is more sensitive to

elastic deformations, whereas at large strains plastic behaviour becomes predominant (Roux and Combe, 2003). These two different strain levels were referred to as type 1 and type 2, respectively (Roux and Combe, 2003). It was also pointed out that type 2 strains are more rate-dependent, which is because particle rearrangement is more significant at large strains. This was further confirmed by Bi et al. (2011), who analysed the different components of the total energy during biaxial numerical tests to demonstrate that plastic dissipation is the most important contribution in the system, particularly as large strains are approached.

Roux and Combe (2010) presented QS simulations of 3D triaxial tests, extending their 2D results (Roux and Combe, 2003). However, the simulations did not reached the critical state, *i.e.* very large strains, although they did achieve the QS limit at small deformations. In this chapter it will be shown that QS conditions can be reached under a very different set of conditions for small and large strains. The numerical findings will be of particular interest with regard to demonstrating the capability of DEM to reproduce critical state conditions.

The QS equilibrium and the transition between different flow regimes, from inertial to quasi-static, were also investigated by Campbell (2002, 2005) using DEM simulations which employed a linear contact model. A sample of 1,000 particles was simulated under full periodic boundary conditions, and a simple shear test was conducted under both stress– and volume–controlled conditions. Different conclusions were drawn for tests under drained and undrained samples for the transition from a dynamic condition towards QS equilibrium. In particular, a flow map was constructed which allowed distinction between three main flow regimes: the elastic-quasi-static, inertial and transitional regimes. This chapter will also focus on the transition between elastic-quasi-static and inertial regimes, but for particles with Hertzian contacts, which are thought to represent more realistically the contact behaviour than linear springs.

It will be shown that the choice of parameters that define the transition between inertial and elastic-quasi-static flow regimes is non-trivial. In particular, two different inertial parameters can be identified to quantify the dynamics of the system by means of dimensional analysis (Radjai and Dubois, 2011; Campbell, 2005). However, it will be shown that the

use of these two parameters, both aiming to define the inertia of the system, do not lead to the same response when independently considered in combination with another parameter, the so-called stiffness parameter (Radjai and Dubois, 2011), which accounts for the soil compressibility.

4.4 Dimensional analysis

During the simulations, a number of physical parameters are used to determine the response of the system both in terms of stresses and volume. These parameters include geometric properties, contact parameters and characteristic times, as listed in Tab. 4.1, where the units are expressed using fundamental dimensions M, L and T, *i.e.* mass, length and time respectively.

	Parameter	Symbol	Unit of Measure
Geometric properties	Number of grains	N	$[-]$
	Average particle size	d	[L]
	Length of the periodic cell	L	[L]
Contact parameters	Young's modulus	E	$[\mathrm{ML^{-1}T^{-2}}]$
	Particle density	ρ	$[\mathrm{ML^{-3}}]$
	Poisson's ratio	ν	$[-]$
	Friction coefficient	μ	$[-]$
	Damping ratio	ζ	$[-]$
Characteristic times	Strain rate	$\dot{\varepsilon}$	$[\mathrm{T^{-1}}]$
Other parameters	Applied pressure	p	$[\mathrm{ML^{-1}T^{-2}}]$

Table 4.1: Units of measure of DEM simulation input parameters.

The soil parameters, which can be measured as outputs from DEM simulations, are the macroscopic elastic parameters E_m and ν_m, the porosity n, the dilatancy Ψ and the friction angle ϕ. Assuming that a link exists between microscopic and macroscopic quantities, a general (loading path-dependent) functional relationship of the following form can be written:

$$E_m, \nu_m, n, \Psi, \phi = f\left(N, d, L, E, \rho, \nu, \mu, \zeta, \dot{\varepsilon}, p\right) \quad . \tag{4.16}$$

Since this thesis mainly deals with quantities related to critical state soil parameters, elastic

properties such as E_m and ν_m are not investigated in detail and will therefore be disregarded in the following discussion. Performing dimensional analysis, and assuming that the inter-particle properties ν and μ are kept the same in all the tests, Eq. 4.16 can be rewritten in the form:

$$n, \Psi, \phi = F\left(N, \frac{d}{L}, k, I, \zeta\right) \quad , \tag{4.17}$$

where the two dimensionless groups k and I, known as stiffness and inertial numbers (da Cruz et al., 2005), are expressed as:

$$I = \dot{\epsilon} d \sqrt{\frac{\rho}{p}} \quad , \tag{4.18}$$

$$k = \left(\frac{E}{p(1-\nu^2)}\right)^{2/3} \quad . \tag{4.19}$$

Firstly, the influence of N on the macroscopic behaviour will be investigated, namely a Representative Elementary Volume (REV) will be identified. Then, a careful examination of the influence of k and I at small and large strains will be carried out. No similar investigation for polydisperse samples like those considered in this study has been identified in the literature. Moreover, a critical assessment of the results at very large strains has not been published, particularly at very small I and for a wide range of pressures.

The inertial number I (Eq. 4.18) is meant to characterise the inertia of the system, as it is the ratio between two characteristic times, $t_{\dot{\epsilon}} = 1/\dot{\epsilon}$, the macroscopic deformation time, and $t_r = d\sqrt{\rho/p}$, the microscopic inertial time for grains to rearrange (Radjai and Dubois, 2011), *i.e.* the time associated with the displacement of a grain subjected to a pressure p. The stiffness number k (Eq. 4.19) characterises the elastic stiffness of the granular assembly, since it is proportional to the inverse of the normal deflection u_n/d (da Cruz et al., 2005; Radjai and Dubois, 2011) for non-linear Hertzian contacts.

Experimental values of I for quartz sand tested in standard triaxial apparatuses are found to be approximately 10^{-8} (Schanz and Vermeer, 1996). As will be discussed later, with the current computational power, it is not possible to perform numerical tests at such a low

inertia (*i.e.* low loading rate), particularly up to large strains.

It will be shown later that a different definition of the inertial parameter is more appropriate when the combined effect of elastic and inertial forces is taken into account. This was earlier investigated by Campbell (2005), who ran experiments on samples using a linear elastic contact model. He used a parameter defined as $k^*/\rho d^3\dot{\epsilon}^2$ to study the influence of inertial forces, where k^* is the constant stiffness of the particles (both shear and normal). Such a parameter expresses the square of the ratio between two characteristic times, $t_{\dot{\epsilon}} = 1/\dot{\epsilon}$, and the binary collision time (*i.e.* the contact duration for a collision between two particles only) for elastic particles with linear contact stiffness, *i.e.* $t_{bc,linear} = \sqrt{\rho d^3/k^*}$.

However, in this work, shear and normal contact stiffnesses are not constant during the simulation but are updated at each time step according to the current particle overlap so that a reference binary collision time is no longer of easy definition (even employing an equivalent linear stiffness would not be possible since the choice of this would depend on the confining pressure). Therefore the pair of parameters (I, k) would appear to be the most appropriate choice in this case since both parameters can be easily and unambiguously identified for each simulation. On the other hand, although there is some freedom in the choice of the dimensionless parameters (Palmer, 2007), such a choice can be non-trivial depending on the physics of the problem. It will be demonstrated that for deformable frictional materials the sole use of the value of I (as defined in Eq. 4.18) as a criterion for establishing QS conditions does not lead to consistent results at the critical state.

4.5 Periodic boundary conditions

The use of periodic boundaries presents two main advantages: firstly the number of particles can be reduced, since boundary effects are completely disregarded, and, as a consequence, some computational time can be saved because smaller samples are employed. Secondly a uniform strain field is applied which should prevent the formation of localizations during shear, so that samples actually remain homogeneous until the attainment of the critical

state, although this is still a point of debate (Thornton and Yin, 2006).

For the above reasons, periodic boundaries were employed in the tests presented in this chapter. They were already implemented in the YADE code and details of the implementation can be found in Smilauer et al. (2010). The uniform strain field was applied by means of a velocity gradient tensor. In such a case, two contributions to particle velocities can be distinguished (Radjai and Dubois, 2011): the first is due to the homogeneous deformation of the periodic cell, whilst the second is the fluctuating component with respect to the homogeneous strain field. That is to say that particle motion is updated both due to the applied velocity gradient (first contribution) and as a result of inter-particle collisions (second contribution).

Stresses and strains were set or adjusted by means of a servo-control mechanism which also permitted either stresses or strains to be controlled along each principal axis. The strain rate of the periodic cell, $\dot{\varepsilon}$, was updated according to the following formula:

$$\dot{\varepsilon} = \dot{\varepsilon} + g\Delta t(\sigma_g - \sigma_c) \quad , \tag{4.20}$$

where σ_g and σ_c are the goal stress and current stress respectively and where the gain parameter, g, was estimated as (Radjai and Dubois, 2011):

$$g = \frac{L}{M_{tot}} \quad , \tag{4.21}$$

where L is the dimension of the periodic cell and M_{tot} the total mass of the sample. It is worth noting that the value given by Eq. 4.21 is only a first estimate, and the user has to follow a calibration procedure in order to find a working value.

4.6 Sample preparation

Very dense samples were generated within a periodic cell (see Fig. 4.2(a)) and prepared following three phases:

(i) isotropic compression with zero contact friction until the pressure of 1kPa was reached and QS conditions are met;

(ii) gradual increase of the intergranular friction angle until the realistic value ($\mu = 0.6$, see Table 4.2) was achieved and subsequent stabilisation of the sample through a sufficient number of time steps;

(iii) isotropic compression until the desired cell pressure was reached, see Fig. 4.2(b).

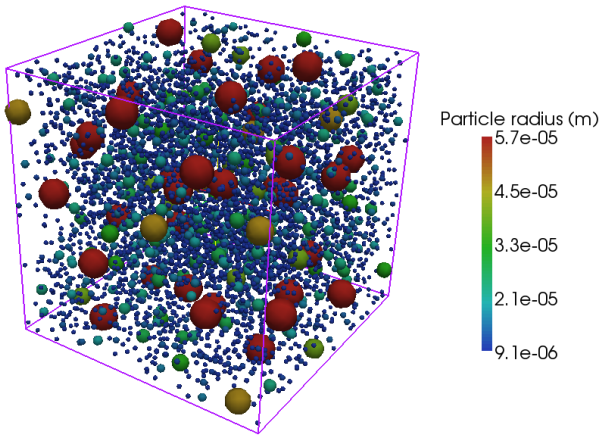

(a) Random generation of a DEM sample of 10,000 particles with no contacts. The sample is generated with 40% of solid fraction corresponding to a cell of length 0.54 mm.

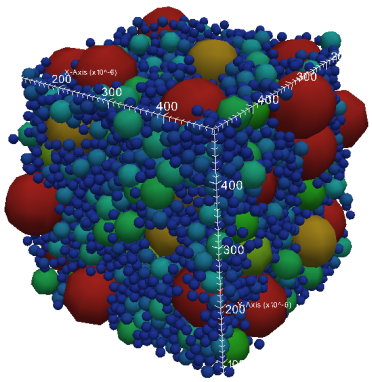

(b) Snapshot of the sample at the end of isotropic compaction ($p = 1$kPa).

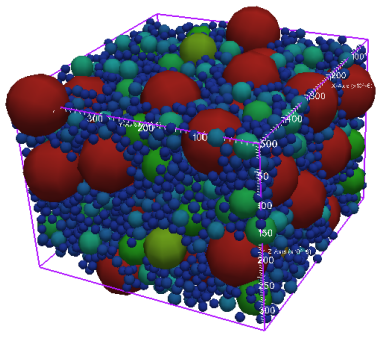

(c) Snapshot of the deformed sample at the end of triaxial phase ($p = 1$kPa).

Figure 4.2: Generation and end of isotropic and triaxial phases of a DEM sample of 10,000 grains (particles are coloured based on their size as indicated in Fig. 4.2(a).).

Samples were compressed isotropically under full stress-controlled conditions. Following that, triaxial compression tests were run at constant vertical strain rate, while lateral stress

control was applied to keep the cell pressure constant (see Fig. 4.2(c)). The reference case considered in this study corresponds to the parameters listed in Table 4.2.

DEM input parameters			
Number of particles	N	10,000	
Young's modulus	E	70	GPa
Poisson's ratio	ν	0.25	
Average particle size	d	72	μm
Particle density	ρ	$2{,}650\times10^{10}$	kg/m^3
Strain rate	$\dot{\varepsilon}$	1×10^{-4}	s^{-1}
Time step	Δt	5.3×10^{-5}	s
Damping ratio	ζ	0.7	
Intergranular friction coefficient	μ	0.6	

Table 4.2: Input DEM parameters of the simulations. Note that damping was only used for sample preparation.

Unless otherwise specified, no damping is introduced during the shearing phase as it is expected that this would influence the solution if the conditions were not truly QS. However, contact damping was always used during the preparation phase to accelerate the attainment of equilibrium under isotropic compression. As can be noted, the density was scaled up in order to reduce the computational time (see Table 4.2). According to the dimensional analysis (see Sec. 4.4), this scaling is equivalent to a strain rate of 10s^{-1} and a particle density of 2,650kg/m^3 (the product $\dot{\epsilon}\sqrt{\rho}$ remains constant).

4.7 The Representative Elementary Volume (REV) and the influence of sample variability

In order to retrieve variables which statistically represent the soil from a macroscopic point of view, it is necessary to select a Representative Elementary Volume (REV), *i.e.* the number of particles in the element should be sufficiently high that the size of the sample has no impact on the results. Therefore, triaxial compression tests at constant cell pressure were run at the confining pressure of 1MPa for two samples made of 2,000 and 10,000 particles,

respectively. The other DEM parameters are shown in Table 4.2.

The stress tensor was defined by invoking micro-macro averaging techniques (Thornton and Antony, 2000). The classical definition involves the sum over all the contact forces internal to the periodic cell which, under the hypothesis of QS equilibrium, reads:

$$\sigma_{ij} = \frac{1}{V} \sum_{p} \sum_{c} l_i^c f_j^c \quad , \tag{4.22}$$

where V is the volume of the periodic cell, l_i the branch vector joining the centres of mass of two contacting grains and f_j the inter-particle force vector. For the simulations carried out under high shear rate, the kinetic contribution to the stress tensor should also be taken into account (see e.g. da Cruz et al., 2005). However, such a contribution turned out to be negligible for all the tests carried out, and therefore will be ignored in the following analysis.

The diagonal components of the strain tensor, *i.e.* the principal strains, were directly computed from the deformation of the periodic cell using the natural strain definition as $\epsilon_i = \ln(l_{c,i}/L_i)$ where $l_{c,i}$ is the current length of the cell along the i-th direction and L_i the length prior to deformation.

Compressive strain components were defined as being positive as in classical soil mechanics. The deviatoric strain was computed as $\epsilon_d = \frac{2}{3}(\epsilon_1 - \epsilon_3)$, where ϵ_1 and ϵ_3 are the vertical and lateral strains respectively, while the volumetric strain was equal to $\epsilon_v = (\epsilon_1 + \epsilon_2 + \epsilon_3)$. The deviatoric stress was calculated as $q = (\sigma_1 - \sigma_3)$, σ_1 and σ_3 being the major and minor principal stresses. Finally the mean effective pressure was defined as $p = (\sigma_1 + \sigma_2 + \sigma_3)/3$. All the stresses are regarded as effective stresses, as all tests were conducted under drained conditions.

Fig. 4.3 compares the stress-strain and volumetric behaviour for the two samples under analysis. Results are also examined at increasing strain rate (*i.e.* inertial number) to investigate the combined effect of rate-dependency and sample size on the macroscopic behaviour. According to Fig. 4.3, it can be concluded that on average the solution is unaltered with the number of particles tested, which suggests that the sample of 2,000 grains can already be

considered an REV. However, the fluctuations due to the discrete nature of the system are substantially reduced for the sample of 10,000 particles, owing to the size of the ensemble. Since high fluctuations can create some uncertainty in the results, particularly towards the critical state where particle rearrangement becomes predominant, the sample of 10,000 particles was used for the rest of the work presented in this chapter. Larger sample sizes were also tested but were found to provide little benefit and so were not used to the increased computational cost.

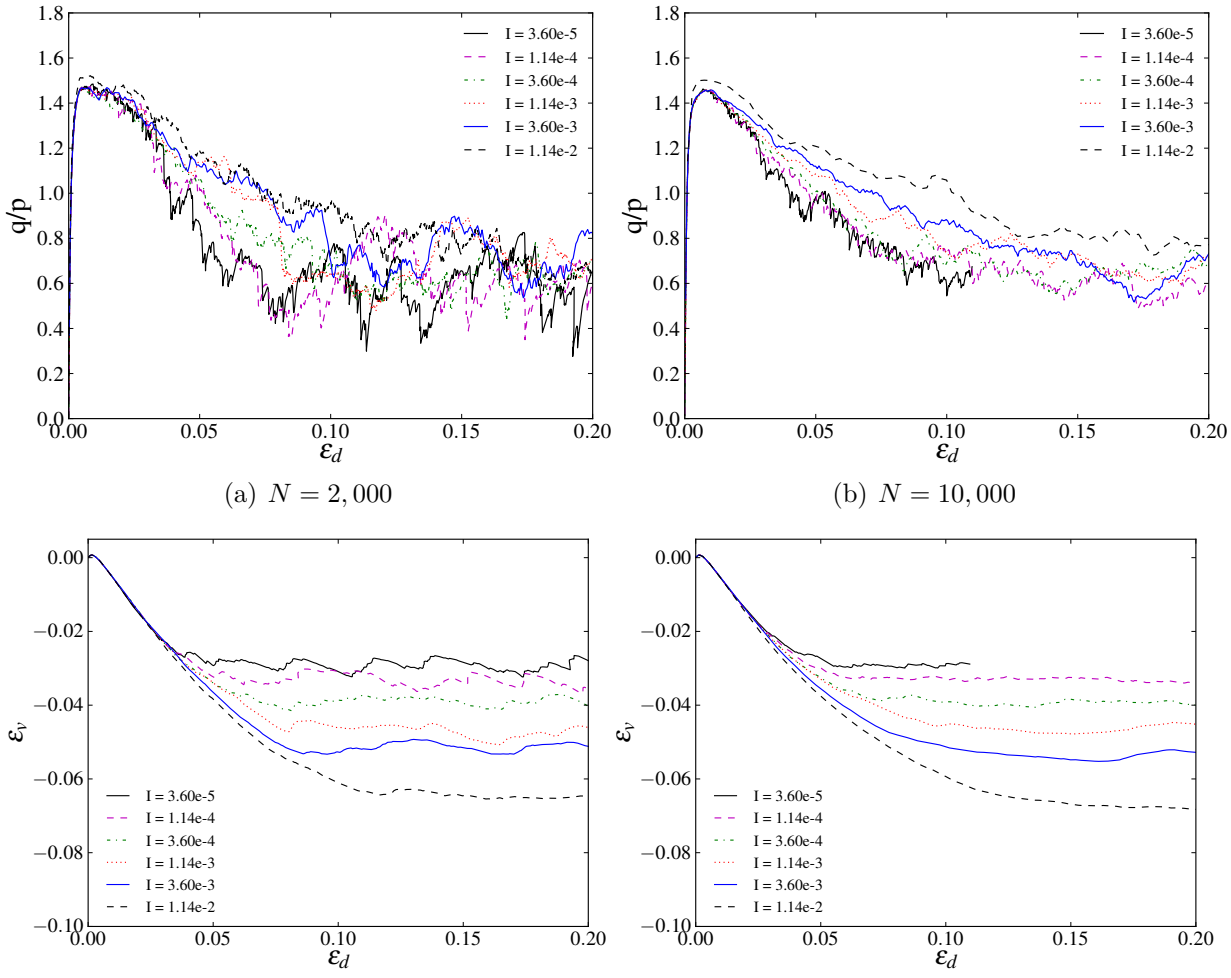

(a) $N = 2,000$ (b) $N = 10,000$

(c) $N = 2,000$ (d) $N = 10,000$

Figure 4.3: Comparison between results for different strain rates and two samples of different dimension, *i.e.* 2,000 (left) and 10,000 particles (right).

It is worth mentioning that smooth curves have often been obtained for DEM simulations on smaller samples, such as the case of 1,000 particles in 3D by Sitharam and Vinod (2009). However, this is likely the result of an arbitrary selection of points to be recorded during the

test made by the authors which is not fully representative of the sample behaviour. Typically, stress-strain relationships obtained by DEM simulations present oscillations owing to the discrete nature of the system. To extract smoother curves, either larger samples should be used, or a mobile average calculated, or an average of a series of similar tests taken.

At this stage, a question that is worth asking is whether the REV is itself also a function of the strain rate; in other words, if the same tendency of macroscopic stresses and porosity to the inertial number is observed for REV of various sizes. Fig. 4.4 illustrates the stress ratio at the peak and critical state and the macroscopic porosity for various values of the inertial number and three REV samples of increasing size, made up of 2,000, 5,000 and 10,000 grains, respectively. It can be noticed that indeed the same tendency is observed in all cases, regardless of the number of grains forming each REV. However, the results corresponding to the sample of 5,000 grains appear to be slightly offset from the common trend (see Fig. 4.4); on the other hand, it is worth recalling that different samples have different initial particle configurations, which in the present case had a small effect on the sample porosity achieved prior to the shearing phase for the 5,000 grains sample. This explains the slighter smaller critical state porosity obtained and so the slightly higher peak stress ratio. Nevertheless, the difference is very small and, most importantly, it does not affect the trend of the macroscopic behaviour with regard to the inertial number. Therefore we confirm that the same sample, previously identified as an REV, can be safely used to investigate rate effects.

Finally, it is also important to verify that the results are reproducible, *i.e.* that a different initial random generation does not affect the macro response. The result of the comparison between three samples sheared at the same loading rate, but independently generated, is shown in Fig. 4.5. The variability is more significant for the smaller sample, but clearly this is due to high fluctuations which occur when the number of particles is low. Overall it can be concluded that the tests are reproducible.

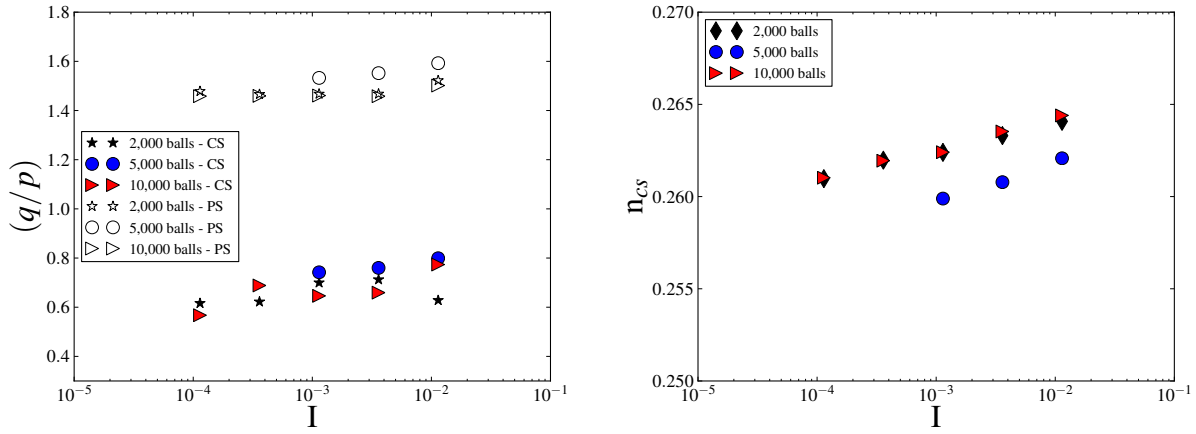

(a) Stress ratio versus inertial number at both the peak and critical states.

(b) Critical state porosity versus inertial number.

Figure 4.4: Macroscopic results for REV samples of increasing size and tested under various strain rates.

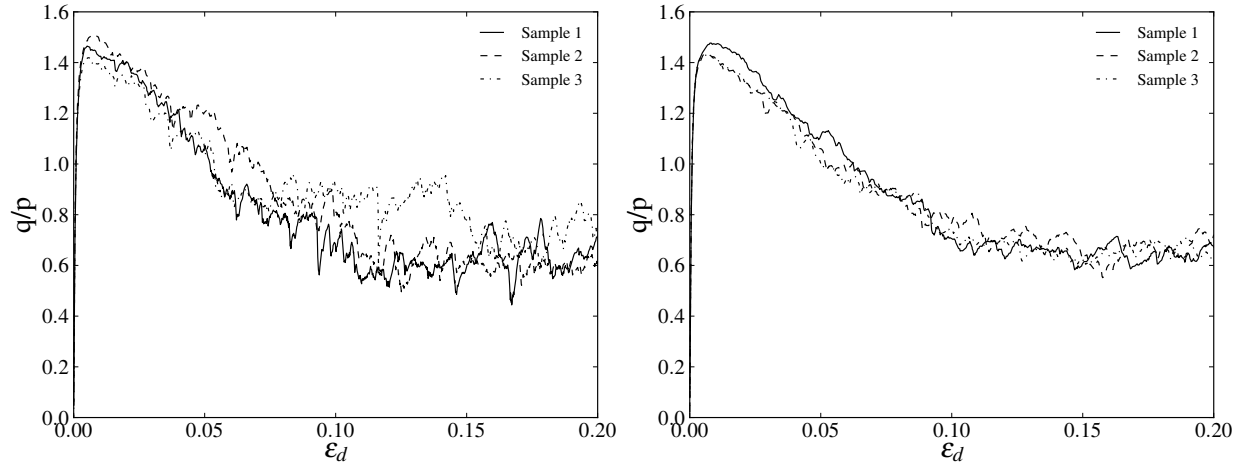

(a) $N = 2,000$

(b) $N = 10,000$

Figure 4.5: Triaxial test results of three DEM samples obtained from different random generations.

4.8 Choice of time step

As previously mentioned in Sec. 4.1, the main advantage in applying particle density scaling is to increase the critical time step (Eq. 4.2) and thus reduce the total computational time. On the other hand, a variation of strain rate implies that a different number of steps is used to reach a predefined ultimate strain level. Therefore simulations conducted for different values of strain rate (or inertial number) and a given time step are run for a different number of iterations. This may lead to solutions which are not purely influenced by strain rate effects

but also by the accuracy of the calculations.

In order to verify that the selected time step was sufficiently small to prevent any significant change in the accuracy of the results, simulations were run at different strain rates but with the same total number of calculation steps. The input parameters of the numerical tests carried out are reported in Table 4.3. Tests 2 and 3 were run with the same total number of steps but at two different strain rates and time steps, therefore reaching the same final strain level. The product between the strain rate and the time step is the same in both tests. The results of the calculation in terms of stress-strain and volumetric behaviours are illustrated in Fig. 4.6. The comparison of Test 2 and 3 indicates that strain rate effects are genuine and are not influenced by the accuracy of the numerical results. In addition, test 1 was run at the same strain rate of test 2 but this time using a larger time step (see Table 4.3). The comparison between tests 1 and 2 shows that the solution has converged and therefore is not influenced by the time step (see Fig. 4.6). This confirms that the time step selected in the simulations provides sufficiently accurate numerical solutions and does not interfere with strain rate induced effects.

Parameter	Unit of measure	Test 1	Test 2	Test 3
Confining pressure, p	kPa	1,000	1,000	1,000
Poisson's ratio, ν	–	0.25	0.25	0.25
Damping ratio, ζ	–	0.0	0.0	0.0
Avg. particle size, d	μm	72	72	72
Density, ρ	kg/m^3	2,650$\times10^{10}$	2,650$\times10^{10}$	2,650$\times10^{10}$
Number of particles, N	–	10,000	10,000	10,000
Strain rate, $\dot{\epsilon}$	Hz	2×10^{-3}	2×10^{-3}	2×10^{-4}
Axial strain, ϵ_d	–	0.1	0.1	0.1
Time step, Δt	s	5.3×10^{-5}	5.3×10^{-6}	5.3×10^{-5}
Inertial number, I	–	7.41×10^{-4}	7.41×10^{-4}	7.41×10^{-5}
Number of steps	–	9.43×10^{5}	9.43×10^{6}	9.43×10^{6}

Table 4.3: Input DEM parameters of Test 1, 2 and 3.

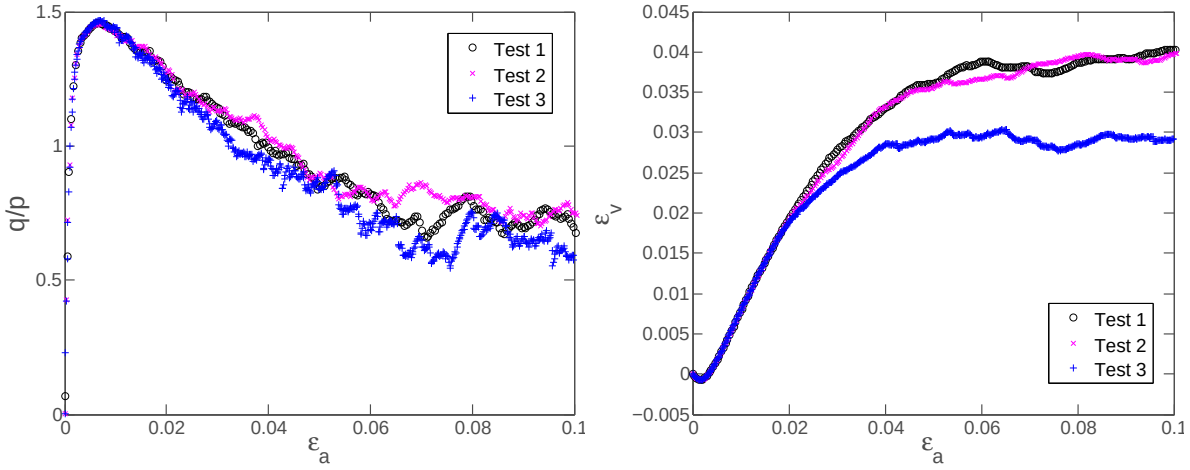

(a) (b)

Figure 4.6: Influence of the time step on the numerical solutions.

4.9 The influence of the inertial parameter I and stiffness parameter k

4.9.1 The effect of I for fixed k

A set of triaxial compression tests, under constant cell pressure of 1MPa, was run for increasing strain rate, which in turn causes increasing inertial number I, with all the other parameters kept constant (see Table 4.2). The results are illustrated in Fig. 4.7 – Fig. 4.9. The figures show the influence of I on the macroscopic behaviour for values of I ranging from 10^{-2} to 10^{-5}. Note that the effect of changing I is only observable at large strains (*i.e.* greater than 2%). There are a number of several observations that can be made:

(i) It is generally assumed in the literature that for $I \leq 10^{-3}$ the QS condition is assured (Roux and Combe, 2003; Radjai and Dubois, 2011; da Cruz et al., 2005). However, in Fig. 4.7 – Fig. 4.9 it is apparent that for these values of inertial number, the mechanical behaviour of the system is strain rate dependent, particularly in terms of volumetric strains. This discrepancy from previously published results is probably a result of the different type of material simulated in this work. In the present simulations a wide PSD was employed ($R_{max}/R_{min} \approx 8$), whereas in the study conducted

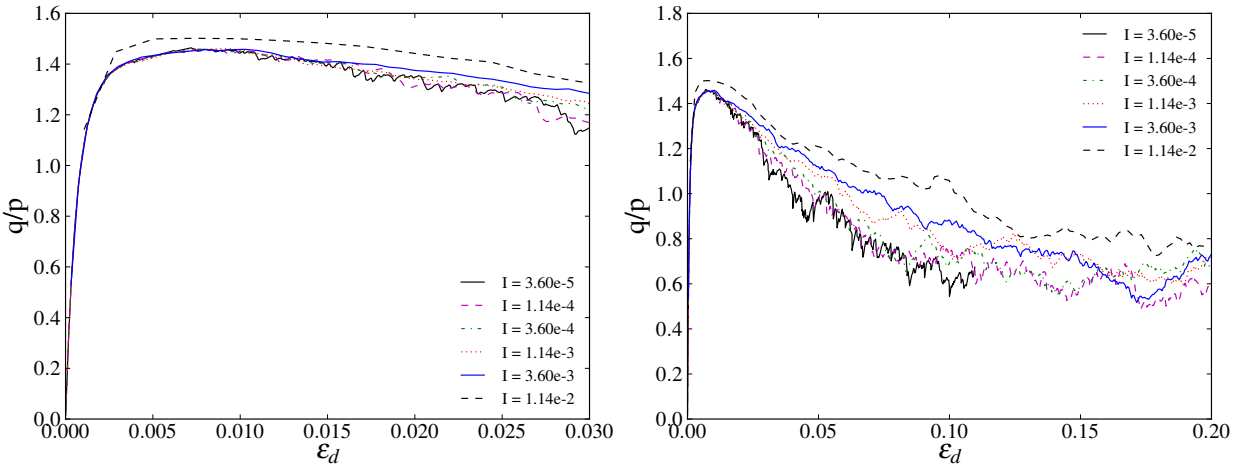

(a) (b)

Figure 4.7: Effect of strain rate on the stress ratio at small (right) and large (left) strain levels ($p = 1$MPa).

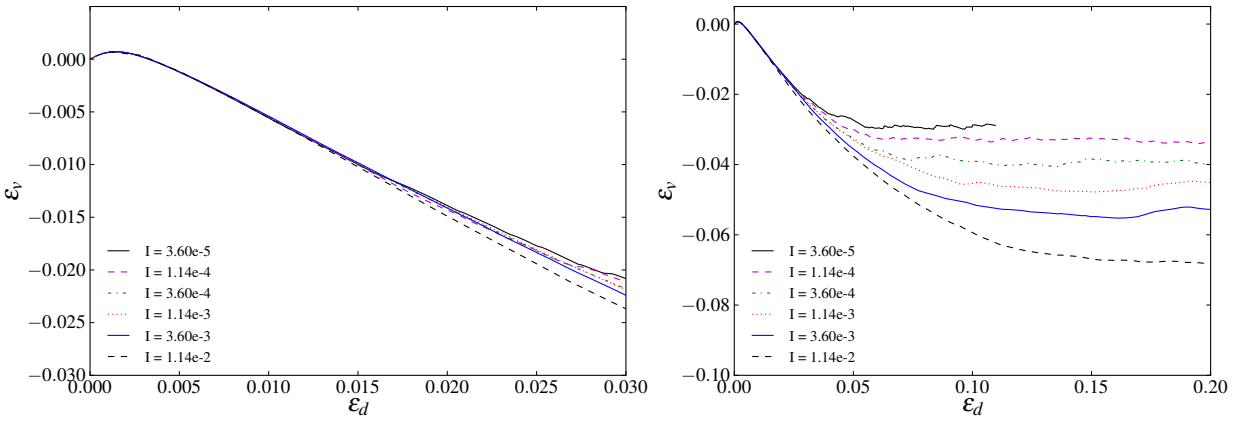

(a) (b)

Figure 4.8: Effect of strain rate on the strain behaviour at small (right) and large (left) strain levels ($p = 1$MPa).

by Roux and Combe (2010), although in 3D under dense conditions as in this work, a monodisperse packing was investigated.

(ii) The influence of strain rate on the volumetric and stress-strain behaviour is dramatically different at small and large strains. For ϵ_d less than 2%, the difference is almost negligible as illustrated in Fig. 4.7 and Fig. 4.8. This shows that the achievement of QS conditions should be addressed at large strains too and not only at the peak state as in common practice (see e.g. Belheine et al., 2009). The fundamental conclusion is that different QS thresholds exist at small and large strains. At small strains, the QS equilibrium was reached for $I \leq 10^{-3}$ (see Fig. 4.7 and Fig. 4.8). However, at

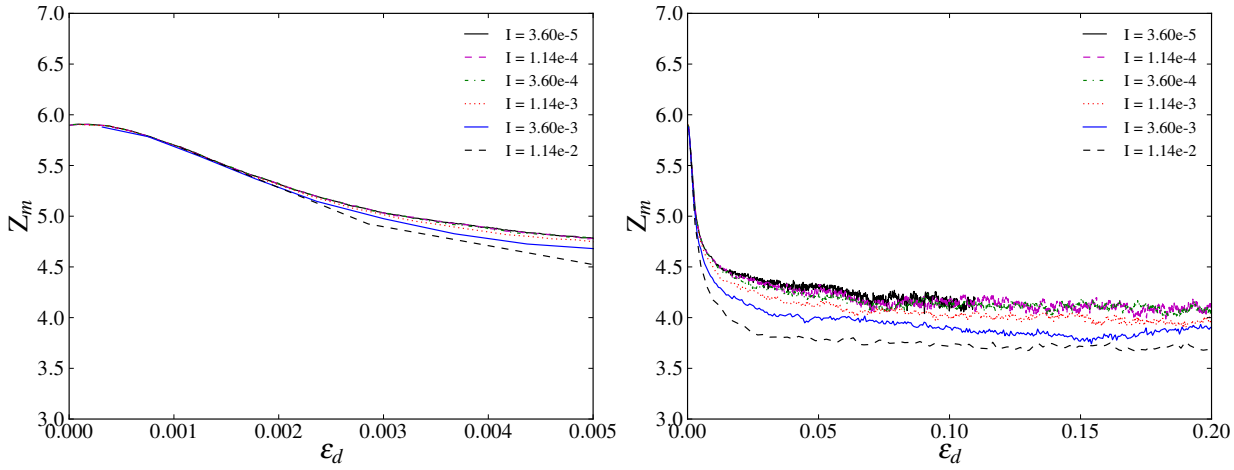

Figure 4.9: Effect of strain rate on the mechanical coordination number at small (right) and large (left) strain levels ($p = 1$MPa).

large strains the QS threshold in terms of I could not be identified as this would have (probably) required an even larger computational time.

(iii) The mechanical coordination number is computed as $Z_m = \frac{2C-N_1}{N-N_0-N_1}$, where C is the total number of contacts, N the total number of particles and N_0 the number of particles with zero contacts (floaters), and N_1 the number of particles with only one contact (rattles), which do not contribute to the mechanical stability of the system (Thornton and Antony, 2000). As shown in Fig. 4.9, Z_m decreases progressively with increasing strain rate. Once again, the difference becomes more accentuated towards the critical state. The coordination number provides some indication about the microstructure of the sample. This is in agreement with the fact that compaction is higher for lower strain rates which in turn leads to a higher coordination number. Ultimately, the loss of contacts exhibited for increasing loading rates corroborated by the tendency of the coordination number depicted in Fig. 4.9, is a by-product of the faster rearrangement that particles are subjected to under inertial conditions.

(iv) The influence of strain rate on the soil mechanical behaviour is not limited to the case of samples generated under dense conditions. The effects of reducing the material compressibility and increasing its peak stress ratio caused by an increased strain rate are also observed for loose samples. This is confirmed by Fig. 4.10, which com-

pares macroscopic triaxial test results of very loose and very dense samples, generated with an initial relative density of 0 and 100% respectively, and run at various strain rates, *i.e.* inertial numbers. Fig. 4.10 illustrates that the REV can exhibit the characteristics of a loose or a dense sample not exclusively as a function of density, but also depending on the shearing rate, provided that the latter is large enough to provoke non-negligible dynamic effects. In addition, for a given strain rate, a unique critical state is identified regardless of the initial relative density, as pictured in Fig. 4.10. This behaviour indicates that the notion of critical or steady state does not rely on the hypothesis of quasi-static conditions, although such an assumption is often implicit, at least in traditional soil mechanics.

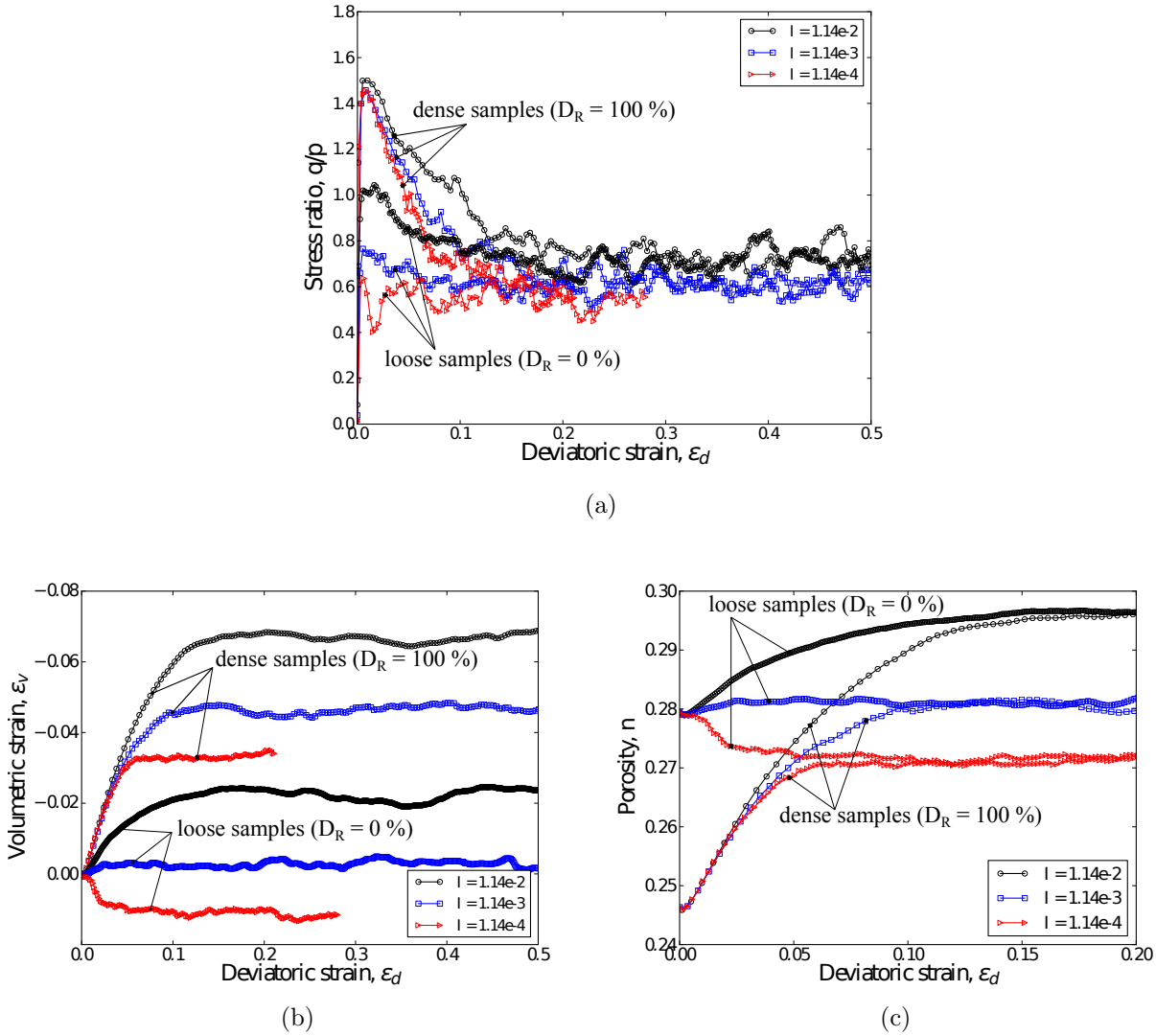

Figure 4.10: Loose and dense samples under different inertial numbers.

(v) Dilatancy, here defined as $-\dot{\epsilon_v}/\dot{\epsilon_d}$, is clearly a function of the strain rate as shown in Fig. 4.11. Two main considerations can be made: first it can be observed that the maximum dilatancy increases with increasing strain rate, which is an expected result since the same tendency holds for the peak strength which is commonly associated with the maximum dilatancy. The same behaviour was also observed in Yamamuro and Lade (2001) who run triaxial test experiments on crushed coral sand at various strain rates.

Second, the rate at which dilatancy approaches zero, *i.e.* the steady or critical state, increases with decreasing strain rate. In other words, the critical state is reached at smaller strains for lower strain rates. This is an interesting finding since many studies on the mechanics of granular materials focus on the results at the critical state while ignoring the actual shape of the stress-strain curve which, on the other hand, is crucial to the understanding of the material behaviour.

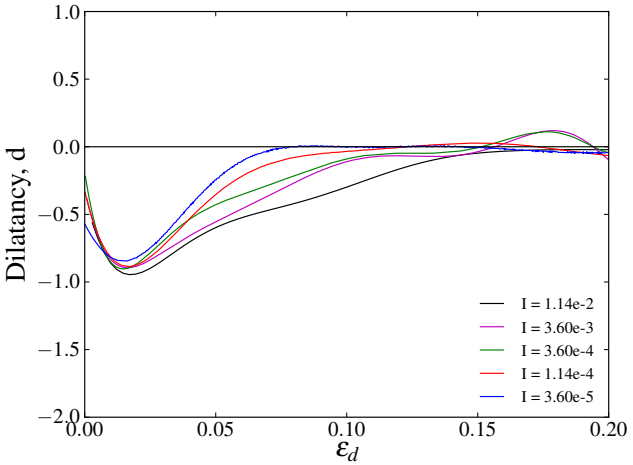

Figure 4.11: Effect of strain rate on dilatancy (p = 1MPa, D_R = 100%) (the experimental data were interpolated by means of polynomial regression and dilatancy was then computed from the resulting curve).

(vi) Quantitative agreement between numerical and laboratory experiments may then not only be difficult to achieve due to different sample preparation procedures but also because the QS regime, with the current computational power, can be only approached but not fully achieved in DEM unless experimental inertial numbers are reproduced in the simulations.

4.9.1.1 The influence of I at the peak and critical states

The effect of different inertial numbers on the macroscopic properties, such as the porosity and stress ratio, at the peak and critical states, is summarised in Fig. 4.12 and 4.13. It can be

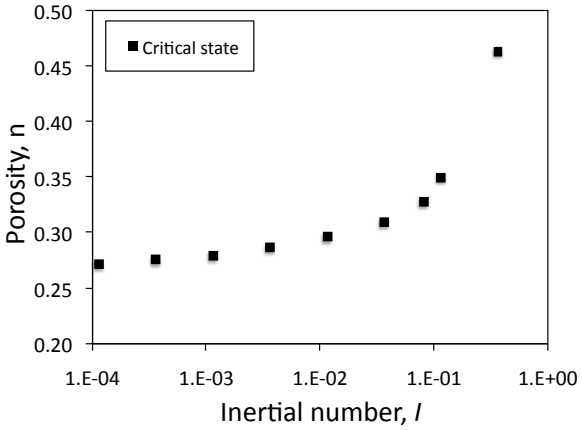

(a) Semilog plot of the critical state porosity versus the inertial number.

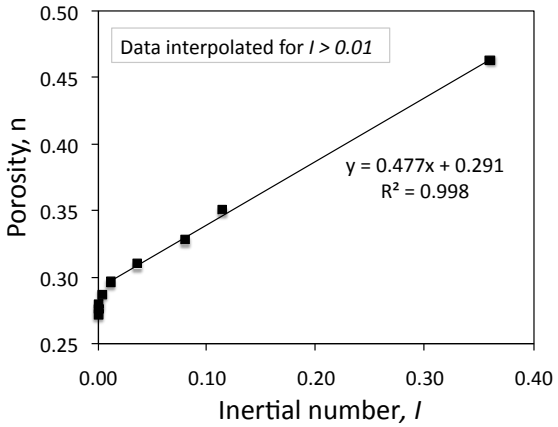

(b) Interpolation of the numerical data for $I \geq 0.01$ using a linear regression analysis.

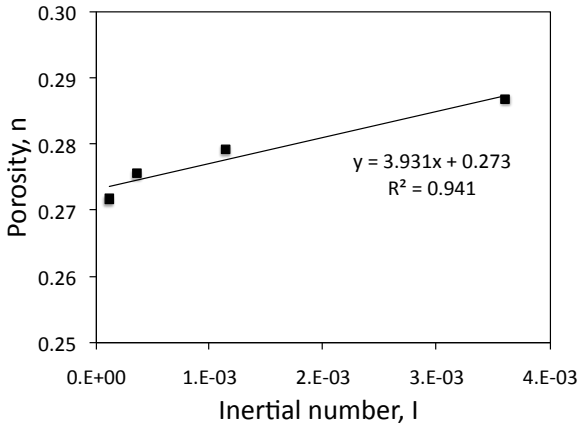

(c) Interpolation of the numerical data for $I \leq 0.01$ using a linear regression analysis.

Figure 4.12: Variation of the macroscopic porosity with the inertial number at the critical state.

observed that the critical state porosity is in linear relationship with the inertial number but also that two different slopes can be identified at small and large inertial numbers respectively (see Fig. 4.12(b) and 4.12(c)). This is in contrast with the results obtained in da Cruz et al. (2005) where a unique linear relationship between the critical solid fraction and the inertial number was observed. This linear relationship, called dilatancy law, was achieved by means of 2D simple shear numerical simulations while employing a linear contact model and a very

uniform particle size distribution. Although the different trend may be attributed to the differences existing with respect to the present simulations (in the paper a linear contact law was used and a very different material was simulated), we note that data at very small inertial numbers were not analysed in detail. On the contrary, we analyse data obtained for a wide range of I, including very small values of I (see Fig. 4.12(c)). Therefore we conclude that towards the quasi-static equilibrium (*i.e.* for $I \ll 10^{-2}$) the critical state porosity is indeed found to decrease linearly with decreasing I but at a higher rate than what observed under dynamic conditions. This is an important finding since it suggests that the influence of I on the critical state behaviour is different in different regimes (from inertial to quasi-static). This feature should be accounted for when advancing new constitutive equations for the modelling of granular materials in the transition from the inertial to the quasi-static regime.

In addition, the present findings indicate that the critical stress ratio is in a non-linear relationship with the inertial number and, as already pointed out, that it is still decreasing even at very low inertial numbers (see Fig. 4.12 and Fig. 4.13). On the other hand, the solution has reached the QS limit at small strains, *i.e.* at the peak state of the material (see Fig. 4.13).

The main conclusion for the tests presented herein is that the QS limit was only approached but not achieved at very large strains. Real laboratory experiments are conducted for inertial numbers of the order of 10^{-9} which are difficult to approach in DEM experiments unless a very small number of particles is employed (Sitharam and Vinod, 2009).

4.9.2 The combined effect of I and k on the mechanical soil behaviour

In this section, the combined influence of the control parameters k and I presented in Sec. 4.4 (*i.e.* the inertial and stiffness ratio numbers), will be examined in detail. To this end, a series of triaxial tests was conducted for different confining pressures and several loading rates.

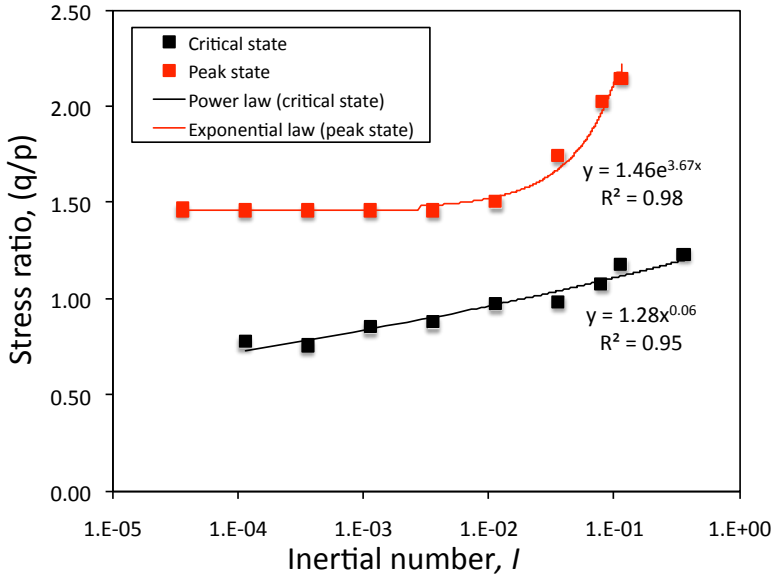

Figure 4.13: Variation of the macroscopic peak and critical state stress ratio against the inertial number (the fitting of the numerical data was obtained in Excel using a power and an exponential law).

The aim of this investigation is twofold: first to evaluate the effect of pressure on the critical state line at various inertial numbers, projected on the (n, p) plane, and second to ascertain the suitability of the control parameters (k, I) to constitute a physically sound method for establishing quasi-static conditions. The outcome will be useful to judge the capability of the DEM technique to investigate granular soils under QS conditions.

Triaxial tests were run for three values of k, 1.77×10^5, 8.23×10^3 and 1.77×10^3 respectively, and various inertial numbers in the range from 10^{-4} to 10^{-1}. Different k values were obtained by varying the confining pressure from 1kPa to 1,000kPa. Since the investigation of inertial effects, conducted in Sec. 4.9.1.1, revealed that the volumetric behaviour is the most sensitive to the strain rate (see Fig. 4.12), the following study will only focus on the analysis of the macroscopic porosity in order to probe the quasi-static condition of the system.

Fig. 4.14(a) illustrates the results in terms of critical state porosity against the inertial number, defined by Eq. 4.18. The various curves, depicted in Fig. 4.14(a), flatten towards a constant critical state porosity at the QS limit, *i.e.* as the inertial number approaches very small values. The quasi-static solution, indicated in Fig. 4.14(a), was approximately determined as the value to which all the curves tend. It is important to recall that the data

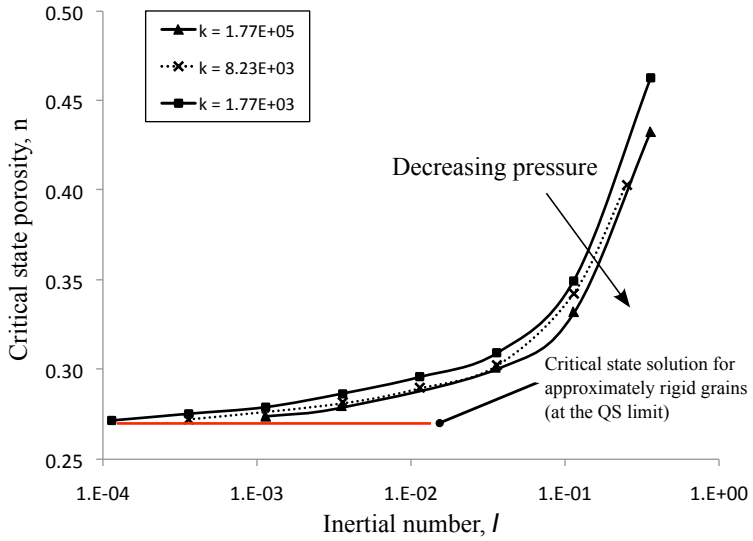

(a) Critical state porosity versus I at various values of k.

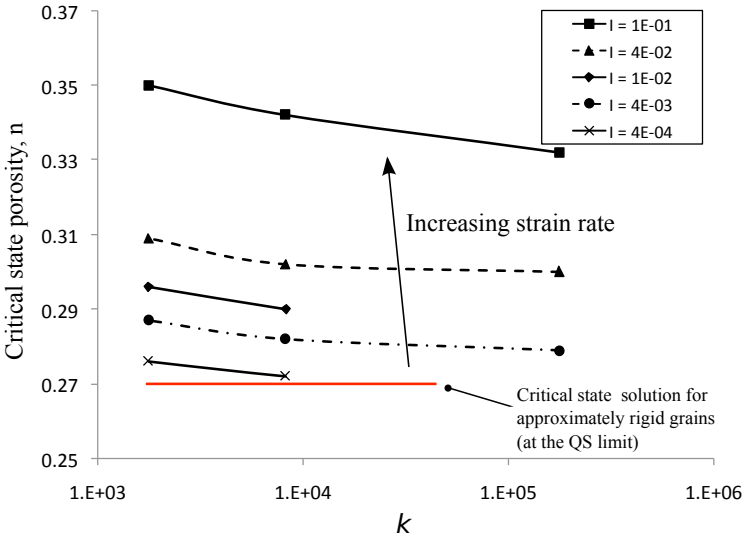

(b) Critical state porosity versus k at various values of I. The results are analogous to the data displayed in Fig. 4.14(a).

Figure 4.14: Effects of the combined influence of the control parameters (k, I) on the macroscopic critical state porosity. Note that $k = \left(\frac{E}{p(1-\nu^2)}\right)^{2/3}$ and $I = \dot{\epsilon} d \sqrt{\frac{\rho}{p}}$.

illustrated in Fig. 4.14(a) was computed for a range of $k > 10^3$, wherein elastic deformations due to the applied load are negligible (da Cruz et al., 2005; Roux and Combe, 2010). Indeed, the average amount of overlap, recorded during the simulations, was always found to be less than 1% of the particle diameter.

Following a careful examination of the results, two main observations can be made: first,

it emerges that the macroscopic mechanical behaviour is sensitive to the pressure change, and second it appears that the critical state porosity decreases with increasing k, *i.e.* decreasing pressure, for tests conducted at constant I.

The first observation contradicts a statement made in previous numerical research (da Cruz et al., 2005), addressing the mechanics of granular materials subjected to shear loading, that the influence of k on the macroscopic behaviour is negligible within the limit of rigid grains (da Cruz et al., 2005). On the other hand, the research presented therein discussed DEM results from 2D simulations whose analysis may disregard effects only visible when simulated in 3D. Furthermore, the authors used the parameter k exclusively as a measure of the elastic deformations of the grains. This is true by definition but it should also be realised that a variation of k implies a variation of pressure, which in turn can give rise to inertial effects (the inertial number is actually defined as a function of p, see Sec. 4.4). In other words, although the parameter k is employed to represent the elasticity of the grains, its variation may also produce inertial effects if the system is not under QS equilibrium.

The second observation is best illustrated by rearranging the results, plotting the porosity as a function of the stiffness number, as reproduced in Fig. 4.14(b). As stated previously, for a given inertial number, the porosity at the critical state is shown to decrease with decreasing pressure. This tendency is in contradiction with the principles of the critical state soil mechanics theory. The macroscopic porosity should instead decrease for increasing values of pressure, according to the equation of the critical state line on the $(\nu - \ln p)$ plane (Schofield and Wroth, 1968):

$$\nu = \Gamma - \lambda \ln p \quad , \tag{4.23}$$

where ν is the specific volume defined as $(1 + e)$ with e the void ratio, λ the slope of the critical state line and Γ the intercept of the line with the vertical axis at 1kPa of confining pressure. For natural sands, not experiencing any particle breakage (Cho et al., 2006), the slope of the critical state line is most likely determined by the amount of elastic deformations undergone at the contacts due to the applied confining pressure.

The projection of the critical state line on the $(n,\, k)$ plane, or likewise the $(n,\, p)$ plane,

can be seen in Fig. 4.14(b) for each prescribed value of I. Because of the relatively high stiffness of the simulated grains, the slopes of the critical state lines drawn in Fig. 4.14(b) for various inertial numbers cannot be attributed to the effects of elastic contact deformations. Ruling out the occurrence of localisation, owing to the presence of periodic boundaries, and excluding viscous effects since no damping was employed during the triaxial tests, the only remaining plausible reason for the anomalous porosity change with pressure can be ascribed to inertial effects. Such a conclusion seems to imply that the inertial number, defined by Eq. 4.18, is not a suitable candidate when the combined study of inertial and pressure effects is sought. In this regard, a new definition of inertial parameter will be proposed in the next section. The purpose is to seek for a method whereby critical state results, consistent with the soil mechanics theory, can be obtained.

4.9.3 A new definition of inertial number

In this section, a new definition of inertial number is proposed. The pressure parameter in Eq. 4.18 is simply replaced with the elastic Young's modulus of the particles, E, leading to the formula:

$$I^* = \dot{\epsilon} d \sqrt{\frac{\rho}{E}} \quad . \tag{4.24}$$

The parameter expressed by Eq. 4.24 is still dimensionless, but holds a different physical meaning than the usual expression of inertia, Eq. 4.18. I^* can be seen as the ratio between two velocities: the speed of loading, $\dot{\epsilon} d$, and the speed of sound, $\sqrt{E/\rho}$. Such a relationship is only approximate because the sound speed is generally defined using the Young's modulus and density of the medium instead of the physical parameters of the constituent grains. However, the macroscopic Young's modulus is proportional to the grain stiffness (e.g. Thornton, 1999; Campbell, 2005).

Although the new inertial parameter I^* is very close to the conventional definition of I, the latter considers the occurrence of inertial forces as a result of the applied pressure but does not account for the way the information propagates within the granular material. On

the other hand, whether or not the information truly propagates in granular materials like waves is still a matter of debate (Luding, 2005; Goldenberg and Goldhirsch, 2005) and the argument is beyond the scope of this thesis.

The same results presented in Fig. 4.14 are plotted with respect to I^* as illustrated in Fig. 4.15. Let us first examine the relationship between the critical state porosity against I^* as depicted in Fig. 4.15(a). Similar to the effects induced by the variation of I, the solution non-linearly decreases as I^* decreases, revealing a tendency towards the quasi-static limit at very small I^*. Accordingly, it can be asserted that both I and I^* provide equivalent results, as regards the relationship between the macroscopic porosity and the strain rate, for a predefined stiffness ratio.

Let us now consider the influence of k for a given I^*. Fig. 4.15(a) indicates that for increasing pressure, the critical state porosity has a tendency to decrease, which is contrary to previous results obtained through the usual definition of inertial number as discussed in Sec. 4.9.2, but is consistent with the principles of soil mechanics. This is best observed in Fig. 4.15(b) where the critical porosity is illustrated with respect to k for various I^*.

Another remarkable observation, arising from the analysis of Fig. 4.15(b), concerns the distance between the curves obtained for different I^* which appears to decrease as k decreases, *i.e.* increasing pressure. This indicates that, for higher pressures, the solution is less sensitive to the strain rate. This is reasonable if we think that the ratio between the kinetic energy and the elastic energy stored by grains, which is often used as a criterion to probe the quasi-static equilibrium of the system (e.g. Luding, 2004), is lower for higher confining pressure under a given loading rate. A contrasting outcome, which can hardly be explained physically, if not by the inadequacy of the control parameters (k, I), can be identified in Fig. 4.14(b). This illustrates that the curves, corresponding to various I, have the same separation within the fairly wide range of k, as investigated in this study.

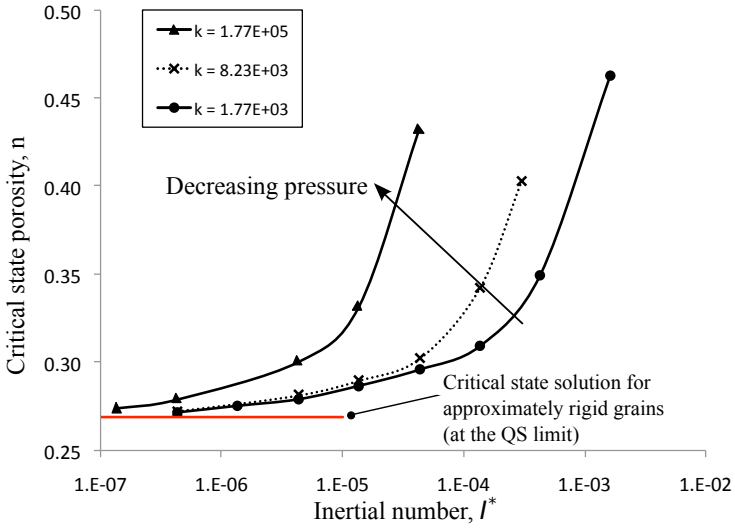

(a) Critical state porosity versus I^* at various k.

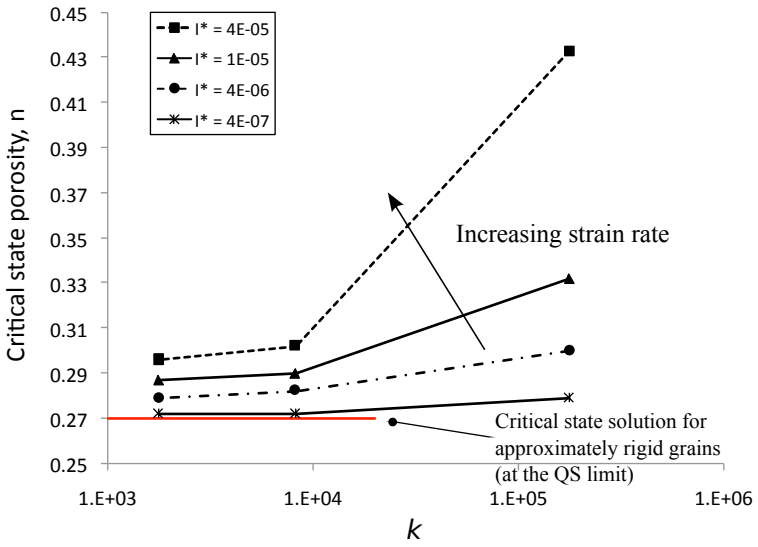

(b) Critical state porosity verus k at various I^*.

Figure 4.15: Investigation of the combined influence of the control parameters (k, I^*) on the tendency of the macroscopic critical state porosity. Note that $k = \left(\frac{E}{p(1-\nu^2)}\right)^{2/3}$ and $I^* = \dot{\epsilon} d\sqrt{\frac{\rho}{E}}$.

4.9.4 Discussion and comparison with published work

A comprehensive dimensional analysis was carried out in order to identify the parameters ruling the behaviour of a particulate system when sheared under triaxial test conditions at constant mean lateral pressure. Under a number of assumptions, the dimensionless parame-

ters controlling the material state were reduced to two possible pairs, (k, I) or (k, I^*), where $k = \left(\frac{E}{p(1-\nu^2)}\right)^{2/3}$, $I = \dot{\epsilon}d\sqrt{\rho/p}$ and $I^* = \dot{\epsilon}d\sqrt{\rho/E}$. Sec. 4.9.2 and 4.9.3 showed that the values of the parameters defined by these two pairs lead to different trends with regard to the combined influence of pressure and strain rate on the macroscopic porosity. The values of k and I considered in the analysis, approximately ranged from 10^3 to 10^5 and from 10^{-4} to 10^0, respectively. The latter corresponded to a range of I^* from 10^{-7} to 10^{-3}. It was also argued that the method established by the control parameters (k, I^*) is the most appropriate, since only in this case did the results appear in agreement with the principles of the critical soil mechanics theory. The explanation for this can be based upon the definitions of I and I^*, as now discussed.

As pointed out in Sec. 4.9.2, the problem arose when the pressure was varied at constant I. The goal was to analyse the effect of pressure on the critical state line at a fixed I, *i.e.* inertial level. However, in order to keep I constant, a variation of p was always accompanied by a variation of $\dot{\epsilon}$ (or ρ likewise). Since the solution is not quasi-static, the dynamics of the system is not only affected by the pressure change but also by the variation of the strain rate. It is of no surprise then that the resultant trend is disconnected from what would be physically expected as a sole consequence of the pressure change. Instead, when I^* is employed as the criterion for QS conditions, the problem disappears simply because I^* is no longer defined as a function of p. This allows the analysis of pressure effects, be they in terms of elastic deformations or inertial effects, to be accounted for whatever value of strain rate.

A similar investigation about the effect of pressure and inertia on the macroscopic behaviour of an ensemble was reported by Campbell (2005), who simulated 1,000 spherical particles subject to simple shear loading at constant vertical pressure and analysed the effects of two parameters derived from dimensional analysis and suitable for linear contacts. These parameters, which we call k_c and I_c respectively as they are comparable to k and I^*

above, are defined as follows (Campbell, 2005):

$$(k_c, I_c) = \left(\frac{pd}{k^*} \, , \, \dot{\epsilon} d \sqrt{\frac{\rho d}{k^*}} \right) \quad , \tag{4.25}$$

where k^* represents the intergranular linear elastic contact stiffness. Note that I_c is actually equal to $(1/\sqrt{I_{cam}})$, where I_{cam} is the original definition of inertial number used in Campbell (2005). The first parameter, k_c, is used to take into account the elastic deformations of the grains, while the parameter I_c is introduced to determine the transition between inertial and elastic quasi-static conditions. In particular, the latter (in its original version) was physically interpreted as the square of the ratio between two velocities: the speed of sound in the medium and the shear velocity in the medium (Campbell, 2002). This was in turn seen as the square of the inverse of the Mach number. The dimensionless Mach number is used in fluid mechanics to indicate a more or less compressible material, *i.e.* in the present case a more or less inertial material.

Although the material characterisation is much simpler when linear contacts are taken into account, it should be possible to draw a qualitative comparison between the present results (achieved for non-linear Hertzian grains) and the macroscopic results discussed in Campbell (2005) (valid for linear and equal size particles).

Fig. 4.16 illustrates part of the results presented in Campbell (2005), which have been rearranged in order to ease the comparison with the present findings. The macroscopic critical state porosity is plotted with respect to the inertial number I_c and for various k_c, as shown in Fig. 4.16. Note that Campbell (2005) explored a very wide range of pressures, including the region where elastic deformations start to play a non-negligible role as represented by the data set which falls below the quasi-static limit for approximately rigid grains (Campbell, 2005). The similarity between the porosity trend of Fig. 4.16 and that of Fig. 4.15(a) is striking. This can be explained with the analogous features held by the control parameters (k_c, I_c) and (k, I^*). While the correspondence between k_c and k is trivial, we note that I_c is actually equivalent to I^*, having replaced the stiffness k^* with the constant product Ed.

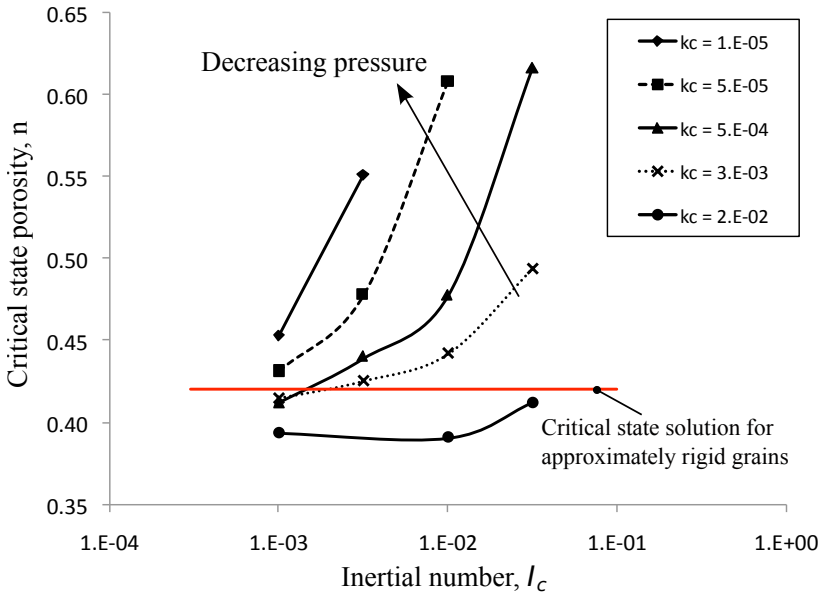

Figure 4.16: Results obtained for a friction coefficient of 0.5 (after Campbell, 2005)

Surprisingly, this appears to be the first time that the inadequacy of inertial parameter I to define QS conditions has become apparent. This is probably because to date the influence of stiffness (or pressure likewise) has generally been disregarded in the analysis of quasi-static deformations at the critical state, except in the work by Campbell (2005), who, in fact, chose to employ an inertial dimensionless number equivalent to the parameter I^* proposed in this study. However, here the parameter proposed is shown to be valid whatever type of elastic contact law is employed.

4.10 Conclusions

We can draw a number of conclusions from the work discussed in this chapter:

(i) The results shown in this chapter illustrate the difficulty in achieving QS conditions in DEM experiments when a wide PSD, typical of lunar soil, and the contact parameters of a quartz sand are adopted. Increasing the particle density, or likewise the strain rate, generated dynamic effects even at very small inertial numbers. Moreover, it was found that the QS threshold is highly influenced by the level of strain. In particular, the QS regime was more easily achieved at small strains whereas at large strains the

QS condition was approached but not reached due to the current limitations on the total computational time.

(ii) The critical state porosity of the samples was found extremely sensitive to the inertia level compared with the influence of inertia on the macroscopic stresses. Several authors were able to identify the QS condition based on information about stresses rather than strains (Belheine et al., 2009; Cheng et al., 2003). However, the solution should be regarded as QS when all the sample descriptors, including the macroscopic porosity, become insensitive to the strain rate. The QS condition was often only assessed at the peak state in prior works, however, the current results showed that the volumetric behaviour at the critical state changes significantly even at very low inertial numbers (*i.e.* less than 10^{-4}), whereas the peak stress is already indifferent to the level of inertia. QS conditions should then be verified based on information at very large strains, *i.e.* at the critical state, since it is in this region that particle rearrangement, and so porosity, is expected to be more sensitive to the level of inertia.

(iii) The comparison between tests conducted with the same value of I, but different k, did not lead to the same macroscopic response. In other words, k had a non-negligible effect on the critical state results. This effect caused the critical porosity to increase with the confining stress. Such a trend is opposite to the principles of the critical state soil mechanics theory. The reason for this was attributed to the difficulty of studying the influence of pressure change on the macroscopic response using the control parameter pair (k, I). In order to run tests under the same I, *i.e.* presumably under the same level of inertia, but various confining pressures, the strain rate has to be adjusted in order to keep I constant because I is also a function of pressure. It is this combined change of strain rate and pressure that was found responsible for the non-physical result achieved at the critical state.

(iv) It was concluded that the usual definition of inertial number as a criterion for QS conditions should be modified in order to enable the study of the influence of pressure or stiffness change on the macroscopic response. A new inertial number I^*, independent of the pressure, was proposed as an alternative candidate to the usual definition of I. It

was found that the new set of parameters (k, I^*) provide reasonable results, no longer in contradiction with the principles of critical state soil mechanics. The new findings were also found in close agreement with previous published research conducted with linear contacts. Finally, it was noted that the physical interpretation of the parameter I^* can also be related to the state of inertia of the system, given its analogy with the definition of the Mach number.

Finally, it should be noted that the calculations presented in this chapter were conducted with a friction coefficient of 0.6 (Table 4.2). Although this value is not uncommon in DEM simulations, experimental results suggest that the real interparticle friction coefficient of quartz particles is much lower than that, with examples of recorded values of around 0.2 or less (Cole and Peters, 2008). The influence of internal friction coefficient was beyond the scope of the present investigation but it could influence the results.

Chapter 5

Numerical simulations of lunar soil by DEM

This chapter presents the numerical results obtained from a series of triaxial tests run at extremely low confining pressures and with surface energy forces. The goal is to reveal the influence of the lunar environment on the macroscopic soil behaviour. Conclusions are drawn with regard to the ability of the DEM model, devised for lunar soil, to capture the unusual cohesive strength properties of lunar material.

5.1 Introduction

The analysis of lunar regolith samples, brought back to Earth from manned and unmanned missions, has provided a detailed description of the mineral and chemical composition of lunar soil. For example, a non-destructive microanalysis technique has been employed to describe accurately the mineral composition of lunar samples (Papike et al., 1991). Despite the advances on the chemistry and mineralogy of lunar soil, the lack of knowledge in terms of lunar soil mechanics has recently required engineers and lunar scientists to perform additional studies. For instance, particular effort has been applied to the production of expensive lunar soil simulants, aiming to replicate and further investigate the fundamental geotechnical properties of real lunar materials (see e.g. Arslan et al., 2010).

The limited success in understanding the mechanical properties of lunar soil can be ascribed to two main difficulties: first, the inability to reproduce typical lunar environmental

conditions in the laboratory, and second the shortage of available lunar material on Earth in an amount necessary to carry out geotechnical tests, such as a shear box or triaxial tests. On the other hand, engineering properties are essential prerequisites for the success of geotechnical engineering design. This is expected to play an important role in forthcoming lunar explorations, where the final goal is to build a permanent outpost on the lunar surface.

The unusual cohesive properties of lunar soil have stimulated the curiosity of scientists and engineers ever the era of Apollo missions. The cohesiveness of lunar soil was first observed from analyses based on in-situ cone penetrometer and vane shear tests, but it was also indicated by the steep slopes of shallow trench excavations sustained on the lunar surface (Carrier et al., 1991). It was noted that the visible cohesion of lunar soil can have several important consequences for future In-Situ Resource Utilisation (ISRU) operations, due to the difficulty in handling materials with cohesive flow properties (Walton et al., 2007). Cohesive forces due to van der Waals interactions, which are deemed to be responsible for the lunar soil cohesion (Walton, 2007), are also of high concern with regard to the performance and durability of mechanical systems operating on the Moon. This is because small particles with adhesive properties are likely to contaminate mechanical components (Walton, 2007).

The aim of this chapter is to use particle-scale numerical simulations by DEM to assess the influence of surface energy forces on the macroscopic strength properties of the soil. A study examining the influence of the main features of the lunar environment, such as very low gravity and ultra-hard vacuum (UHV) conditions, will be presented for both spherical and non-spherical particles. The modelling of non-spherical particles will be tackled in two ways: the first using artificial rolling resistance at the contacts, and the second using the simulation of clumps, *i.e* particles comprised of spheres clumped together to form non-convex particle shapes.

The outcome of the analysis will be evaluated against the best estimates of lunar soil shear strength derived both from in-situ experimental observations and from geotechnical laboratory tests of lunar regolith prototypes (e.g. Klosky et al., 2000; Alshibli and Hasan, 2009; Oravec et al., 2010).

5.2 Sample preparation at different relative densities

In Section 4.6, a numerical procedure to prepare very dense samples ($D_R = 100\%$) was outlined. The method will now be extended to generate samples of various relative densities. This is needed because the influence of relative density on the material strength parameters will be later assessed.

The aim is to create isotropic samples compressed to a certain stress level while maintaining a uniform structure. There are several ways of generating isotropic samples by DEM, however, it is well-known that not all of them lead to both uniform and isotropic samples. Some authors, for instance, prefer to prepare the specimens via gravity deposition (Hasan and Alshibli, 2010), aiming to reproduce the actual density of laboratory samples. Unfortunately this method is likely to produce anisotropic ensembles, and for this reason is disregarded in the present study. However, Sadrekarimi and Olson (2011) have recently demonstrated that the specimen preparation, *i.e.* the initial fabric, does not appear to affect the value of friction angles obtained from laboratory triaxial tests. This means that the choice of preparation method is not so critical, provided that the selected procedure leads to reproducible, uniform, specimens. A similar conclusion was previously reached numerically by Ng (2004).

A dynamic procedure, similar to the one adopted by Salot et al. (2009), was selected as the best way of reproducing isotropic and uniform samples, as mentioned in Section 4.6. First, particles are randomly generated in a cubical domain using an algorithm (Smilauer et al., 2010) that aims to place the given number of particles within prescribed boundaries, without permitting any contacts, and at a prescribed initial porosity. The minimum initial porosity is set through a trial and error procedure which relies on the ability of the algorithm to place all the particles in the given space within a maximum number of trials. Particles are generated according to the characteristic PSD previously determined for the lunar soil (see Section 2.2.1). The domain has periodic boundaries to avoid boundary effects (see Section 4.5).

The next step consists of an isotropic compression with zero contact friction until 1kPa

confining stress is reached and quasi-static conditions are met (see Chapter 4). Figure 5.1 shows the orientations of the normal contact vectors projected along the planes XY, YZ, XZ which confirms the uniformity of the numerical ensemble.

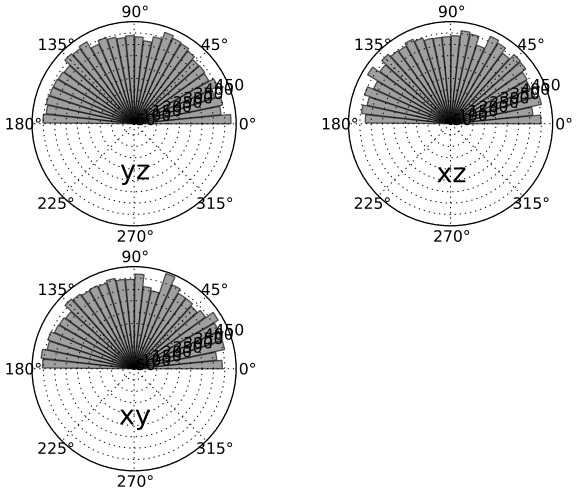

Figure 5.1: Distribution (rose diagram) of contact orientation vectors projected on the planes XY, YZ and XZ at the end of the preparation phase ($p = 1$kPa).

The concept of relative density D_R, is a very useful one in soil mechanics as it accounts for the amount of packing of the ensemble relatively to its loosest and densest possible conditions, thus containing information about both particle shape and particle arrangement (see Sec. 2.2.3). We recall that it is defined as:

$$D_R = \frac{e_{\max} - e}{e_{\max} - e_{\min}} \quad , \tag{5.1}$$

where $e_{\max}$ and $e_{\min}$ are the maximum and minimum void ratios.

Unfortunately, it is difficult to define a suitable value of D_R for a DEM assembly because it is difficult to determine numerically $e_{\max}$ and $e_{\min}$. The difficulty is also partly due to the spherical shape of the simulated particles, unlike the irregular shapes of real grains. These discrepancies prevent direct comparison between numerical and real soil densities. On the other hand, it seems reasonable to introduce the notion of relative density but in relation to the numerical ensemble as detailed below.

The values of $e_{\max}$ and $e_{\min}$ can be computed at the reference confining pressure of 1kPa. This is achieved by means of isotropic compression, with and without contact friction, to obtain a relative density of 0 and 100%, respectively. Samples with intermediate relative densities can be obtained by choosing an appropriate contact friction angle during the isotropic compression. The contact friction angle is then gradually brought back to the value of the real material (input value). A similar method was previously advanced by Salot et al. (2009), who successfully compared numerical and experimental results through a quantitative approach.

Very dense samples ($D_R = 100\%$) will be generated, following the above procedure, using both the HM and JKR contact models described in Chapter 3. Note that the JKR model has one additional input parameter compared to the HM model, this being the interface surface energy γ, which is used to account for the effects of adhesion upon contact deformations (see Chapter 3). In the following investigation, γ is set as non-zero from the beginning of the generation procedure for samples simulating lunar soil. It may be argued that this choice will preclude the isolation of the effects of γ when performing a direct comparison between the results obtained with and without surface energy forces, since the micromechanical structure and the fabric of the samples is expected to be dissimilar at the start of the shearing phase. However, samples generated with and without surface energy will be compared at the same initial D_R (which accounts for the initial microstructure of the material) and will be sheared at the same confining pressure. These conditions will assure a meaningful comparison between samples with and without surface energy and so the identification of the effects of γ on the macroscopic behaviour.

5.3 Results of triaxial compression tests at low stresses with surface energy

There are two main factors which are likely to affect the mechanical response of the soil in the lunar environment: the very low gravitational field ($g = 1.6249\text{m/s}^2$, *i.e.* approximately

one sixth the gravity that on Earth's surface) and the UHV conditions (in the range of 1.33×10^{-10}Pa (nighttime) to 1.33×10^{-8}Pa (daytime) (Johnson, 1971)).

Due to the very low lunar gravity, the lunar surface soil experiences very small levels of confinement. This is likely to affect the macroscopic behaviour of the soil since shear strength parameters can significantly vary with the stress level. For instance, both dilatancy and friction angle were observed to increase significantly under very low confining pressures (Sture et al., 1998; K. A. Alshibli and Costes, 2000).

The UHV of the lunar environment is also expected to influence the soil behaviour. This is corroborated by experimental evidence which indicates an increase in the shear strength of granular soils under UHV for a variety of different mineralogies (Vey and Nelson, 1966).

To understand the extent that the above factors influence the lunar soil mechanics, a series of drained triaxial simulations was carried out. Results with and without surface energy forces will be presented and compared in this chapter. First, the influence of the strain rate will be assessed at the peak state of the material. Note that the peak state is chosen here as reference condition, although in Chapter 4 it was shown that the most sensitive condition to strain rate effects is the critical state. This choice is because extremely low confining pressures and high surface energy forces (which were not examined in Chapter 4) are expected to introduce strain rate effects at the peak as well at the critical state. Moreover, it was shown that QS conditions at the critical state can only be approached but not achieved by the DEM due to the current limitations on the computational time. Instead, the selection of the (maximum) value of strain rate corresponding to the QS equilibrium can be confidently made at the peak state, as demonstrated in Chapter 4. However, it will also be checked that the selected loading rate does not introduce significant rate effects at the critical state.

Following that, macroscopic observations will be separately examined at small and large strains respectively, both with and without adhesion. Finally, the soil strength parameters, such as cohesion and friction angle, will be critically assessed as a function of pressure, surface energy and strain level.

5.3.1 Input parameters and loading paths

Very dense samples of 10,000 grains were reproduced following the procedure presented in Section 5.2. Particles were generated according to the PSD determined for lunar soil in Chapter 2 and were attributed with material properties typical of quartz sand as listed in Table 5.1. The motivation for using a fictitiously high particle density was discussed in Chapter 4.

DEM input parameters			
Number of particles	N	10,000	
Young's modulus	E	70	GPa
Poisson's ratio	ν	0.25	
Average particle size	d	72	μm
Particle density	ρ	$2{,}650\times10^{10}$	kg/m^3
Surface energy	γ	0.07	J/m^2
Damping ratio (in both normal and shear directions)	ζ	0.7	
Friction coefficient	μ	0.6	
Strain rate	$\dot{\epsilon}$	1×10^{-4}	Hz

Table 5.1: Micromechanical parameters attributed to the DEM particles. Note that damping is used exclusively during the generation phase (*i.e.* prior the shearing phase). Surface energy is activated only in the tests run with adhesive forces.

Previously, a series of triaxial simulations was run for adhesive elastic frictional spherical particles at constant (lateral) cell pressure and up to a stress level of 1MPa (Modenese et al., 2012c). The aim was to show the influence of surface energy on the peak and critical strength envelopes over a wide range of stresses. However, because of the importance of low stress levels we concentrate here only on tests conducted at very small stresses, *i.e.* less than 10kPa. In particular, tests run at a constant mean confining pressure, allow data to be obtained at even lower stress levels than when a standard triaxial compression path is followed.

The stress level was chosen in the range of 1 to 10kPa. This range of stresses corresponds to a depth from 0.4 to 4m below the lunar surface. The stress paths followed during the tests are illustrated in Fig. 5.2, using the coordinates q and p, *i.e.* the deviatoric and mean confining pressures.

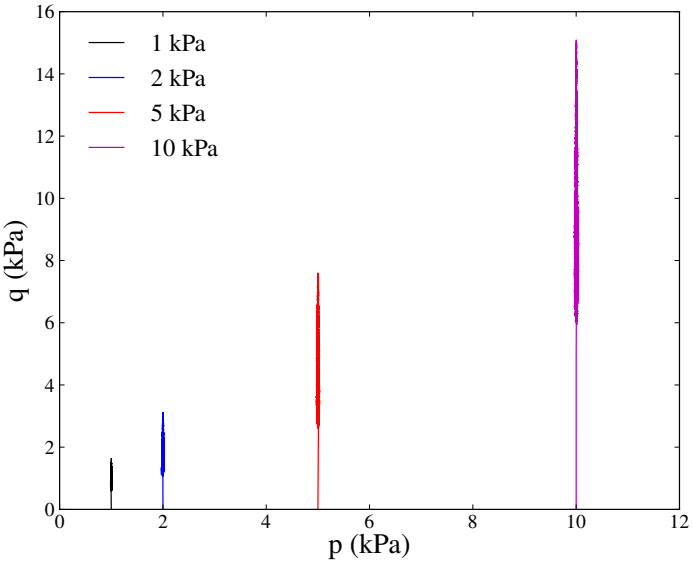

Figure 5.2: Stress paths of triaxial tests run at very small confining pressures in the range of 1 to 10kPa.

All the stresses computed in this study are regarded as effective stresses. In the presence of adhesion, the stress tensor could be thought of as the sum of two contributions: a first due to the presence of attractive contact forces, and a second due to the remaining action of repulsive elastic interactions. However, no such distinction is made in this study, since these contributions actually exert a reciprocal influence, in agreement with the JKR contact theory, and cannot be considered separately. Thus, the stress tensor will be computed in the same way both with and without adhesion, according to Eq. 4.22.

Finally, note that a mixed type of control was employed during the tests. In particular, the samples were loaded in the vertical direction at a constant displacement rate, whereas the lateral boundaries were adjusted in order to keep the mean stress constant within a prescribed tolerance. Despite the very low stress levels, the servo-control algorithm, described in (Smilauer et al., 2010), allowed the desired stress path to be followed, as demonstrated by Fig. 5.2.

5.3.2 Effect of loading rate on the peak state

When running DEM simulations, the loading rate must be small enough to maintain under QS conditions, as pointed out in Chapter 4. This is particularly true for tests carried out at

very low stress levels since the kinetic energy of the system can be significant compared to the amount of stored elastic energy, which in turn results in large unbalanced forces. Thus, an analysis of the influence of the strain rate on the maximum stress ratio was conducted for tests at 1kPa of confining pressure, with and without surface energy forces.

The results are illustrated in Fig. 5.3 and 5.4. Various strain rates were employed to

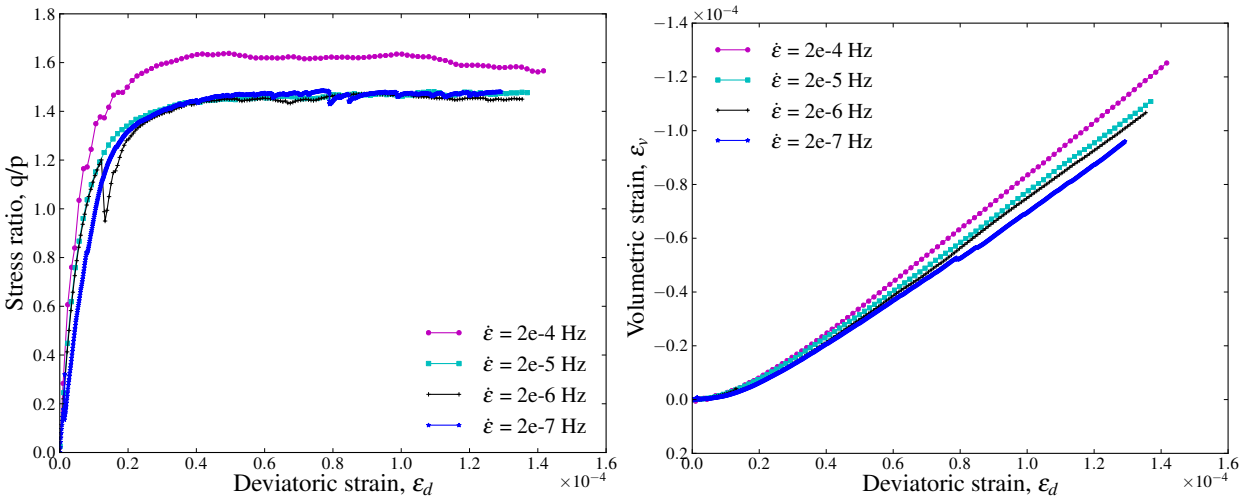

Figure 5.3: Influence of strain rate at very small strain levels for triaxial tests run under 1kPa of confining pressure (HM model).

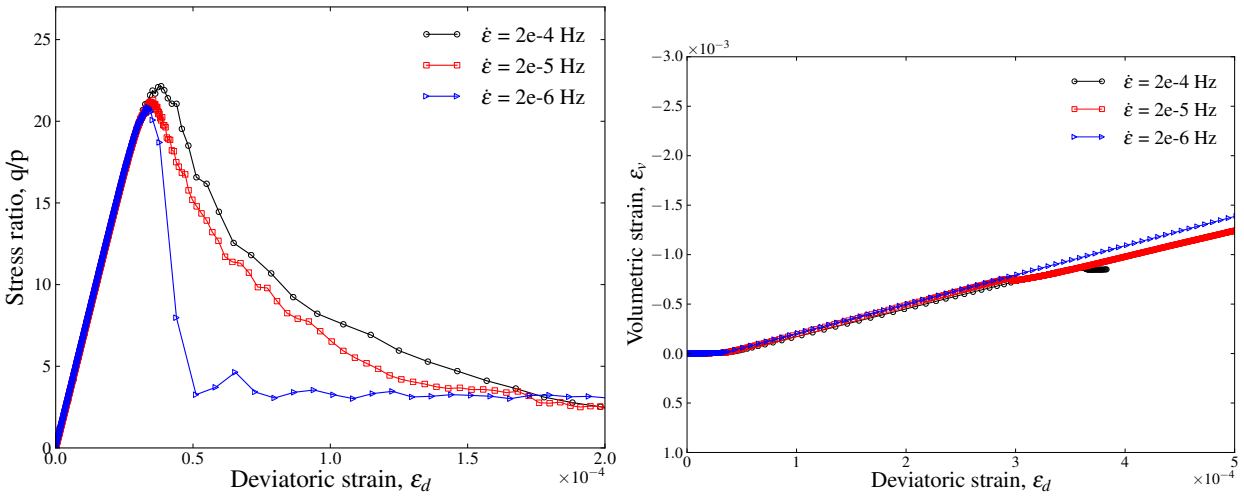

Figure 5.4: Influence of strain rate at very small strain levels for triaxial tests run under 1kPa of confining pressure and surface energy $\gamma = 0.07\text{J/m}^2$ (JKR model).

run the tests up to the peak failure point. The surface energy adopted in the simulations with adhesion was equal to 0.07J/m^2, in line with the estimated value for lunar soil (see Chapter 3). The stress ratio q/p, and the volumetric strain ϵ_v, are plotted versus the devia-

toric strain ϵ_d, in Fig. 5.3 and 5.4. It is illustrated that for decreasing strain rate, the peak stress at which failure occurs decreases and so does the maximum dilatancy. The goal is to identify the highest value of $\dot{\epsilon}$ which does not affect the response, in order to minimise the computational time. According to Fig. 5.3 and 5.4, the strain rate at which both materials (with and without adhesion forces), are close to the QS solution is $\dot{\epsilon} = 2 \times 10^{-5}$.

A strain rate of 2×10^{-5} will then be kept constant when running triaxial tests at stress levels higher than 1kPa, in agreement with the method for QS conditions outlined in Chapter 4.

5.3.3 Soil behaviour at very small strains

Triaxial tests were run at different mean confining pressures, ranging from 1 to 10kPa. The purpose was to investigate the effects of pressure on the peak material behaviour, both with and without adhesion. The results of the tests at small strains are reported in Fig. 5.5 and 5.6, both in terms of q versus ϵ_d and q/p versus ϵ_d.

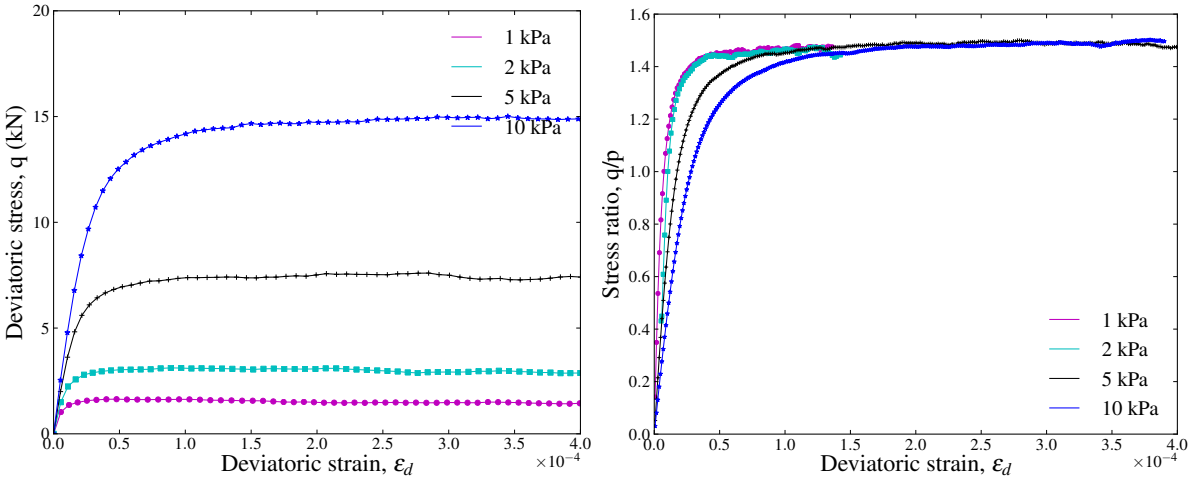

(a) Deviatoric stress vs deviatoric strain.

(b) Stress ratio vs deviatoric strain.

Figure 5.5: Influence of small stress levels on the peak strength at very small strains (HM model).

It can be observed that increasing the confining pressure causes an increase in the small-strain soil stiffness as expected, both with and without adhesion (see Fig. 5.5(a) and 5.6(a)). The small-strain elastic Young's modulus E (tangent value), calculated from the initial slope

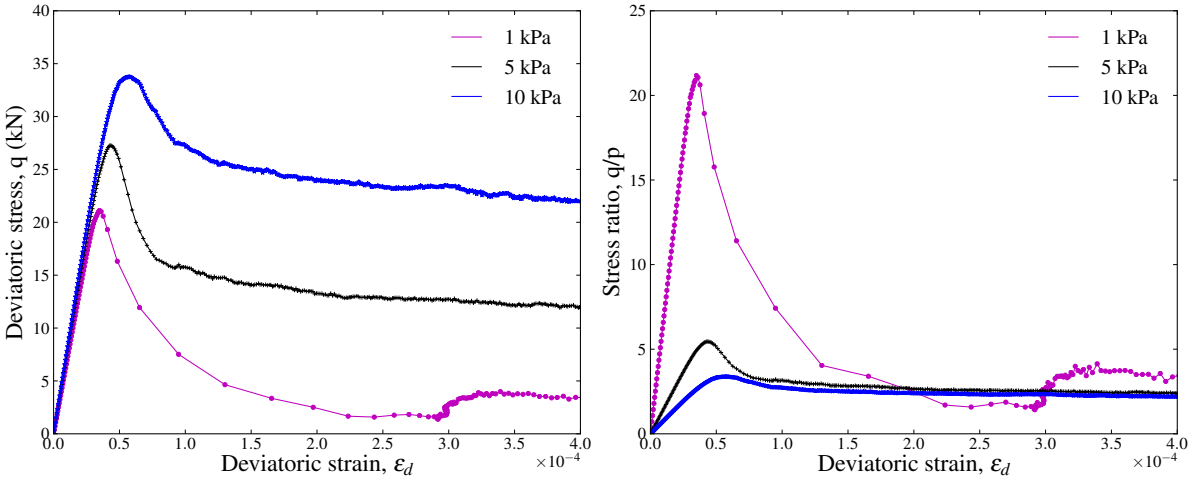

(a) Deviatoric stress vs deviatoric strain.

(b) Stress ratio vs deviatoric strain.

Figure 5.6: Combined influence of small stress levels and surface energy forces at very small strains (JKR model, $\gamma = 0.07\text{J/m}^2$).

of the (q, ϵ_a) curves, is found in the range between 200MPa and 500MPa (increasing as p increases) for the tests run without adhesion. Higher values of E, ranging from 600MPa to 800MPa, are obtained with surface energy forces. We conclude that the presence of adhesion has the effect to increase the small-strains Young's modulus. This may be explained by the fact that adhesion has a strong influence on particle arrangement and on the contact network (as will be shown later) which in turn appears to result in higher shear strength (see Table 5.2) and greater soil stiffness. Small-strain elastic constants were computed in the range of 50MPa to 200MPa for lunar soil simulant JSC-1 (with a PSD similar to that of lunar soil) by means of triaxial tests run at low confining pressures ($p < 100$kPa) and high relative densities (up to 95%) (Klosky et al., 2000). These findings were compared with experimental observations obtained for normal sand and indicated that lunar soil simulant JSC-1 has higher elastic soil stiffness than normal sand, which supports the trend shown in this study.

It can also be noted that the peak strength occurs at slightly larger strains as the stress level increases. Moreover, peaks occur almost instantly once the deviatoric load is applied, due to the very small stress levels. This holds particularly true for the tests carried out with surface energy forces (see Fig. 5.6(a)). The exact details of the calculations in terms of both stresses and strains at which peak failure occurs are reported in Table 5.2. A similar trend

was observed by Sture et al. (1998), who found that samples tested at less than 1kPa showed an unusually high initial soil stiffness and peak strength occurring at very small strain levels.

$\gamma = 0.00\text{J/m}^2$, $\dot{\epsilon} = 2 \times 10^{-5}$			$\gamma = 0.07\text{J/m}^2$, $\dot{\epsilon} = 2 \times 10^{-5}$		
p (kPa)	q_{max} (kPa)	$\epsilon_1 - \epsilon_3$ (%)	p (kPa)	q_{max} (kPa)	$\epsilon_1 - \epsilon_3$ (%)
1	1.60	0.007	1	22	0.004
2	3.10	0.013	2	24.2	0.004
5	7.60	0.043	5	28.6	0.005
10	15.00	0.044	10	35.1	0.006

Table 5.2: Peak state results from triaxial compression tests at small stress levels, with and without adhesion.

Plotting the stress ratio versus deviatoric strain highlights the fact that with surface energy the peak strength ratio increases as the stress level decreases, as shown in Fig. 5.6(b). While on the other hand, in the absence of adhesion, the effect of confining pressure on the peak of the stress ratio turns out to be negligible (see Fig. 5.5(b)).

It is also of interest to investigate the combined effect of stress level and surface energy on the volumetric behaviour and dilatancy of the soil. Dilatancy can be computed following the most common definition used in soil mechanics, which, for triaxial state conditions, reads:

$$d = \sin(\psi) = \frac{(\dot{\epsilon_1} + \dot{\epsilon_2} + \dot{\epsilon_3})}{(\dot{\epsilon_1} - \dot{\epsilon_3})} \quad , \tag{5.2}$$

where ψ is the dilatancy angle with ϵ_1 and ϵ_3 the principal major and minor strain. The dilatancy and corresponding volumetric behaviour of samples sheared with and without adhesion, are illustrated in Fig. 5.7 and 5.8. Note that to compute dilatancy, the volumetric curves were first interpolated using the method of least squares linear regression; following that, $\sin\psi$ was computed according to Eq. 5.2. Interpolation of the numerical data was necessary in order reduce the scattering of the results.

In the range of confining pressure between 1 and 10kPa, the maximum dilatancy for assemblies of non-adhesive grains seems unaffected by the stress level, which is in agreement with the previous observations of peak stress ratio being insensitive to pressure (see Fig. 5.7). Instead, with adhesion the maximum dilatancy turns out to increase with confining pressure

decreasing, as illustrated in Fig. 5.8. Note that for the tests with surface energy the maximum dilatancy angle ψ_{max} cannot be computed since the maximum (absolute) value of $\sin\phi$ is higher than 1 (see Fig. 5.8). This proves to be consistent with the fact that the peak friction angle corresponding to each single test (*i.e.* the secant value of the friction angle, see Fig. 5.16) cannot be evaluated, as will be discussed later in Sec. 5.3.5. For cohesionless soils, the maximum dilatancy has been generally associated with the peak friction angle (Bolton, 1986). However, this relationship is intrinsic to the definition of friction angle which is different for cohesive and cohesionless materials.

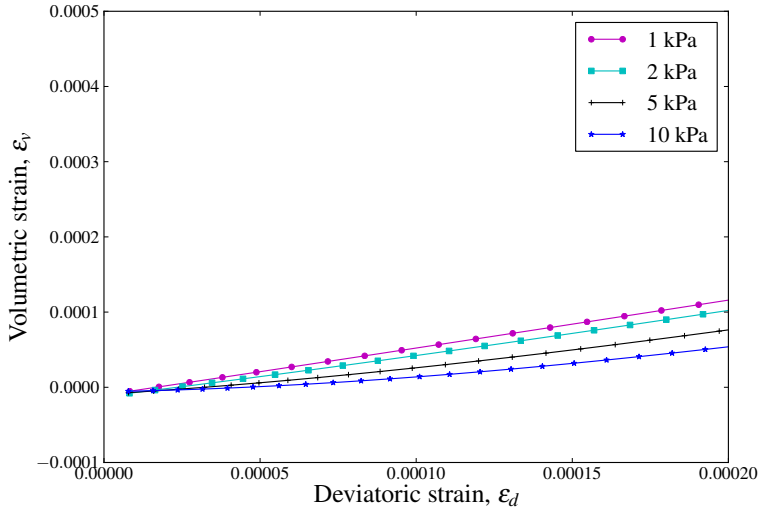

(a) Volumetric behaviour at small strains.

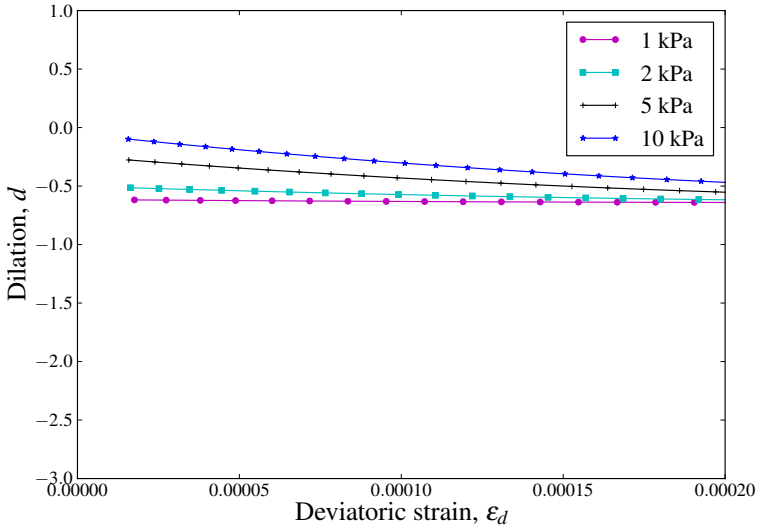

(b) Behaviour of dilatancy.

Figure 5.7: Detail of the volumetric behaviour and dilatancy at very small strains without surface energy forces (HM model).

Finally, let us examine the influence of pressure and surface energy on the mechanical

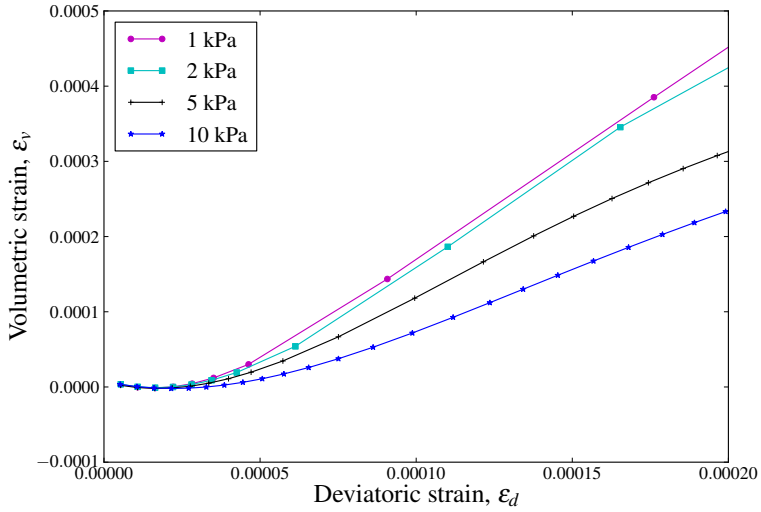

(a) Volumetric behaviour at small strains.

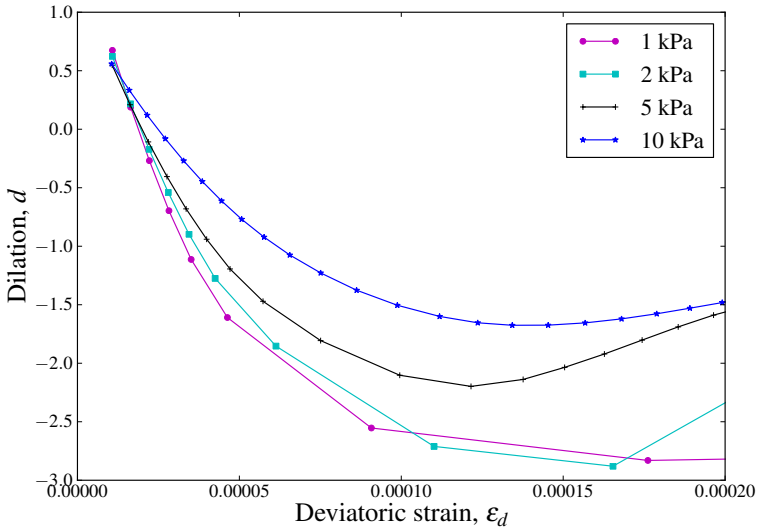

(b) Behaviour of dilatancy.

Figure 5.8: Detail of the volumetric behaviour and dilatancy at very small strains with surface energy forces (JKR model, $\gamma = 0.07\text{J/m}^2$).

coordination number Z_m at small strains. This is illustrated in Fig. 5.9 both with and without adhesion. At the peak state of the material the presence of surface energy leads to a slightly higher coordination number, which is in contrast with the higher porosity obtained with adhesion, as will be discussed later (see Fig. 5.12). This tendency, however, is in close agreement with the experimental observations reported in Nelson and Vey (1968) where the effect of vacuum was found responsible for the increase of soil porosity and the formation of clusters (which may explain the present increase in Z_m).

Without surface energy, increasing the confining pressure causes an increase of the me-

chanical coordination number as observed in Fig. 5.9(a). This is an expected result and is in agreement with previous numerical findings (e.g. Agnolin and Roux, 2008). On the other hand, the influence of pressure on Z_m is less pronounced in the presence of attractive adhesive forces than without them (see Fig. 5.9(b)). Furthermore, Z_m is found to be higher in the presence of adhesion only for $p \leq 5$kPa. This indicates that the combined influence of surface energy and pressure on state variables of micro-mechanical origin (such as the coordination number) is non-negligible and that the effect of surface energy is visible only at vey low pressures.

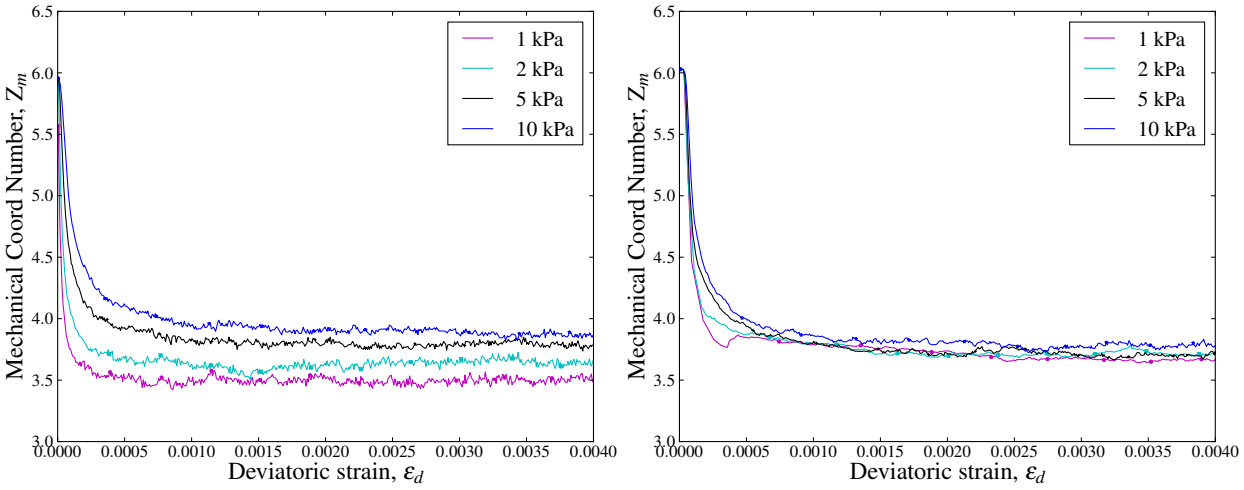

(a) HM model.

(b) JKR model (γ=0.07J/m^2).

Figure 5.9: Influence of surface energy and confining pressure on the mechanical coordination number at very small strains.

5.3.4 Soil behaviour at very large strains

The samples were subsequently sheared up to very large strains, until conditions of critical state were achieved. First, the results obtained with the HM contact model will be analysed. The influence of confining pressure on the stress-strain behaviour is illustrated in Fig. 5.10(a).

It can be observed that in the post-peak behaviour, the samples exhibit significant softening up to the critical state, where the deviatoric stress approximately reaches a constant value, which increases with confining pressure. It is also interesting to note that fluctuations

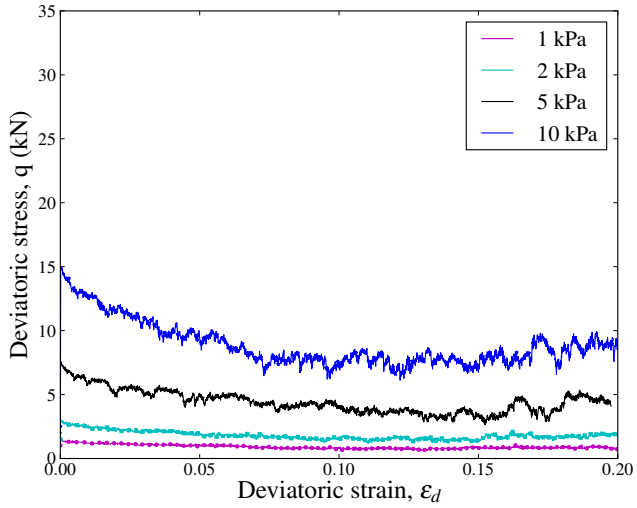

(a) HM model.

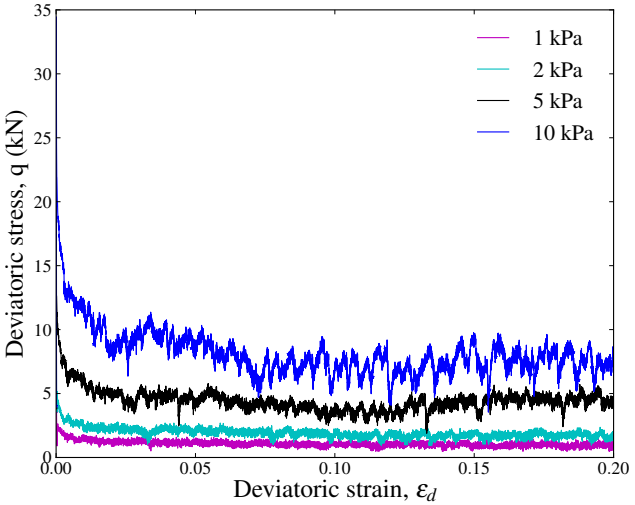

(b) JKR model ($\gamma = 0.07\text{J/m}^2$).

Figure 5.10: Influence of confining pressure on the stress-strain behaviour of the soil sheared up to very large strains, with and without surface energy forces.

in the macroscopic response become larger as stress level increases (see Fig. 5.10(a)). The presence of these oscillations may have a dual origin. On one hand, they are due to the discrete nature of the system, as already pointed out in Chapter 4. While on the other, they could be amplified by the effects of local instabilities produced by the so-called stick-slip behaviour, typical of samples sheared at relatively small strain rate (Evesque and Adjemian, 2002; Alshibli and Roussel, 2006). The wide PSD used in this study may also have the effect of increasing the amount of oscillations characterising the stress-strain behaviour, as laboratory experiments of glass beads have previously demonstrated, although for much higher pressures up to 200kPa (Alshibli and Roussel, 2006). Note that a stick-slip behaviour was

also observed for a quartz Ottawa sand tested at very low effective pressures during a US space shuttle mission (Sture et al., 1998). However, a quantitative comparison with the present data is not possible since in that paper a very uniform gradation was employed.

The macroscopic stress-strain behaviour obtained for various confining pressures, in the presence of surface energy forces, is illustrated in Fig. 5.10(b). Increasing the stress level also results in increased deviatoric stress and increased fluctuations of the response. However, both the frequency and amplitude of the oscillations appear accentuated with adhesion.

At a given stress level, tests conducted with surface energy forces present a higher peak shear strength than when the HM model is employed (see Fig. 5.10(b) and 5.10(a)). At the critical state, however, only a little increase in the deviatoric load can be detected due to adhesion. After the peak, a sudden loss of strength in the softening regime occurs for the tests with surface energy forces, revealing a behaviour typical of brittle soils. Similarly, Bromwell (1966) reported a significant increase in peak friction angle associated with a sudden failure, when running shear box experiments of Ottawa sand under UHV and elevated temperatures. This behaviour was attributed to the catastrophic collapse of columns of particles previously bonded together (Bromwell, 1966). A detailed analysis of the values of peak and critical state friction angles derived from the current tests will be presented in the next section.

The volumetric behaviour up to large strain levels is illustrated in Fig. 5.11, with and without surface energy forces. A behaviour typical of a dense sample is exhibited in both cases.

It can be observed that without adhesion, the total volumetric deformation at the critical state appears to slightly increase as the pressure decreases (see Fig. 5.11(a)), in agreement with the principles of soil mechanics. A similar but more remarkable tendency is experienced by the samples tested with surface energy forces. Fig. 5.11(b) illustrates that the critical volumetric deformation decreases significantly as confining pressure increases. This could be explained by the fact that adhesion allows the formation of a very porous structure. This tendency, however, is affected by the relative importance of the applied load and the level of surface energy. It is also worth pointing out that the condition of constant volume is

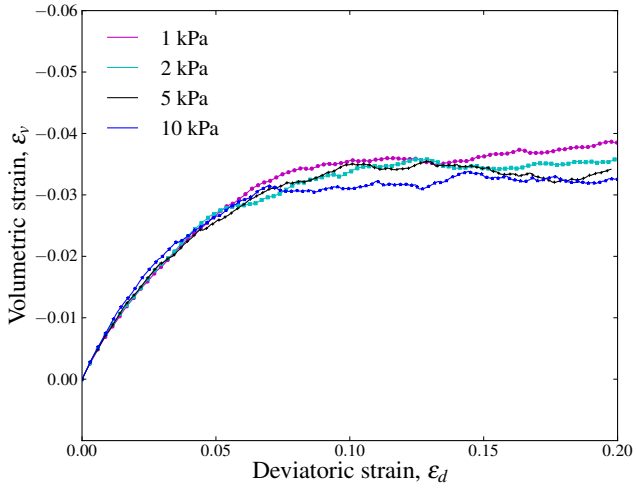

(a) HM model ($\gamma = 0.00\text{J/m}^2$).

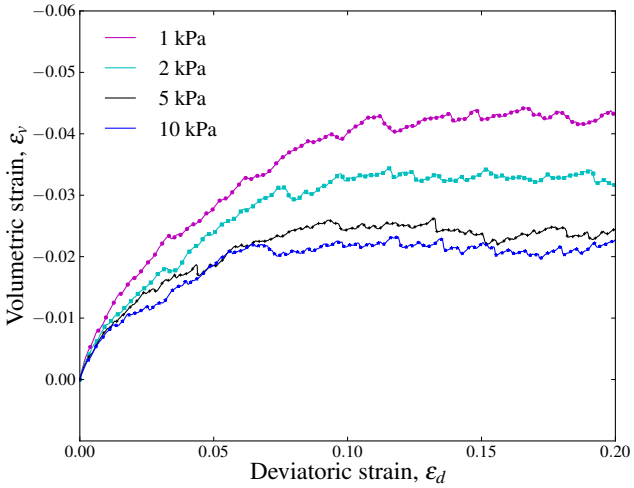

(b) JKR model ($\gamma = 0.07\text{J/m}^2$).

Figure 5.11: Influence of confining pressure and surface energy forces on the volumetric behaviour sheared up to very large strains, with and without adhesion.

achieved at strains larger than 15%, both with and without adhesion. Finally, it is interesting to note that volume changes are found higher for tests run with adhesion although only for $p \leq 2$kPa (see Fig. 5.11). This indicates that a threshold of confining pressure (in this case equal to 2kPa) can be identified. At stresses higher than this the influence of pressure on the volumetric behaviour becomes opposite when comparing tests with and without adhesion (Fig. 5.11). This finding confirms that a strong interplay exists between confining pressure and surface energy forces, although a rigorous explanation for the inverse trend observed in terms of volumetric changes could not be identified.

The porosity of the numerical ensembles is illustrated in Fig. 5.12. All samples show

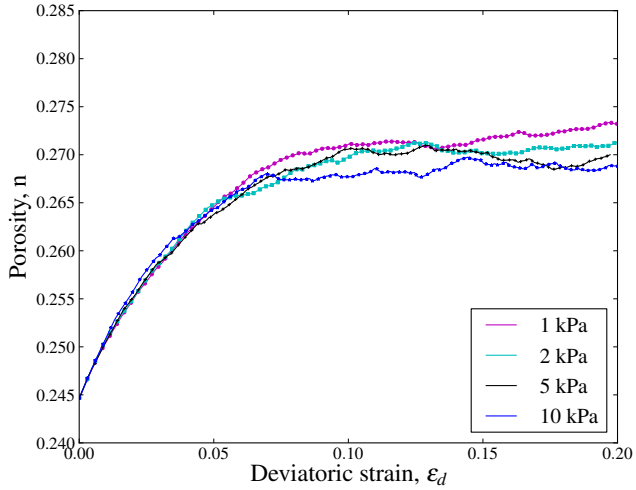

(a) HM model ($\gamma = 0.00\text{J/m}^2$).

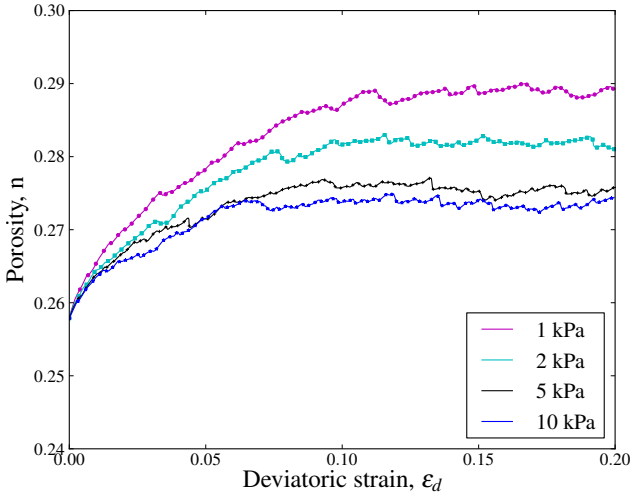

(b) JKR model ($\gamma = 0.07\text{J/m}^2$).

Figure 5.12: Influence of confining pressure and surface energy forces on the macroscopic porosity computed at large strains.

pronounced dilatant behaviour. In addition, it can be noted that the initial porosity is significantly higher for samples prepared under the effects of attractive forces (Fig. 5.12). The different initial porosity (or likewise density) is an indication of the strong influence that attractive forces have on particle rearrangement.

In terms of critical state porosity, this is very similar for the tests run using the HM model, regardless of the confining pressure (see Fig. 5.12(a)). However, the critical porosity tends to be smaller with increasing pressure when modelling adhesive particles, as shown in Fig. 5.12(b). This can be related to the fact that the influence of adhesion is relative to the stress level.

The tendency of porosity to increase under the effects of UHV was previously observed experimentally by Nelson and Vey (1968) for very fine soils ($D_{60} < 20\mu$m). The experiments consisted in the deposition of very fine sand under various vacuum levels. It was found that the soil porosity increased with higher vacuum, although the amount of this increase was a function of mineralogy. This behaviour was attributed to the formation of clusters, owing to the development of strong interparticle bonds (Nelson and Vey, 1968). The nature of these forces, however, could not be identified. On the other hand, the present results suggest that vdW interactions could be responsible for this phenomenon.

Finally, the mechanical coordination number Z_m (see Sec. 4.8) is plotted versus the deviatoric strain in Fig. 5.13. It can be seen that the mechanical coordination number slightly increases with the presence of surface energy forces, which might be attributed to the formation of clusters.

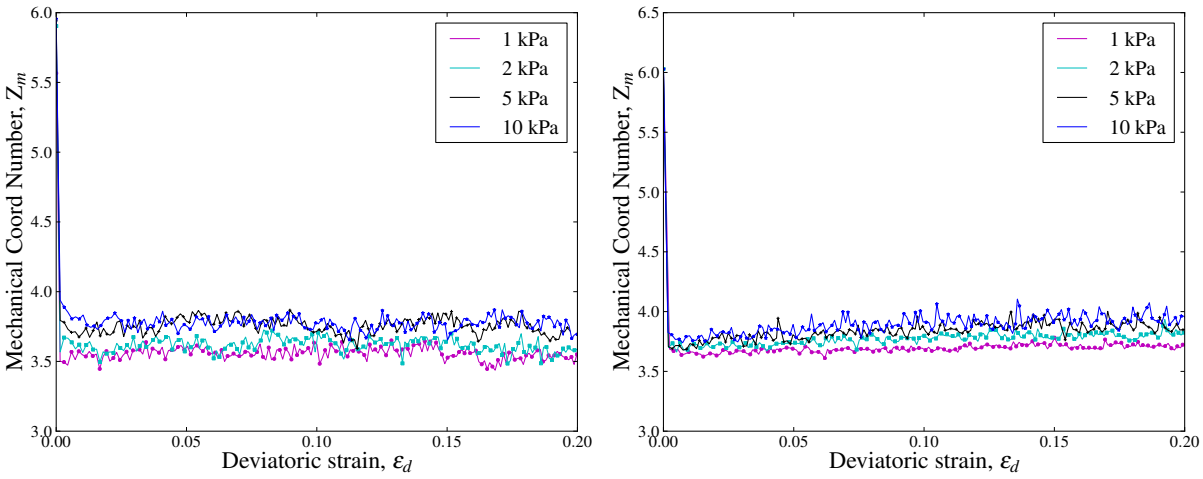

(a) HM model ($\gamma = 0.00\text{J/m}^2$). (b) JKR model ($\gamma = 0.07\text{J/m}^2$).

Figure 5.13: Influence of confining pressure and surface energy forces on the mechanical coordination number, Z_m, up to large strains.

5.3.5 The relationship between surface energy and shear strength parameters

It is of fundamental importance to identify the relationship existing between surface energy and the soil shear strength parameters. This knowledge will assist with the physical

interpretation of the numerical results in light of the shear strength estimated for lunar soil.

Triaxial tests at constant mean stress level ranging from 0.1 to about 10kPa, were run for four increasing values of surface energy: 0.0, 0.02, 0.07 and 0.14J/m^2 respectively. The salient points of the tests are illustrated on the (q, p) plane in Fig. 5.14, both at the peak and critical states.

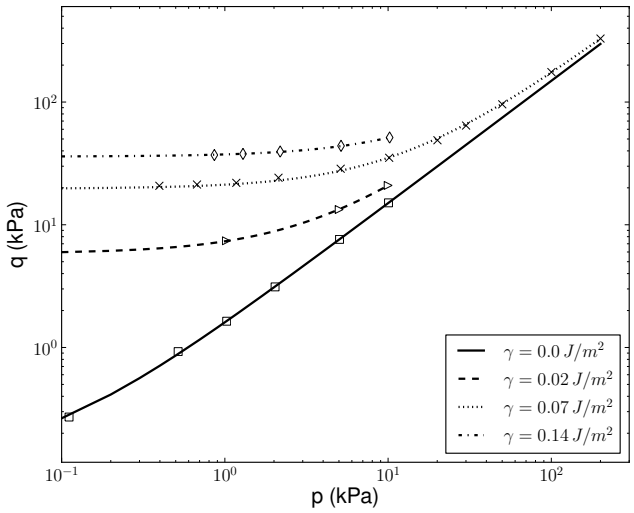

(a) Peak state.

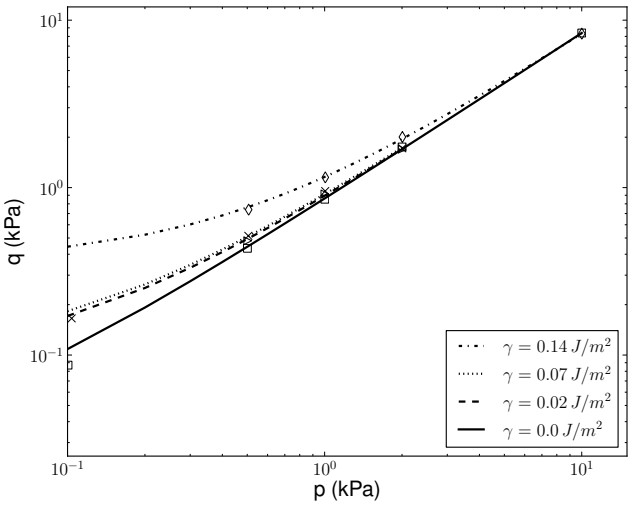

(b) Critical state.

Figure 5.14: Influence of surface energy on the macroscopic behaviour at the peak and critical state under very small confining stresses ($p \leq 10$kPa). A log-log scale is used in this case for better visualisation of the results.

The corresponding results in terms of macroscopic soil friction angle and cohesion for each value of γ are also reported in Table 5.3. In particular, the peak strength results indicate that an approximately linear relationship exists between the input surface energy parameter,

γ (J/m^2)	ϕ_{ps} (°)	ϕ_{cs} (°)	c$_{ps}$ (kPa)	c$_{cs}$ (kPa)
0.00	36	22	0.00	0.00
0.02	36	21	2.98	0.04
0.07	36	21	10.18	0.05
0.14	36	21	17.85	0.14

Table 5.3: Peak and critical state parameters in terms of macroscopic friction angle and cohesion (tangent parameters computed for $p \leq 10$kPa).

of microscopic origin, and the output macroscopic cohesion, as Fig. 5.15 illustrates.

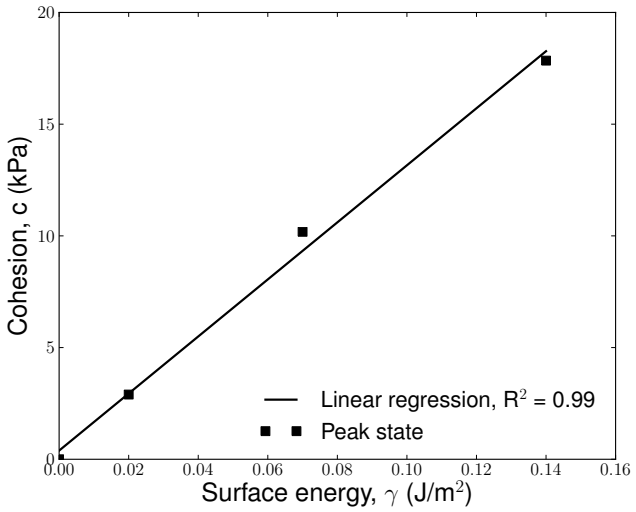

Figure 5.15: Relationship between the macroscopic cohesion c and the surface energy γ obtained by means of linear regression analysis. The relationship can be considered valid only within the range of pressures examined ($p \leq 10$kPa).

The values of the strength parameters were computed under the assumption of a linear Mohr-Coulomb (MC) failure criterion. In this case, the soil friction angle is a function of the gradient M of the line of best fit to the failure points on the (q, p) plane, according to (Schofield and Wroth, 1968):

$$M = \frac{6\sin(\phi)}{3-\sin(\phi)} \quad \Rightarrow \quad \phi = \arcsin\left(\frac{3M}{M+6}\right) \quad . \tag{5.3}$$

The soil cohesion, on the other hand, is linked to both the gradient and the intercept i with

the vertical axis of the failure line, such that:

$$i = \frac{c}{\tan(\phi)} \frac{6\sin(\phi)}{3-\sin(\phi)} \quad \Rightarrow \quad c = i\,\frac{3-\sin(\phi)}{6\cos(\phi)} \quad . \tag{5.4}$$

The values of ϕ and c correspond to the mathematical parameters of the MC failure line $\tau = c + \tan(\phi)$, which is a suitable model for frictional-cohesive soils. The cohesion parameter is generally regarded as an apparent cohesion when it lacks a clear physical meaning. In the present case, however, cohesion derives from the presence of adhesion generated by vdW interactions. Thus the cohesion obtained from the numerical simulations can be regarded here as a real cohesion, in the sense that it derives from the physical conditions to which the samples are subjected.

It is also important to emphasise that in this work friction angles are derived as tangent parameters, and not as secant values obtained from each single triaxial test. The distinction between tangent and secant parameters is made clear in Fig. 5.16. It is understood that the

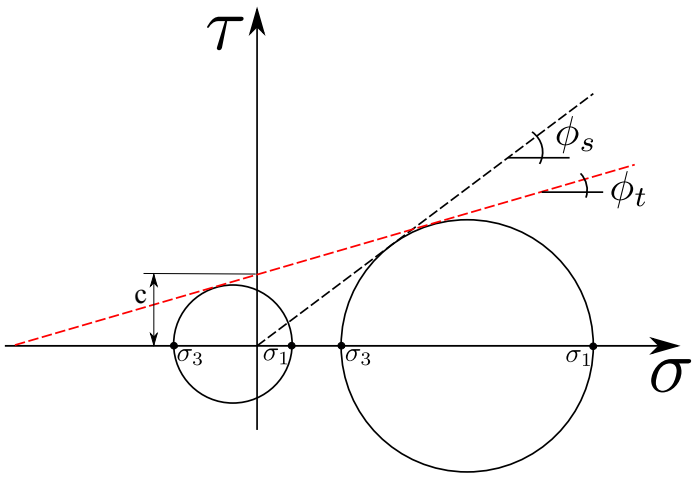

Figure 5.16: MC circles at the point of failure plotted on the MC plane using the maximum and minimum principle stresses σ_1 and σ_3. The figure illustrates that a secant friction angle can be obtained by drawing a line passing through the origin and tangent to each single MC circle, while a tangent friction angle corresponds to the slope of the line tangent to two or more MC circles from simulations run at different stress levels. Note that the cohesion parameter can only be computed when a tangent friction angle is sought (see Eq. 5.4).

computation of a secant friction angle becomes meaningless for cohesive soils, since the MC circle corresponding to the failure point at the peak state of the material can extend up to the tensile range of normal stresses. In order to clarify this point, Fig. 5.17 illustrates the

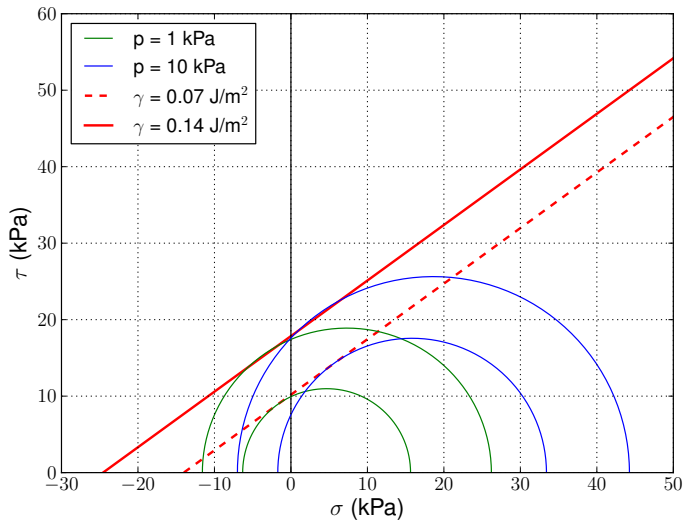

Figure 5.17: MC circles drawn for mean stresses of 1 and 10kPa, and two values of surface energy of 0.07 and 0.14J/m^2. It can be noted that the minimum principal stress, σ_3, is negative for the MC circles corresponding to 1kPa of confining pressure.

MC circles drawn for mean stresses of 1 and 10kPa, and two values of surface energy, 0.07 and 0.14J/m^2. It can be observed that the minimum principal stress, σ_3, is negative for all the tests with adhesion, making it impossible to draw a tangent line to the single circle while passing through the origin. Therefore, the value of friction angle, tangent to the MC circles, are computed for each prescribed value of γ rather than for a single test.

Referring back to the macroscopic observations illustrated in Fig. 5.14, we note that a log-log scale was preferred in order to make the visualisation of the results easier. It appears that the strength envelopes on the (q, p) plane are linear both at the critical and peak states, when computed for the pressure range examined. In order to verify the accuracy of this observation, the MC circles corresponding to the peak state of the material (where γ has a more significant effect) are plotted in Fig. 5.18 for various confining pressures ranging from 1 to 10kPa and $\gamma = 0.07$J/m^2. The strength criterion is represented by the curve that is tangential to the MC circles at failure. Two lines of best fit, a linear and non-linear one, were found using linear regression analysis, as illustrated in Fig. 5.18. The linear relationship coincides with the MC law from which the (tangent) parameters c and ϕ can be obtained as previously discussed. The non-linear relationship adopted in the analysis has the form of the model proposed by Hoek and Brown (1980) which was originally introduced to represent the strength of rock masses. A generalised form of this criterion, expressed on the Mohr plane,

which will be referred to as HB criterion, was presented in Baker (2004):

$$\tau = P_a A \left(\frac{\sigma}{P_a} + T \right)^n \quad , \tag{5.5}$$

where P_a is the atmospheric pressure and (A, n, T) a series of dimensionless physical parameters which depend on the type of material. In particular, T is the non-dimensional tensile strength which determines the intersection of the failure line on the horizontal axis (Baker, 2004). The best fit of Eq. 5.5 to the numerical data is obtained with $A = 0.4$, $n = 0.5$ and $T = 0.07$ (see Fig. 5.18). The coefficients of determination for the MC and HB criterion, which were found equal to 0.94 and 0.98 respectively, indicate that both models are applicable, with the HB criterion performing only slightly better than the linear case. Hence, the linear failure criterion can be considered a sensible choice for the range of pressure examined. Note that for design purposes, the adoption of the MC criterion makes the choice of the strength parameters a lot easier since they (c and ϕ) are both independent of the stress level over the range of interest.

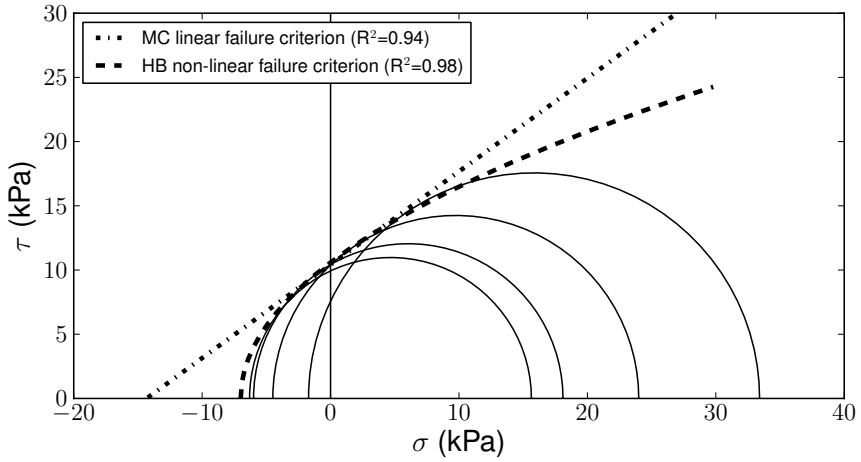

Figure 5.18: MC circles corresponding to the peak states of the material obtained from tests run at various confining pressures ranging from 1 to 10kPa and $\gamma = 0.07\text{J/m}^2$. The linear MC criterion is compared against the non-linear HB criterion (Hoek and Brown, 1980). Both relationship were best fitted to the data using linear regression analysis.

By examining the results of Fig. 5.14 we also note that the effect of adhesion on the soil shear strength reduces with the increase of pressure, until the influence becomes almost nil at confining stresses higher than 100kPa for the peak and 10kPa for the critical state

(see Fig. 5.14). This result can be due to the fact that the micro-mechanical contact model used in this investigation predicts the maximum pull-off force independently of the external applied load. In other words, particles can only deform elastically, while assuming a constant adhesion force (see Chapter 3). It seems unreasonable to think that at such small pressures (that are typical of the lunar soil), plastic deformations play any significant role, which is the primary reason why their influence has not been accounted for in the current study.

Furthermore, it is very important to observe that the presence of adhesion only influences the cohesive contribution to the soil shear strength (and not the frictional contribution), and predominantly at the peak state of the material. Very little cohesion is observed at the critical state, although the cohesion that is present increases with surface energy (see Table 5.3).

It is worth recalling that the present findings are not only a function of the employed contact model but also of the simplified spherical particle shape adopted in the simulations. We will focus later on the combined study of particle shape effects and vdW attractive forces (see Sec. 5.4).

Note that the contact model employed in the tests above is in contrast with the model for lunar soil employed by Chang and Hicher (2009), where the adhesion force was defined as a function of the contact area and thus pressure (but without accounting for plastic deformations). In fact, the model proposed by Chang and Hicher (2009) is based on the Dahneke solution (Dahneke, 1970) to model the effects of vdW forces, which was proven to be wrong by Derjaguin et al. (1975).

It should also be noted that the values of friction angle obtained from the numerical tests and reported in Table 5.3, are far from the realistic values obtained from direct and indirect strength measurements for real lunar soil. These were found to be in the range between 30 to 50° (see Chapter 2). The reason is well known and is because the interlocking between particles due to particle shape effects is completely disregarded when spherical particles are employed. The influence of particle shape with and without surface energy will be addressed in the next section.

Finally, it is worth drawing attention to the remarkable similarity between the present results, obtained with surface energy forces, and the macroscopic behaviour of cemented sand. Cemented sands are above all characterised by a bonded material, in which bonds are of chemical origin (e.g. Poul and Daniel, 1989; Wang and Leung, 2008; Jiang et al., 2011). Experimental results of drained triaxial compression tests on Ottawa sand prepared with different proportions of cement content, have shown that the peak cohesion increases significantly in the presence of cement, whereas this affects friction only slightly (Wang and Leung, 2008). At the critical state, on the other hand, friction angle still increases with increasing cement content but no cohesion is observed at all because the majority of cementing bonds are destroyed at large strains (Wang and Leung, 2008). Enhanced dilatancy and brittle post-failure behaviour are also typical of cemented soils (Poul and Daniel, 1989). Moreover, by means of 2D DEM simulations, Jiang et al. (2011) reported that for cemented sands higher shear strength and a more pronounced strain-softening behaviour are not only dependent on the cement content but can also be induced by a reduction of the stress level.

Notwithstanding the correspondence between the above observations and the behaviour of adhesive particles presented so far in this chapter, we recall that the chemical bonds due to surface energy forces can form again once destroyed, whereas the bonds due to the cement content can only form once. The current comparison, however, suggests that the soil behaviour under UHV shares similar characteristics to that of cemented sands, primarily due to the presence of chemical bonds, although of very different physical origin.

The percentage of adhesive contacts, *i.e.* the contacts which experience a tensile force (negative in sign, according to the convention adopted in this thesis), can be easily computed in a DEM analysis. The ratio between the number of adhesive contacts and the total number of contacts was computed for tests run with increasing γ and at the constant mean confining pressure of 1kPa. The result of the comparison at very small strains is shown in Fig. 5.19(a).

It can be observed that the percentage of adhesive contacts increases with surface energy and reaches a peak value at the same time as the peak deviatoric stress, Fig. 5.19(b).

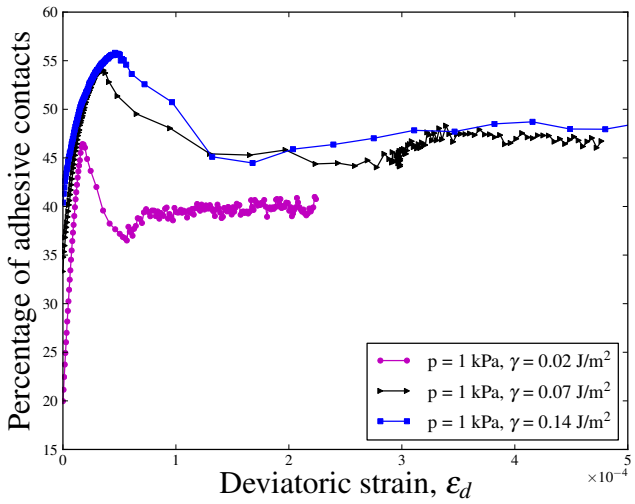

(a) Percentage of adhesive contacts at very small strains for different values of γ.

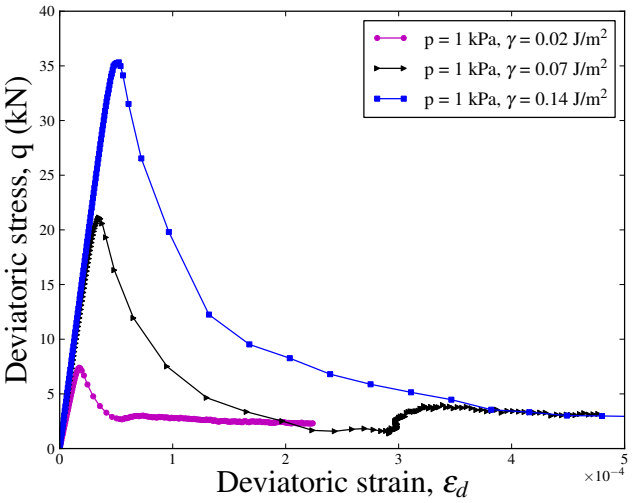

(b) Stress-strain behaviour at very small strains for different values of γ.

Figure 5.19: Effect of γ on the percentage of adhesive contacts (Fig. 5.19(a)) and the maximum deviatoric stress occurring at small strains (Fig. 5.19(b)).

This finding confirms the fact that the increase in shear strength is effectively linked to the presence of interparticle attractive forces, which become more significant for increasing interface energy (Fig. 5.19(a)). Soon after the peak is reached, the percentage of adhesive contacts becomes constant. Moreover, the percentage of adhesive contacts at the critical state increases with γ (Fig. 5.20).

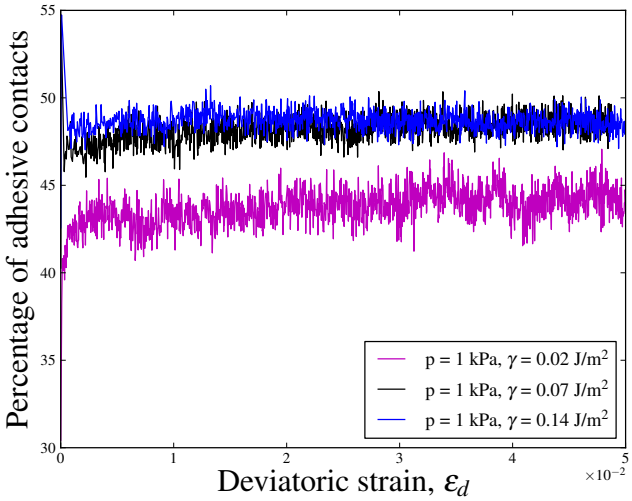

Figure 5.20: Percentage of adhesive contacts for increasing surface energy up to the critical state and under 1kPa of mean stress level.

5.3.5.1 Effect of surface energy on soil dilatancy

In this section, the influence of surface energy on soil dilatancy will be briefly examined. Soil dilatancy is an important feature of soil behaviour. According to Rowe (1962), the shear strength of granular materials is due to three contributions: the interparticle friction angle, particle rearrangement and soil dilatancy. These contributions are interdependent: firstly because soil dilatancy is determined by the degree of freedom that particles have to rearrange, and secondly because the occurrence of dilatancy has been shown to disappear when modelling frictionless grains subject to shear (Peyneau and Roux, 2008).

The fact that the microscopic friction angle is not solely responsible for soil shear strength was confirmed by the 3D simulations discussed in Thornton and Antony (2000). In the paper, the authors pointed out that shear strength does not indefinitely increase with contact friction angle, but that a maximum threshold can be identified.

In the current investigation, a constant friction coefficient was maintained, in order to allow the influence of surface energy on soil dilatancy to be studied in detail. The increase in soil dilatancy due to surface energy is remarkable, as illustrated in Fig. 5.21. The influence of γ is shown in Fig. 5.21, Fig. 5.22 and Fig. 5.23 in terms of volumetric deformations, macroscopic porosity and mechanical coordination number respectively. A higher porosity and a higher coordination number are both indicators of the strong influence played by the

adhesion forces at the microstructural level.

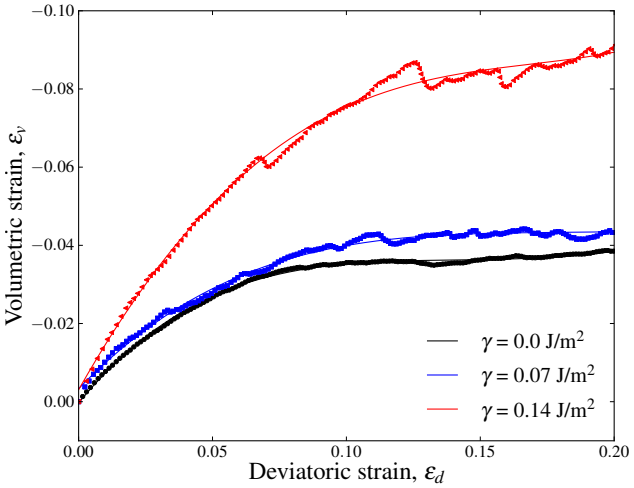

Figure 5.21: Effect of surface energy forces on soil dilatancy. The volumetric behaviour is captured for three values of surface energy, $\gamma = 0.0$, 0.07 and 0.14J/m^2 respectively, and 1kPa of confining pressure. Linear regression analysis is used to calculate a best fit to the numerical data.

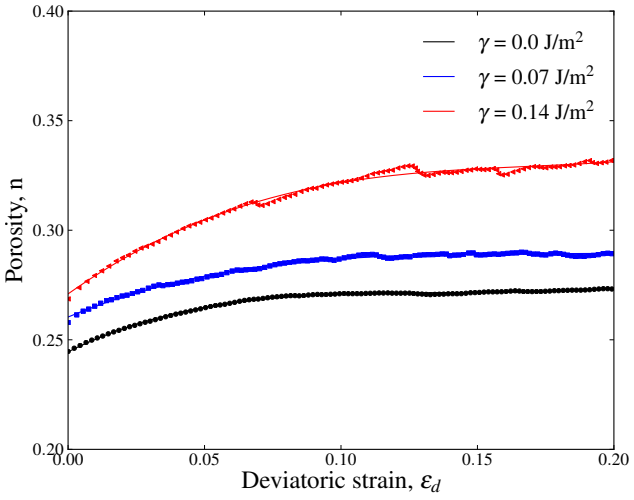

Figure 5.22: Effect of surface energy forces on the macroscopic porosity at the confining pressure of p = 1kPa.

5.4 Combined study of particle shape effects and surface energy forces

The influence of particle shape on the shear strength of granular materials has been extensively investigated in the literature (Hart et al., 1988; Rothenburg and Bathurst, 1993;

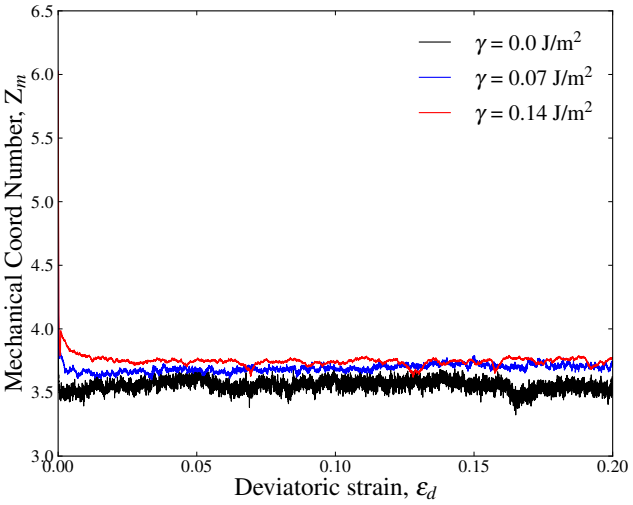

Figure 5.23: Effect of surface energy forces on the mechanical coordination number at the confining pressure of p = 1kPa.

Santamarina and Cho, 2004; Cho et al., 2006; Estrada et al., 2008; Lee et al., 2012; Shamsi and Mirghasemi, 2012). It is now well known that the use of spherical particles in DEM experiments produces macroscopic friction angles which are not typical of sand. It has also been demonstrated that particle shape effects not only have an influence on soil shear strength, but also on other important state variables, such as density, dilation, coordination number, particle rearrangement, soil fabric and anisotropy (e.g. Cho et al., 2006; Peña et al., 2007).

There are several ways to model non-spherical particle shapes using DEM. The simplest method from a conceptual point of view is to use clusters of particles (clumps) in which spheres are often rigidly connected to each other to form a single body of non-convex shape (Lane et al., 2010). Other particle shapes, modelled by DEM, include ellipsoids and superquadratic surfaces. The latter, in particular, can be adapted to produce arbitrary shapes and polyhedral particles (Lane et al., 2010).

The ability of DEM to model non-spherical particles is limited by the available amount of computational power, and also by the efficiency of complex contact detection algorithms. It is currently not computationally affordable to combine the modelling of irregular particle shapes, using any of the aforementioned methods, with the relatively complex contact model for lunar soil used in this thesis.

Nevertheless, it is important to make an effort towards a more realistic modelling of lunar soil by accounting for the effects of irregular particle shapes, similar to those characterising the real lunar grains (Rickman et al., 2012; Walton, 2010; Matsushima et al., 2009).

In the following, two viable solutions will be explored. The aim is not only to obtain more realistic results in terms of lunar soil shear strength, but also to provide insight into the underlying microstructural phenomena behind the macroscopic response of irregular adhesive particles.

At first, interparticle rolling resistance will be added to the HM and JKR contact models. Secondly, simple particle shape models, formed by spherical grains rigidly clumped together, will be considered. Macroscopic results will be analysed in both cases and conclusions will be drawn based on the comparison with the best estimates for the lunar soil shear strength (see Chapter 2).

5.4.1 Interparticle rolling resistance to simulate particle shape effects

The use of interparticle rolling resistance in DEM modelling was initially introduced to investigate strain localisations in sheared granular materials, since it was realised that impeding the rotation of the grains produced a closer match with the observed experimental behaviour (Iwashita and Oda, 1998). However, the method is now frequently adopted as an attempt to reproduce the shear strength of granular materials and study the influence of particle shape on the macroscopic response (Estrada et al., 2008; Mohamed and Gutierrez, 2010; Estrada et al., 2011).

A rolling resistance model will be used in this study to account for the interlocking of irregular shaped grains in lunar soil. In the case of adhesive particles, it can be argued that surface energy forces are responsible for some rolling resistance, as discussed in Dominik and Tielens (1995). This type of rolling resistance will be neglected in the following investigation because the underlying JKR contact model predicts a symmetric contact stress distribution,

which in principle does not allow for contact moments to be generated.

The research on the effects of interparticle rolling resistance in granular media has taken two distinct directions: on one hand, contact models with rolling resistance are often introduced to describe a more realistic contact behaviour, such as the case for cemented soils (Jiang et al., 2006); on the other hand, rolling resistance is being employed to mimic the particle interlocking due to highly non-spherical particle shapes (Plassiard et al., 2009). The latter is the type of model simulated in this study, as described below.

The rolling resistance model used in this work falls into the category of elastic-plastic spring models, following the classification presented in Ai et al. (2011). Contact models belonging to this category have been described as providing stable torques and satisfying equilibrium in comparison to other solutions.

The origin of a rolling contact moment exerted between two non-spherical bodies derives from the fact that the contact point is no longer found in line with the direction of the normal contact force. The eccentricity between the normal contact force and the centre of mass of the contacting particles gives rise to an overturning moment, as schematically drawn in Fig. 5.24. Therefore a rolling stiffness, k_r, is added to the contact model and a simple

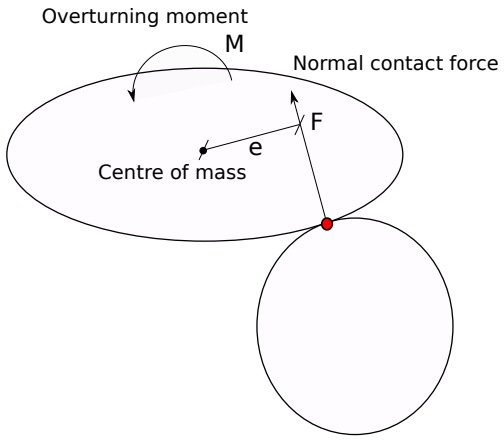

Figure 5.24: Rolling moment generated due to the interaction of non-spherical particles.

linear relationship is defined between the contact moment and the relative rotation between the two contacting particles (see Eq. 5.9). The rolling resistance model was implemented in

Yade by the author. A description of the algorithm adopted is given in Bourrier et al. (2013). The total relative rotation, $\vec{\theta}$, of two contacting particles is first computed in an incremental fashion. This is then used to define torsional and rolling contributions, calculated respectively as (Bourrier et al., 2013):

$$\vec{\theta_t} = (\vec{\theta} \cdot \vec{n})\vec{n} \quad , \tag{5.6}$$

$$\vec{\theta_r} = (\vec{\theta} - \vec{\theta_t}) \quad , \tag{5.7}$$

where $\vec{n}$ is the unitary vector defining the contact normal. The torsional moment is disregarded while the bending moment is finally computed as:

$$\vec{M_r} = k_r\vec{\theta_r} = \beta k_s R^2 \vec{\theta_r} \quad , \tag{5.8}$$

$$\tag{5.9}$$

where β is a dimensionless parameter. The maximum rolling moment that can be exchanged between two particles is then limited by the normal contact force, P, in a form equivalent to the MC criterion, according to (see Fig. 5.25):

$$M_r \leq M_{max} = |P| R\eta \quad , \tag{5.10}$$

where η is another dimensionless parameter.

The dimensionless parameters η and β will be calibrated against the macroscopic shear strength parameters. A calibration procedure is required because the introduction of rolling resistance artificially accounts for particle shape. Note that the rolling stiffness k_r is purely expressed as a function of k_s for convenience (Eq. 5.8). Furthermore, the parameter β will be kept equal to 1 to reduce the number of variables in the analysis, whilst a parametric analysis will be run to assess the influence of η in isolation. As previously said, the parameter η dictates the maximum moment that can be sustained between two particles due to rolling resistance. Once this limit is achieved, free rolling can occur between the particles. Thus it can be stated that η is the key parameter which dictates the strength of the material, as

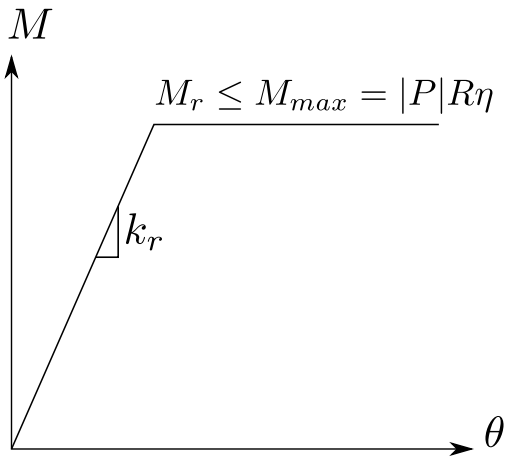

Figure 5.25: Moment-relative rotation contact relationship (note that the relationship is linear only if the normal contact force, and hence k_s and k_r, is constant).

will be illustrated below.

Finally, it is also worth highlighting that the same model for rolling resistance defined in Fig. 5.25, was implemented in the DEM code for both the HM and JKR contact laws. Indeed, the proposed rolling moment is not in any way related to the sign of the contact normal force, be it negative (tensile) or positive (compressive). This is because the direction of the rolling moment is solely determined by the relative rotation vector, as by definition (see Eq. **??**). In other words, the implemented rolling model is irrespective of the actual contact behaviour, *i.e.* of the normal and shear stress contact distributions. The goal, on the other hand, is to introduce a parameter that can effectively account for particle interlocking, regardless of the micro-mechanical phenomena occurring at the point of contact. Although this may sound somewhat unphysical, it is a necessary approximation in order to keep the computational time within affordable limit.

5.4.2 Results without adhesion

Very dense samples of frictionless grains were generated and then compressed until 1kPa of confining pressure. The friction angle was then gradually increased back to the actual value (see Table 5.1). The rolling resistance was activated only at this stage, in order to avoid the creation of extremely loose samples which can potentially lead to material instabilities, owing

to the very low stress level ($p \leq 10$kPa). Samples were prepared at different stress levels and for various values of η, ranging from 0.1 to 1.0. Triaxial tests at constant mean confining pressure were run for the same loading rate used in the previous analysis ($\dot{\epsilon} = 2 \times 10^{-5}$), which was proved to maintain the system close to the QS equilibrium.

It can be noted that the peak deviatoric stress occurs at very small strains for tests run with different values of η and a stress level of 10kPa, as illustrated in Fig. 5.26(a).

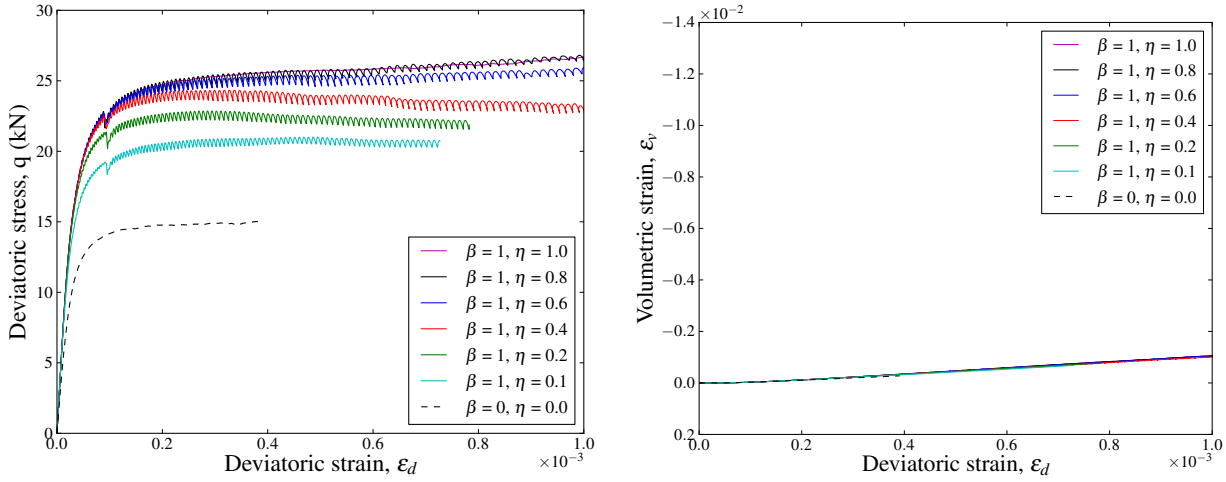

(a) Peak deviatoric stress vs deviatoric strain. Detail at very small strain levels.

(b) Volumetric behaviour at very small strains.

Figure 5.26: Effect of the rolling parameter η at the peak state of the material. Tests were run at a constant mean stress level of 10kPa and for different values of η. Note that the stress-strain curves present frequent oscillations which are, at least in part, to be attributed to the calibrated servo-control algorithm used to maintain the mean confining stress constant.

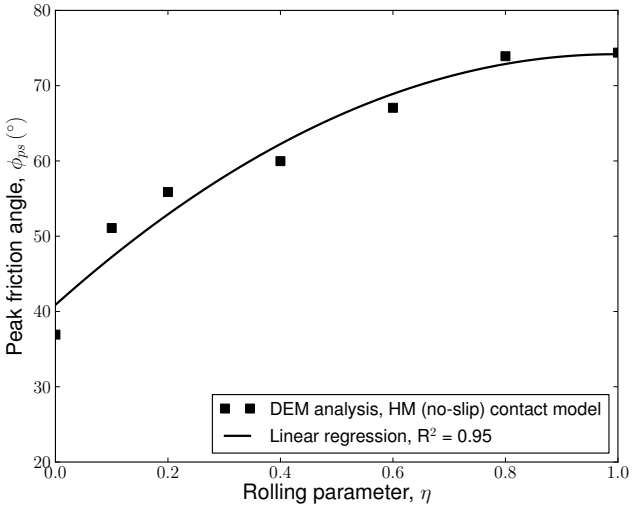

Figure 5.27: Effect of the rolling parameter η on the peak friction angle (note that tangent parameters are equal to secant parameters for cohesionless grains).

Moreover, the initial stiffness of the material appears insensitive to the introduction of rolling resistance, which confirms other findings from previous numerical studies (see (Mohamed and Gutierrez, 2010) and references therein). While the rolling parameter η has the effect of increasing the peak strength as shown in Fig. 5.26(a), it has no influence on the volumetric behaviour at very small strains, as illustrated in Fig. 5.26(b). Indeed, the relationship between the peak failure points and the rolling parameter η is highly non-linear, as can be observed in Fig. 5.27. Note that the friction angles reported in Fig. 5.27 are computed from individual tests, thus they are regarded as secant parameters. Moreover, the stress ratios plotted with respect to the deviatoric strain and obtained at two different stress levels, present the same maximum stress ratio, as depicted in Fig. 5.28. Thus, it can be concluded that no cohesion is introduced as a result of rolling resistance, *i.e.* secant and tangent friction angles coincide in this case.

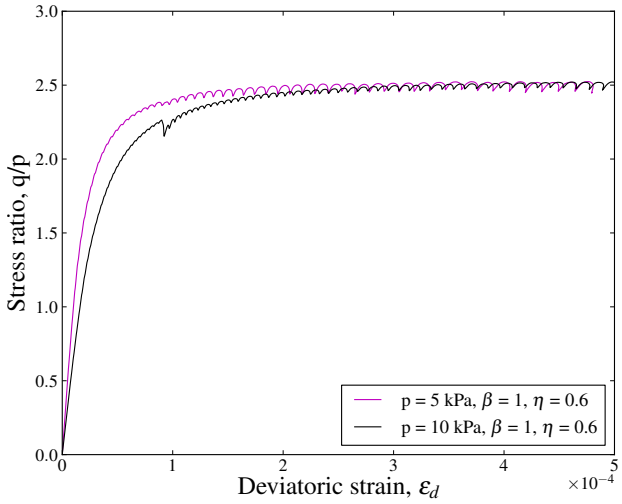

Figure 5.28: Stress ratio for tests at two different stress levels and with rolling resistance.

Results at the peak state are also reported on the MC plane in Fig. 5.29, indicating the strong influence of η on the gradient of the MC failure line.

The influence of η on the stress-strain and volumetric behaviour obtained all the way up to very large strains, is shown in Fig. 5.30. It can be seen that for $\eta \geq 0.6$, the macroscopic response appears almost the same, confirming the highly non-linear relationship between the macroscopic material behaviour and the rolling parameter η. From the current results, it can be stated that the introduction of rolling resistance is shown to increase both the peak and

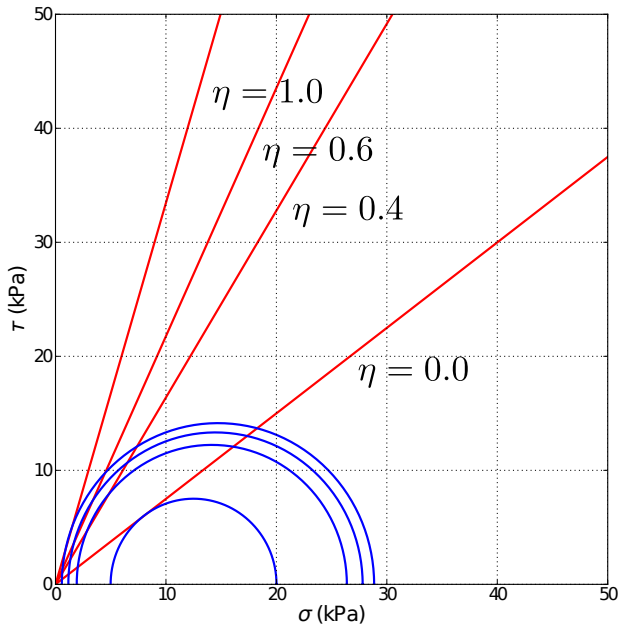

Figure 5.29: Influence of the rolling parameter η on the MC failure criterion for the HM contact model.

critical shear strength (see Fig. 5.31), enhancing dilatancy at large strains, and reducing the mechanical coordination number (see Fig. 5.30). These findings are in line with expectations and can be thought of as a result of the interlocking caused by particles of irregular shape.

Finally, it is worth underlying that the rolling parameter η, has an influence on both the peak and critical shear strength of the material. A specific rolling parameter, however, must be selected in order to calibrate the numerical model so that it best fits experimental results. In other words, η must be fitted to both the peak and critical state parameters simultaneously, and not in isolation.

The above results will now be briefly compared against the relevant literature. The model for rolling resistance used in this study was previously adopted by Plassiard et al. (2009), in combination with a linear elastic spring in both the shear and normal directions. The influence of the two parameters β and η (corresponding to β_r and η_r in the paper) were assessed on the material response. It was found that β had an effect on both the peak and critical state, whereas η only influenced the peak stress. This is in contrast with the present results where η has an influence on both the peak and critical state, indicating that the details of the contact models are important to determine the macroscopic response of the

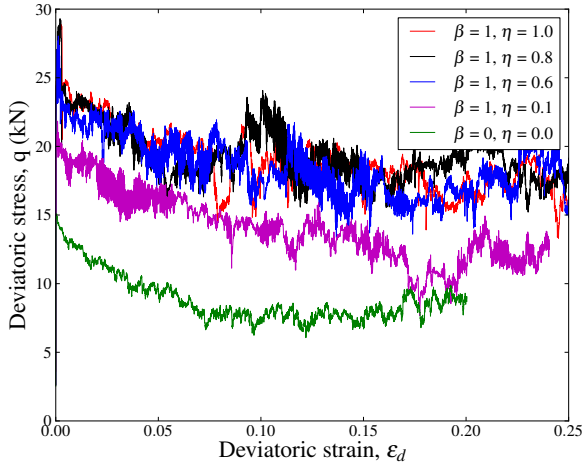

(a) Deviatoric stress vs deviatoric strain.

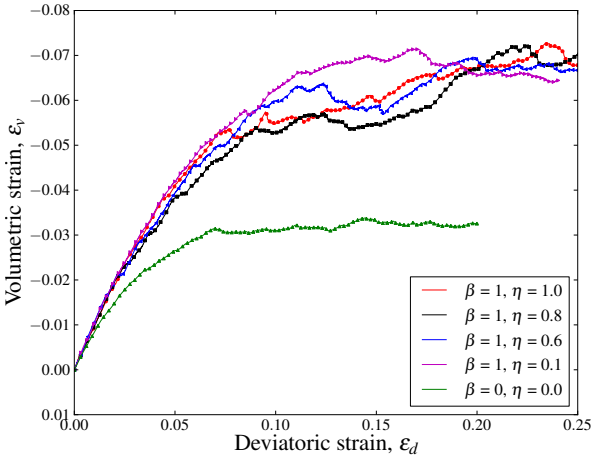

(b) Volumetric behaviour.

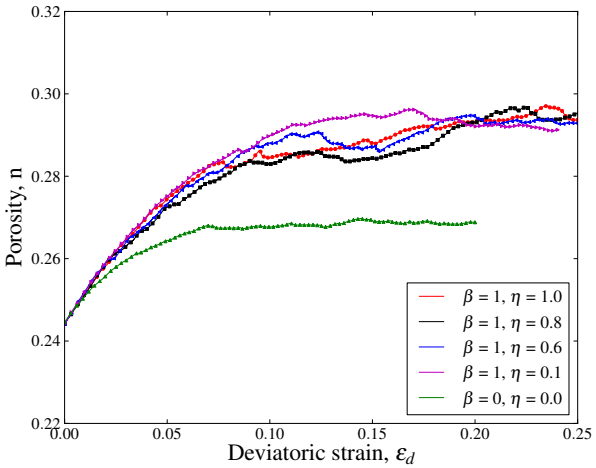

(c) Macroscopic porosity.

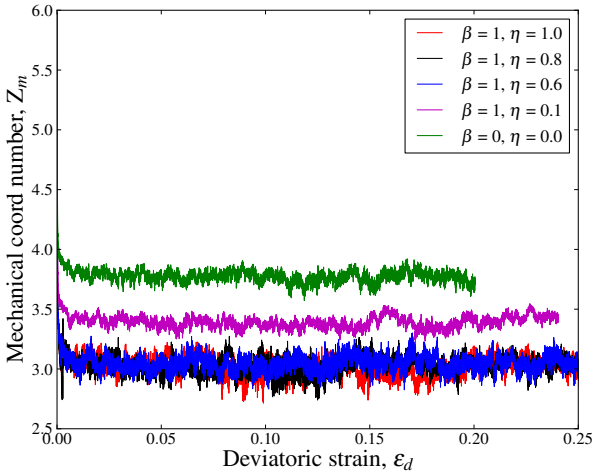

(d) Mechanical coordination number.

Figure 5.30: Tests run up to very large strains at a stress level of 10kPa and for different values of η.

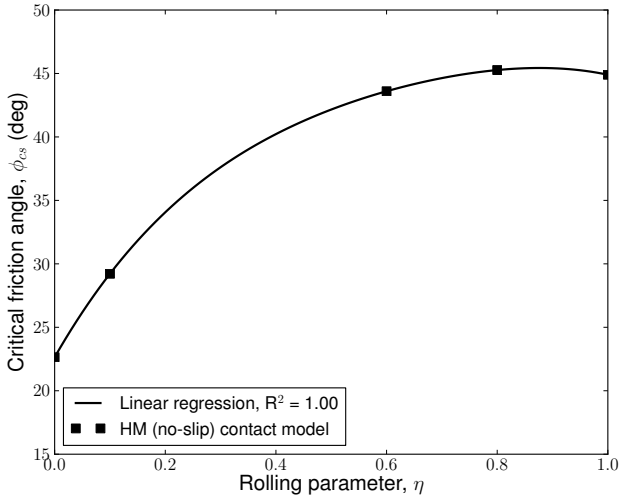

Figure 5.31: Effect of rolling resistance on the critical state friction angle ϕ_{cs}.

system.

The effects of rolling resistance on the soil shear strength were also extensively investigated by Mohamed and Gutierrez (2010). The rolling resistance model used in their paper was conceptually more simple than the current one, with a single rolling coefficient introduced to limit the maximum rolling moment. It was found the the peak friction angle, as well as dilatancy, increase with rolling resistance (Mohamed and Gutierrez, 2010). In addition, a tendency of the peak secant friction angle to increase non-linearly with the rolling coefficient (Mohamed and Gutierrez, 2010) confirms the present results (Fig. 5.27). Some macroscopic cohesion was also observed but it was interpreted as an artificial cohesion resulting from the MC mathematical description of the material failure.

Finally, the effect of relative density was investigated for the tests carried out at the confining pressure of 1kPa and for a prescribed rolling parameter η of 0.6. Different relative densities were obtained following the procedure outlined in Sec. 5.2. As can be observed in Fig. 5.32, the relationship between the friction angle and the relative density is approximately linear. A linear trend was also observed for tests conducted on JSC-1 lunar soil simulant (Klosky et al., 2000), which is characterised by a PSD similar to the one adopted in this study (see Chapter 2).

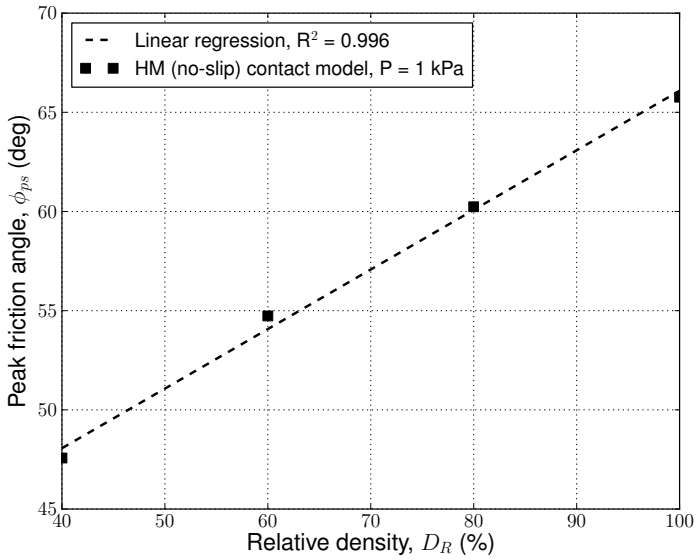

Figure 5.32: Relationship between relative density and peak friction angle for the HM contact model ($\eta = 0.6$).

5.4.3 Results with adhesion

The series of triaxial tests conducted without adhesion was repeated with surface energy forces to assess the combined effect of γ and interparticle rolling resistance. The investigation was run for a constant value of surface energy of 0.07J/m^2 (which is thought to be representative of lunar soil) and various degrees of rolling resistance. The results are plotted in Fig. 5.33, illustrating the peak friction angle with respect to the rolling parameter η. In a way similar to the tests run with the HM model, a highly non-linear relationship between the peak friction angle and the rolling parameter η is obtained. In particular, a constant peak friction angle is achieved for $\eta \geq 0.6$.

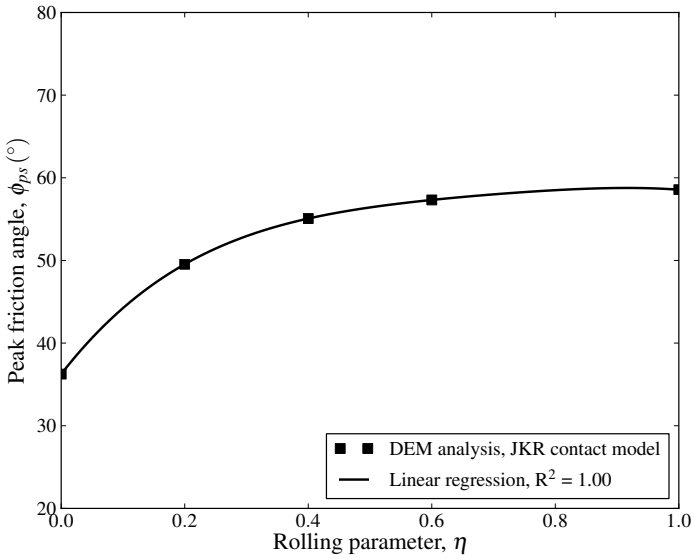

Figure 5.33: Effect of the rolling parameter η on the peak friction angle for the JKR contact model ($\gamma = 0.07\text{J/m}^2$).

The relationship between the macroscopic cohesion and the rolling parameter η is also found to be highly non-linear, as shown in Fig. 5.34. Similar to the tendency obtained for the peak friction angle, an asymptotic value of cohesion is reached for $\eta \geq 0.6$. The results are also visualised on the MC plane for different values of η, as seen in Fig. 5.35.

At the critical state, the influence of rolling resistance is mainly on the peak friction angle, although some small cohesion is also observed, slightly increasing with η (see Fig. 5.36). For a prescribed value of η, the values of critical friction angle obtained with adhesion matches very closely to the results without adhesion (see Fig. 5.36 and Fig. 5.31). This demonstrates

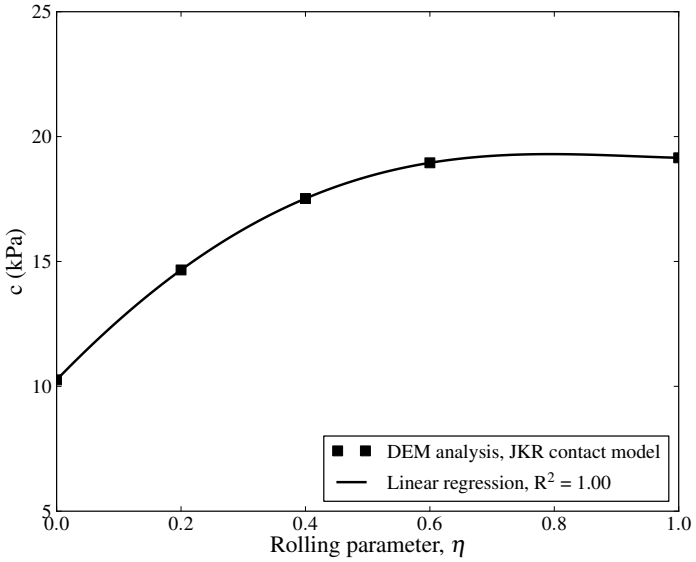

Figure 5.34: Effect of the rolling parameter, η, on the peak state cohesion ($\gamma = 0.07\text{J/m}^2$).

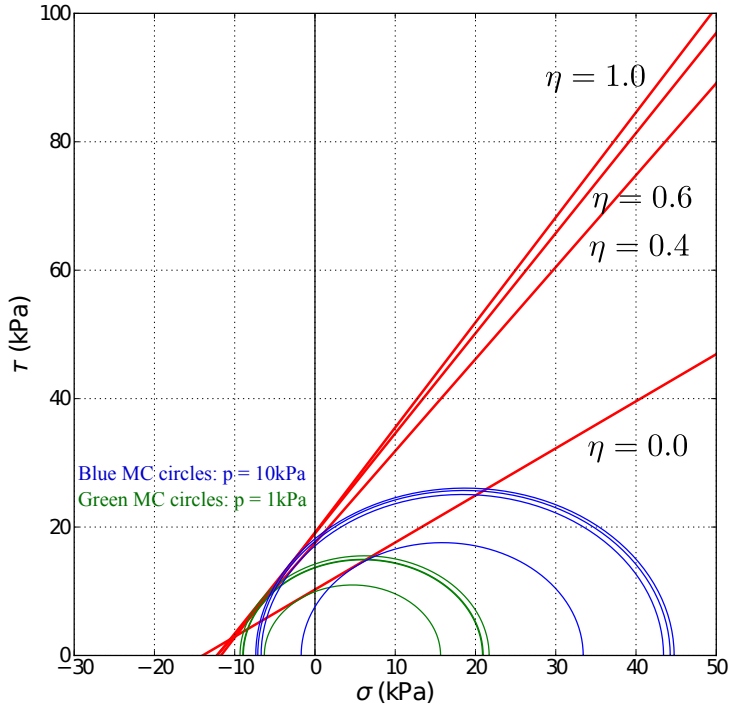

Figure 5.35: Effect of the rolling parameter η on the MC failure criterion at the peak state of the material ($\gamma = 0.07\text{J/m}^2$).

the lack of influence of surface energy on the critical state parameters, both in terms of friction angle and cohesion, which was also previously observed with particles without rolling resistance (see Sec. 5.3). This is an interesting result since it suggests that a remarkably

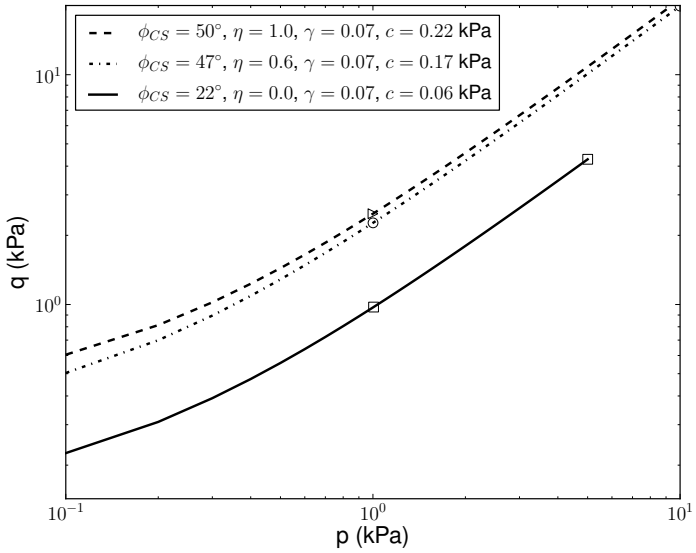

Figure 5.36: Influence of the rolling resistance parameter, η, on the critical state in the presence of adhesion ($\gamma = 0.07\text{J/m}^2$). A log-log plot is preferred in order to highlight the effect of the rolling resistance on the macroscopic cohesion.

different mechanical behaviour is expected at the peak and critical state when surface energy forces are considered. This has profound implications in geotechnical applications, as will be seen in Chapter 6.

Finally, the influence of relative density was assessed for tests performed with a rolling parameter of 0.6 and at the confining pressures of 1 and 10 kPa, respectively. The results are reported in terms of peak friction angle and cohesion for three values of relative density, as illustrated in Fig. 5.37. It can be seen that both the macroscopic soil parameters (cohesion and friction) increase with relative density, as observed in the experimental behaviour of JSC-1 lunar soil simulant (Klosky et al., 2000).

5.4.4 Comparison with empirical lunar soil data

In Chapter 2, the shear strength of lunar soil and lunar soil simulants was discussed in detail. It was found that the friction angle of lunar soil ranges from 42^o to 54^o, increasing with relative density (Carrier et al., 1991). The strength parameters of lunar soil simulants were very similar to the real lunar soil, producing a friction angle between 40^o and 56^o, and in the case of very low confining stresses (see Sec. 2.2.4), such as in the present study, it was

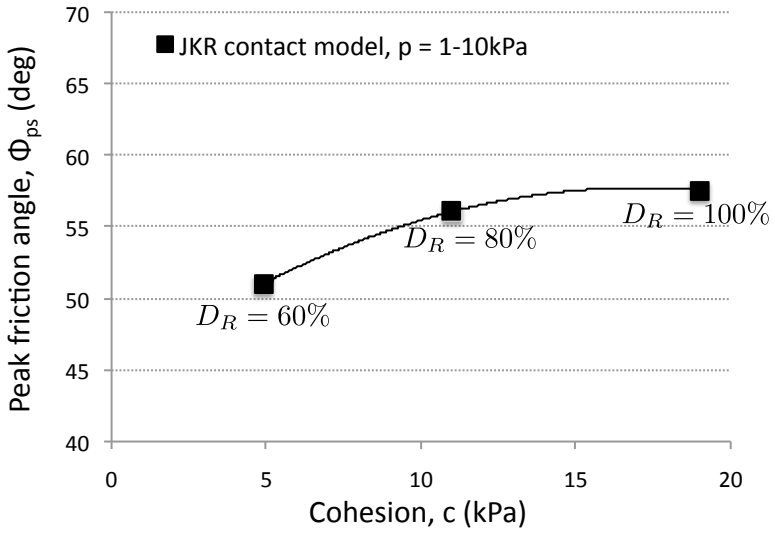

Figure 5.37: Influence of relative density, D_R, on macroscopic peak friction angle and cohesion (JKR contact model, $\gamma = 0.07\text{J/m}^2$, $\eta = 0.06$).

up to 67^o (Klosky et al., 2000).

The DEM simulations obtained with rolling resistance are able to match closely the best estimates of lunar soil shear strength, when a rolling coefficient $\eta = 0.6$ is employed. Without surface energy forces, this rolling coefficient corresponded to a peak and critical state friction angle of 65^o and 44^o respectively (see Sec. 5.4.2). With adhesion, on the other hand, these were 57^o and 47^o, and the macroscopic cohesion was 19 and 0.17kPa respectively (see Sec. 5.4.3).

The peak values of the friction angle obtained with and without adhesion, were computed for very dense samples. Therefore they should be compared with the lunar soil friction angle estimated at very high density which, according to the above data, is equal to 55-56^o. The close match between the numerical and experimental results shows that the DEM model is able to capture the very high friction angle of lunar soil predicted under very dense conditions. The numerical data predicted at the critical state, corresponding to the lowest values predicted for lunar soil (under less dense conditions), are also in close agreement.

Note that the above comparison does not include experimental curves of stress-strain behaviour for two primary reasons: firstly, because no empirical data of triaxial tests conducted

on real lunar soil are available, and secondly because although empirical results of lunar soil simulants have been previously published in the literature, they have been conducted under terrestrial conditions while ignoring the presence of vdW forces. Nevertheless, the current DEM model presents two advantages: (i) it is able to reproduce the high shear strength of lunar material, and (ii) it accounts for the effect of intermolecular vdW forces responsible for the macroscopic soil cohesion.

Lunar soil cohesion has been estimated to be in the range of 0.52 to 3kPa (see Chapter 2), increasing with soil density. The current results show that cohesion is clearly a function of both soil density and surface energy. Using the value of γ typical of lunar soil, the critical state cohesion (corresponding to loose soil conditions) was found closer to the lower bound of real soil cohesion ($\approx$0.52kPa). On the other hand, much higher cohesion was detected at very high density, above the average value predicted for real lunar soil ($\approx$3kPa). Nevertheless, the lunar soil cohesion under extremely dense conditions has never been measured before. Therefore the value obtained from the numerical tests can be regarded as an upper bound, which will await confirmation from geotechnical testing on real lunar soil. Finally, it is worth noting that the present numerical results not only provide a means to achieve the high shear strength parameters of lunar soil, but also present valuable information on the soil behaviour in the presence of vdW forces, which is currently not possible to achieve by laboratory experiments alone.

5.4.5 Clusters of spheres to simulate particle shape effects

We now aim to investigate the combined effect of surface energy forces and irregular particle shapes, simulated by means of simple clump models. The results will be presented at the peak and critical state, both with and without adhesion. A comparison will be made against the findings obtained by using rolling resistance, in order to assess the suitability of the artificial model with hindered particle rotations to account for real particle interlocking.

5.4.5.1 Generation of clump models

Clumps are collections of more than two spheres joined together to form a single, non-convex, body. Connections between spheres forming a clump are treated as rigid links rather than physical contacts.

Clumps were already available in Yade and a description of their implementation can be found in Smilauer et al. (2010). A special feature of the existing implementation concerns the algorithm used for the integration of the rotational motion of non-spherical bodies (such as clumps), which is a variation of the standard second-order Leapfrog integration scheme applied for spherical bodies in Yade. This was introduced in the code to add accuracy to the calculations when clumps are employed, given that the elements on the principal diagonal of the inertial matrix (expressed in the local reference frame) no longer coincide for non-spherical particles. The algorithm is detailed in Allen and Tildesley (1987) and resembles the general form of the Fincham algorithm which was originally devised for implicit calculations of molecular dynamic simulations.

Clumps in Yade were successfully used to investigate the sand behaviour by means of drained triaxial compression tests (Kozicki et al., 2012). Following a calibration of the input parameters (PSD and microscopic properties) the results obtained from the DEM simulations (conducted using rigid boundaries) were shown to match closely with the experimental behaviour of Karlsruhe sand.

In order to keep the computational time within acceptable limits, very simple clump models, made of two, three and four spheres, respectively, were considered, as illustrated in Fig. 5.38.

The clump models selected in this study present increasing complexity (Fig. 5.38). For instance, the two-sphere model has one preferential direction, the three-sphere model develops in plane, while the four-sphere model involves a third out-of-plane direction. However, it should be noted that there is no easy way to determine a priori the soil strength resistance based on the geometry of the single grain. From a DEM perspective, particle shape is then

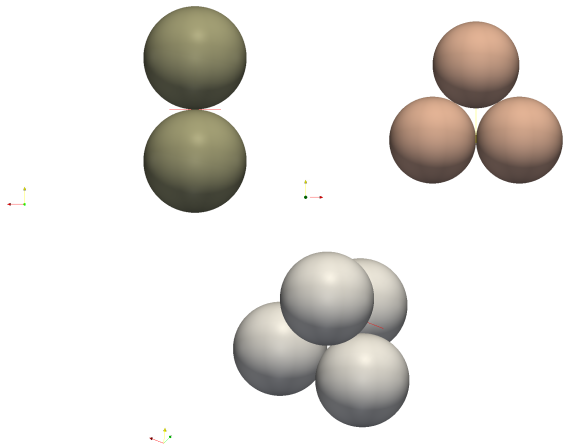

Figure 5.38: Spherical particles clumped together in three different ways of increasing complexity to form non-spherical particle shapes.

regarded as a calibration parameter.

The sample generation followed the same procedure discussed in Sec. 5.2. However, a modification was applied in order to generate clumps in place of spheres. At first, 5,000 spheres were generated, following the PSD typical of lunar soil (see Sec. 2.2.1). Following that, spheres were deleted and replaced by clumps of identical shape, with the same mass of the original spheres. Each clump was generated within the volume occupied by the initial sphere, in order to avoid initial overlapping between the elements. Furthermore, a calibrated material density was assigned to the clumps in order to match the mass of the original particle, as according to the following expression:

$$\rho_{cl} = \rho_{sp} \frac{V_{sp}}{\sum_{m} V_m} \quad , \tag{5.11}$$

where ρ_{cl} is the equivalent density of the clump, ρ_{sp} the initial density of the spheres, V_{sp} the volume of the initial sphere, V_m the volume of the m^{th} member of the clump. It was also verified that QS conditions were maintained throughout the tests.

Following the classification introduced by Salot et al. (2009), the models proposed in

Fig. 5.38 correspond to an angularity factor equal to 1, the latter being defined as:

$$ang = \frac{d}{2R} \quad , \tag{5.12}$$

where d is the distance between two spheres composing the clump and R their radius (Salot et al., 2009). The choice of having a high angularity factor for all the clump models is made to resemble as close as possible the interlocking generated by very irregular lunar soil grains. In the following, samples generated using the clump models discussed above will be compared.

The definition of the stress tensor, expressed by Eq. 4.22, was conceptually derived to account for any particle shape (Bagi, 1996). Thus it does not need to be modified, although the general definition of branch vector l_i now reads as the distance between the centre of mass of the clump, around which all forces are applied, and the centre of mass of the particle in contact with the clump. For spherical particles in mutual contact, the branch vector simply reads as the vector between the centroids of the two spheres, as it is a special case where its direction passes through the contact point.

The macroscopic porosity is computed in the usual manner, *i.e.* $n = \frac{V_t - V_s}{V_t}$, where V_t is the total volume of the cell and V_s the total volume of the particles, notwithstanding that the space enclosed by the particles forming the clump in the models composed of 3 and 4 spheres should in fact be considered as part of the solid volume V_s.

5.4.5.2 Peak state results

Samples prepared at 100% of relative density without surface energy were sheared, until the maximum shear strength was achieved, as depicted in Fig. 5.39. Based on a series of tests, a sample of 2,000 clumps was identified as the smallest REV for the current investigation. It is of particular importance to keep a minimum number of clumps, since it is still the total number of spheres (not clumps) that determines the total computation time.

Fig. 5.39 shows the results from triaxial tests in terms of stress ratio and volumetric strain

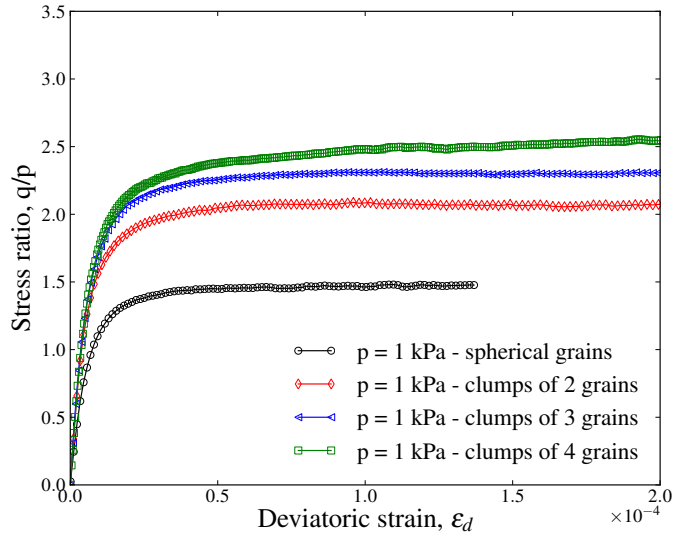

(a) Stress ratio versus deviatoric strain.

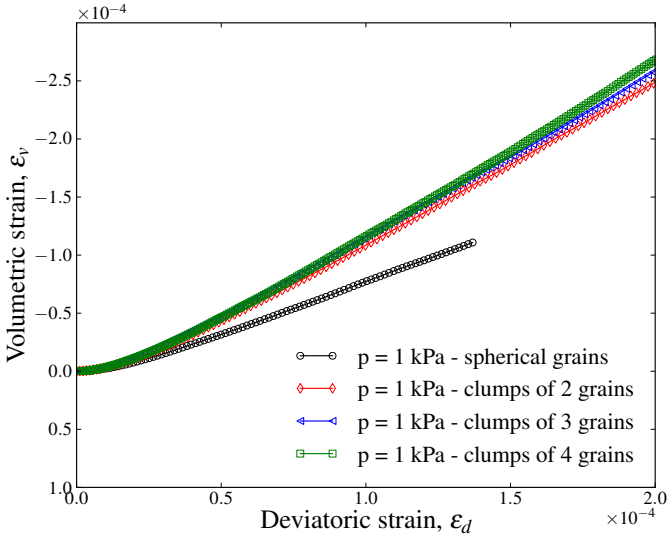

(b) Volumetric behaviour.

Figure 5.39: Stress ratio and volumetric behaviour of various clump models at very small strain levels (2,000 clumps).

versus deviatoric strain for different clump models under a constant mean confining pressure of 1kPa. Note that all the microscopic parameters used in the tests are the same as were used in the previous tests, see Table 5.1. The peak shear strength resistance is higher for the clump models compared to the results obtained for the model with spheres only. Moreover, increasing the complexity of the model, *i.e.* from two to four spheres per clump, leads to higher peak strength (see Fig. 5.39). In terms of volumetric deformations, the difference appears to be very small although dilatancy generally increases when passing from single-sphere to multiple-sphere element model. The present results are in line with the numerical

findings presented by Salot et al. (2009), who conducted a similar investigation, although the load was applied by means of rigid walls and a simple linear model was employed at the contacts. They also further investigated the effect of angularity and it was found that increasing angularity increases the soil shear strength and dilatancy angle of the soil (Salot et al., 2009).

The same tests were carried out using the JKR contact model. The results of the simulations are illustrated in Fig. 5.40. The same tendency observed for non-adhesive particles in terms of peak strength, is also observed with adhesion, except for the four-sphere clump model which shows lower strength than the analogous three-sphere clump model. The soil stiffness increases with the increasing complexity of the clump model. On the other hand, the peak is located almost at the same strain level, whereas very little effect of particle shape is observed in terms of dilatancy, Fig. 5.40(b).

5.4.5.3 Critical state results

The macroscopic results in terms of stress ratio and volumetric behaviour of the simulations run up to large strains and without adhesion are reported in Fig. 5.41 and Fig. 5.42. The results show that shear strength is highly affected by particle shape and it is higher for more irregular grain shapes.

The oscillations of the stress-strain response are more pronounced as the number of spheres per clump model increases (see Fig. 5.41(a)). The strength at the critical state shows little variation among all the three clump models. On the other hand, samples experience increased volume expansion for increased particle irregularity.

Both the initial as well as the final critical porosity are increased for more irregular particle shapes, as shown in Fig. 5.42. This tendency was also observed for the tests run with rolling resistance, which leads to the following remarks:

(i) particle irregularity may be understood at the particle-level as a phenomenon that hinders particle rotations;

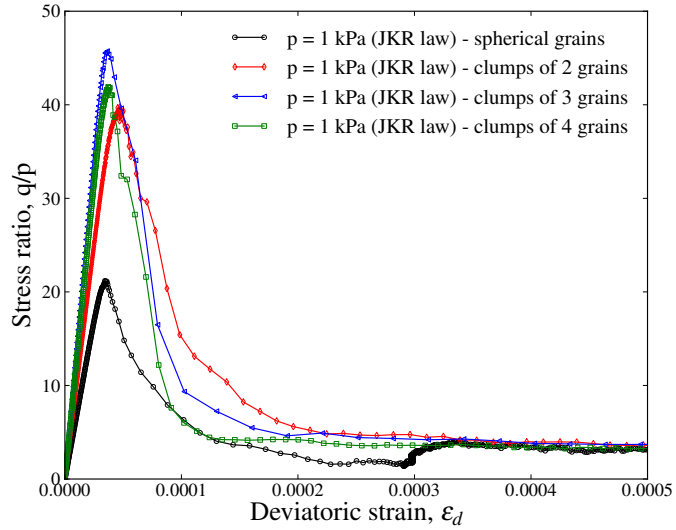

(a) Stress ratio versus deviatoric strain.

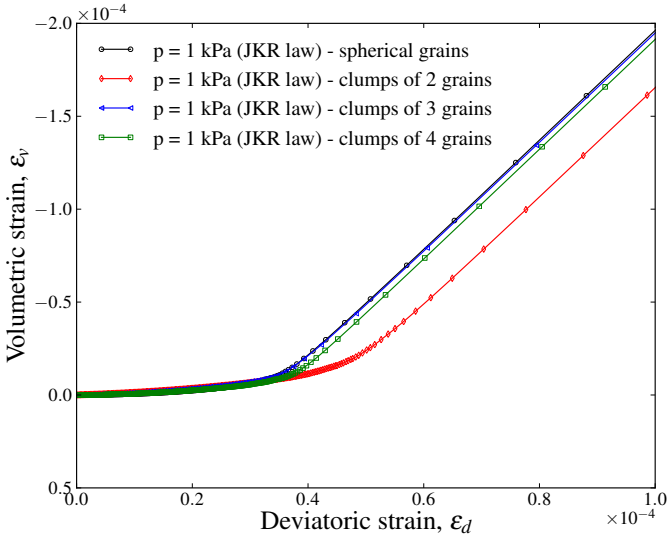

(b) Volumetric behaviour.

Figure 5.40: Stress ratio and volumetric behaviour of various clump models at very small strain levels using the JKR contact model (2,000 clumps).

(ii) in both cases, particle irregularity can be associated with higher interlocking, which sustains a more porous structure under stable conditions.

Soil fabric is often taken as an indicator of the structural anisotropy of an ensemble (Thornton and Antony, 1998), which in turn is often found to be responsible for high shear strength resistance (see Azéma et al., 2009, and references therein). The fabric tensor is generally defined from the distribution of the contact orientations, according to (Cheng

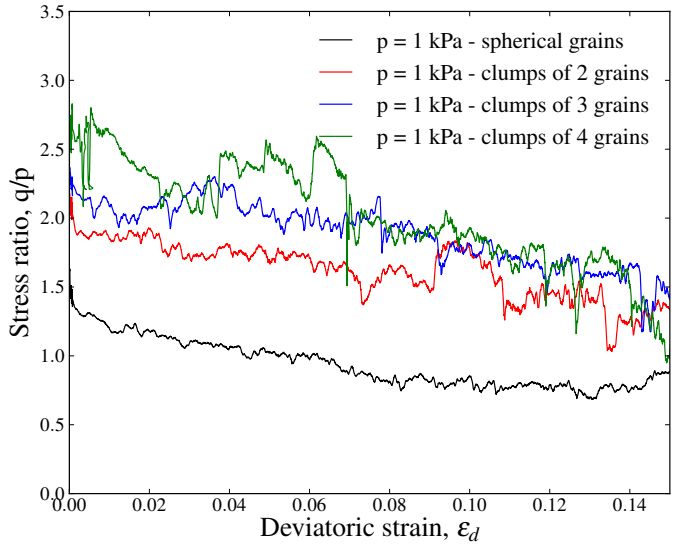

(a) Stress ratio versus deviatoric strain.

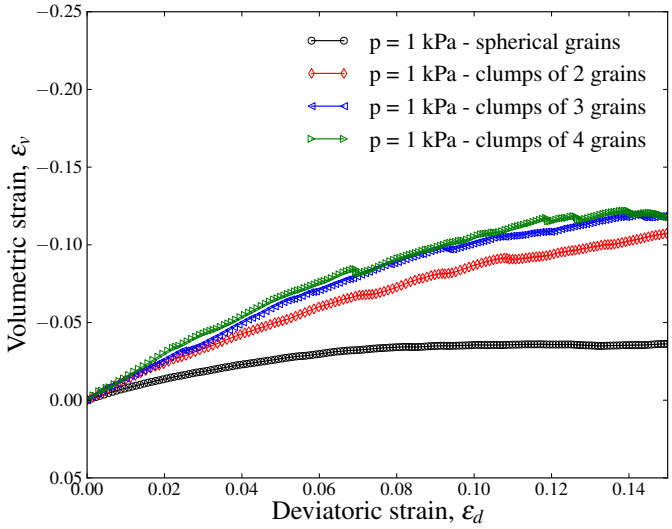

(b) Volumetric behaviour.

Figure 5.41: Stress ratio and volumetric behaviour of various clump models at very small strain levels (2,000 clumps).

et al., 2008; Thornton and Antony, 1998):

$$\phi_{i,j} = \frac{1}{2C} \sum_{V} n_i n_j \quad . \tag{5.13}$$

The deviatoric fabric is taken as the difference between the major and minor principal components of the fabric tensor, *i.e.* $\phi_q = \phi_1 - \phi_3$. The behaviour of the deviatoric fabric during the simulations (without surface energy forces) is illustrated in Fig. 5.43. It can be noticed that ϕ_q increases rapidly in the small strain regime, then reaches a peak, and finally

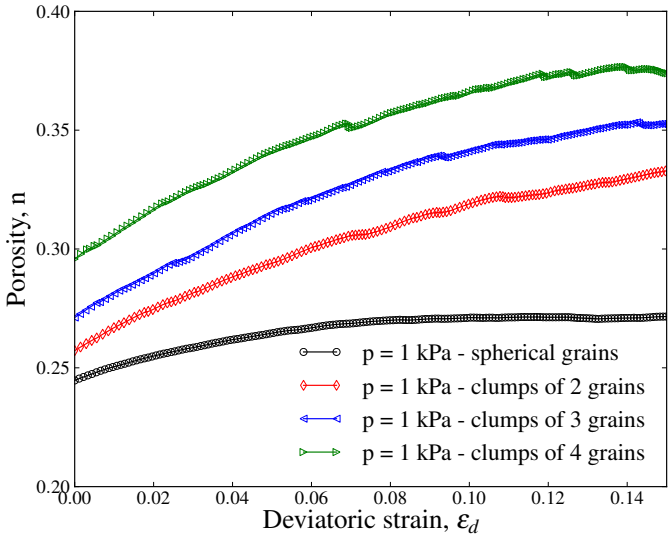

Figure 5.42: Macroscopic porosity for different particle shapes (2,000 clumps).

decreases gradually to critical state conditions. It can also be observed that ϕ_q is generally higher for increasing particle irregularity (or complexity) than when only spherical particles are employed. It can then be stated that higher anisotropy, developed during shearing, may explain the higher strength shown by the clump models examined in this study.

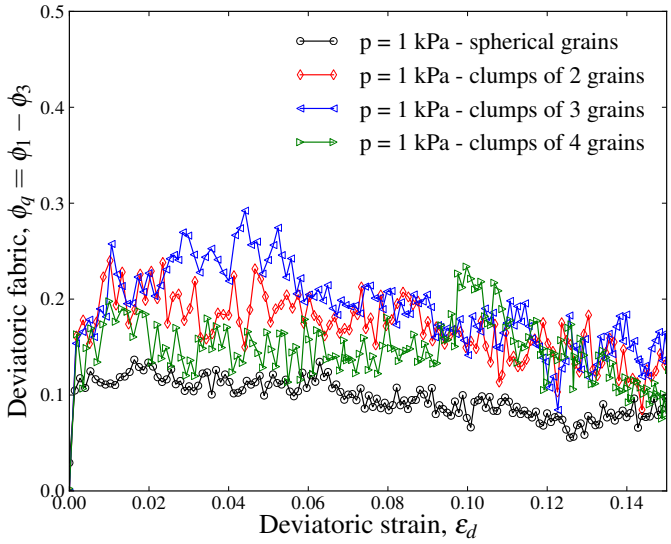

Figure 5.43: Deviatoric fabric for different particle shape models (2,000 clumps).

Adhesive particles were also tested up to the critical state but only for the two- and three-sphere clump models, since the four-sphere model curiously produced lower peak shear strength than the three-sphere model. The stress-strain behaviour, volumetric behaviour and macroscopic porosity are reported in Fig. 5.44 and Fig. 5.45. In a way similar to the case of

non-adhesive grains, the following observations can be advanced:

(i) the critical shear strength is influenced by particle irregularity, and some difference can be appreciated for different clump models;

(ii) higher volumetric strains and porosities are induced by particle shape effects.

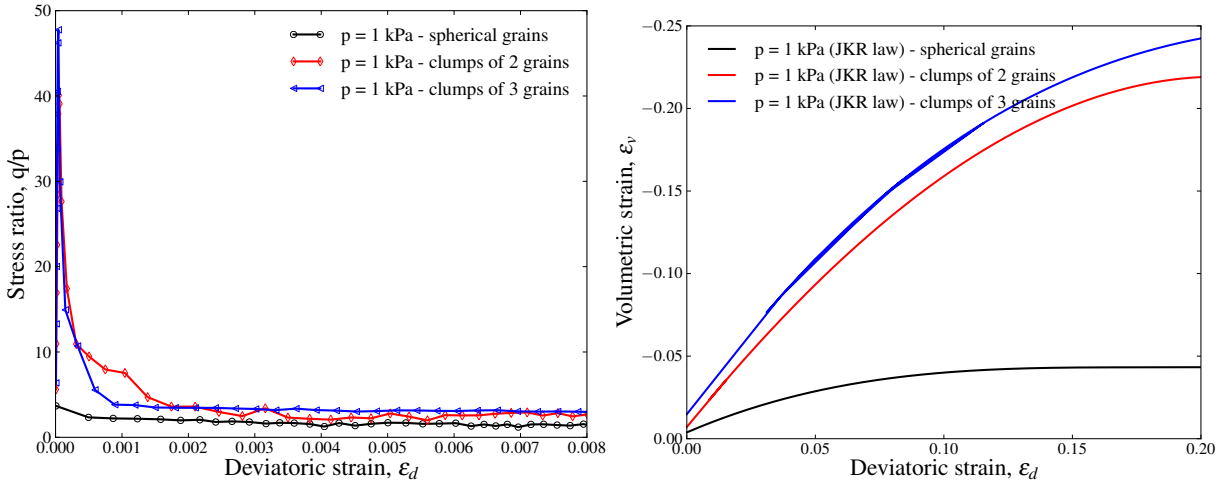

(a) Stress ratio versus deviatoric strain.

(b) Volumetric behaviour.

Figure 5.44: Stress ratio and volumetric behaviour of various clump models obtained with the JKR contact model (2,000 clumps).

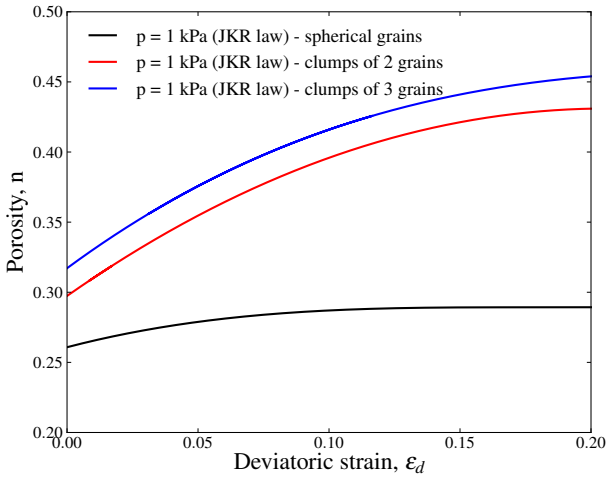

Figure 5.45: Macroscopic porosity for different particle shapes obtained with the JKR contact model (2,000 clumps).

The effect of confining pressure was also investigated for tests with surface energy forces, since tests at two or more different confining pressures have to be run in order to obtain the peak and critical state parameters (tangent values). According to Fig. 5.46, showing the macroscopic response of two tests run at 1 and 10kPa respectively, the influence of

the increased pressure is to greatly reduce the peak strength of the material, but without affecting the critical value. Both dilatancy and volumetric strain are also found to be lower with increasing stress.

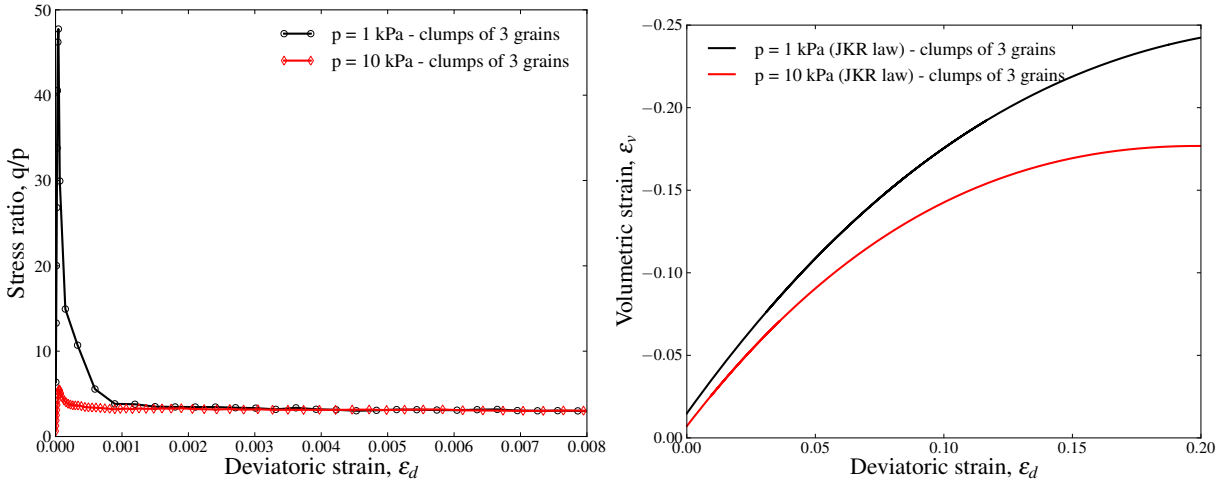

(a) Stress ratio versus deviatoric strain.

(b) Volumetric behaviour.

Figure 5.46: Stress ratio and volumetric behaviour of various clump models obtained with the JKR contact model at 1 and 10kPa of confining pressure (2,000 clumps).

Fig. 5.47 and 5.48 illustrate the failure lines at both the peak and critical states for various clump models, with and without adhesion respectively. Using the JKR contact model, and referring to the tests run for various particle shapes, the peak friction angle is found to range from 35^o to 21^o, as the complexity of the grain shape increases. The peak cohesion, on the other hand, is obtained in the range between 10 to 21kPa. At the critical state, the friction angle ranges from 21^o to 38^o, whilst the macroscopic cohesion is found in the range between 0.14 and 0.04kPa. According the above results, the following observations hold true for the DEM simulations performed using various clump models:

(i) cohesion is generated as a result of surface energy forces, but only at the peak strength of the material, while very little cohesion is detected at the critical state;

(ii) the peak friction angle observed in clump models contributes less than spherical particles do to the total soil shear strength, since macroscopic cohesion takes up a larger contribution.

Without adhesion, the peak friction angle is found to be between 36^o to 63^o, while the

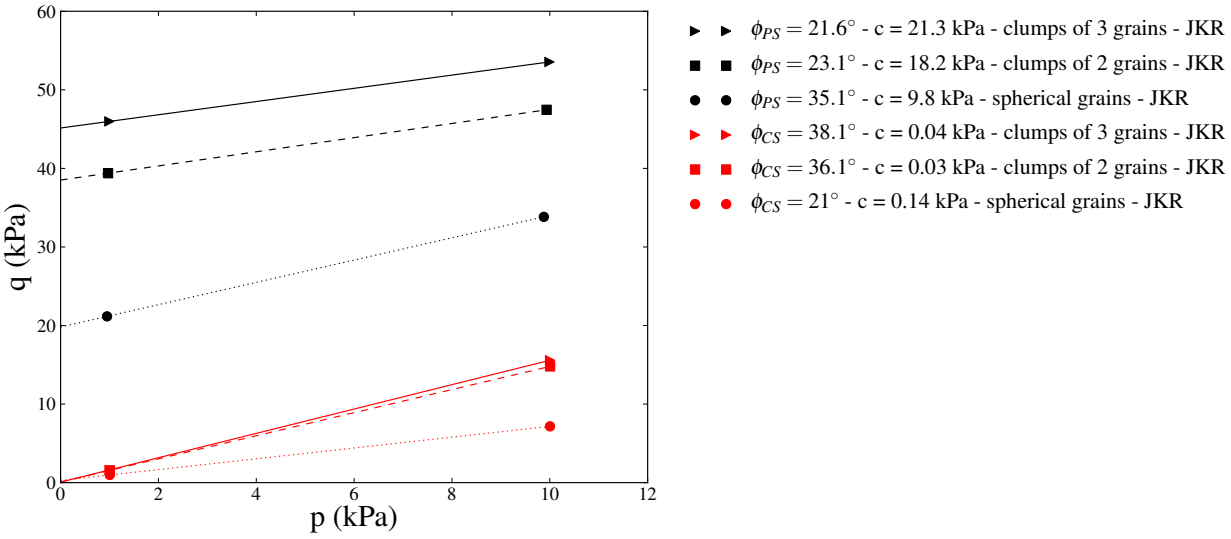

Figure 5.47: Critical and peak state results for various clump models using the JKR contact model (2,000 clumps).

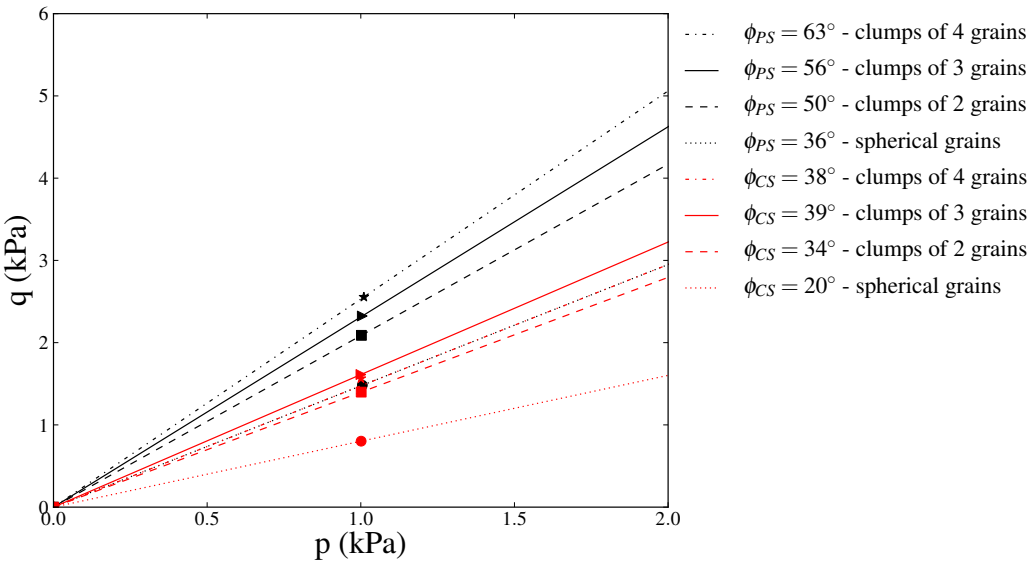

Figure 5.48: Critical and peak state results for various clump models using the HM contact model (2,000 clumps).

critical friction angle ranges from 20^o to 39^o, having also included the results obtained with the four-sphere clump model (see Fig. 5.48). In addition, no cohesion was observed without surface energy forces. The individual values of the peak friction angles are found to be higher than with adhesion, but the total shear strength is still higher, as would be expected. On the other hand, there is little difference in the critical friction angle with or without adhesion. This is in complete agreement with the findings obtained with rolling resistance, confirming the suitability of the rolling resistance model to account artificially for realistic

particle interlocking.

However, the critical state friction angles obtained with the clump models are lower than with rolling resistance, suggesting that a more detailed description of simulated lunar grains would be required to model the high shear strength of lunar soil.

5.5 Summary and conclusions

In this chapter, a series of triaxial tests were carried out with three main objectives: (i) to match the high shear strength estimated for real lunar soil, (ii) to provide a reliable explanation for the unusual cohesion of lunar soil, and (iii) to give insight into the mechanical soil behaviour in the presence of surface energy forces.

At first, the effect of micromechanical forces of vdW origin was assessed on the macroscopic response of the soil. The soil behaviour was examined at both small and large strains, with and without adhesion. Particular emphasis was placed on the relationship between the microscopic surface energy and the macroscopic shear strength parameters, such as cohesion and friction angle.

Two different approaches were followed to investigate the effect of interparticle adhesion and its combined influence with particle shape effects. The first approach considered the use of spherical particles whose rotations were hindered by means of some artificial rolling resistance. The latter was characterised by the introduction in the DEM model of one single parameter. In the second approach, irregular grains were simulated by means of simplified clump models of increasing irregularity.

The numerical findings have shown that the behaviour of cohesive soils made of spherical particles, in which cohesion originates at the microscale level due to attractive vdW forces, results in significant cohesion at the peak state of the soil. However, this effect was seen to almost disappear at the critical state. Adhesion was not seen to have any effect on the friction angle at either the peak or critical state. The overall findings are that a direct link

is established between the microscopic surface energy and the macroscopic cohesion at the peak state of the soil, and that adhesion is expected to have little influence at the critical state, both in terms of friction angle and cohesion.

Taking into account particle shape effects by means of rolling resistance, has resulted in significantly higher peak shearing resistance. Cohesion also increased with particle interlocking, implying that this is not solely a function of the input surface energy but also of particle shape. The use of clump models, simulating more realistically the non-convex shapes of lunar grains, has confirmed these findings.

Comparison between the numerical and experimental findings for lunar soil, has shown that the DEM model with rolling resistance is able to reproduce the high shear strength of lunar soil and also to predict the macroscopic soil cohesion with the introduction of surface energy forces. A full comparison between numerical and experimental stress-strain curves was not possible due to the lack of empirical data on real lunar soil.

The engineering implications of the numerical results presented herein will be discussed in the next chapter with regards to the geotechnical applications of interest in future lunar operations.

Chapter 6

Geotechnical engineering implications

The implications of the high lunar soil shear strength parameters that were obtained earlier are discussed in this chapter with respect to three geotechnical engineering applications. These are (a) the problem of bearing capacity of shallow foundations, (b) and analytical approach for the solution of a rigid wheel-soil interaction using an adaptation of the Terzaghi expression of ultimate bearing capacity and (c) the slope stability of a vertical cut on the lunar surface. The second problem, in particular, is crucial in the study of the performance of lunar rovers.

6.1 Introduction

In this chapter, the numerical results obtained for the lunar soil in terms of shear strength will be employed to investigate the solution of three fundamental geotechnical applications: the problem of bearing capacity of a shallow circular footing (resembling the shape of a typical footpad of a lunar lander), a simplified wheel-soil interaction problem, valid for the case of a rigid wheel rolling on top of a deformable terrain resembling the lunar surface, and the problem of slope stability of a vertical wall on the lunar surface.

It might be thought that the problem of bearing capacity is not going to be an issue on the Moon, owing to the high shear strength estimated for lunar soil and matched by the numerical findings presented in the previous chapter. However, the geotechnical design of a future outpost on the Moon will be sensitive to the strength characteristics chosen to represent the mechanical behaviour of lunar soil. These are expected to be very different

at the peak and critical state (*i.e.* at small and large strains), particularly in the presence of surface energy forces as discussed in Chapter 5. Therefore, a thorough evaluation of the bearing capacity of lunar soil for shallow circular foundations will be useful to identify the peculiarities and subsequent engineering implications brought about by the high shear strength of lunar soil.

In addition, the solution of a simple wheel-soil interaction problem will be addressed by means of a new analytical approach based on the Terzaghi theory of bearing capacity. Understanding the physical mechanisms ruling this type of interaction is a very challenging task even when considering terrestrial environmental conditions. On the other, the solution to wheel-soil interaction problems is crucial to allow the design of future lunar rover's wheels to create more efficient systems. Unfortunately, the lack of empirical results and the complexity of the problem have confined recent developments to numerical studies and small-scale laboratory experiments (e.g. Li et al., 2010; Knuth et al., 2012), which lack general applicability and do not provide a solid theoretical understanding of the wheel-soil interaction mechanics. In this chapter, an analytical method will be introduced in order to provide an easy tool able to evaluate the mechanical performance of a wheel rotating on a deformable terrain as a function of shear strength parameters, such as soil cohesion and friction angle. The method presents the advantage of being independently formulated from the need to define complex wheel-soil contact stress distributions, which can only be evaluated by means of semi-empirical methods, while at the same time being able to tackle the three different dynamic conditions of towed, self-propelled and driven wheels.

Finally, the problem of slope stability on the lunar soil will be tackled by means of limit analysis (upper bound solutions). This is important to evaluate since it is concerned with the safety of future operations on the Moon, involving digging operations and excavations of deep trenches on the lunar terrain. Previous experimental evidence indicated that vertical faces can be sustained on the Moon up to 3m deep with a safety factor of 1.5 (Carrier, 2005). This finding will be compared with the slope stability results obtained while employing the cohesive and frictional contributions derived from the lunar soil DEM simulations (see

Chapter 5). The outcome will provide more reliable predictions of slope stability analysis for the lunar soil.

6.2 Bearing capacity of circular shallow foundations on lunar soil

6.2.1 Background

The effect of lunar environmental conditions on the soil bearing capacity was assessed in Perko and Nelson (2000) by means of vertical static and dynamic penetration tests on quartz sand under UHV and reduced gravity conditions. A 1/6 scale LEM (Lunar Exploratory Module) footpad was used in the experiment while gravity was set by adjusting the drop rate of the load (Perko and Nelson, 2000). It was found that the effect of vacuum was to increase the peak resistance. In particular, the peak strength was attributed in part to the presence of strong attractive intergranular forces and in part to the inertial resistance of the soil (Perko and Nelson, 2000). Evidence of progressive shear failure was also found during the dynamic penetration tests.

Perkins and Madson (1996) conducted a number of experiments to test the bearing capacity of the two lunar soil simulants MLS-1 and JSC-1. Various footing widths and different gravity conditions were analysed by employing a geotechnical centrifuge. Under such conditions, it was shown that the bearing capacity of both lunar soil simulants increases with width of the footing. A significant difference between the peak and the residual resistance was also observed with the difference found to decrease with the depths of embedment (*i.e.* with increasing density) (Perkins and Madson, 1996).

A comprehensive study of the bearing capacity of lunar soil had been earlier conducted by Jaffe (1971), who obtained results in terms of bearing capacity versus penetration depth by testing a 1.3g lunar sample under terrestrial conditions (Jaffe, 1971). It was found that the bearing capacity varies exponentially with the soil bulk density. In addition, the range

of bearing capacity for a small indenter of 2mm in diameter and measured at the indenter tip was found to range from 0.2–0.4kPa up to 300–1,000kPa, increasing with increasing bulk densities.

From the studies mentioned above it can be concluded with some evidence that the characteristics of the lunar environment have non-negligible effects on the bearing capacity of lunar soil. Jaffe (1971) demonstrated that the bearing capacity of lunar soil appears to increase with bulk density, Perko and Nelson (2000) observed an increase of peak shear resistance under UHV, while according to Perkins and Madson (1996) the bearing capacity of lunar soil simulants increases with footing width and a significant difference was found between peak and residual resistance.

The fact that the soil bearing capacity increases in the presence of UHV can be related to a corresponding increase in the soil shear strength under UHV and low confining pressures. In the previous chapter, the soil strength parameters have been computed by means of numerical simulations while taking into account the effects of vdW forces and employing interparticle rolling resistance in order to mimic the high interlocking of lunar grains. These parameters will now be used to calculate the bearing capacity of lunar soil using the classical Terzaghi's formulation. It will be shown that the results of the calculations are in line with the empirical observations mentioned above.

6.2.2 The classical Terzaghi approach

The Buisman-Terzaghi (Terzaghi, 1943) equation provides an expression for the ultimate bearing capacity of a shallow footing of width B on a cohesive frictional soil, which is given by:

$$q_u = cN_c + qN_q + 0.5\gamma_s BN_\gamma \quad , \tag{6.1}$$

where c is the soil cohesion, q is the equivalent surcharge due to the overburden soil, and γ_s is the soil unit weight. The remaining parameters N_c, N_q, N_γ are so-called dimensionless bearing capacity factors which depend only on the angle of internal friction, ϕ. They are

expressed as:

$$\begin{aligned} N_q &= e^{\pi \tan\phi} \tan^2\left(\frac{\pi}{4} + \frac{\phi}{2}\right) \quad , \\ N_c &= (N_q - 1)\cot\phi \quad , \\ N_\gamma &\approx 2(N_q + 1)\tan\phi \quad . \end{aligned} \tag{6.2}$$

The expressions for N_c and N_q are due to Prandtl (1920) and Reissner (1924) whereas the formulation of N_γ was introduced by Vesic (1973). According to Terzaghi, Eq. 6.1 holds true when the load is applied vertically at the centre of a strip footing. In the following, a circular footing of various diameters will be considered, which resembles the shape of the footpad typical of a lunar lander. In this case, Eq. 6.1 needs to be modified to introduce three dimensionless shape factors, such that:

$$q_u = cN_c\zeta_c + qN_q\zeta_q + 0.5\gamma_s B N_\gamma \zeta_\gamma \quad , \tag{6.3}$$

where ζ_c, ζ_q, ζ_γ are the dimensionless shape factors defined as (Vesic, 1973):

$$\begin{aligned} \zeta_q &= 1 + \frac{B}{L}\tan\phi \quad , \\ \zeta_c &= 1 + \frac{B}{L}\frac{N_q}{N_c} \quad , \\ \zeta_\gamma &= 1 - 0.4\frac{B}{L} \quad , \end{aligned} \tag{6.4}$$

where B is the width of the foundation and L its length. For a circular footing, they become equal to:

$$\begin{aligned} \zeta_q &= 1 + \tan\phi \quad , \\ \zeta_c &= 1 + \frac{N_q}{N_c} \quad , \\ \zeta_\gamma &= 0.6 \quad . \end{aligned} \tag{6.5}$$

For the computation to be meaningful it is important that the strength parameters used in Eq. 6.3 be selected such that they correspond to the state of stress below the foundation. However, the latter is not so easy to identify since shear failure below the foundation is a phenomenon that occurs progressively and depends on several factors such as stress level, density and footing size (Vesic, 1991; Perkins and Madson, 2000; Simonini, 2005). Re-

searchers have shown that the mobilised friction angle varies along slip lines owing to the progression of failure and the combined influence of stress level and relative density on the soil shear strength. In the following, the mean average pressure below the foundation will be estimated by taking the geometric mean between the following pressure values:

$$\begin{aligned} p_1 &= \frac{q_u}{6}\left[0.52 - 0.04\frac{L}{B}\right] \quad , \\ p_2 &= \gamma_s H_{infl} \quad , \end{aligned} \tag{6.6}$$

where p_1 is a simplified formula proposed in Perkins and Madson (2000) to compute the average pressure below a foundation as it was found to agree well with a number of experimental data sets, while p_2 is the pressure computed at the depth of maximum influence H_{infl} (see later Eq. 6.7).

Overall, two aspects need to be considered. On one hand, the strength parameters must be computed for the state of stress corresponding to the average pressure caused by the foundation load; on the other hand, owing to the high dilatancy of lunar soil at low confining pressures and under UHV, a significant difference exists between the peak and critical state parameters so that the choice of parameters is non-trivial if reliable predictions of the bearing capacity of lunar soil are to be achieved.

First, let us consider the case of a circular footing with no surcharge load ($q = 0$ in Eq. 6.3). Table 6.1 summarises the shear strength parameters obtained in Chapter 5 for the DEM model with rolling resistance considered in the modelling of lunar soil (with and without surface energy, both at the peak and critical state).

The two cases with and without surface energy (and rolling resistance) are compared in Fig. 6.1 and 6.2 in terms of ultimate bearing capacity and corresponding mean vertical stress for increasing footing diameter, computed according to Eq. 6.3 and 6.6 respectively. The soil weight γ_s of Eq. 6.3 is calculated as an average value corresponding to an influence depth of (Vesic, 1991):

$$H_{infl} = 0.5B \tan\left(45 + \frac{\phi}{2}\right) \quad , \tag{6.7}$$

while the formula prescribing the average in-situ lunar soil weight as a function of depth is used with reference to Eq. 2.2.

Surface energy, γ (J/m^2)	Rolling parameter, η (-)	ϕ_{ps} (°)	c_{ps} (kPa)	ϕ_{cs} (°)	c_{cs} (kPa)
0.00	0.6	65	0.0	44	0.00
0.07	0.6	57	19	47	0.17

Table 6.1: Summary of peak and critical state strength parameters, such as macroscopic friction angle and cohesion, obtained using the DEM model with rolling resistance proposed for lunar soil in Chapter 5.

Samples at 100% of relative density were employed. Relative density affects dilatancy which in turn affects the peak strength parameters. By examining Fig. 6.1, it can be observed that the effect of significant peak cohesion influences the ultimate bearing capacity in such a way that it remains almost constant with increasing footing diameter. In other words, the cohesive term of Eq. 6.3 prevails over the contribution due to the soil weight, since no surcharge was considered in the analysis. Therefore it can be concluded that bearing capacity does not seem to be a concern on the lunar soil.

At the critical state, the results affected by cohesion tend to line up with the cohesionless solutions as the footing diameter increases, see Fig. 6.2. This is consistent with the fact that increasing the footing size should result in an increase of soil stresses due to the higher foundation load, which in turn entails a lesser effect of surface energy forces on the macroscopic strength (see chapter 5).

Note that the strength parameters were computed from triaxial tests run at confining pressure less than 10kPa (see Chapter 5). As mentioned earlier, bearing capacity results should also be judged against the stress levels associated with their values. The mean confining pressure due to the foundation load, in particular, should be in line with the stress levels at which the strength parameters were computed (*i.e.* $p \leq$ 10kPa). At the critical state, a footing diameter less than 10cm satisfies this requirement, see Fig. 6.2(b). At the peak state, on the other hand, the limit would be one order of magnitude lower, thus around 1cm (see Fig. 6.1(b)). This finding leads to two main observations. Firstly,

the high shear strength parameters of lunar soil computed at low confining pressures (where cohesion plays an important role) result in very high mean stress levels even for very small foundation diameters, meaning that the calculations should be repeated with parameters obtained at higher confining pressure. Note that in such a case the presence of surface energy forces would play a negligible contribution, since the numerical simulations demonstrated that macroscopic cohesion (due to vdW forces) disappears with increasing stress level (see Chapter 5). Secondly, there is a huge discrepancy between the peak (obtained at very high relative density) and critical state results. This is a result of the difference obtained between the peak and critical state parameters which poses the question of whether the bearing capacity calculations should consider peak or critical state strengths. This issue will be dealt with in the next section where a method recently developed to yield more realistic bearing capacity calculations, is adopted.

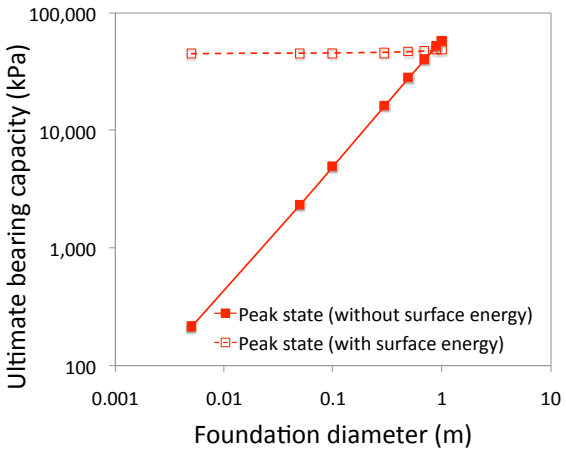

(a) Ultimate bearing capacity calculated for peak strength parameters obtained by DEM analyses versus footing diameter.

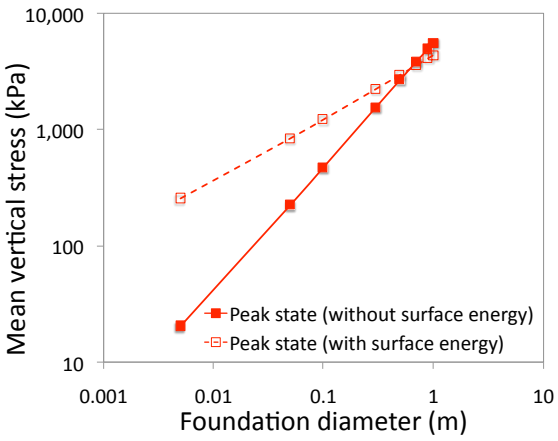

(b) Mean vertical stress below the footing vs footing diameter.

Figure 6.1: Peak state results obtained for the various DEM models presented in Chapter 5.

6.2.3 An alternative method to compute bearing capacity using soil dilatancy

It was pointed out by Perkins and Madson (2000) that there are some important limitations to the classical semi-empirical bearing capacity equation expressed by Eq. 6.1. First, it was

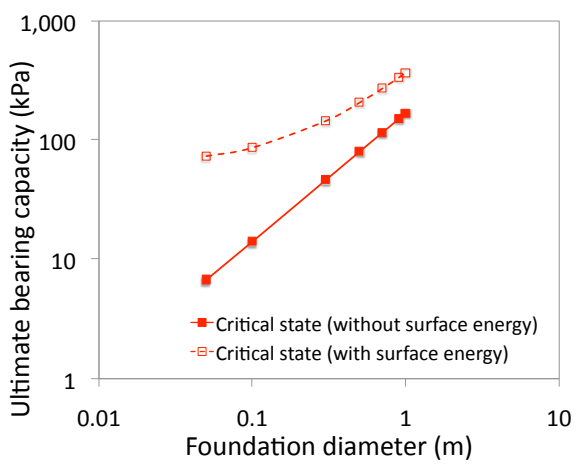

(a) Ultimate bearing capacity vs footing diameter for critical state parameters obtained using various DEM models.

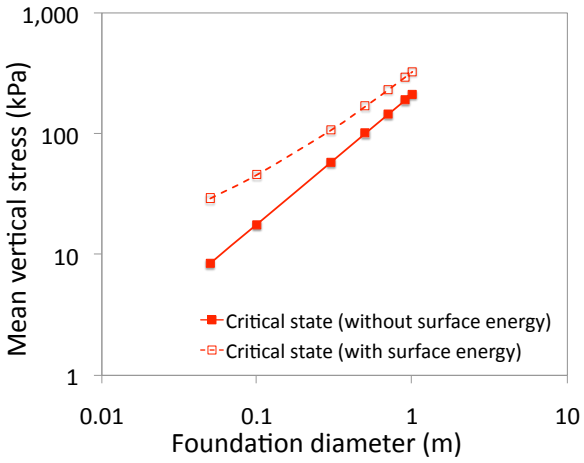

(b) Mean vertical stress below the footing vs footing diameter.

Figure 6.2: Critical state results obtained for the various DEM models presented in Chapter 5.

observed that the resistance does not increase linearly with the footing width (Kumar and Khatri, 2008). In other words, the bearing capacity factor N_γ is found to depend on the footing size (Kumar and Khatri, 2008) and this dependency becomes particularly strong as the footing width reaches large values. Ultimately this effect is due to the fact that the mobilised friction angle decreases with increasing stress level (Kumar and Khatri, 2008). Second, Eq. 6.1 is valid under the assumption of plane strain conditions, whereas the soil shear strength is often computed by means of triaxial tests. Friction angles derived under axisymmetric conditions can be significantly higher than those corresponding to plane strain conditions, owing to the very different failure modes occurring in the two cases (Zhao and Evans, 2011; Alshibli et al., 2003).

At least some of these limitations can be overcome by adopting an approach that aims to account for the progressive failure mode characterising the soil under a footing as attempted by Perkins and Madson (2000).

Perkins and Madson (2000) proposed an approach which computes an intermediate bearing capacity lying in between the peak and critical state values. The method is of empirical nature and requires the knowledge of the following parameters: the soil relative density,

the buoyant unit soil weight (which in our case coincides with γ_d), the strength parameters and the geometry of the foundation (Perkins and Madson, 2000). The main purpose of the method is to calculate a reduced peak bearing capacity which provides a better fit with the experimental data than what predicted by the Terzaghi equation (Eq. 6.1). This can be achieved by computing an index of progressive failure I_{PF} (whose formula was found to best fit experimental data from tests conducted on various sands, including lunar soil simulants), which was defined as:

$$I_{PF} = 0.044 I_R + 0.65 \quad , \tag{6.8}$$

where I_R is a dilatancy index based on Bolton's equation (Bolton, 1986) defined as:

$$I_R = D_R(Q - \ln p) - R \quad , \tag{6.9}$$

$$A = \frac{1}{3}\left(\frac{L}{B} + 8\right) \quad , \tag{6.10}$$

where Q and R are empirical parameters which are generally taken equal to 10 and 1 respectively. The index of progressive failure is then used to compute a reduced peak bearing capacity such that:

$$q_{u,predicted} = I_{PF} q_{u,cv} + (1 - I_{PF}) q_{u,peak} \quad , \tag{6.11}$$

where $q_{u,peak}$ and $q_{u,cv}$ correspond to the peak and constant volume bearing capacities. The method is also complemented by an iterative procedure to compute $q_{u,peak}$, assuming that only the critical state parameters are known. This is not required in the present case since the parameters have been numerically obtained at the peak as well at the critical state.

The reduced bearing capacity given by Eq. 6.11 was calculated using the strength parameters of lunar soil (corresponding to the case with surface energy forces and rolling resistance, see Table 6.1) and it is presented in Fig. 6.3 for various footing diameters. The corresponding mean stress is also illustrated in Fig. 6.4. The results indicate that the bearing capacity predicted by the above method lies between the critical and peak strength, with a leaning toward the peak values. According to Perkins and Madson (2000) this is the case when a progressive failure is unlikely and therefore experimental results could resemble the peak

bearing capacity.

Although the aforementioned observations need further studies and experimental work on real lunar soil to be certain, the above method provides a sensible solution which estimates the soil bearing capacity as an intermediate value between peak and critical strength. This becomes particularly useful when a huge difference exists between the two conditions, such as the case for low loading level and/or small foundation width (the level of confinement is a consequence of foundation width and loading).

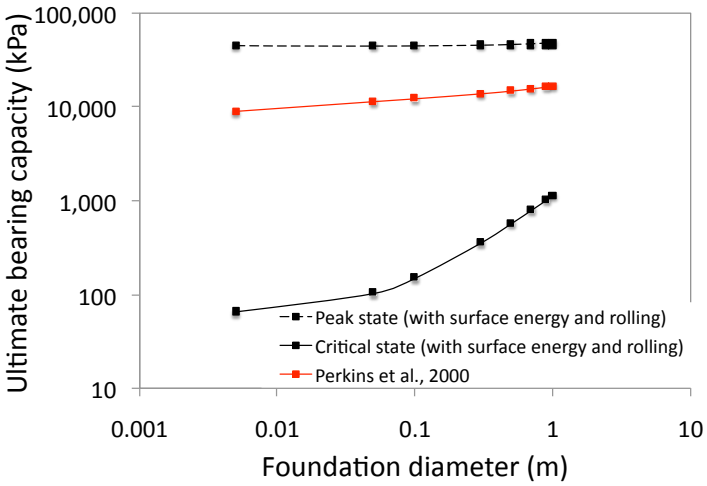

Figure 6.3: Bearing capacity of a circular footing of various diameter (no surcharge load is considered). The DEM solutions obtained at both the peak and critical states (with rolling resistance and surface energy forces) are compared with the intermediate solution obtained using the method by Perkins and Madson (2000).

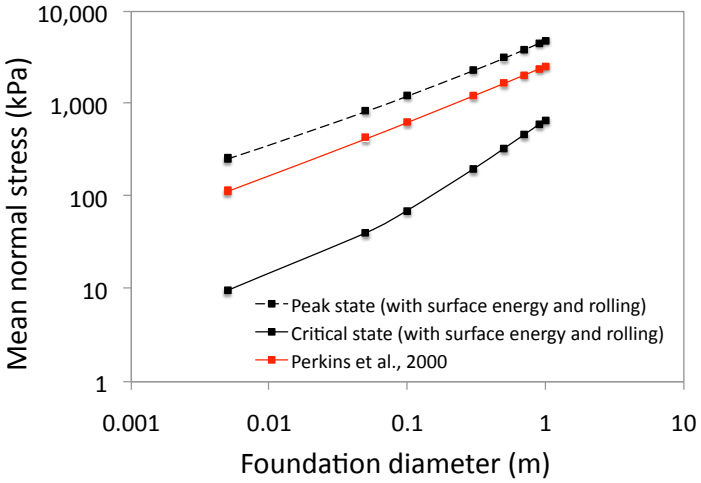

Figure 6.4: Mean normal vertical stress due to the bearing load of a circular footing of various diameters and without surcharge. Comparison of peak and critical state DEM results (obtained with rolling resistance and surface energy forces) with the method proposed by Perkins and Madson (2000).

6.3 Implications for trafficability and wheel-soil interaction studies

This section will deal with the analysis of the performance of a wheeled vehicle travelling on the lunar terrain. Such analyses are known in the literature as trafficability studies (Bekker, 1956). Terramechanical analyses have received enormous attention in previous lunar exploration programs because of the need to develop machines able to operate successfully on the Moon. However, once again problems have been related to the difficulties in accounting for the peculiarities of the lunar environment (temperature fluctuations, hard vacuum) and hence obtain reliable experimental results with regards to the mobility performance of lunar rovers (Asnani et al., 2009, e.g.).

The implications of the high lunar soil shear strength parameters (as derived in Chapter 5 for samples with surface energy and rolling resistance) will be examined, with regards to the mobility performance of a wheeled robotic vehicle. As an example, we will take a vehicle that has already been designed for lunar soil explorations, which is the Apollo Lunar Rover Vehicle (LRV), illustrated in Fig. 6.5 (Costes et al., 1972). More specifically, the fundamental

problem of wheel-soil interaction will be addressed and suggestions regarding the vehicle performance will be given based on its solution.

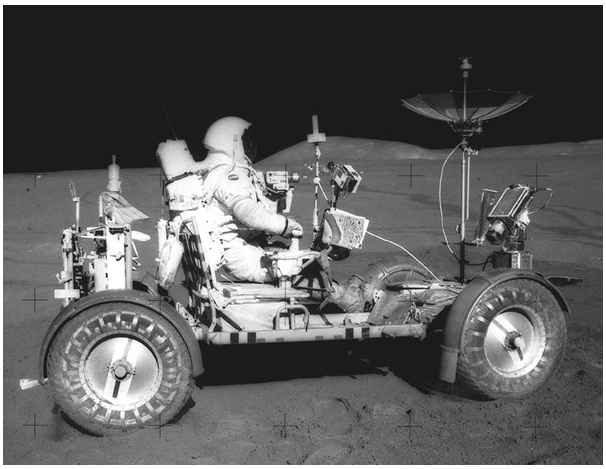

Figure 6.5: Apollo LRV (NASA Image AS15-85-11471).

The problem of wheel-soil interaction is rather complex, and still not well understood. It requires the combined effort of different branches of science and engineering, including soil and contact mechanics, material characterisation and advanced laboratory techniques to be solved and analysed. The problem has been previously tackled chiefly by means of empirical or semi-empirical approaches (e.g. Bekker, 1960). Bekker (1960) theory is still largely considered the most appropriate method for the analysis of a vehicle performance on a given terrain. It defines a pressure-sinkage relationship of the kind $p = kz^n$, where p is the applied pressure, z the corresponding wheel sinkage and k a constant parameter which in turn is a function of empirically determined constants as for the exponent n. Such constants can be determined by means of the so called Bevameter test (Bekker, 1960). In terms of shear strength versus shear displacement, an analogous relationship has been developed by Janosi and Hanamoto (1961), which is also based on a number of material constants determined empirically by means of the Bevameter test. Since no information is available on the constant parameters characterising the aforementioned relationships for the lunar terrain, a lunar soil simulant, GRC-1, has been designed with the objective to provide a reliable soil simulant that reproduces the deformation characteristics of the lunar terrain for vehicle testing on Earth (Oravec et al., 2010). The design of GRC-1 was mainly influenced by the cone penetrometer test results from Apollo 15 and 16 missions. As such, GRC-1 did

not prove to have the same high strength of lunar soil although it was proven to be useful for large scale vehicle testing (Oravec et al., 2010).

In recent studies, the DEM approach has also been adopted in an attempt to capture the salient features of the wheel-soil interaction behaviour observed in laboratory experiments and to conceive a better wheel design concept through parametric studies (Nakashima et al., 2007, 2010; Li et al., 2010; Knuth et al., 2012). However, DEM studies of boundary value problems are currently affected by significant limitations such as the dependency of the results on scale effects and the difficulty in validating 2D simulations against experimental findings carried out under 3D conditions. Moreover, given the complexities introduced by the wheel-soil interaction problem, a comprehensive numerical study of vehicle mobility on the lunar terrain is out of the scope of this thesis and the interested reader is referred to the relevant literature for further insight into the topic (Costes et al., 1972; Asnani et al., 2009; Oravec et al., 2010; Chhaniyara et al., 2012, e.g.). Nevertheless, the main scope here remains to inquire about the effects of the shear strength of lunar soil on the wheel performance by taking an approach which relies only on the knowledge of the soil strength parameters, such as cohesion and friction angle. This can be achieved by means of a simplified analytical approach, without the need to run further experiments, as illustrated in the following subsection.

6.3.1 Overview

An approximate analytical method to solve the wheel-soil interaction problem will now be presented. The method is an extension of the approach proposed in Hambleton and Drescher (2009) for the special case of a rigid towed wheel on a deformable terrain. It is sought to develop a more general approach able to handle all the three possible working conditions of a rotating wheel interacting with the soil, which include a self-propelled, a driven and towed wheel respectively (Fig. 6.6).

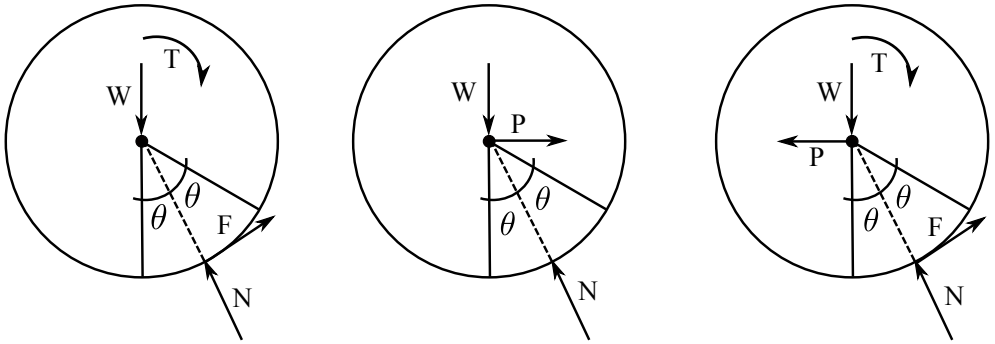

(a) Self-propelled wheel. (b) Towed wheel. (c) Driven wheel.

Figure 6.6: Free body diagram for the wheel-soil interaction problem of a towed, driven and self-propelled wheel respectively.

6.3.2 Self-propelled wheel

A simple analytical approach will now be outlined to solve the problem of wheel-soil interaction for a rigid self-propelled wheel in rolling motion on a deformable terrain. In such a case, only an input torque is applied in addition to the vertical weight, W, carried by the wheel (see Fig. 6.6(a)). The vertical equilibrium requires that the reaction force between the soil and the wheel be equal to W. The contact force can be split into two contributions, a tangential frictional force $F = W \sin\theta$ and a normal force $N = W \cos\theta$, with θ being half of the wheel-soil contact angle as indicated in Fig. 6.7. The sinkage is related here to the geometry of the wheel and the soil deformation and is therefore equal to (see Fig. 6.7):

$$z = R(1 - \cos 2\theta) \quad . \tag{6.12}$$

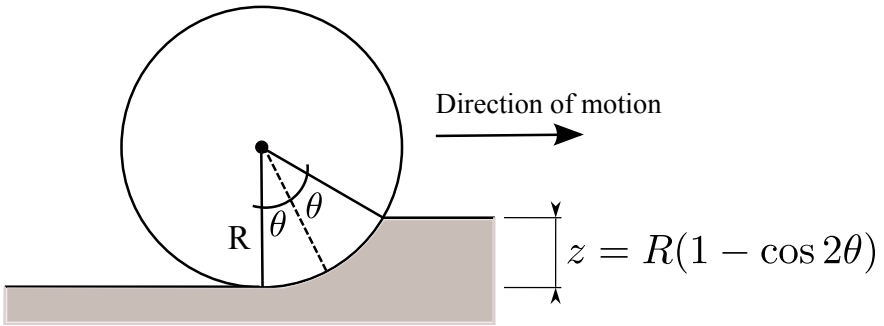

Figure 6.7: Geometry of the wheel and definitions of wheel-soil contact angle and sinkage.

The wheel-soil contact problem can now be solved as a bearing capacity problem where the rectangular footing base is provided by the region of the wheel in contact with the soil and where the load is provided by the wheel-soil interaction. Now, to further simplify the problem, let us make the assumption that the contact angle is negligible, *i.e.* $\theta \approx 0$. In such a case, the vertical load is simply equal to the weight W and $F = 0$ (see Fig. 6.8). According

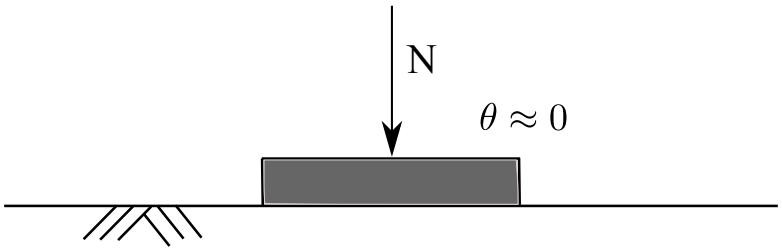

Figure 6.8: For negligible contact angle the footing is horizontal and the load is vertical.

to Terzaghi (Terzaghi, 1943), the ultimate bearing capacity load for cohesive-frictional soils and rectangular footing can be found using the formula expressed by Eq. 6.3 which, ignoring any overburden, reduces to:

$$q_u = cN_c\zeta_c + 0.5\gamma_s B N_\gamma \zeta_\gamma \quad , \tag{6.13}$$

where the shape factors were reported in Eq. 6.4. Note that the above equation could be replaced by the reduced bearing capacity expression given by Eq. 6.11. However, this would lead to a too complex final expression for the contact angle θ. Apart from this complexity, it seems reasonable for now to neglect the occurrence of progressive failure in the soil beneath the wheel, which is the fundamental reason on which the reduced bearing capacity method was based (Perkins and Madson, 2000).

In the current case, L is the width of the wheel and $B = R\sin 2\theta$. Substituting all the terms into Eq. 6.13 it can be shown that:

$$\begin{aligned} \frac{W}{L(R\sin 2\theta)} = {} & c(N_q - 1)\cot\phi \left(1 + \frac{R\sin 2\theta}{L}\frac{N_q}{(N_q-1)\cot\phi}\right) \\ & + 0.5\gamma_s(R\sin 2\theta)(N_q+1)\tan\phi\left(1 - 0.4\frac{R\sin 2\theta}{L}\right) \quad . \end{aligned} \tag{6.14}$$

Given a weight W applied to the wheel and soil properties such as cohesion and friction angle, it is then possible to obtain the wheel-soil contact angle, 2θ, by numerically solving Eq. 6.14. Once the contact angle is known, the sinkage can be then evaluated according to Eq. 6.12. The torque and the total power can also be determined such as:

$$T = WR\sin\theta \quad , \tag{6.15}$$

$$P_{ow} = T\omega = \frac{Tv}{R} \quad , \tag{6.16}$$

where ω and v are the angular and linear velocity, respectively. For a purely cohesive soil ($\phi = 0$), and ignoring the foundation shape effects, the total power P_{ow} is equal to $(W^2 v)/(2LcN_cR)$.

The above solution can be compared with a more exact formulation which accounts for both the effects of the load inclination and the tilting of the foundation base. Fig. 6.9 illustrates a more realistic representation of the bearing capacity problem devised for a self-propelled wheel.

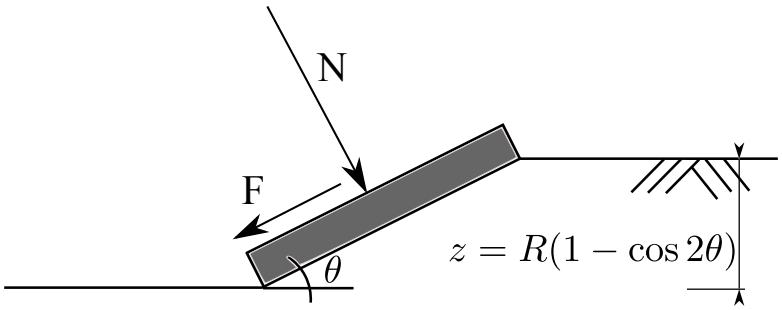

Figure 6.9: Tilting of the footing and inclination of the load.

The base of the foundation is inclined of an angle equal to half the wheel-soil contact angle, i.e. θ. Because of that, the reaction load applied to the footing can be split into a shear and normal contribution, F and N respectively. According to Vesic (1973), the bearing capacity equation can be modified to account for load inclination and the tilting of the base through the introduction of some additional factors to Eq. 6.13. The amended

formula reads (Vesic, 1973):

$$q_u = \frac{N}{L2R\sin\theta} = cN_c\zeta_c\zeta_{ci}\zeta_{ct} + 0.5\gamma_s BN_\gamma\zeta_\gamma\zeta_{\gamma i}\zeta_{\gamma t} \quad , \tag{6.17}$$

where the inclination factors are defined as (Vesic, 1973):

$$\zeta_{qi} = \left(1 - \frac{F}{N + 2R\sin\theta Lc\cot\phi}\right)^2 \quad , \tag{6.18}$$

$$\zeta_{\gamma i} = \left(1 - \frac{F}{N + 2R\sin\theta Lc\cot\phi}\right)^3 \quad , \tag{6.19}$$

$$\zeta_{ci} = 1 - \frac{2F}{2R\sin\theta LcN_c} \quad , \tag{6.20}$$

and the base tilt factors as (Vesic, 1973):

$$\zeta_{qt} = (1 - \alpha\tan\phi)^2 \quad , \tag{6.21}$$

$$\zeta_{ct} = 1 - \frac{2\alpha}{\pi + 2} \quad , \tag{6.22}$$

where α is the inclination of the base expressed in radians which, in this study, is equal to θ. Eq. 6.17 is more cumbersome than Eq. 6.14 but it can be likewise solved numerically as a function of θ.

While conceiving the above method, a series of assumptions have been implied, such as:

(i) the normal contact stress distribution has been assumed to be symmetric and to reach its maximum at the midway point of the wheel-soil contact angle, in agreement with previous authors (Hovland, 1973);

(ii) rutting, often manifested as a load-dependent process (Hambleton and Drescher, 2009), has been completely dirsegarded;

(iii) the rotating circular wheel is rigid and is moving on a deformable soil;

(iv) plane-strain conditions have been assumed;

(v) soil inertia forces have been neglected, which has been argued to be a reasonable assumption (Hovland, 1973);

(vi) finally, it is noted that no relationship between slip and contact angle has been used

to solve the problem in the current analysis, meaning that slip remains unknown but not necessarily zero.

The two solutions proposed above for a self-propelled wheel, with and without inclined load and tilting base, were compared using the parameters of an LRV wheel as reported in Table 6.2. The comparison between the two solutions is presented in Fig. 6.10 in terms of

Weight (N)	Radius (m)	Width (m)
286	0.41	0.23

Table 6.2: LRV wheel parameters (Costes et al., 1972; Oravec, 2009).

wheel-soil contact angle, wheel sinkage and total power. The wheel-soil contact angles were obtained by numerically solving Eq. 6.13 and 6.17 considering a friction angle in the range between 40 and 50^o and different values of cohesion representative of the results obtained for lunar soil at both the critical and peak state (with surface energy and rolling resistance). The results are also compared against the results for cohesionless soil, as shown in Fig. 6.10.

It is interesting to observe that very little difference exists between the solutions for tilted and non-tilted base, whereas some divergence is detected only in case of low friction angles and cohesionless soil, see Fig. 6.10. The solutions indicate that θ decreases with increasing friction angle in a non-linear manner as shown in Fig. 6.10(a). The same tendency applies to the wheel sinkage, Fig. 6.10(b), as well as to the total power, see Fig. 6.10(c). As expected, the higher the strength of the material, the lower the sinkage experienced by the wheel in contact with the terrain, or in other words the material experiences less deformation. Increasing the soil cohesion also turns out in lower sinkage and so power as shown in Fig. 6.10. With cohesion ($c = 19$kPa), the power requirement is reduced by two orders of magnitude as shown in Fig. 6.10(c).

Note that Hambleton and Drescher (2009) used a similar solution applied to a towed wheel but with a given contact angle 2θ. The load perpendicular to the wheel-soil contact area was computed for different values of sinkage and wheel-soil contact angle under prescribed soil properties. Results for a tilted and non-tilted base were assessed and compared against

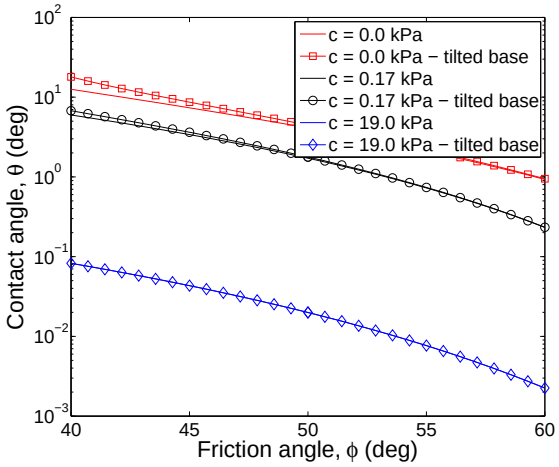

(a) Wheel-soil contact angle.

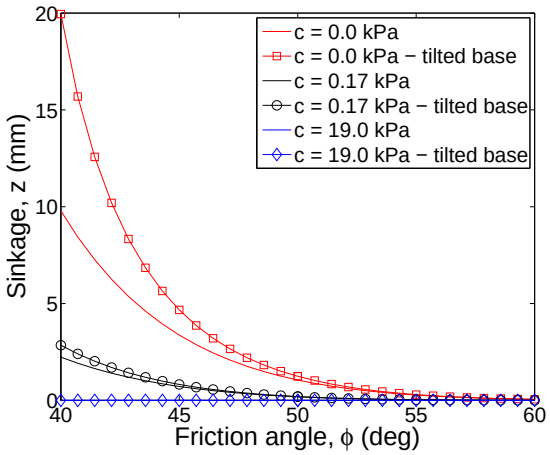

(b) Wheel sinkage.

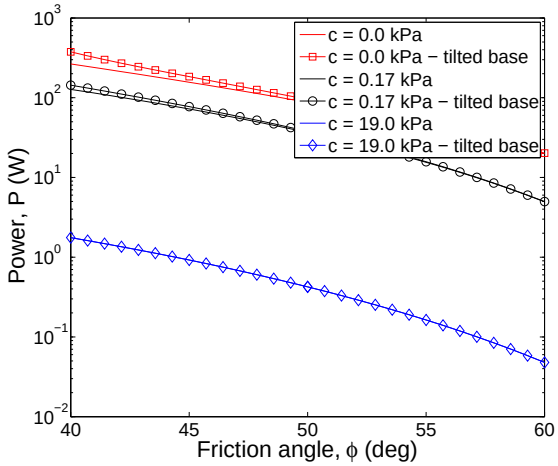

(c) Total power.

Figure 6.10: Solution of the wheel-soil interaction problem for a self-propelled wheel. The two cases of tilted and non-tilted base are compared. A wheel's velocity of 4.27m/s was assumed in the analysis.

FEM numerical results in terms of vertical force versus wheel sinkage. Analytical results were also compared with experimental data from clay and dense sand. The comparison was quite encouraging despite the uncertainty on the strength parameters corresponding to the soil used for experimental testing.

6.3.3 Towed wheel

The above method will be now used to solve the wheel-soil contact problem for a towed wheel. The free body diagram of a towed wheel is illustrated in Fig. 6.6(b). As usual, a

vertical load is applied to the centre of mass of the wheel but no torque is required. Instead, the drawbar pull force P is applied in the direction of motion and a normal contact force, equal to $W/\cos\theta$, develops at the wheel-soil interface. Once again, the contact angle is computed following Eq. 6.17 but without the need to consider the inclination factors ζ_i since this time $F = 0$; thus, only the tilting factors will be included. The drawbar pull force is computed as $P = -W\tan\theta$ while the associated power required results in $P_{ow} = Pv$. The sinkage is computed as usual from Eq. 6.12. The results in terms of wheel-soil contact angle, sinkage, drawbar pull force and total power for increasing friction angle and three different values of cohesion are reported in Fig. 6.11. Once again, the parameters are found to be lower, in absolute terms, for a higher material strength.

6.3.4 Driven wheel

For a driven wheel, many forces are present such as the drawbar pull force, the applied torque and the vertical load W, as indicated in Fig. 6.6(c). Therefore, in order to satisfy the equilibrium, both a normal and shear force must be applied at the wheel-soil interface, given by:

$$\begin{aligned} N &= W\cos\theta - P\sin\theta \quad , \\ F &= W\sin\theta + P\cos\theta \quad . \end{aligned} \tag{6.23}$$

The torque and the required power are then equal to:

$$T = WR\sin\theta + PR\cos\theta \quad , \tag{6.24}$$

$$P_{ow} = \frac{Tv}{R} - Pv \quad . \tag{6.25}$$

Considering a four wheeled vehicle where the front wheels are driven whilst the rear wheels are towed, it follows that P can be determined by first solving the problem of a towed wheel for P (see above) which can be subsequently used to determine F and N according to Eq. 6.23. A comparison of the results between the three cases of self-propelled, towed and driven wheels is presented for different values of cohesion in Figures 6.12, 6.13 and 6.14.

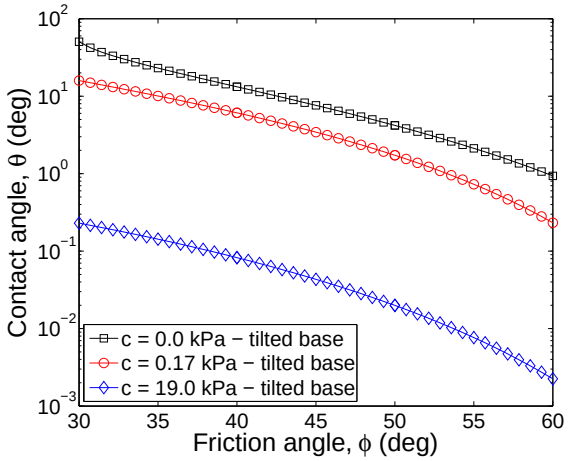

(a) Contact angle solution.

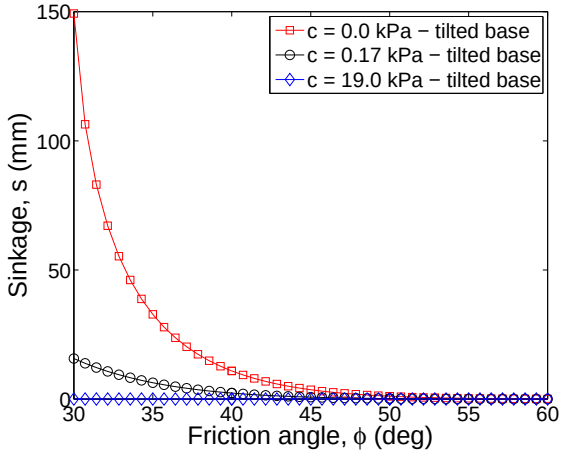

(b) Sinkage.

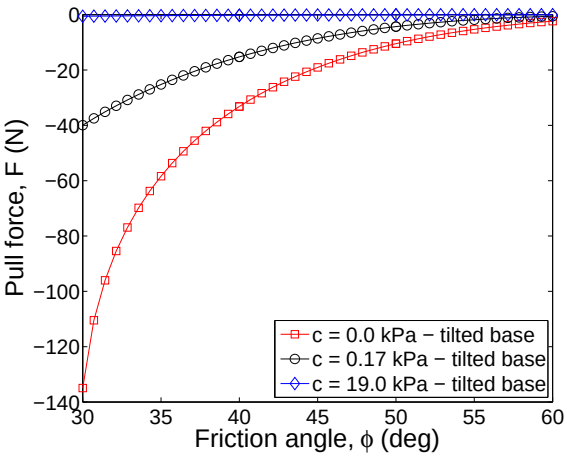

(c) Drawbar pull force.

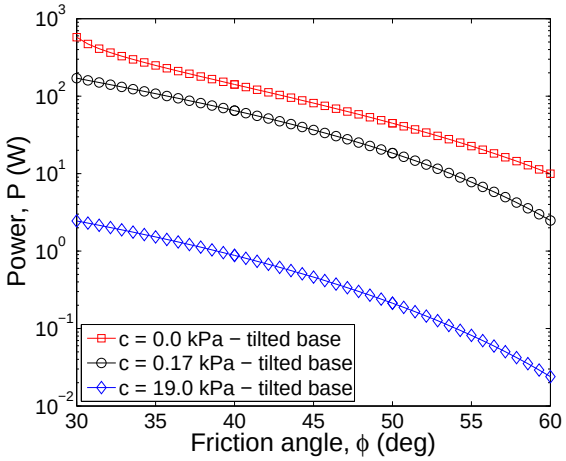

(d) Power.

Figure 6.11: Solution of the wheel-soil interaction problem for a towed wheel. The results are illustrated for the case of tilted base. A wheel's velocity of 4.27m/s was assumed in the analysis.

Wheel-soil contact angle, sinkage and total power were computed for each case and for increasing friction angle. Regardless of the cohesion value, it is a common feature for all the parameters to decrease as the friction angle increases. However, for higher values of cohesion, the difference between the three cases becomes almost nil as seen in Fig. 6.14.

The comparison between all three cases above can be particularly interesting in terms of power consumption of a typical four wheeled vehicle. For instance, let us consider two four-wheeled vehicles, the first distinguished by all four wheels being driven and the second provided with two driven wheels and two towed wheels. For a cohesionless soil and a friction angle of 45^o, the total power required to move the four-wheeled drive vehicle equals 368W,

whereas for the two-wheeled drive vehicle it would be equal to 375W. It follows that a vehicle designed with four self-propelled wheels requires slightly less power consumption to move than a combination of driven and towed wheels. This is a very welcome observation particularly as regard the design of lunar planetary rovers, whose electric resources available for mobility are often extremely limited.

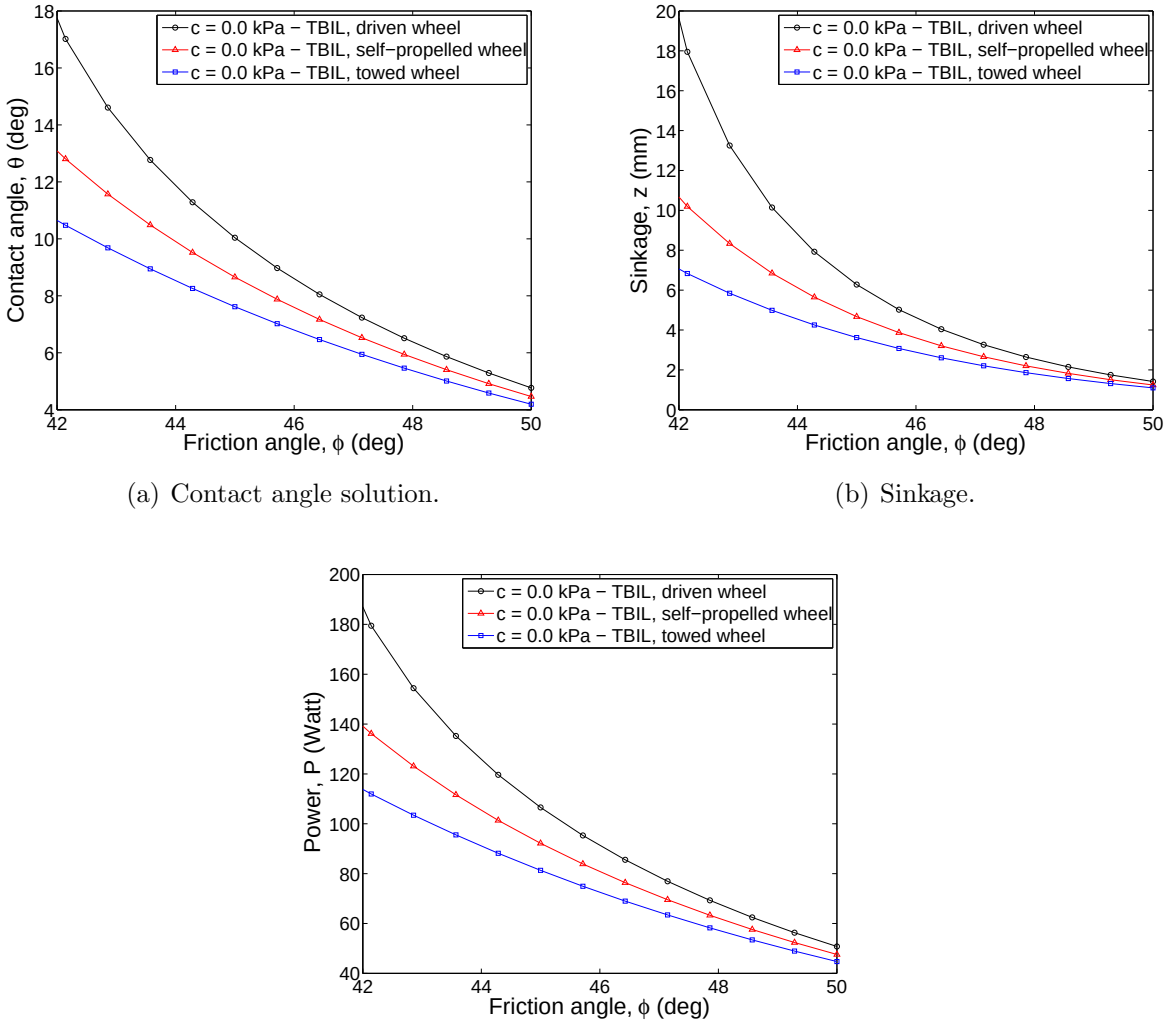

(a) Contact angle solution.

(b) Sinkage.

(c) Power.

Figure 6.12: Comparison of the solutions obtained for a self-propelled, towed and driven wheel for different friction angles and without soil cohesion. The solutions are obtained for a tilted base and with inclined load. A wheel's velocity of 4.27m/s was assumed in the analysis.

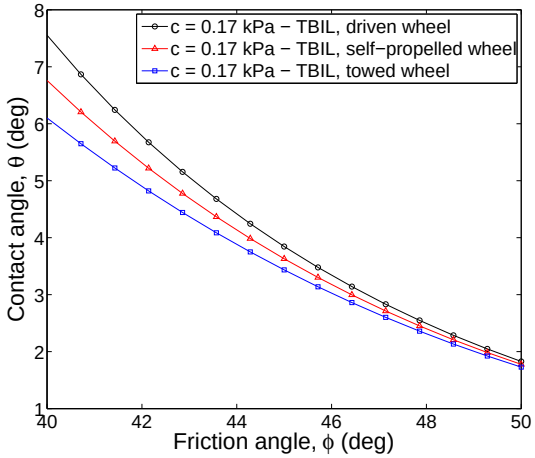

(a) Contact angle solution.

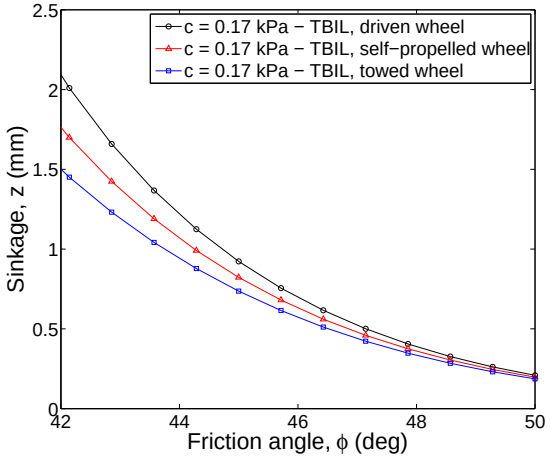

(b) Sinkage.

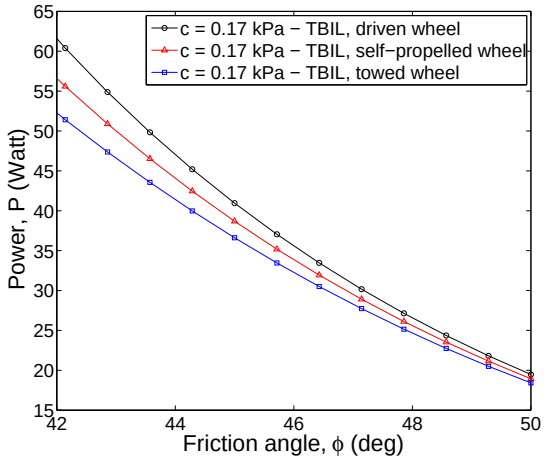

(c) Power.

Figure 6.13: Comparison of the solutions obtained for a self-propelled, towed and driven wheel for different friction angles and with a constant cohesion of 0.17kPa. The solutions are obtained for a tilted base and with inclined load. A wheel's velocity of 4.27m/s was assumed in the analysis.

6.3.5 Summary

The above study has illustrated that a simple yet comprehensive method, founded on the analogy between the bearing capacity problem of a shallow foundation and the contact mechanics of the wheel-soil interaction, can be used to compute some of the important parameters characterising the mobility performance of a rigid wheel in rolling motion on a deformable terrain.

Although the method has not been tested against experimental results, its derivation

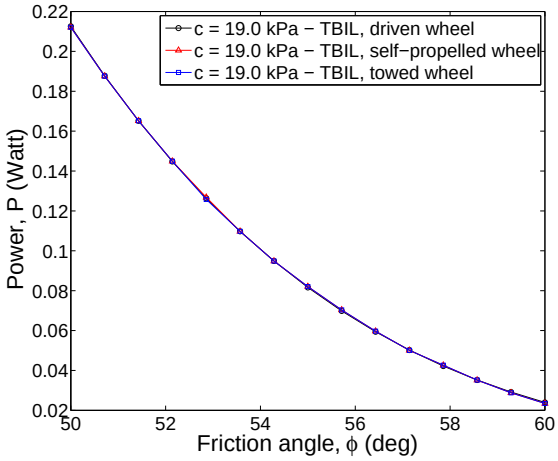

Figure 6.14: Comparison between the solutions between a self-propelled, towed and driven wheel for increasing friction angle and constant cohesion of 19kPa. The solutions are obtained for a tilted base and with inclined load. A wheel's velocity of 4.27m/s was assumed in the analysis.

has been simply based on the laws of equilibrium and under the assumption that the soil beneath the wheel is at impeding shear failure. Progressive soil failure has been neglected in this case, as its consideration was not thought to provide a significant contribution given the other limitations of the model. Soil strength parameters have been obtained from triaxial laboratory experiments, however, we note that the deformation mode affecting the portion of soil beneath the wheel is not yet well understood and therefore a different kind of laboratory test might be more appropriate to use in future investigations (*e.g.* a ring shear test).

It has been shown that the method is capable of solving the wheel-soil interaction problem under various dynamic conditions, such that of a self-propelled, towed and driven wheel. Wheel sinkage, wheel-soil contact angle and total power consumption could be computed by numerically solving a set of equations which were formulated based on the above assumptions. The influence of shear strength parameters on the mechanical response of the wheel were investigated for the three different dynamic conditions. It was found that for all case a higher shear strength corresponds to a lower wheel sinkage and thus total power. This is an expected result since it can be imagined that for a prescribed load high shear strength results in a lower contact area, which in turn is associated with a lower wheel sinkage (and thus power usage), as also predicted by the Bekker semi-empirical model. Finally, it was

also found that the best performing situation would correspond to that of a vehicle equipped with all four self-propelled wheels.

In conclusion, although several assumptions have been required to formulate a simple analytical solution of the wheel-soil interaction problem, its use will allow designers to make predictions concerning vehicle power consumption. The method will also allow different shear strength parameters to be considered, and therefore soils under different environmental conditions, as illustrated in this study.

6.4 Slope stability analysis on lunar soil

Several methods have been proposed in the literature to assess the stability of homogenous soil slopes. In particular, limit equilibrium and limit analysis methods have been developed and applied to slope stability analysis (e.g. Chen et al., 1969; Michalowski, 2002; Utili, 2006). Typically, slope stability charts have been produced in terms of a dimensionless number known as stability factor, N_s, defined as $\gamma_s H/c$ according to Chen et al. (1969), where γ_s is the soil unit weight, H is the height of the slope and c the soil cohesion. In traditional geotechnics the factor of safety for cohesive-frictional slopes is defined as the reduction of the value of the slope strength parameters (c, ϕ) for which the slope would be at impending collapse:

$$F_s = \frac{c}{c_f} = \frac{\tan(\phi)}{\tan(\phi_f)} \quad , \tag{6.26}$$

with c_f and ϕ_f the cohesion and angle of friction at failure.

The assessment of the influence of the strength parameters computed for lunar soil (with rolling resistance and surface energy, see Table 6.1) on the stability of a uniform vertical slope will be now carried out by means of limit analysis. This method will now be briefly recalled.

The limit analysis method is based on two theorems of plasticity theory, the so-called lower- and the upper-bound solution respectively. They are both based on the assumption

that the soil is suitably described by an associated elasto-perfectly plastic constitutive law. While the former is used to find a set of stresses which satisfy the equilibrium conditions under the applied loads, the latter identifies a collapse mechanism per which the work done by the external forces is equal to the energy dissipated internally. In the following, the upper-bound solution will be employed according to the energy balance equation achieved by Chen et al. (1969).

Chen et al. (1969) assumed that the slip failure line matches a log-spiral line. In such a case, the upper bound solution to the slope stability is both a function of the soil properties, c, ϕ and γ_s, as well of the geometrical features of the soil slope (see Fig. 6.15). Chen

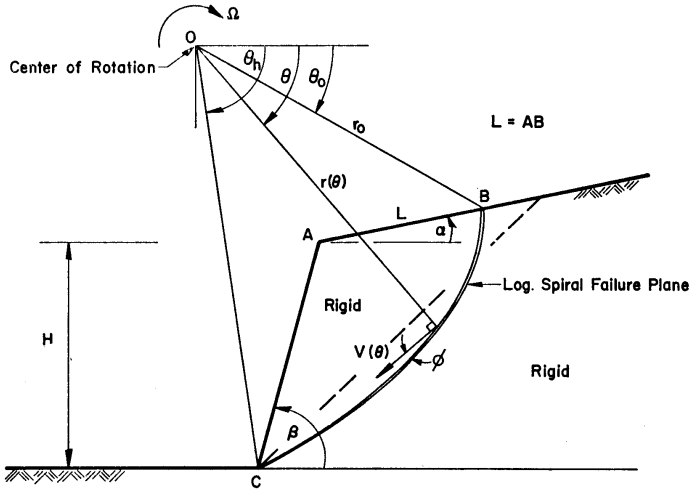

Figure 6.15: Formulation of the slope stability problem and geometry of the slip failure line (Chen et al., 1969, after).

et al. (1969) derived numerically the solution for several friction angles and slope angles, β and α (see Fig. 6.15). However, the values of friction angle considered in the analysis did not include the high shear strength values obtained for lunar soil in Chapter 5. More recently, other researchers have published stability charts for several friction angles and cohesion values (Michalowski, 2002) but the charts are often prone to difficult interpretation, particularly in the range of interest for lunar soil. Thus, the numerical analyses were repeated in this study using a Matlab code to find the upper-bound solution for the stability of a uniform vertical slope (β = 90 deg and α = 0.0 deg) employing the method proposed by Chen et al. (1969).

The results in terms of stability number versus friction angle are illustrated in Fig. 6.16(a) for a unitary safety factor. As expected, N_s decreases non-linearly with the reduction in friction, and eventually reaches an upper bound solution of approximately 4 (Martin, 2011) which is valid for the case of undrained shear strength ($c = s_u$). The corresponding critical height of the same slope is computed from the expression of the stability number as $H_c = cN_s/\gamma_s$ (see Fig. 6.16(b) and Fig. 6.16(c)), where c is taken equal to 19kPa and 0.17kPa respectively, *i.e.* the values of peak and critical cohesion previously computed for lunar soil.

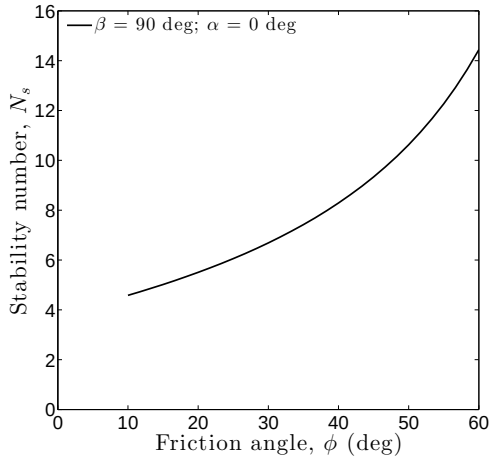

(a) Stability number for different friction angles.

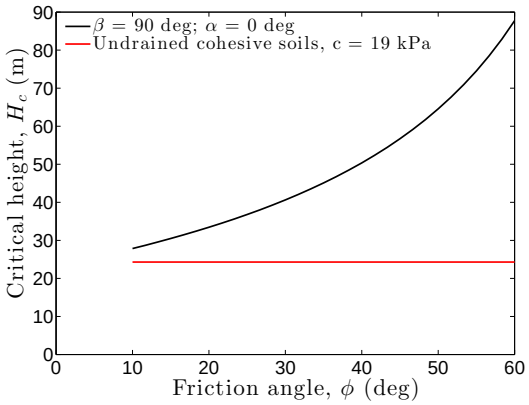

(b) Critical height for different friction angles and for the value of lunar soil cohesion identified at the peak state.

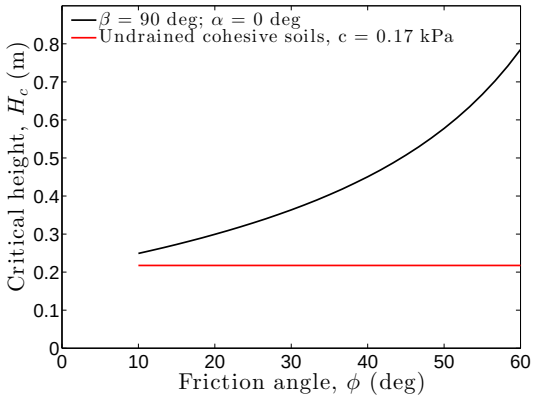

(c) Critical height for different friction angles and for the value of lunar soil cohesion identified at the critical state.

Figure 6.16: Stability number and critical height for a vertical cut in a uniform soil for different values of friction angle ($\gamma_s = 3{,}127\text{N/m}^3$).

The results of the upper-bound limit analysis corresponding to the peak and critical state parameters of lunar soil are also reported in Table 6.3. Once again, the key observation is that the critical height of the slope is significantly different at the peak and critical state of the material. The critical height at the peak state is exceptionally high due to the high peak shear strength parameters. The large discrepancy between critical and peak state results prevents a conclusive answer since there is no clear way to suggest which parameters should be selected for the problem of slope stability, as was previously done for the bearing capacity problem (see Sec. 6.2).

Table 6.3 also compares the results produced for frictional-cohesive soil with the results obtained for undrained shear strength (cohesive only soil). The comparison shows that the undrained shear strength solution provides a good estimate of H_c but only at the critical state. At the peak state, instead, the two solutions significantly diverge owing to the high peak state friction angle.

ϕ_{ps} (deg)	c_{ps} (kPa)	N_s	H_c (m)
57	19.0	13.05	79.3
0	19.0	4	24.3
ϕ_{cs} (deg)	c_{cs} (kPa)	N_s	H_c (m)
47	0.17	9.82	0.53
0	0.17	4	0.22

Table 6.3: Maximum slope of a vertical cut on the lunar soil according to the upper bound limit analysis solution ($\gamma_s = 3{,}127\text{N/m}^3$). Comparison with the results for cohesive only soil.

Finally, Carrier (2005) predicted that lunar soil would be able to withstand a vertical trench up to a depth of 3m based on direct observations of astronauts' footprints, and for a factor of safety of 1.5 (see Fig. 6.17). This result is found in between the peak and critical state solution, suggesting that instead operational shear strength parameters (which are often a source of uncertainty) should be adopted in the analysis of slope stability.

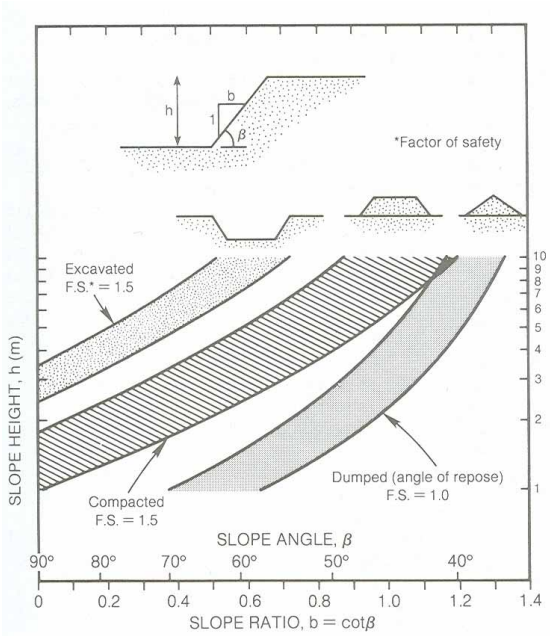

Figure 6.17: Estimates of slope stability on lunar soil from direct observations on the lunar surface (after Carrier et al., 1991).

6.5 Summary

This chapter discussed some of the engineering implications that the high shear strength of lunar soil might have on future lunar surface operations. Three problems of relevance in geotechnical engineering were examined: the first concerned the ultimate bearing strength of shallow circular foundations, the second with the solution of a simplified wheel-soil interaction problem and the third dealt with the maximum height that a vertical slope is able to withstand due to the cohesive and frictional properties obtained for lunar soil in the previous chapter.

It emerged that the significant difference existing between the critical and peak state parameters of lunar soil produces a substantial difference in terms of ultimate bearing strength. This led to a reconsideration of the Terzaghi's bearing capacity solution, given the need to account for the stress and density dependency of the soil strength parameters. Such a dependency can be realised by noticing that a progressive shear failure characterises the soil beneath a foundation. This was achieved by adopting a semi-empirical method proposed by Perkins and Madson (2000) which suggested that an intermediate bearing strength, lying

in between the critical and peak state strengths, should be used instead.

The wheel-soil interaction problem was solved using the Terzaghi expression of ultimate bearing capacity. An analytical approach was devised in order to investigate the wheel-soil interaction problem under three different dynamic conditions, involving a self-propelled, a towed and a driven wheel. The goal was to gain a better understanding of the performance of a four-wheeled vehicle operating on the lunar terrain. The results of the computations were presented in terms of wheel-soil contact angle, wheel sinkage and total power consumption. It was realised that in terms of total power, the solution of a vehicle with four self-propelled wheels is the most efficient one. Notwithstanding the restrictive assumptions lying behind the proposed model, and despite the fact that no comparison with experimental results was made, the new procedure may pave the way for a more reasonable soil-mechanics-based solution to wheel-soil interaction problems.

Finally, the stability factor of a vertical slope, obtained from slope stability computations based on the upper-bound limit analysis solution, was also found to be very different when considering the shear strength parameters at the critical and peak state. Similar to the case of bearing capacity, a method which accounts for the progressive strength of the soil should probably be adopted. Thus the limitations of the current approach prevents a conclusive answer to the problem of slope stability to be obtained. Although it may be tempting to say that the solution corresponding to the critical state should be chosen because it is more conservative for design purposes, it seems important to call for an approach which does not underestimate the soil strength and which is able to account for the high shear strength occurring at such low stresses and high density conditions.

Chapter 7

Conclusions and recommendations for further work

This chapter presents a summary of the main points of conclusions reached in the course of this thesis. The chief contributions, involving separate but closely related fields of study, are outlined and suggestions are advanced for future research developments.

7.1 Summary and conclusions

In this thesis, the results of a series of numerical experiments have been presented with the attempt to answer important questions related to the unusual behaviour showed by lunar soil. The answer to the question of how the characteristics of the lunar environment influence the fundamental soil behaviour is central to the success of future lunar operations, be they manned or robotic. In particular, it is of interest to know how, and to what extent, the presence of ultra-high vacuum and a low gravitational field modify the lunar soil shear strength. Previous attempts to provide a satisfactory answer have either been limited by the technology available at the time or have failed to include all the relevant features.

A number of steps have been required in order to provide a reliable answer to the above questions. As a consequence, the relevance of this research work has expanded to fields of study unrelated to lunar soil. Overall, the main contributions of this thesis have involved

the following studies: (i) a critical analysis of the current literature on microscopic adhesion phenomena, (ii) the investigation of DEM as a suitable tool to numerically model the soil behaviour, (iii) the study of the influence of surface energy forces and particle shape effects on the macroscopic behaviour of lunar soil, and finally (iv) geotechnical implications of the observed lunar soil behaviour with regards to soil bearing capacity, slope stability and trafficabiliy analyses. The key findings from each of the aforementioned studies will now be summarised.

(i) Critical review of the literature on lunar soil-related adhesion phenomena

- A contact model suitable for the modelling of frictional elastic adhesive macroscopic bodies with application to lunar soil was identified. The choice was based on the comparison between available continuum-based theories accounting for adhesion phenomena as well as the feasibility of their implementation into a DEM code. The selected model combines the JKR contact solution for adhesive bodies, a shear behaviour complying with the HM without micro slip solution, and the Kendall shear failure criterion to account for the presence of adhesion.
- Although an experimental campaign of the behaviour of real lunar soil tested in a lunar-like environment is still pending, it was found that there is sufficient experimental evidence to indicate that ultra-high vacuum may be responsible for the high shear strength shown by lunar soil compared to terrestrial soils of similar gradation (e.g. Vey and Nelson, 1966).

(ii) DEM as a suitable numerical tool to model the mechanical soil behaviour

- An in-depth investigation was conducted on the effects of a selected number of dimensionless physical parameters upon the macroscopic behaviour of a synthetic sample resembling the particle size distribution of lunar soil. The goal was to demonstrate that the DEM is an efficient tool to simulate the critical state of the soil under quasi-static conditions. It was found that the loading rate has non-negligible effects on the stress-strain and volumetric soil behaviour, even at very small values as recommended by previous DEM-led studies.
- The effect of strain rate was found to be more significant at large rather than

small strains. In other words, the value of strain rate at which the quasi-static conditions could be achieved at small strains did not coincide with the minimum strain rate satisfying the same conditions at the critical state. Moreover, the influence of strain rate at the critical state was particularly visible in terms of macroscopic porosity.

- The influence of pressure on the macroscopic behaviour was also also found non-negligible at the critical state. This led to a reconsideration of the method, involving the inertial number, which is generally used to tell if the numerical system has reached quasi-static equilibrium. Use of an alternative dimensionless inertial parameter as a basis for determining QS conditions was observed to lead to consistent results at the material critical state, and was proposed as a new method to study the critical state of soils under quasi-static conditions by means of DEM.

(iii) Study of the influence of surface energy forces and particle shape effects on the macroscopic behaviour of lunar soil

- Drained triaxial tests of very dense samples, with a particle size distribution and contact parameters typical of lunar soil, were performed at very low confining pressures, *i.e.* less than 10kPa, both with and without surface energy forces. Macroscopic stresses, volumetric deformations and microscopic variables, such as the mechanical coordination number, were recorded and compared at both the peak and critical state. It was observed that adhesion leads to a much higher peak stress ratio which tends to decrease with increasing stress. Significant cohesion was detected at the peak state only in the presence of adhesion. Moreover, the failure envelopes of the material tested with and without adhesion were found to be linear and parallel, at least within the stress range examined. At the critical state, though, very little cohesion was observed, similar to the observed experimental behaviour of cemented sands, where the cement content leads to the formation of strong interparticle bonds of chemical origin.
- The study of the combined effect of pressure and surface energy on the macroscopic shear strength, showed that the failure line tends to approach the solution

obtained without adhesion as the level of stress increases. This tendency was explained by the fact that the microscopic model used to simulate contact adhesion predicts a maximum adhesion force independent of the applied pressure, having disregarded the occurrence of plastic contact behaviour.

- A series of tests were carried out at different stress levels and for different values of surface energy. A linear relationship was obtained between the microscopic surface energy parameter and the macroscopic soil cohesion, demonstrating that a physical link exist between them.
- Dilatancy was found to be significantly enhanced by the presence of attractive forces. A higher porosity and coordination number were also indicators of the strong influence of vdW forces on mechanical soil behaviour. In particular, the ability of the sample to sustain a more porous structure due to surface energy forces, is in perfect agreement with the experimental observations of quartz sand tested under ultra-high vacuum conditions.
- The study of particle shape effects was first approached by introducing a simple rolling resistance model. The partial hindering of particle rotations led to a much higher shear strength, which was able to replicate the high shear strength observed for lunar soil and lunar soil simulants. This finding confirmed the importance of particle shape in determining the mechanical behaviour of granular materials. Furthermore, the existence of the interplay between adhesion and particle shape effects was proved by the increased cohesion compared to the free-rolling solution. In this case, the macroscopic cohesion was observed to vary non-linearly with the rolling coefficient, while reaching a maximum value for $\eta \geq 0.6$. A very similar tendency was observed for the peak state friction angle. Finally, very little cohesion was observed at the critical state, in agreement with the findings obtained for spherical particles.
- Clumps of rigidly connected spherical particles were used as a more realistic method to account for the combined influence of particle shape effects and intergranular adhesion. Samples made of non-convex particles of increasing com-

plexity were generated and tested under the same loading conditions. Tests were run for different confining pressures, and peak and critical state parameters were obtained both with and without surface energy. A comparison of the results obtained with different clump models revealed that the macroscopic shear strength does not necessarily increase with the clump model's complexity. In the presence of adhesion, cohesion was found to be significantly high at the peak state but, as in all cases, it was shown to disappear towards the critical state regime. However, the high shear strength obtained with the calibrated rolling resistance model could not be achieved by means of simple clump models. This indicated that a more accurate description of the particle shape of lunar soil grains may be required.

(iv) Geotechnical implications of the observed lunar soil behaviour

- The macroscopic shear strength results obtained for lunar soil in the presence of adhesion and with calibrated rolling resistance, were used to solve three problems typical of geotechnical engineering: the problem of bearing capacity of a circular shallow foundation, wheel rolling resistance and the problem of slope stability of a vertical cut on the lunar surface. In all cases, owing to the remarkable difference between critical and peak state strength values, it was difficult to argue any conclusive solution. It was stated that this will depend on the level of operational strength, and so strain, required by the specific design study. However, a possible solution for the problem of bearing capacity was identified in the literature, which is able to account for the density and stress dependency of the soil strength parameters.
- A simple analytical solution was conceived to provide a reasonable solution to the complex wheel-soil interaction problem. The method had previously been applied for the sole case of a towed rigid wheel rotating on a deformable soil. The same approach was extended in this thesis in order to include the analogous cases of self-propelled and driven wheels. Parameters such as the total power consumption, the wheel sinkage into the soil and the normal and shear components of the

force exchanged at the wheel-soil interface were easily computed. The effect of different values of cohesion and friction angle were analysed and it was observed that a higher shear strength leads to a lower wheel sinkage and therefore lower requirement for total power. It turned out that the most efficient solution would be represented by a four-wheel vehicle with self-propelled wheels.

7.2 Recommendations for further work

Based on the research conducted in this thesis, recommendations for further studies include:

(i) The present DEM model should be integrated with a more faithful representation of the irregular particle shapes of lunar grains, *e.g.* using polyhedral particles to represent information from recently developed techniques, such as x-ray measurements Matsushima and Chang (2011).

(ii) Triaxial test experiments on real lunar soil, or representative lunar soil simulants, should be run under ultra-high vacuum conditions in order to obtain quantitative information about the stress-strain behaviour of real lunar material. This will allow the numerical and experimental findings to be closely compared.

(iii) Measurements of surface energy for real lunar soil should be carried out. As illustrated in this thesis, a more detailed knowledge of this parameter would lead to more accurate modelling of the shear strength properties of lunar soil. Research by NASA scientists is currently ongoing to devise a method that would allow the adhesion force to be precisely quantified (Wohl et al., 2011). A better understanding of the influence of surfaced roughness on the strength of surface energy forces would also be a welcome result from the analyses.

(iv) It is recommended that the DEM simulations, carried out for different inertial and stiffness numbers and presented in Chapter 4, be rerun for more realistic values of interparticle friction coefficient, i.e. much lower than 0.6. The importance of analysing the influence of friction on the quasi-static limit was clearly observed in the DEM

simulations with linear contacts discussed by Campbell (2005). Indeed it was noticed that the limiting quasi-static values in terms of stresses and porosities are significantly different for low friction particles. A similar investigation should be perform with non linear contacts to complement the findings presented in this thesis. In particular, it would be interesting to show how the influence of the dimensionless numbers on the critical state parameters varies with the interparticle friction coefficient.

(v) The current numerical model could be used in large-scale numerical simulations of boundary value problems, for instance to explore potential issues such as those related to cone penetration tests carried out on the lunar surface or trafficability analysis.

(vi) Finally, it would be useful to combine the current model with the influence of electrostatic interactions and apply this to solve some of the open issues involving lunar dust phenomena, in order to assist with the development of new methods to mitigate the potential threats (*e.g.* surface abrasion, respiratory distress) due to lunar dust (*i.e.* the very fine portion of the lunar regolith, with particle size $\leq 20\mu$m).

7.3 Concluding remarks

This thesis has been concerned with the development and testing of a suitable model for computational simulation of lunar soil. The need for this is related to the difficulties in reproducing lunar environmental conditions in laboratory experiments. A particle-based microscopic approach was conceived as the best way to model a very fine sandy soil, such as lunar soil, while considering the effects of van der Waals forces acting between soil grains. The DEM approach led to representative quantitative results in terms of macroscopic lunar soil behaviour. Further insight was gained based on the introduction of micro-mechanical contact parameters, such as surface energy, which illustrated the non-negligible effects of UHV and low gravity on the macroscopic shear strength of the simulated lunar material.

Overall this research has demonstrated the benefit of using the DEM as a viable tool to model otherwise unresolved material behaviour through implementing contact models based

on continuum mechanics theories. Today's challenge, however, remains that of obtaining more quantitative and reliable data which requires some improvements on two fronts: increasing the computational power available and working on the development of technologies used to characterise the experimental grain-scale behaviour. The latter will lead to the implementation of more realistic contact models.

Bibliography

I. Agnolin and J.-N. Roux. Internal states of model isotropic granular packings. I. Assembling process, geometry, and contact networks. *Physical Review E*, 76, 2007.

I. Agnolin and J.-N. Roux. On the elastic moduli of three-dimensional assemblies of spheres: Characterization and modeling of fluctuations in the particle displacement and rotation. *International Journal of Solids and Structures*, 45:1101 – 1123, 2008.

J. Ai, J.-F. Chen, J. M. Rotter, and J. Y. Ooi. Assessment of rolling resistance models in discrete element simulations. *Powder Technology*, 206(3):269–282, 2011.

M. P. Allen and D. J. Tildesley. *Computer simulation of liquids*. Clarendon Press, 1987.

A. K. Alshibli and E. L. Roussel. Experimental investigation of slip-stick behaviour in granular materials. *International Journal for Numerical and Analytical Methods in Geomechanics*, 30(14), 2006.

K. A. Alshibli and A. Hasan. Strength Properties of JSC-1A Lunar Regolith Simulant. *Journal of Geotechnical Engineering*, 135(5):673–679, 2009.

K. A. Alshibli, S. N. Batiste, and S. Sture. Strain Localization in Sand: Plane Strain versus Triaxial Compression. *Journal of geotechnical and geoenvironmental engineering*, 129: 483–494, 2003.

H. Arslan, S. Batiste, and S. Sture. Engineering Properties of Lunar Soil Simulant JSC-1A. *Journal of Aerospace Engineering*, 23(1):70–83, 2010.

V. Asnani, D. Delap, and C. Creager. The development of wheels for the Lunar Roving Vehicle. *Journal of Terramechanics*, 46(3):89–103, 2009.

E. Azéma, F. Radjai, and G. Saussine. Quasistatic rheology, force transmission and fabric properties of a packing of irregular polyhedral particles. *Mechanics of Materials*, 41(6): 729–741, 2009.

K. Bagi. Stress and strain in granular assemblies. *Mechanics of Materials*, 22:165–177, 1996.

R. Baker. Nonlinear Mohr Envelopes Based on Triaxial Data. *Journal of geotechnical and geoenvironmental engineering*, 130:498–506, 2004.

O. Baran, A. Degennaro, and R. A. Wilkinson. Dem simulations of a schulze ring shear tester. In *Powders and Grains 2009: Proceedings of the 6th International Conference on Micromechanics of Granular Media, AEMMG*, Golden, CO., 2009.

M. G. Bekker. *Theory of land locomotion: the mechanics of vehicle mobility*. Ann Arbor, 1956.

M. G. Bekker. *Off-the-road locomotion: research and development in terramechanics*. University of Michigan Press, 1960.

N. Belheine, J. P. Plassiard, F. V. Donzé, F. Darve, and A. Seridi. Numerical simulation of drained triaxial test using 3D discrete element modeling. *Computers and geotechnics*, 36 (1-2):320–331, 2009.

Z. Bi, Q. Sun, F. Jin, and M. Zhang. Numerical study on energy transformation in granular matter under biaxial compression. *Granular Matter*, 13:503–510, 2011.

P. Blum, J. R. Roehrig, and M. J. Hordon. Adhesion of lunar soil simulated by rock comminuted in vacuum. In *Space simulation conference*, pages 1–8, Philadephia, Pennsylvania, 1967.

M. D. Bolton. The strength and dilatancy of sands. *Geotechnique*, 36(1):65–78, 1986.

Franck Bourrier, Franois Kneib, Bruno Chareyre, and Thierry Fourcaud. Discrete modeling of granular soils reinforcement by plant roots. *Ecological Engineering*, pages –, 2013.

L. G. Bromwell. Research in earth physics: the friction of quartz in high vacuum. Technical report, NASA, 1966.

C. S Campbell. Granular shear flows at the elastic limit. *Journal of Fluid Mechanics*, 465: 261–291, 2002.

C. S Campbell. Stress-controlled elastic granular shear flows. *Journal of Fluid Mechanics*, 539:273–297, 2005.

W. D. Carrier. Particle size distribution of lunar soil. *Journal of Geotechnical and Geoenvironmental Engineering*, 129:956–959, 2003.

W. D. Carrier. The four things you need to know about the geotechnical properties of lunar soil. Research note, Lunar Geotechnical Institute, 2005.

W. D. Carrier, G. R. Olhoeftm, and W. Mendell. Physical properties of the lunar surface. In G H Heiken, D T Vaniman, and B M French, editors, *Lunar sourcebook: a user's guide to the moon*. Cambridge University Press, 1991.

C. S. Chang and P. Y. Hicher. Model for granular materials with surface energy forces. *Journal of Aerospace Engineering*, 22:43–52, 2009.

W. F. Chen, M. W. Giger, and H. Y. Fang. On the limit analysis of stability of slopes. *Soil and foundation*, 9(4):23–32, 1969.

Y. P. Cheng, Y. Nakata, and M. D. Bolton. Discrete element simulations of crushable soil. *Geotechnique*, 7:633–641, 2003.

Y. P. Cheng, Y. Nakata, and M. D. Bolton. Micro- and macro-mechanical behaviour of DEM crushable materials. *Géotechnique*, 58(6):471–480, 2008.

S. Chhaniyara, C. Brunskill, B. Yeomans, M. C. Matthews, C. Saaj, S. Ransom, and L. Richter. Terrain trafficability analysis and soil mechanical property identification for planetary rovers: A survey. *Journal of Terramechanics*, 49(2):115–128, 2012.

G. C. Cho, J. Dodds, and J. C. Santamarina. Particle shape effects on packing density, stiffness, and strength: natural and crushed sands. *Journal of Geotechnical and Geoenvironmental Engineering*, 132(5):591–602, 2006.

D. M. Cole and J. F. Peters. Grain-scale mechanics of geologic materials and lunar simulants under normal loading. *Granular Matter*, 10(3):171–185, 2008.

N. C. Costes, J. E. Farmer, and E. B. George. Mobility performance of the lunar roving vehicle: terrestrial studies - Apollo 15 results. Technical report, NASA, 1972.

P. A. Cundall. A computer model for simulating progressive, large-scale movements in blocky rock systems. In *Proc. Symp. Int. Soc. Rock Mech.*, 1971.

P. A. Cundall and O. D. L. Strack. A discrete numerical model for granular assemblies. *Geotechnique*, 29(1):47–65, 1979.

F. da Cruz, S. Emam, M. Prochnow, J.-N. Roux, and F. Chevoir. Rheophysics of dense granular materials: Discrete simulation of plane shear flows. *Physical Review E*, 72, 2005.

B. Dahneke. The influence of flattening on the adhesion of particles. *Journal of Colloid and Interface Science*, 40(1):1–13, 1970.

B. Derjaguin. Untersuchungen über die reibung und adhäsion, iv. *Kolloid-Zeitschrift*, 69: 155–164, 1934.

B. V. Derjaguin, V. M. Muller, and Y. P. Toporov. Effect of contact deformations on the adhesion of particles. *Journal of Colloid and Interface Science*, 53(2):314–326, 1975.

C. di Prisco and S. Imposimato. Experimental analysis and theoretical interpretation of triaxial load controlled loose sand specimen collapses. *Mechanics of Cohesive-Frictional Materials*, 2:93–120, 1997.

L. Ding, Z. Deng, H. Gao, K. Nagatani, and K. Yoshida. Planetary rovers' wheel–soil interaction mechanics: new challenges and applications for wheeled mobile robots. *Intelligent Service Robotics*, 4(1):17–38, 2010.

C. Dominik and A. G. G. M. Tielens. Resistance to rolling in the adhesive contact of two elastic spheres. *Philosophical Magazine A*, 72(3):783–803, 1995.

Douglas Aircraft Company. Ultrahigh vacuum adhesion related to the lunar surface. Technical Report CR-1090, NASA, 1968.

N. Estrada, A. Taboada, and F. Radjaï. Shear strength and force transmission in granular media with rolling resistance. *Physical Review E*, 78(2), 2008.

N. Estrada, E. Azéma, F. Radjai, and A. Taboada. Identification of rolling resistance as a shape parameter in sheared granular media. *Phys. Rev. E*, 84, 2011.

P. Evesque and F. Adjemian. Stress fluctuations and macroscopic stick-slip in granular materials. *The European Physical Journal E - Soft Matter*, 9:253–259, 2002.

C. Goldenberg and I. Goldhirsch. Friction enhances elasticity in granular solids. *Nature*, 435:188–191, 2005.

J. Graf. Lunar soil grain size catalog. Technical report, NASA, 1993.

J. A. Greenwood. Adhesion of elastic spheres. *Proceedings of the Royal Society A: Mathematical, Physical and Engineering Sciences*, 453(1961):1277–1297, 1997.

J. J. Grossman, J. A. Ryan, N. R. Mukherje, and M. W. Wegner. Surface Properties of Lunar Samples. *Science*, 167(3918):743–745, 1970.

J. P. Hambleton and A. Drescher. Modeling wheel-induced rutting in soils: Rolling. *Journal of Terramechanics*, 46(2):35–47, 2009.

R. Hart, P. A. Cundall, and J. Lemos. Formulation of a three-dimensional distinct element model—Part II. Mechanical calculations for motion and interaction of a system composed of many polyhedral blocks. *Int. J Rock Mech. Min. Sci. & Geomech.*, 25(3):117–125, 1988.

A. Hasan and K. A. Alshibli. Discrete Element Modeling of Strength Properties of Johnson Space Center (JSC-1A) Lunar Regolith Simulant. *Journal of Aerospace Engineering*, 23 (3):157–165, 2010.

C. He. *Geotechnical characterization of lunar regolith simulants*. PhD thesis, Case Western Reserve University, 2010.

H. Hertz. On the contact of rigid elastic solids and on hardness. In Hertz H. and Schott J. A., editors, *Miscellaneous papers by*. London: MacMillan, 1882.

E. Hoek and E. T. Brown. Empirical strength criterion for rock masses. *Journal of Geotechnical Engineering*, 106(9):1013–1035, 1980.

W. N. Houston and L. I. Namiq. Pentration Resistance of Lunar Soils. *Journal of Terramechanics*, 8(1):59–69, 1971.

H. J. Hovland. Mechanics of wheel-soil interaction. Technical report, NASA, 1973.

H. J. Hovland and J. K. Mitchell. Boulder tracks and nature of lunar soil. *Earth, Moon, and Planets*, 6(1):164–175, 1973.

J. Israelachvili. *Intermolecular & Surface Forces*. Academic Press, 1991.

Itasca. *PFC-3D Manual*. 1999.

K. Iwashita and M. Oda. Rolling resistance at contacts in simulation of shear band development by DEM. *Journal of Engineering Mechanics*, 124(3):285–292, 1998.

L. D. Jaffe. Bearing strength of Lunar Soil. In *The Moon 3*, pages 337–345, 1971.

Z. Janosi and B. Hanamoto. Analytical determination of drawbar pull as a function of slip for tracked vehicles in deformable soils. In *Proceedings of the first international conference on terrainvehicle systems*, Torino, Italy, 1961.

M. J. Jiang, H. S. Yu, and D. Harris. Bond rolling resistance and its effect on yielding of bonded granulates by DEM analyses. *International Journal for Numerical and Analytical Methods in Geomechanics*, 30(8):723–761, 2006.

M. J. Jiang, H. B. Yan, H. H. Zhu, and S. Utili. Modeling shear behavior and strain localization in cemented sands by two-dimensional distinct element method analyses. *Computers and Geotechnics*, 38:14–29, 2011.

B. V. Johnson, W. W. Roepke, and K. C. Strebig. Shear Testing of Simulated Lunar Soil in Ultrahigh Vacuum. Technical report, NASA, 1973.

F. S. Johnson. Lunar atmosphere. *Review of geophysics*, 9(3):813–823, 1971.

K. L. Johnson. *Contact Mechanics*. Cambridge University Press, 1985.

K. L. Johnson, K. Kendall, and A. D. Roberts. Surface energy and the contact of elastic solids. *Proceedings of the Royal Society of London. Series A: Mathematical and Physical Sciences*, 324(1558):301–313, 1971.

S. Sture K. A. Alshibli and N. C. Costes. Constitutive and stability behaviour of soils in microgravity environment. In *Space Technology and Applications International Forum*, 2000.

K. Kendall. Inadequacy of coulomb's friction law for particle assemblies. *Nature*, 319(1986): 203–205, 1986.

J. L. Klosky, S. Sture, Hon-Yim Ko, and F. Barnes. Geotechnical Behaviour of JSC-1 Lunar Soil Simulant. *Journal of Aerospace Engineering*, 13(4):133–138, 2000.

M. A. Knuth, J. B. Johnson, M. A. Hopkins, R. J. Sullivan, and J. M. Moore. Discrete element modeling of a Mars Exploration Rover wheel in granular material. *Journal of Terramechanics*, 49(1):27–36, 2012.

J. Kozicki, J. Tejchman, and Z. Mróz. Effect of grain roughness on strength, volume changes, elastic and dissipated energies during quasi-static homogeneous triaxial compression using DEM. *Granular Matter*, 14(4):457–468, 2012.

J. Kumar and V. N. Khatri. Effect of footing width on bearing capacity factor N for smooth strip footings. *Journal of Geotechnical and Geoenvironmental Engineering*, 134 (9):1299–1310, 2008.

G. Kuwabara and K. Kono. Restitution coefficient in collision between two spheres. *Japanese Journal of Applied Physics*, 26:1230–1233, 1987.

C. Q. LaMarche, J. S. Curtis, and P. T. Metzger. Permeability of JSC-1A: A lunar soil simulant. *Icarus*, 212(1):383–389, 2011.

J. E. Lane, P. T. Metzger, and R. A. Wilkinson. A Review of Discrete Element Method (DEM) Particle Shapes and Size Distributions for Lunar Soil. Technical report, NASA, 2010.

S. J. Lee, Y. M. A. Hashash, R. A. Wilkinson, and J. H. Agui. Simulation of Experimental tests on the JSC-1A Lunar Soil Simulant with Polyhedral Discrete Elements. In *Earth and Space 2010: Engineering, Science, Construction, and Operations in Challenging Environments*, 2010.

S. J. Lee, Y. M. A. Hashash, and E. G Nezami. Simulation of triaxial compression tests with polyhedral discrete elements. *Computers and geotechnics*, 43:92–100, 2012.

W. Li, Y. Huang, Y. Cui, S. Dong, and J. Wang. Trafficability analysis of lunar mare terrain by means of the discrete element method for wheeled rover locomotion. *Journal of Terramechanics*, 47(3):161–172, 2010.

M. Lu and G. R. McDowell. The importance of modelling ballast particle shape in the discrete element method. *Granular Matter*, 9(1-2):69–80, 2006.

S. Luding. Micro–macro transition for anisotropic, frictional granular packings. *International Journal of Solids and Structures*, 41, 2004.

S. Luding. Granular media: Information propagation. *Nature*, 435:159–160, 2005.

C. M. Martin. The use of adaptive finite-element limit analysis to reveal slip-line fields. *Geotechnique Letters*, 1(2):23–29, 2011.

T. Matsushima and C. S. Chang. Quantitative evaluation of the effect of irregularly shaped particles in sheared granular assemblies. *Granular Matter*, 13(3):269–276, 2011.

T. Matsushima, J. Katagiri, K. Uesugi, A. Tsuchiyama, and T Nakano. 3D Shape Characterization and Image-Based DEM Simulation of the Lunar Soil Simulant FJS-1. *Journal of Aerospace Engineering*, 22(1):15–23, 2009.

D. Maugis. Adhesion of spheres: the JKR-DMT transition using a Dugdale model. *Journal of Colloid and Interface Science*, 150(1):243–269, 1992.

D. S. McKay, J. L. Carter, W. W. Boles, C. A. Carlton, and J. H. Allton. JSC-1: A new lunar simulant. In *Proc., Symp. 94*, 1994.

R. L. Michalowski. Stability Charts for Uniform Slopes. *Journal of Geotechnical and Geoenvironmental Engineering*, 128(4):351–355, 2002.

R. D. Mindlin. Compliance of elastic bodies in contact. *Journal of Applied Mechanics*, 16 (1):259–344, 1949.

R. D. Mindlin and H. Deresiewicz. Elastic spheres in contact under varying oblique force. *Journal of Applied Mechanics*, 16(1):259–344, 1953.

J. K. Mitchell, W. N. Houston, R. F. Scott, N. C. Costes, W. D. Carrier, and L. G. Bromwell. Mechanical properties of lunar soil: Density, porosity, cohesion, and angle of internal friction. In *Proceedings of the Third Lunar Science Conference*, 1972.

C. Modenese, S. Utili, and G.T. Houlsby. A numerical investigation of quasi-static conditions for granular media. In *Discrete Element Modelling of Particular Media (Special Publication)*. Royal Society of Chemistry, 2012a.

C. Modenese, S. Utili, and G.T. Houlsby. A study of the influence of surface energy on the mechanical properties of lunar soil by dem. In *Discrete Element Modelling of Particular Media (Special Publication)*. Royal Society of Chemistry, 2012b.

C. Modenese, S. Utili, and G.T. Houlsby. Dem modelling of elastic adhesive particles with application to lunar soil. In *Earth and Space 2012. Engineering, Science, Construction, and Operations in Challenging Environments*. ASCE, 2012c.

A. Mohamed and M. Gutierrez. Comprehensive study of the effects of rolling resistance on the stress–strain and strain localization behavior of granular materials. *Granular Matter*, 12(5):527–541, 2010.

V. M. Muller, V. S. Yushchenko, and Derjaguin, B.V. On the influence of molecular forces on the deformation of an elastic sphere and its sticking to a rigid plane. *Journal of Colloid and Interface Science*, 77(1):91–101, 1980.

H. Nakashima, H. Fujii, A. Oida, M. Momozu, Y. Kawase, H. Kanamori, S. Aoki, and T. Yokoyama. Parametric analysis of lugged wheel performance for a lunar microrover by means of DEM. *Journal of Terramechanics*, 44(2):153–162, 2007.

H. Nakashima, H. Fujii, A. Oida, M. Momozu, H. Kanamori, S. Aoki, T. Yokoyama, H. Shimizu, J. Miyasaka, and K. Ohdoi. Discrete element method analysis of single wheel performance for a small lunar rover on sloped terrain. *Journal of Terramechanics*, 47(5): 307–321, 2010.

J. D. Nelson and E. Vey. Relative cleanliness as a measure of lunar soil strength. *Journal of Geophysical Research*, 73(12):3747–3764, 1968.

T. T. Ng. Macro- and micro-behaviors of granular materials under different sample preparation methods and stress paths. *International Journal of Solids and Structures*, 41, 2004.

T. T. Ng. Discrete element method simulations of the critical state of a granular material. *International Journal of Geomechanics*, 9(5):209–216, 2009.

H. A. Oravec. *Understanding Mechanical Behaviour of Lunar Soils for the Study of Vehicle*. PhD thesis, Case Western Reserve University, 2009.

H. A. Oravec, X. Zeng, and V. M. Asnani. Design and characterization of GRC-1: A soil for lunar terramechanics testing in Earth-ambient conditions. *Journal of Terramechanics*, 47 (6):361–377, 2010.

A. C. Palmer. *Dimensional Analysis and Intelligent Experimentation*. World Scientific Publishing Co. Pte. Ltd., 2007.

J. Papike, L. Taylor, and S. Simon. Lunar minerals. In G H Heiken, D T Vaniman, and B M French, editors, *Lunar sourcebook: a user's guide to the moon*. Cambridge University Press, 1991.

M. D. Pashley. Further consideration of the DMT model for elastic contact. *Colloids and surfaces*, 12:69–77, 1984.

A. A. Peña, R. García-Rojo, and H. J. Herrmann. Influence of particle shape on sheared dense granular media. *Granular Matter*, 9(3-4):279–291, March 2007.

A. A. Peña, R. García-Rojo, F. Alonso-Marroquín, and H. J. Herrmann. Investigation of the critical state in soil mechanics using DEM. In *AIP Conference Proceedings*, pages 185–188, 2009.

S. W. Perkins and C. R. Madson. Mechnical and Load-Settlement Characteristics of Two Lunar Soil Simulants. *Journal of Aerospace Engineering*, 9(1):1–9, 1996.

S. W. Perkins and C. R. Madson. Bearing capacity of shallow foundations on sand: A relative density approach. *Journal of Geotechnical Engineering*, 126(6):521–530, 2000.

H. A. Perko and J. D. Nelson. Effects of vacuum and reduced gravity on bearing capacity. In S W Johnson, K M Chua, R Gallowang, and P Richter, editors, *Proceedings of Space 2000: Int. Conf. and Expo. on Eng., Const., and Ops. in Space*, 2000.

H. A. Perko, J. D. Nelson, and W. Z. Sadeh. Surface cleanliness effect on lunar soil shear strength. *Journal of Geotechnical and Geoenvironmental Engineering*, 127(4):371–383, 2001.

P.-E. Peyneau and J.-N. Roux. Frictionless bead packs have macroscopic friction, but no dilatancy. *Phys. Rev. E*, 78:011307, 2008.

J.-P. Plassiard, N. Belheine, and F. Donzé. A spherical discrete element model: calibration procedure and incremental response. *Granular Matter*, 11(5):293–306, 2009.

V. L. Poul and D. O. Daniel. Cementation Effects in Frictional Materials. *Journal of Geotechnical Engineering*, 115:1373–1387, 1989.

L. Prandtl. ber die Eindringungs-festigkeit (Hrte) plastischer Baustoffe und die Festigkeit von Schneiden. *Zeitschrift fr Angewandte Mathematik und Mechanik*, 1(1):15–20, 1920.

F. Radjai and F. Dubois, editors. *Discrete-element Modelling of Granular Materials*. ISTE and Wiley, 2011.

E. Ramé, A. Wilkinson, A. Elliot, and C. Young. Flowability of lunar soil simulant JSC-1A. *Granular Matter*, 12(2):173–183, 2010.

H. Reissner. Zum Erddruckproblem. In *Proc. First Congr. Appl. Mech.*, pages 295–311, 1924.

D. Rickman, C. Immer, P. Metzger, E. Dixon, M. Pendleton, and J. Edmunson. Particle Shape In Simulants of the Lunar Regolith. *Journal of Sedimentary Research*, 82(11): 823–832, 2012.

L. Rothenburg and R. J. Bathurst. Influence of particle eccentricity on micromechanical behavior of granular materials. *Mechanics of Materials*, 16(1):141–152, 1993.

J.-N. Roux and G. Combe. On the meaning and microscopic origins of quasistatic deformation of granular materials. In *16th ASCE Engineering Mechanics Conference, University of Washington, Seattle*, 2003.

J.-N. Roux and G. Combe. How granular materials deform in quasi static conditions. In *IUTAM-ISIMM Symposium on Mathematical Modeling and Physical Instances of Granular Flows*, 2010.

P. W. Rowe. The stress-dilatancy relation for the static equilibrium of an assembly of particles in contacts. *Proceedings of the Royal Society A: Mathematical, Physical and Engineering Sciences*, pages 500–527, 1962.

A. Sadrekarimi and S. M. Olson. Critical state friction angle of sands. *Geotechnique*, 9: 771–783, 2011.

C. Salot, P. Gotteland, and P. Villard. Influence of relative density on granular materials behavior: DEM simulations of triaxial tests. *Granular Matter*, 11(4):221–236, 2009.

J. C. Santamarina and G. C. Cho. Soil behaviour: The role of particle shape. In *Skempton Conference*, pages 1–14, London, 2004.

T. Schanz and P. A. Vermeer. Angles of friction and dilatancy of sand. *Géotechnique*, 46 (1):145–151, 1996.

A. Schofield and P. Wroth. *Critical State Soil Mechanics*. McGraw-Hill, 1968.

C. M. Schrader, J. E. Edmunson, and D. L. Rickman. Generation of Requirements for Simulant Measurements. Technical Report TM–2010-216445, NASA, 2010a.

C. M. Schrader, D. L. Rickman, C. A. McLemoew, and J. C. Fikes. Lunar Regolith Simulant User's Guide. Technical Report TM–2010-216446, NASA, 2010b.

R. F. Scott. Failure. *Géotechnique*, 37:423–466, 1987.

M. M. M. Shamsi and A. A. Mirghasemi. Numerical simulation of 3D semi-real-shaped granular particle assembly. *Powder Technology*, 221:431–446, 2012.

L. Sibille, P. Carpenter, R. Schlagheck, and R. A. French. Lunar Regolith Simulant Materials: Recommendations for Standardization, Production and Usage. Technical Report TP–2006-214605, NASA, 2005.

P. Simonini. Influence of relative density and stress level on the bearing capacity of sands. *International Journal for Numerical and Analytical Methods in Geomechanics*, 17(12): 871–890, 2005.

T. G. Sitharam and J. S. Vinod. Critical state behaviour of granular materials from isotropic and rebounded paths: DEM simulations. *Granular Matter*, 11(1):33–42, 2009.

V. Smilauer, E. Catalano, B. Chareyre, S. Dorofeenko, J. Duriez, A. Gladky, J. Kozicki, C. Modenese, L. Scholts, L. Sibille, J. Strnsk, and K. Thoeni. Yade Reference Documentation. In V. milauer, editor, *Yade Documentation*. The Yade Project, 1st edition, 2010. http://yade-dem.org/doc/.

Vaclav Smilauer. *Cohesive Particle Model using the Discrete Element Method on the Yade Platform*. PhD thesis, Czech Technical University in Prague, Faculty of Civil Engineering & Universit Grenoble I – Joseph Fourier, cole doctorale I-MEP2, 2010.

S. Sture, N. C. Costes, S. N. Batiste, M. R. Lankton, K. A. Alshibli, and R. A. Swanson. Mechanics of Granular Materials at Low Effective Stresses. *Journal of Aerospace Engineering*, 11(3):67–72, 1998.

D Tabor. Surface forces and surface interactions. *Journal of Colloid and Interface Science*, 58(1):2–13, 1977.

K. Terzaghi. *Theoretical soil mechanics*. Wiley, 1943.

S. Thomas and P. Thorsten. Coefficient of restitution and linear-dashpot model revisited. *Granular Matter*, 9:465–469, 2007.

C. Thornton. On the relationship between the modulus of particulate media and the surface energy of the constituent particles. *Journal of Physics D: Applied Physics*, 26(10), 1999.

C. Thornton and S. J. Antony. Quasi-static deformation of particulate media. *Philosophical transactions of the Royal Society. Series A: Mathematical, Physical and Engineering Sciences*, 1998.

C. Thornton and S. J. Antony. Quasi-static shear deformation of a soft particle system. *Powder Technology*, 109:179–191, 2000.

C. Thornton and Z. Ning. A theoretical model for the stick/bounce behaviour of adhesive, elastic-plastic spheres. *Powder Technology*, 99(2):154–162, 1998.

C. Thornton and K. K. Yin. A numerical examination of shear banding and simple shear non-coaxial flow rules. *Philosophical Magazine*, 86(21):3425–3452, 2006.

C. Thornton, S. J. Cummis, and P. W. Cleary. An investigation of the comparative behaviour of alternative contact force models during elastic collisions. *Powder Technology*, 210:189–197, 2011.

T. Ueda, T. Matsushima, and Y. Yamada. Effect of particle size ratio and volume fraction on shear strength of binary granular mixture. *Granular Matter*, 13(6):731–742, 2011.

S. Utili. *Evolution of natural slopes subject to weathering: An analytical and numerical study.* PhD thesis, Politecnico di Milano, 2006.

A. S. Vesic. Analysis of ultimate loads of shallow foundations. *Journal of the Soil Mechanics and Foundation Division*, 99(1):45–73, 1973.

A. S. Vesic. *Foundation Engineering Handbook*, chapter Bearing capacity of shallow foundation. Springer, 1991.

E. Vey and J. D. Nelson. Studies of lunar soil mechanics - Phase 1. Technical report, NASA, 1963.

E. Vey and J. D. Nelson. Studies of lunar soil mechanics - Phase 2. Technical report, NASA, 1965.

E. Vey and J. D. Nelson. Studies of lunar soil mechanics - Phase 3. Technical report, NASA, 1966.

O. Walton. Review of adhesion fundamentals for micron-scale particles. *KONA Powder and Particle Journal*, 26, 2008.

O. R. Walton. Adhesion of lunar dust. Technical Report CR–2007-214685, NASA, 2007.

O. R. Walton. DEM Simulations of the Effects of Particle Shape, Interparticle Cohesion and Gravity on Rotating Drum Flows of Lunar Regolith. In *Earth and Space 2010: Engineering, Science, Construction, and Operations in Challenging Environments*, pages 36–41, 2010.

O. R. Walton and R. L. Braun. Viscosity, granular?temperature, and stress calculations for shearing assemblies of inelastic, frictional disks. *Journal of rheology*, 30, 1986.

O. R. Walton, C. P. De Moor, and K. S. Gill. Effects of gravity on cohesive behaviour of fine powders: implications for processing Lunar regolith. *Granular Matter*, 9:353–363, 2007.

Y. H. Wang and S. C. Leung. Characterization of cemented sand by experimental and numerical investigations. *Journal of geotechnical and geoenvironmental engineering*, 134: 992–1004, 2008.

A. Wilkinson. Surface Energy of Lunar Soil Simulants. In *41st Central Regional Meeting of the American Chemical Society*, Cleveland, Ohio, 2009.

B. M. Willman, W. W. Boles, D. S. McKay, and C. C. Allen. Properties of Lunar Soil Simulant JSC-1. *Journal of Aerospace Engineering*, 8(2):77–87, 1995.

C. J. Wohl, B. M. Atkins, and J.W. Connell. Method and Apparatus for the Quantification of Particulate Adhesion Forces on Various Substrates. Technical report, NASA, 2011.

M. D. Wood and K. Maeda. Changing grading of soil: effect on critical states. *Acta Geotechnica*, 3(1):3–14, 2008.

J. A. Yamamuro and P. V. Lade. Drained sand behavior in axisymmetric tests at high pressures. *Journal of Geotechnical Engineering*, 122(2):109–119, 2001.

X. Zeng, C. He, H. Oravec, A. Wilkinson, J. Agui, and V. Asnani. Geotechnical Properties of JSC-1A Lunar Soil Simulant. *Journal of Aerospace Engineering*, 23(2):111–116, 2010.

X. Zhao and T. M. Evans. Numerical analysis of critical state behaviors of granular soils under different loading conditions. *Granular Matter*, 13(6):751–764, 2011.